Tensile behaviour of steel-reinforced elements made of strain-hardening cement-based composites

Zum Zugtragverhalten von stahlbewehrten Bauteilen aus hochduktilem Beton

Von der Fakultät Bauingenieurwesen

der Technischen Universität Dresden

zur Erlangung der Würde eines Doktor-Ingenieurs (Dr.-Ing.)

genehmigte

DISSERTATION

vorgelegt von

Dipl.-Ing. Eric Mündecke

aus Waren (Müritz)

eingereicht am 17.08.2017

Tag der mündlichen Prüfung: 27.11.2017

Gutachter:

Prof. Dr.-Ing. Viktor Mechtcherine

Prof. Dr.-Ing. habil. Peter Mark

Prof. dr. ir. Gideon P.A.G. van Zijl

Herausgeber: Prof. Dr.-Ing. Viktor Mechtcherine

Institut für Baustoffe
Fakultät Bauingenieurwesen
Technische Universität Dresden
01062 Dresden

Telefon: +49 351 463 36311
Telefax: +49 351 463 37268
Email: i.baustoffe@tu-dresden.de

Druck: Druckerei & Verlag Fabian Hille, Boderitzer Straße 21e, 01217 Dresden

ISBN 978-3-86780-564-3

Abstract

This study investigates the load-bearing behaviour of steel-reinforced elements made of strain-hardening cement-based composites (SHCC) subjected to tensile loading. Previous research has shown that the combination of steel reinforcement and high performance cementitious materials such as SHCC can lead to an enhanced structural behaviour in terms of mechanical properties and durability. These properties are achieved by the specific material design and use of short polymer fibres embedded into the cementitious matrix of SHCC, which stabilise the crack growth and enable multiple cracks to develop.

While considerable research has been performed at the material level, only limited information is available on the performance of structural members made of SHCC, specifically, of those reinforced with steel bars. Previous studies have shown that the behaviour of such composite elements is – among other factors – influenced by the degree of reinforcement, the material properties of steel and SHCC as well as the bond properties of the rebar interface.

In this thesis, experimental investigations were performed to systematically analyse the effect of the production process and specimen size on the material properties of SHCC, as well as the effect of steel reinforcement on the deformation behaviour of large-scale reinforced SHCC (R/SHCC) tension members. The material properties of specimens produced in a concrete plant were analysed and compared to reference specimens obtained from laboratory mixes. The results showed that the production process of SHCC can considerably influence the material properties of SHCC. In particular, tensile strength and strain capacity were reduced in the study at hand as a result of changes in the micro-structure of the cement-based composite. Uniaxial tension tests with large unreinforced SHCC slabs showed a further decrease in tensile strength and strain capacity. It was shown that a portion of these changes stem from eccentricities and imperfections, which were found to increase with specimen size.

The tensile behaviour of structural R/SHCC members was analysed by means of uniaxial tension tests on large reinforced slab elements. The aim of this experimental investigation was to study the contribution of SHCC to the global load-bearing behaviour of reinforced tension members with special attention to the effect of steel yielding on the crack development of the fibre-reinforced cement-based composite. The tests revealed that steel reinforcement – especially in a symmetrical configuration – can reduce the effect of eccentricities and enhance control of crack widths. However, the maximum strain capacity of R/SHCC elements was found to be limited to the yielding strain of steel reinforcement.

The experimental results were discussed with respect to their implications for constitutive modelling of the tensile load-bearing behaviour. Specific attention was devoted to the effect of local steel yielding and the cracking behaviour of SHCC. It was shown that a superposition of the tensile stress-strain curves of SHCC and steel reinforcement may overestimate total deformations and hence structural ductility.

Kurzfassung

Hochduktiler Beton ist ein mit kurzen Kunststofffasern bewehrter Hochleistungsverbundwerkstoff auf Zementbasis, der unter Zugbelastung eine hohe nichtelastische Verformbarkeit und ein verfestigendes Materialverhalten aufweist. Dieses Verhalten wird durch die Zugabe von diskontinuierlich verteilten Kurzfasern aus Kunststoff erzielt. Dabei wird die rissüberbrückende Wirkung der Kurzfasern genutzt, um Zugspannungen über feine Risse zu übertragen, wobei eine weitere Steigerung der Zugspannung ermöglicht wird.

Der alleinige Einsatz von Fasern als Bewehrung ist im konstruktiven Ingenieurbau jedoch auf wenige Anwendungsgebiete beschränkt, sodass in tragenden Bauteilen eine Kombination von hochduktilem Beton und konventioneller Stahlbewehrung sinnvoll erscheint. Das Zusammenwirken von hochduktilem Beton mit Stabstahlbewehrung bei Zugbeanspruchung, wird dabei im Wesentlichen von der Kombination der mechanischen Eigenschaften der Bewehrung, des hochduktilen Betons und des Verbundes zwischen den beiden Komponenten bestimmt. Um diese Zusammenhänge im bauwerksrelevanten Maßstab zu analysieren, wurden in der vorliegenden Arbeit einachsige Bauteilzugversuche durchgeführt auf deren Basis das globale und lokale Zugtragverhalten der großformatigen Versuchskörper beschrieben werden kann.

Ausgangspunkt sind experimentelle Untersuchungen zum Tragverhalten des Stabstahls und des hochduktilen Betons sowie zu deren gemeinsamen Verbundverhalten. Für die Herstellung großformatiger Versuchskörper wurde zusätzlich der Einfluss des Herstellungsprozesses auf das Verfestigungsverhalten des hochduktilen Betons und das Schwindverhalten untersucht. Die Untersuchungen zeigen, dass der Herstellungsprozess das Betongefüge und damit auch das mechanische Verhalten von hochduktilem Beton beeinflusst und dieser auf Grund seiner Zusammensetzung ein ausgeprägtes Schwindverhalten aufweist. Beides muss bei der Untersuchung großformatiger Versuchskörper berücksichtigt werden. Dazu wurden sowohl unbewehrte als auch bewehrte Dehnkörper mit unterschiedlichem Bewehrungsgehalt unter kontrollierten Herstellungsbedingungen in einem konventionellen Mischwerk hergestellt. Anhand dieser Probekörper wurde das Last-Verformungsverhalten sowie das Rissverhalten unter einachsiger Zugbeanspruchung analysiert.

Die Ergebnisse der experimentellen Untersuchung erlauben die Abbildung des Last-Verformungsverhaltens unter Berücksichtigung der hohen Schwindmaße durch isoliert ermittelte Spannungs-Dehnungs-Beziehungen des hochduktilen Betons und des reinen Stahls. Dieses Verfahren erlaubt eine einfache Beschreibung des kombinierten Tragverhaltens unter Berücksichtigung der rissüberbrückenden Wirkung der Fasern und der daraus resultierenden deutlichen Steigerung der Tragfähigkeit im Zustand II.

Vorwort des Herausgebers

Eine neue, vielversprechende Faserbetonart, der sog. hochduktile Beton mit Kurzfaserbewehrung (engl.: Strain-hardening Cement-based Composites, SHCC), weist unter Zugbeanspruchung ein hohes Verformungsvermögen mit einer Bruchdehnung von ca. 5 % auf. Die Verwendung solcher Betone im konstruktiven Ingenieurbau ist aus heutiger Sicht jedoch erst dann aussichtsreich, wenn die Aufnahme von bemessungsrelevanten Zugkräften zusätzlich durch eine konventionelle Stahlbewehrung abgesichert ist. Durch die Kombination von Kurzfaserbewehrung und Stabbewehrung aus Stahl soll die Tragfähigkeit von Bauteilen unter quasi-statischen Zugbeanspruchungen deutlich gesteigert werden. Außerdem werden überaus positive Auswirkungen auf die Dauerhaftigkeit, das Verhalten unter zyklischer Belastung und die Impaktsicherheit der Bauteile erwartet.

Zwar sind in den letzten Jahren in einigen Ländern erste Untersuchungen zum Zusammenwirken des hochduktilen Betons mit Stahlbewehrung durchgeführt worden, jedoch unter Verwendung meist kleiner und wenig repräsentativer Prüfkörper. Die vorliegende Datenbasis ermöglichte bisher weder das Verständnis der maßgebenden Mechanismen in Bezug auf das mechanische Verhalten des neuen Verbundwerkstoffes noch abgesicherte Aussagen zum Kraft-Verformungsverhalten der daraus hergestellten Bauteile. Die vorliegende Arbeit konnte diese Kenntnislücken schließen, indem das Zugtragverhalten von stahlbewehrten Bauteilen aus hochduktilem Beton experimentell untersucht und eine wissenschaftliche Grundlage für die Bemessung solcher Bauteile geschaffen wurde.

Im Mittelpunkt der Dissertation von Herrn Mündecke stehen die Zugversuche an Bauteilen aus unbewehrtem und mit Stahlstäben bewehrtem hochduktilem Beton. Diese unikalen Experimente ermöglichen neue, tiefgehende Einblicke in die Verformungs- und Versagensmechanismen des entwickelten Verbundwerkstoffes auf der Bauteilebene. Die Ausarbeitung, Durchführung, Auswertung und Interpretation dieser komplexen und aufwendigen Versuche bilden den zentralen Beitrag der vorliegenden Arbeit zur Erweiterung des Standes der Technik. Des Weiteren ist die modellhafte Beschreibung des mechanischen Verhaltens von bewehrtem hochduktilem Beton auf Bauteilebene hervorzuheben. Die Promotionsschrift ist hiermit eine bedeutende Leistung, die die Überführung moderner Faserverbundwerkstoffe in die Praxis vorbereitet, insbesondere im Hinblick auf die Verwendung von hochduktilem Beton in der Kombination mit Stahlbewehrung.

Die Dissertation von Herrn Mündecke entstand auf der Basis eines Kooperationsforschungsvorhabens des Instituts für Baustoffe an der TU Dresden, des Ingenieurbüros Grassl und der Firma SWING & CUT, welches durch die Arbeitsgemeinschaft industrieller Forschungsvereinigungen "Otto von Guericke" e.V. (AiF) gefördert wurde. Die Zusammenarbeit war überaus angenehm und fruchtbar, was einerseits auf die Persönlichkeit des Doktoranden und anderseits auf ein hohes

Engagement der Industriepartner zurückzuführen ist. In seiner heutigen Tätigkeit im Ingenieurbüro Grassl ist Herr Dr. Mündecke weiterhin an überaus innovativen Forschungsprojekten beteiligt, wodurch die Implementierung der wissenschaftlichen Erkenntnisse in die Baupraxis gefördert wird. Ich freue mich über die Fortsetzung des gemeinsamen Wirkens und wünsche Eric Mündecke weiterhin viel Erfolg und alles Gute!

Viktor Mechtcherine

Acknowledgements

My first steps in the field of fibre-reinforced cementitious composites started with the experimental, analytical and numerical examination of pull-out tests at Stellenbosch University in South Africa under the supervision of Prof. W.P. Boshoff, whose help is gratefully acknowledged. However, many questions remained unanswered, which inspired me to continue in this field and study the effect of the material and bond properties on the structural behaviour.

This was only possible with the support and encouragement of my supervisor Prof. V. Mechtcherine, to whom I would like to express my deepest gratitude for his guidance and support throughout this work. I would also like to thank Prof. P. Mark and Prof. G.P.A.G. van Zijl for taking an interest in this work and for their participation as co-advisors. I would like to express my gratitude to the thesis committee members namely Prof. F. Wellner, Prof. U. Häußler-Combe and Dr. C. Scheffler for their interest in my work.

Special thanks are due to my colleagues at the Institute of Construction Materials at the TU Dresden, in particular S. Müller and former member A.E. Brüdern, for sharing their experience with SHCC mix design and production procedures. I would also like to thank the staff members of the laboratory Dr. M. Butler, K.U. Mehlisch, T. Günzel, C. Stahn, S. Hempel and A. Willomitzer for the assistance with the extensive laboratory work.

Further thanks should go to the Institute of Reinforced Concrete Structures at the TU Dresden, especially former members Dr. L. Eckfeldt and Dr. S. Schröder, for their professional advice and fruitful discussions as well as the staff of the Otto-Mohr-Laboratory including Dr. T. Hampel and K. Dietz among many others for their cooperation and assistance with the handling of the extensive experimental work.

This work was performed in the course of the research project “Development of SHCC Elements for the Application in Bridge Structures”, funded by the Arbeitsgemeinschaft industrieller Forschungsvereinigungen "Otto von Guericke" e.V. (AiF), which is greatfully acknowledged. Thanks are also due to SWING & CUT for their help in the production of the large-scale specimens as well as BERGER BETON for providing the materials and production facilities.

I would also express my deepest gratitude to Manfred and Martin Grassl for their ongoing interest and support in this research project. Last but not least, I would like to thank my dearest family and friends for their support and patience, which was required quite a few times.

Dresden, March 2018

Eric Mündecke

Table of Contents

1 Introduction

1.1 Background

Advances in concrete technology have led to a wide variety of cement-based materials, which are used in practice of construction today. Such materials are often characterised by a high brittleness and a low tensile strength. Once the tensile strength of the cementitious matrix is exceeded, cracks form and the material loses its ability to carry tensile loads. Due to the brittle mode of failure, unreinforced cement-based materials are often unsuitable for typical loading conditions of load-bearing structures. These disadvantages are commonly compensated by the use of reinforcement, which transfers tensile forces after concrete has cracked and ensures the functionality of a structural element. Over time, various types of materials, e.g. steel, polymer or glass fibre, have been used as reinforcement. The most common type of reinforcement is steel rebars, while fibre-reinforced polymer (FRP) rebars are gaining increasing importance. A recent development in this field is textile reinforced concrete (TRC), which can further enhance the load-bearing capacity and durability of a structure [16, 17, 96, 97, 132].

Even though the mechanical interaction between reinforcement and concrete can prevent element failure, cracking is still likely to occur. These cracks can cause an early deterioration of the reinforced element – for example, due to steel corrosion – which limits the durability of a structural element. Possible solutions to address this problem include the application of non-corrosive reinforcement materials or the limitation of crack widths. The latter is usually achieved by providing the required minimum reinforcement in the serviceability limit state, which can conflict with an economic design of the structure.

Therefore, a promising approach to address this problem is the application of strain-hardening cement-based composites (SHCC), which have a significantly higher ductility than ordinary concrete (OC). SHCC belongs to the group of high performance fibre-reinforced cement-based composites (HPFRCCs) and is developed especially for strain-hardening, quasi-ductile[1] behaviour. Both are achieved through the combined interaction of short polymer fibres dispersed in the cementitious matrix, which facilitate a gradual formation of micro-cracks with limited crack widths. The multiple cracking accompanied by tensile strain-hardening behaviour allows the material to reach an ultimate tensile strain beyond 3% [83].

Even though SHCC provides enhanced ductility at the material level, reinforcement is still required to ensure structural reliability. The design of structural members containing SHCC – especially in combination with steel reinforcement (R/SHCC) – requires sufficient knowledge of the mechanical behaviour under tensile loading.

---

[1] The term “quasi-ductile” is chosen, since the material experiences cracks combined with local damage.

For most HPFRCCs, efforts have been made to develop recommendations and code-type models, which enable engineers to apply these materials in practice. Such models have found their way from international research reports and recommendations (see e.g. [2, 41, 128]) to national design guidelines and codes, for example, in Germany [22, 25], France [4], Australia [29], Japan [58] or China [20]. Nonetheless, the application of fibre-reinforced cementitious materials remains limited to specific applications, such as:

- non-structural segments, e.g. surface beds and pavement overlays;
- pre-stressed beams with some contribution of fibres to the shear resistance;
- conventional and segmental tunnel linings;
- structural joints;
- thin walled roof elements; and
- structural elements that are predominantly subjected to impact and fatigue loading.

Other applications of fibre-reinforced cementitious materials in load-bearing structures usually require extensive experimental investigations of material parameters and the structural behaviour [68]. This highlights the necessity to establish reliable material models that can be used to describe the material behaviour at a structural level.

1.2 Aim and scope

The goal of the thesis at hand is to analyse the structural behaviour of R/SHCC elements subjected to tensile loading and the contribution of each component, i.e. SHCC and steel bars. A multiscale investigation is chosen in which the individual mechanical behaviour of the components as well as their mechanical interaction is analysed. An outline of the experimental and theoretical framework to study the structural behaviour of R/SHCC is given in Figure 1.1.

Experimental investigations at the material macro-level include uniaxial tension tests on SHCC and steel reinforcement. By analysing the mechanical behaviour of the components, a deeper understanding of the interaction between steel and SHCC as well as the underlying mechanical processes is possible. The applicability of the results to SHCC containing fibre materials other than PVA and reinforcement other than steel rebar are beyond the scope of this research.

At the structural level, experimental investigations are conducted on SHCC slabs reinforced with untensioned steel bars as well as unreinforced slabs. Special attention is devoted to the load-deformation response as well as the crack development. All experimental investigations are conducted under quasi-static, short-term loading conditions. The effects of dynamic loading conditions are not considered within this study.

Based upon the experimental results, constitutive relationships are developed describing the individual behaviour of the components, i.e. SHCC and steel, as well as the combined behaviour of a R/SHCC element.

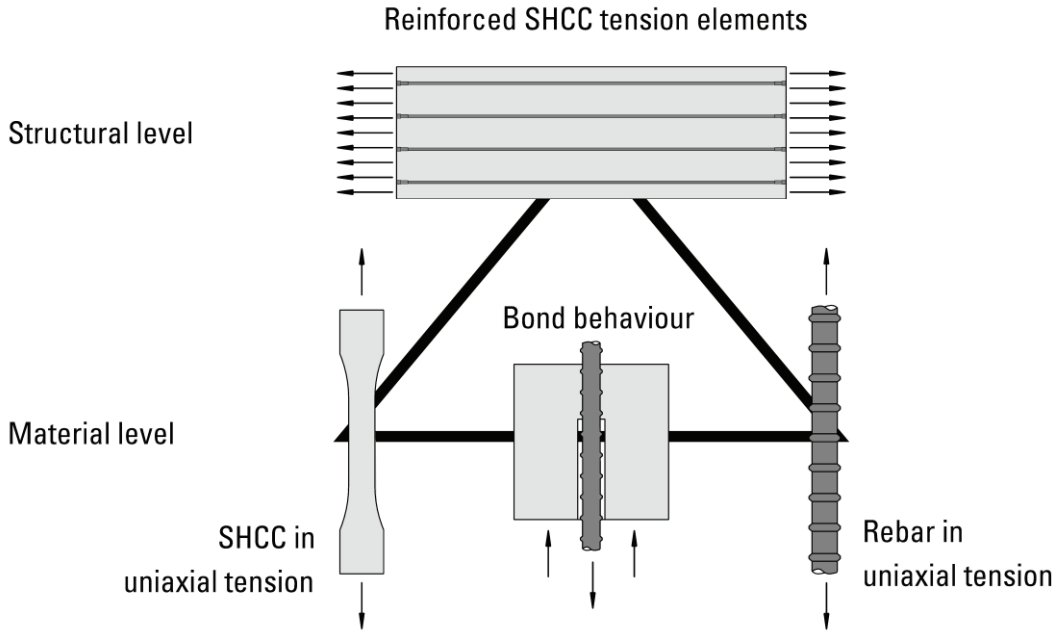

Figure 1.1: Overview of the different levels of observation used to investigate the tensile behaviour of R/SHCC elements

1.3 Outline

The thesis at hand is organised into six chapters. **Chapter 1** presents the motivation for this work and outlines the structure of this thesis.

Chapter 2 provides a review of literature relevant for the scope of this thesis. It includes a brief overview of the development and typical SHCC compositions. A basic introduction to the mechanical principles of the cracking process in cement-based materials is presented as a basis for the characterisation of the material properties. Additional background information is provided for the mechanical behaviour of steel, as well as the bond interaction of SHCC and steel reinforcement.

Experimental investigations on SHCC and steel reinforcement at the material level of observation are presented in **Chapter 3**. The aim of this investigation is to derive a sound understanding of the material behaviour of the individual components as a basis for the experimental investigations on R/SHCC elements.

A detailed presentation of the materials used, their individual components and the production process is given. The obtained properties of SHCC in its fresh and hardened states are summarised and discussed regarding their effects on the structural behaviour. Special consideration is hereby given to the influence of the production process on the material properties with a focus on the tensile behaviour. The chapter is complemented by the testing of the steel reinforcement under tensile loading.

Chapter 4 reports on the experimental investigations of large-scale R/SHCC members. The reinforcement configurations, the specimen production and curing procedures are described. Additional information on the experimental setup and testing equipment is given as a basis for the discussion of the test results. The results are analysed regarding the global load-bearing behaviour, as well as the effect of the different parameters under investigation. For a deeper understanding of the mechanical behaviour, the crack development on the specimen surface and around the steel bars is analysed, as well as the development of local steel strains.

The results are also used to develop constitutive models for R/SHCC elements, which are presented in **Chapter 5.** Moreover, an approach for the modelling of the structural behaviour based upon constitutive relations is presented as a prerequisite for a design concept. Similar to the experimental framework of this thesis, the material responses of the SHCC and steel are first considered separately and subsequently their individual behaviours are combined. The underlying mechanical processes are described and transferred into constitutive relationships, which can be used to estimate the structural behaviour.

Chapter 6 concludes the thesis with a summary of the theoretical and experimental findings and provides an outlook of possible future developments.

2 State of the art

2.1 Strain-hardening cement-based composites (SHCC)

SHCC is a class of HPFRCC, which exhibits strain-hardening behaviour when subjected to uniaxial tension. Such behaviour is usually achieved by the application of short, well-distributed fibres in combination with a tailored design of the mix composition and specific production procedures [81, 90].

In comparison to OC, these novel cement-based materials are characterised by higher toughness, ductility and high energy absorption capacity. General publications on the classification of HPFRCC are [83, 87, 118] while brief overviews of the development are given in [84, 85, 117].

This section provides basic information on the material properties of SHCC with special emphasis on the tensile behaviour and the underlying mechanical principles of SHCC. These properties are only covered up to the point which is necessary to understand the load-deformation behaviour of SHCC and its effect on the structural level. A deeper discussion at the micro-mechanical level of the cementitious composite will be omitted. For further information on such aspects, the reader is referred to the relevant literature.

2.1.1 Classification of cement-based composites

Cement-based materials can be classified by their load-deformation behaviour under tensile loading. Numerous test methods have been developed to examine the tensile response of cement-based materials, which are further discussed in Section 2.1.4. A schematic illustration of typical load-deformation behaviour for cement-based composites under uniaxial tension is given in Figure 2.1.

When tensile stresses exceed the matrix tensile strength σ_{mu} in the weakest plane, a crack forms. Depending on the subsequent progression of the stress-strain curve, the material can be classified as either strain-softening or strain-hardening[2] [117]. Tensile deformations Δ_l of strain-softening cement-based materials remain localised in the plane of the first crack, while tensile stresses decrease as indicated by Figure 2.1a. Materials that show strain-hardening behaviour exhibit an increase in tensile stress and large tensile strains ε until localisation of failure occurs, i.e. when one main crack develops as presented in Figure 2.1b.

[2] For fibre-reinforced cement-based composites, strain-hardening is always accompanied by the gradual formation of multiple cracks, before deformations start localizing in one crack. For this reason, “pseudo strain-hardening” or “strain-hardening like” is commonly used instead.

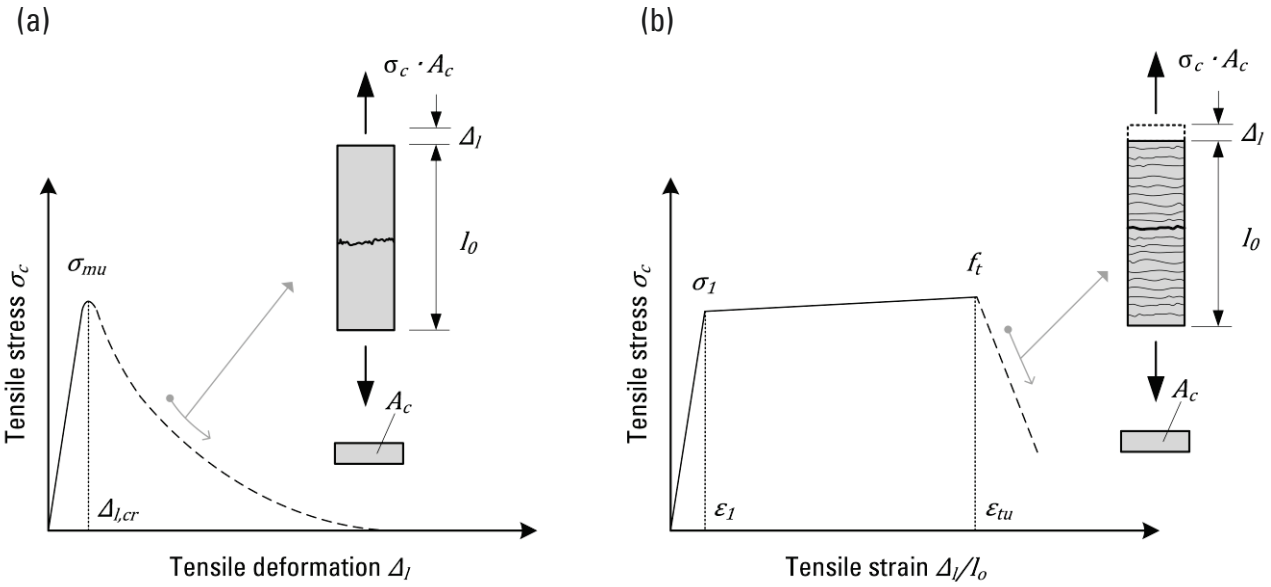

Figure 2.1: Typical tensile behaviour of cement-based materials showing (a) strain-softening and (b) strain-hardening response after initial cracking of the cementitious matrix

Due to its properties engineered on a micro-mechanical basis and its ductile behaviour in tension, similar mixture compositions are also often referred to as engineered cement-based composites (ECC) or ductile fibre-reinforced cementitious composites (DFRCC). A complete overview of the different classifications of SHCC can be found among other aspects in [56, 116, 119].

The first design guideline established to provide a basis for the application of such novel construction materials was issued by the Japanese Society of Civil Engineers [59]. It was followed by a RILEM technical committee focussing specifically on SHCC [140]. Beforehand and subsequent various applications of SHCC as a construction material were conducted, see e.g. [70, 86, 140, 141]. The most important projects, for which SHCC has been applied are:

- a composite steel/SHCC deck of the Mihara bridge in Hokkaido, Japan [70, 140];
- a SHCC link slab highway bridge in Michigan, USA [77, 88]; and
- R/SHCC coupling beams in high-rise buildings Tokyo and Yokohama, Japan [70, 129, 140, 141].

Furthermore, several symposia have been held in the past focussing on the development in SHCC, also such dedicated exclusively to this new composite material:

- International RILEM Conference on Strain-hardening Cement-based Composites SHCC in 2005 [125], 2009 [143], 2011 [43], 2014 [133] and 2017 [106].

2.1.2 Material composition

It has become commonplace to characterise a cement-based composite by means of different levels of observations. While SHCC can be regarded as a homogenous material at the macro-level, specific properties are best described by considering the structure and specific characteristics on the meso- and micro-level of observation. At the meso-level the composite structure is usually grouped into several phases, i.e. cementitious matrix (cement paste, aggregates, air-voids), discontinuous fibres and the interface transition zone between fibres and cementitious matrix.

2.1.2.1 Matrix composition

Compared to OC, SHCC generally contains smaller aggregates and a higher binder content. The maximum aggregate size is usually limited to 300 µm and can be regarded as integral part of the matrix. In combination with a relatively low water content this renders a dense micro-structure of the cement paste. The micro-structure of the cement paste is primarily influenced by the mixture composition and the degree of hydration. Parameters affecting the degree of hydration are the water-to-cement ratio, type of cement, clinker content, use of additives and admixtures as well as age and curing conditions. Table 2.1 presents typical mixture compositions of SHCC.

Table 2.1: Typical mixture compositions of SHCC made with PVA or HDPE fibre [kg/m³]

Reference / **Components** [kg/m³]	Kunieda et al. [69]	Kesner and Billington [65], Fischer and Li [44]	Yun et al. [151, 152]	Curosu et al. [23, 24]	Kanda [64], Kanakubo et al. [63]	Mechtcherine and Jun [100]	Lepech and Li [77], Wang and Li [147]	Lárusson and Fischer [72]	Moreno et al. [110, 111]
Water	292	504	418	315	364	335	298	320	312
Portland cement	1243	1295	1047	1460	554	321	583	430	547
Fly ash	-	-	-	-	237	749	700	860	656
Silica fume	223	144	-	292	-	-	-	-	-
Sand	149	-	418	145	506	535	469	300	438
Super plasticizer	14.9	3.02	-	25	[3]	16.6	19	4.3	6.0
Viscosity agent	-	-	2.09	-	[3]	3.2	-	0.48	1.32
PVA/HDPE fibres	14.6[1]	19.4[1]	14.6[1]	20[1]	20.0	29.3	26	26	26
Air reducer	2.98	-	-	-		-	-		-
Shrinkage reducing agent	-	-	-	-	15	-	-		-
w/c	0.23	0.39	0.45	0.22	0.46	1.04	0.51	0.74	0.57
$(w/c)_{eq}$[2]	0.21	0.35	0.45	0.19	0.62	0.80	0.44	0.59	0.49

[1] HDPE fibres, [2] $(w/c)_{eq} = w/(c + 0.4 \cdot f + 1.0 \cdot s)$ with max $f = 0.33$ and max $s = 0.11 \cdot c$ as defined in DIN EN 206-1 [38], [3] not specified

It can be seen from Table 2.1 that cement is usually supplemented by pozzolanic additives such as micro-silica or fly ash. It has been reported that the addition of fibres usually results in a decrease of workability [54]. Consequently, chemical admixtures such as superplasticisers (SP) and viscosity agents (VA) are required to maintain or even enhance the dispersion and prevent segregation the fresh mixture (e.g. bleeding).

An appropriate workability is found to facilitate a uniform fibre distribution and influence the pore structure of the matrix. The fibre content should be selected in good agreement with the desired mechanical properties of the composite. Thus, typical fibre contents V_f for SHCC range from 1 to 3% by volume. Furthermore, the interfacial bond properties of fibre-matrix interface can have a profound impact on the mechanical properties of the composite. A comprehensive overview of the effect of the mixture composition regarding fibre volume, fibre bond strength and matrix composition on the mechanical properties of the composite are given, for example, by VAN ZIJL [142].

2.1.2.2 Short fibres

Short fibres are a crucial part of the mixture composition and are found to have a significant influence on the mechanical performance of the composite. Types of polymer fibres that have been incorporated into cement-based matrices include polyethylene (PE), high-density polyethylene (HDPE), polypropylene (PP), acrylics (PAN), polyvinyl alcohol (PVA), polyamides (PA), aramid and polyester (PES). The main differences between these fibres – which are relevant for the use in cement-based composites – are:

- geometry (length, diameter, shape);
- material characteristics (tensile strength, elastic modulus, durability in alkaline environment);
- bond-related properties (surface roughness, chemical affinity to cement paste).

Geometries of commonly used polymer fibres are twisted single strand or monofilament fibres. Polymer fibres can also be cut from plastic sheets, which are delivered as net-shaped or fibrillated fibres. Most polymer fibres have a circular or elliptical cross-section, whereas fibrillated fibres can be flat.

Depending on their geometry, fibres can be separated into macro-fibres, micro-fibres or a combination of both, often referred to as hybrid fibres [118]. Micro-fibres are usually defined as fibres with a diameter $d_f < 100\ \mu m$ and a length to diameter ratio $l_f/d_f > 100$. The lengths l_f of micro-fibres used for SHCC matrices range from 6 to 20 mm. Depending on the type of polymer, fibre diameters d_f can range from 10 to 80 µm.

Important mechanical parameters of the fibres are the tensile strength f_{tu} and modulus of elasticity E_f as well as the interfacial bond properties. Table 2.2 summarizes characteristic material properties of different types of fibres incorporated into SHCC.

Table 2.2: Typical properties of synthetic fibres used in cement-based materials according to NAAMAN [118] and LÖFGREN [94]

Type of fibre	Diameter	Specific weight	Tensile strength	Strain capacity	Modulus of elasticity
	d_f		f_{tu}	ε_{tu}	E_f
	[µm]	[g/cm³]	[MPa]	[%]	[GPa]
Acrylic (PAN)	5-17	1.18	200-1000	7.5-50	14.6-19.6
Aramid (Kevlar)	10-12	1.4-1.5	2000-3500	2.1-2.5	62-130
Carbon (low modulus)	7-18	1.6-1.7	800-1100	2.0-4.6	38-43
Carbon (high modulus)	7-18	1.7-1.9	1500-4500	1.3-1.8	200-800
Polyamide (PA)	20-25	1.16	965	20	5.17
Polyester (PES)	10-8	1.34-1.39	280-1200	10-50	10-18
Polyethylene (PE)	25-1000	0.96	80-600	12-100	5.0
Polyethylene (HDPE)	20	0.97	3000-4100	2.9-4.1	80-150
Polypropylene (PP)	10-200	0.91	310-760	6-15	3.5-4.9
Polyvinyl alcohol (PVA)	10-100	1.2-2.5	880-1600	4-12	25-40

The interfacial bond properties of the fibre-matrix interface depend on the fibre surface characteristics, the fibre aspect ratio and the properties of the cementitious matrix. The effects of fibres – especially regarding fibre material and shape – on the mechanical properties of the composite are discussed by SUWANNAKARN et al. [138], for example.

2.1.3 Mechanisms of crack formation and propagation

The heterogeneity of cementitious matrices leads to a pronounced non-linear fracture behaviour of plain cement-based composites in tension. The formation and propagation of micro- and macro-cracks in cementitious matrices have been investigated in detail by many researchers (see, e.g. [30, 49, 95]. In fibre-reinforced cement-based composites, the cracking process is influenced by the action of fibres, which are found to improve the post-cracking behaviour, e.g. toughness, ductility, the tensile strain capacity and in some cases the tensile strength [14]. The reasons for this can be found in the bridging properties of well-distributed short fibres.

A comprehensive overview of the principles of fibre bridging – especially regarding the micro-mechanical modelling of single fibre pull-out and crack-bridging behaviour – was given by JUN [60]. The following section will provide an outline of these principles for a better understanding of the material behaviour and its impact on the meso- and macro-level of observation.

2.1.3.1 Single fibre pull-out

One fundamental basic for the crack bridging of fibres in cement-based materials is the interfacial bond interaction between fibres and cementitious matrix. The mechanical behaviour of the embedded fibre is best described by means of fibre pull-out tests and it generally depends on the properties of the fibre as well as its interaction with the matrix. Figure 2.2 depicts the schematic stress-slip curve of a single fibre with an embedment length l_{fb}.

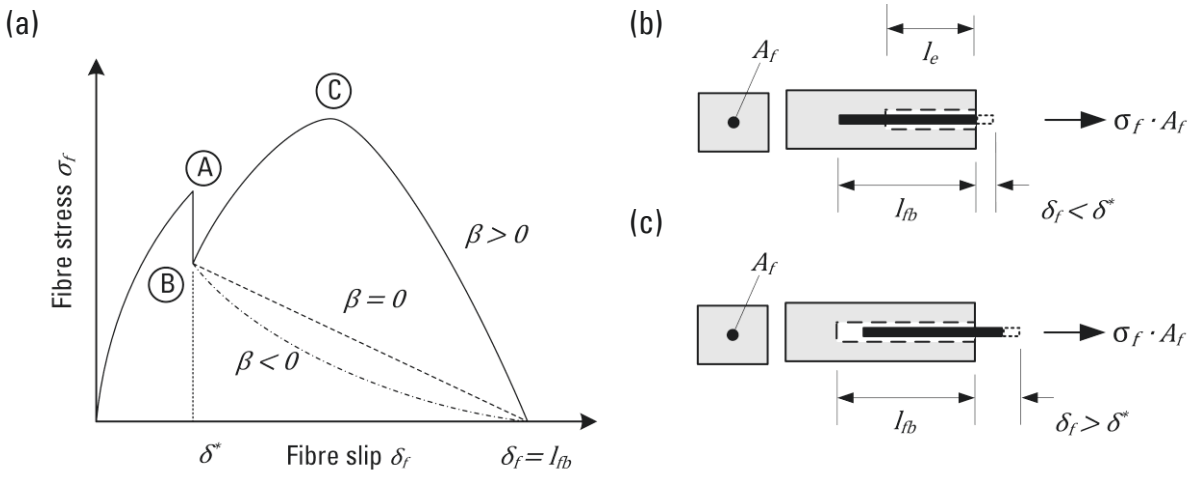

Figure 2.2: (a) Schematic stress-slip curve during fibre pull-out with a schematic representation of a single fibre embedded into a cementitious matrix (b) during the activation phase and (c) during the pull-out phase, adapted from YANG [150] and LIN [92]

The progress of the stress-slip curve can generally be classified into two phases: fibre activation, governed by adhesive bond properties and pull-out, governed by frictional bond properties [150]. The activation phase, ranging from 0 to δ^*, is characterised by a gradual de-bonding of the fibre along the de-bonding length l_e. Parameters affecting the fibre slip δ_f during this phase are the chemical bond over the remaining embedded fibre length $l_{fb} - l_e$, the frictional bond along the de-bonding length l_e as well as the mechanical properties of the fibre. When the adhesive bond strength is exceeded over the entire fibre length, bond decay occurs and the release of elastic deformation energy results in a sudden decline of the pull-out force (A-B).

Depending on the interfacial bond properties, the resulting pull-out curve can be categorised into slip-softening or slip-hardening, which is described by the coefficient β. The maximum fibre bond strength is reached when either the adhesive or frictional strength (C) reach their maximum values. Thus, slip softening fibres reach their maximum bond strength before de-bonding ($\beta < 0$), while slip-hardening fibres develop their maximum bond stress after de-bonding ($\beta > 0$).

During the following pull-out phase, complete de-bonding occurs and the remaining resistance can be attributed to frictional bond properties.

For single filament fibres, adhesive and frictional bond strength primarily depend on the interfacial bond properties as well as the interfacial surface area. Parameters that govern the interfacial bond properties are the surface characteristic of the fibre, the bond quality (mechanical properties of the interface between fibre and matrix) as well as loading conditions (pull-out rate [15, 23, 24, 113], temperature [105], etc.).

In general, slip-hardening behaviour of fibres was found to facilitate multiple cracking and high strain levels in SHCC [90]. Anyway, it is necessary to select the type of fibre in good agreement to the matrix properties, while in some cases additional fibre treatment may be required. Fibre treatment such as oiling can be applied to reduce the fibre bond strength, especially in case of PVA fibres which tend to develop a strong fibre-matrix bond due to their hydrophilic nature [45].

2.1.3.2 Crack bridging

The effect of fibres on the cracking behaviour of cementitious materials is usually analysed on the meso-scale by means of uniaxial tension tests on notched specimens. In this case, the local stress concentration around the notches forces the localisation of deformations at a specified cross-section, which simplifies control and monitoring of the crack development. This method is often used to derive the crack opening behaviour of an individual crack. In respect to SHCC, one weakness of this method is the inconsistency of results regarding the development of the crack process zone around the notches. JUN [60] observed a considerable influence of the size of the notches on the crack opening displacement and the tensile strength of SHCC. Recent methods to monitor the individual crack development include digital close-range photogrammetry. This technique allows the continuous supervision of individual cracks independent of the size of the crack process zone. More information on this method is provided in Section 4.5.3.1.

Matrix bridging

The reduction of the crack process zone to a single crack level enables describing the corresponding crack opening behaviour, which is depicted for a plain cementitious matrix in Figure 2.3. For an ideal crack-free cementitious matrix, the first stage (A) of the tensile load-deformation response would show an almost linear-elastic response, while tensile deformations Δ_l can be assumed to be evenly distributed over the entire specimen length. However, cement-based composites tend to have a large number of pores, flaws and micro-cracks inherent to the matrix even before being subjected to any external load. Much of these micro-defects stem from segregation, excess water, restrained shrinkage or thermal deformation.

Local stress concentrations at the crack tip can lead to further micro-crack growth, resulting in a disproportionate increase in tensile strain (B). With further loading, pre-existing and newly-formed micro-cracks accumulate and merge into a discrete crack. At this point the matrix tensile strength σ_{mu} is reached.

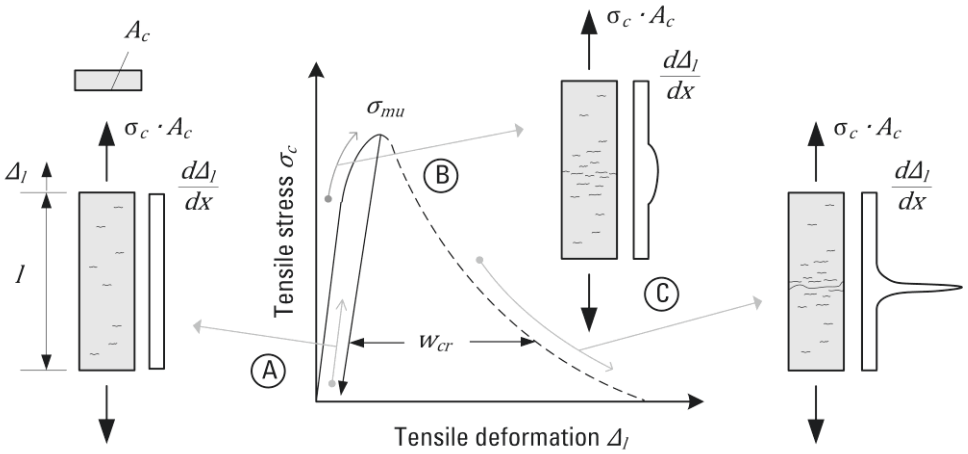

Figure 2.3: Schematic tensile deformation response of unreinforced cementitious materials with crack development during different stages, adapted from DUDA [30]

If the test is performed in a deformation-controlled regime, subsequent crack opening and a rapid decrease of tensile stresses can be observed (C). It is generally accepted that this phenomenon is based upon friction and interlocking of the crack-surfaces [30]. The progression of the stress-deformation curve during this stage is influenced by the composite structure, i.e. degree of concrete heterogeneity, maximum aggregate size and cement paste properties among others. However, one should bear in mind that the progression of the curve is also influenced by the test setup, e.g. gauge length, control regime and loading rate as well as specimen geometry, especially regarding specimen length (snap-back effect)[3] [95].

The energy required to advance the matrix crack tip is also referred to as fracture energy G_f and it corresponds to the area under the stress-deformation curve (subtracted by the elastic deformations). G_f can be regarded as a characteristic material property of concrete, it depends on a variety of parameters such as water-to-cement ratio, size of aggregates and the properties of the cement-paste bond interface [103]. The fracture energy of plain concrete can be estimated according to HILLERBORG at al. [53] with Eq. (2.1).

$$\int_0^{w_1} \sigma_c(w_{cr}) dw_{cr} \tag{2.1}$$

with σ_{mu} matrix tensile strength

w_1 crack width when the softening curve has fallen to zero

For SHCC matrices having a fine micro-structure and aggregates of relatively small size, the crack-bridging ability can be expected to be less than that of OC usually containing larger aggregates.

[3] The snap-back effect describes the phenomenon that a negative decline of the stress-strain curve can be observed during the strain-softening stage when a certain specimen length is exceeded.

Fibre bridging

The gradual delamination of fibre from the matrix and eventually fibre pull-out represents the ideal response of a single fibre crossing a crack plane. However, on the meso-level the fibre-reinforced cementitious composite contains a large amount of randomly dispersed fibres. Due to their random distribution and orientation, multiple fibres are found to be crossing a crack plane at various angles and having various embedment lengths. The crack opening leads to an activation of the fibres to different extents.

Due to the pull-out resistance of fibres, tensile stresses are transferred across the crack plane, which dramatically changes the subsequent crack opening response in comparison with that of a plain matrix. The continuous opening of a crack results in an increased activation of fibres as depicted in Figure 2.4 by the dashed line[4]. The interaction of both processes, i.e. strain-softening due to the heterogeneity of the matrix and slip-hardening due to the action of randomly distributed fibres, can consequently be described as a superposition of the two crack opening curves, as represented by the solid line in Figure 2.4.

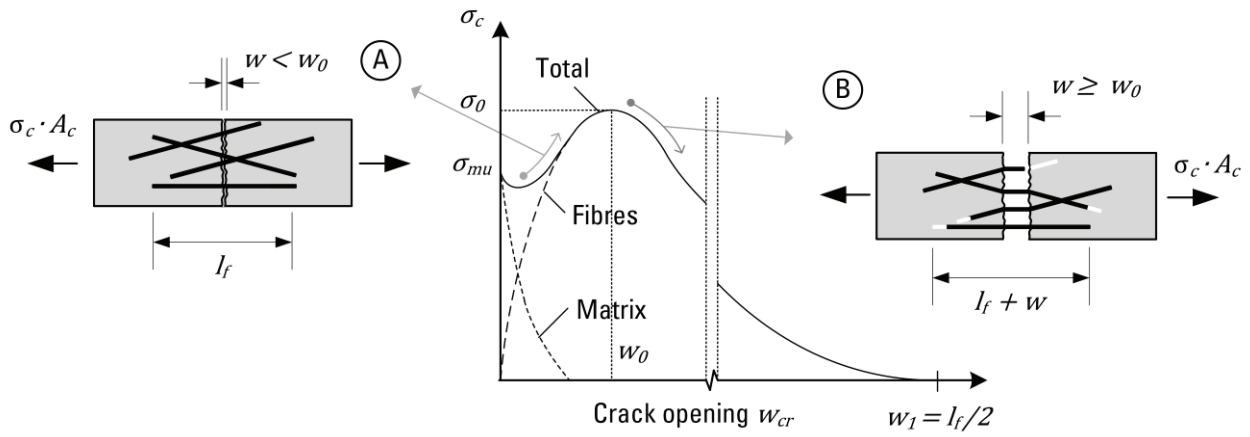

Figure 2.4: Effect of the combined matrix and fibre bridging on the tensile behaviour of fibre-reinforced cement-based materials for (A) small and (B) large crack opening stages, adapted from LÖFGREN [94] and JUNGWIRTH [61]

Thus, the fibre bridging behaviour on a single crack level can be characterised by the matrix tensile strength σ_{mu}, which represents the maximum bridging stress of the matrix and the maximum bridging strength σ_0, which represents the maximum bridging stress of the fibres corresponding to the critical crack width w_0.

[4] Because of the (partial) bond to the matrix fibres are usually activated even before discrete cracks are initiated. For limited fibre volumes, however, it can be assumed that fibre contribution in the pre-cracking stage is negligible.

The ratio of the matrix tensile strength σ_{mu} and the maximum bridging strength σ_0 depends on the amount and orientation of fibres, as well as the fibre pull-out behaviour [87]. If fibre rupture is avoided, fibres can stabilise the matrix cracks by bridging them. It is generally accepted that for strain-hardening behaviour, the pull-out resistance stemming from the slip-hardening properties of the fibres, i.e. the maximum bridging strength, should be higher than the matrix tensile strength σ_{mu} as expressed by Eq. (2.2).

$$\sigma_0/\sigma_{mu} \geq 1.0 \tag{2.2}$$

The pull-out resistance of the randomly distributed fibres is also referred to as fibre effectiveness. Parameters affecting the fibre effectiveness are at least partly the number of fibres crossing a crack plane, their embedment length and their orientation. In general, the number of the fibres crossing the crack plane depends on the fibre volume and orientation of fibres. Fibres crossing the plane in a flat angle are found to increases the pull-out resistance of single fibres (snubbing effects [82]), but may lead to concrete spalling or higher pull-out forces [78]. In addition, the length of fibres influences the embedment length and determines the bond force [91].

2.1.3.3 Multiple cracking

To achieve strain-hardening behaviour, brittle cement-based materials should develop multiple cracks, which allow the necessary deformations to occur [57]. One basic requirement is expressed by Eq. (2.2), which holds true as long as the crack opening displacement δ of the first crack remains smaller than the critical crack width δ_0. The second requirement is the energy criterion, which states that the energy necessary to advance the matrix crack must be less than the complementary energy dissipated by the fibres.

In this case, the crack surface can be completely bridged by the fibres after the stress at first cracking σ_1 is exceeded, which allows the transfer of tensile stresses and – in some cases – a further increase of stresses. Due to the random distribution of matrix properties, another crack forms as soon as the matrix tensile strength σ_{mu} in the next weakest cross-section is reached. Therefore, the stress at first cracking σ_1 corresponds to the lowest matrix tensile strength σ_{mu} of the regarded element. The process of multiple cracking continues as long as the conditions of Eq. (2.2) and energy criterion remain satisfied. In this case each crack is bridged by fibres, which carry the tensile stresses exceeding the stress at first cracking σ_1.

Thus, such fibre-reinforced cementitious composites experience multiple cracking along the regarded element. At the macro-level, the resulting stress-strain response is assumed to follow the upper envelope as shown in Figure 2.5, which depicts a schematic illustration of the theoretical stress-strain response (solid line) and the upper envelope (dashed line). The tensile strain ε_c can be regarded as the sum of all individual crack widths along the entire specimen (the elastic deformation of the matrix is neglected here) divided by the specimen length $\varepsilon_1 = \Delta_l/l_0$.

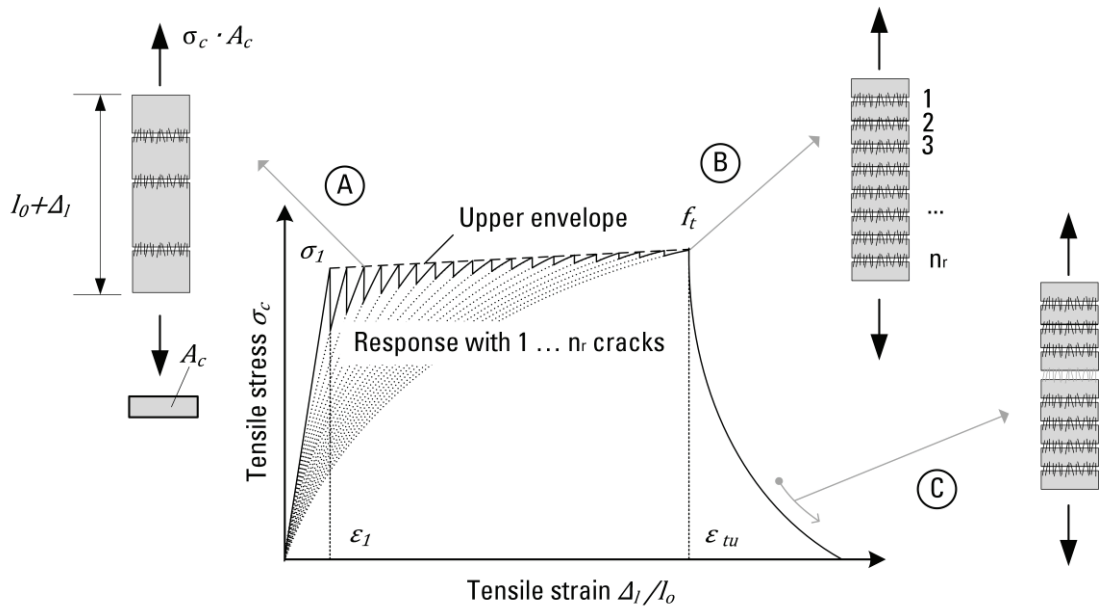

Figure 2.5: Process of multiple cracking as a result of the individual crack opening behaviour of 1 to n_r cracks and the resulting global tensile behaviour for SHCC adopted from KABELE [62]

The stress can be increased until the weakest crack reaches the maximum bridging stress σ_0. At this point the tensile strength of the composite f_t is reached at the corresponding tensile strain capacity ε_{tu}, which depends on the number and the width of all individual cracks along the specimen[5].

This point is characterised either by fibre rupture after exceeding the maximum bridging stress σ_0 or fibre pull-out failure after exceeding the critical crack width δ_0. The subsequent progress of the stress-strain curve is influenced by the strain-softening properties of the macro-crack as well as the unloading of the matrix and the remaining cracks.

To achieve high tensile strain capacity ε_{tu}, it is generally pursued to combine: (1) a low modulus of elasticity E_f to achieve high fibre strain; (2) a relatively low matrix tensile strength σ_{mu} and high tensile strength σ_{fu} of the fibres to avoid fibre rupture as well as (3) an appropriate fibre bond strength to avoid pull-out failure. Studies conducted on FRC by KIM [57] showed that the combined effects of high slip-hardening capacity and large slip during fibre pull-out help to achieve strain-hardening behaviour.

[5] The matrix tensile strength σ_{mu} varies between the stress at first cracking σ_1 and the tensile strength of the composite f_t due to the random distribution of matrix properties. Therefore, an increase of the upper envelope can usually be observed.

2.1.4 Mechanical properties of SHCC

The material behaviour at the macro-level is usually described by constitutive relations based on the mechanical processes at the micro- and meso-level, as presented in the previous section. Such constitutive relations reproducing the state of stresses representative for structural applications are best determined by means of experimental investigations. In this context, the material behaviour in compression and tension belong to the most important characteristics of construction materials.

For structural design purposes and quality control, plain concrete is usually classified by its compressive strength. However, the use of fibres changes the compressive, but most importantly and first of all the tensile response. Hence, the conventional approach is not sufficient for describing the material behaviour and additional testing is required.

In the case of SHCC, it becomes necessary to analyse the specific load-deformation behaviour based upon an explicit determination of the stress-strain relationship. Even though this enables a straightforward description of the material behaviour, the results are inevitably affected by various boundary conditions. In this context, some considerations on effects influencing the compressive and tensile material properties are given below.

2.1.4.1 Compressive properties

The compressive strength f_c usually defines the maximum value of the measured compressive stress during a compression test and is often used for a general description of cement-based composites. The compressive strength is influenced by various parameters, e.g. material composition, curing conditions, specimen geometry or testing techniques. With a relatively low volume fraction of aggregates (which are also very fine) and high binder content, the resulting properties of typical SHCC compositions are expected to be similar to that of plain mortar with a corresponding water-to-cement ratio.

At the meso-level, the strength of plain cementitious composites is influenced by the size, quantities and mechanical properties of the aggregates as well as the properties of the cement paste. The compressive strength may substantially vary depending on the material properties of the aggregates in use, i.e. strength and stiffness, as well as the bond between aggregates and hydrated cement paste. It is also influenced by the pore structure of the cement-based composite, especially regarding the effect of fibres, which were found to increase the porosity of the matrix [89].

Parameters affecting the cement paste can be found at the micro-level where the properties are influenced by the type of cement, the w/c ratio, the degree of hydration, as well as the type and content of additives. In the case of SHCC, the type of additive generally depends on the desired strength level and includes either silica fume or fly ash. Silica fume – which has one to two orders of magnitude smaller particle size than cement – can increase the strength of the cement paste and the bond to aggregates and fibres due to its high packing density and strong pozzolanic reactivity.

In combination with a low water-to-binder ratio this facilitates a dense micro-structure with reduced pore spaces and a homogeneous structure of the cement-based composite. Therefore, compressive strengths f_c ranging from 70 to 85 MPa have been reported for SHCC containing silica fume [89].

By contrast, partial replacement of cement by fly ash may cause a reduction in compressive strength and a slower strength development over time, stemming from its lower pozzolanic reactivity, as shown by the dotted line in Figure 2.6 [31]. Due to the various material compositions, testing ages and curing conditions a broad range of compressive strengths f_{ck} between 30 and 60 MPa have been reported [99, 140] for SHCC containing fly ash.

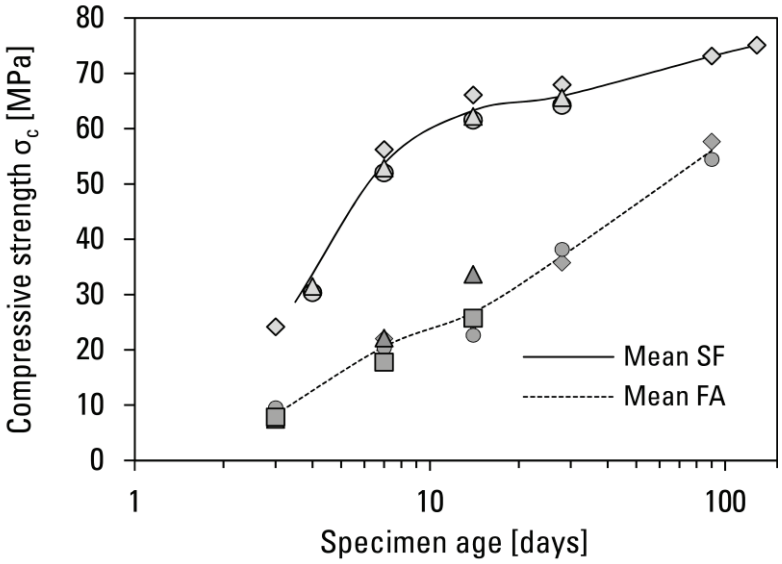

Figure 2.6: Comparison of SHCC compressive strength development with addition of fly ash (mean FA) and silica fume (mean SF), adapted from LEPECH [76] and WANG [147, 148]

The degree of hydration is influenced by the testing age and the curing conditions of the specimen. It can be assumed that insufficient water is available for complete hydration of cement paste when the water-to-binder ratio does not exceed 0.4, which influences the micro-structure of the matrix. It was also found that curing in water can lead to a further densification of the micro-structure resulting from the continuing hydration of unhydrated binders, which can give rise to the compressive strength over time [112].

In the frame of the doctoral work at hand, only SHCC compositions with addition of fly ash and small aggregates were used. A composite age of 28 days was chosen to determine the characteristic compressive strength of the specimens.

2.1.4.2 Tensile behaviour

The most important material characteristic of SHCC is the distinctive deformation behaviour under tensile loading, which has been well studied. Especially the characteristic behaviour of SHCC under monotonic, quasi-static loading conditions was of particular interest to many researchers. A detailed analysis of the behaviour of SHCC under uniaxial monotonic tensile loading is given in Section 3.2.4 as part of the own investigations.

For conventional cementitious materials, such as OC, tensile properties are usually derived from indirect tension tests, such as splitting tests or bending tests, due to their simple implementation. The results of such test can be used, for example, to determine the uniaxial strength based on explicit relationships as given by CEB-FIP Model Code 2010 [41]. A more accurate, but at the same time more complicated method to determine the actual uniaxial behaviour are direct tension tests.

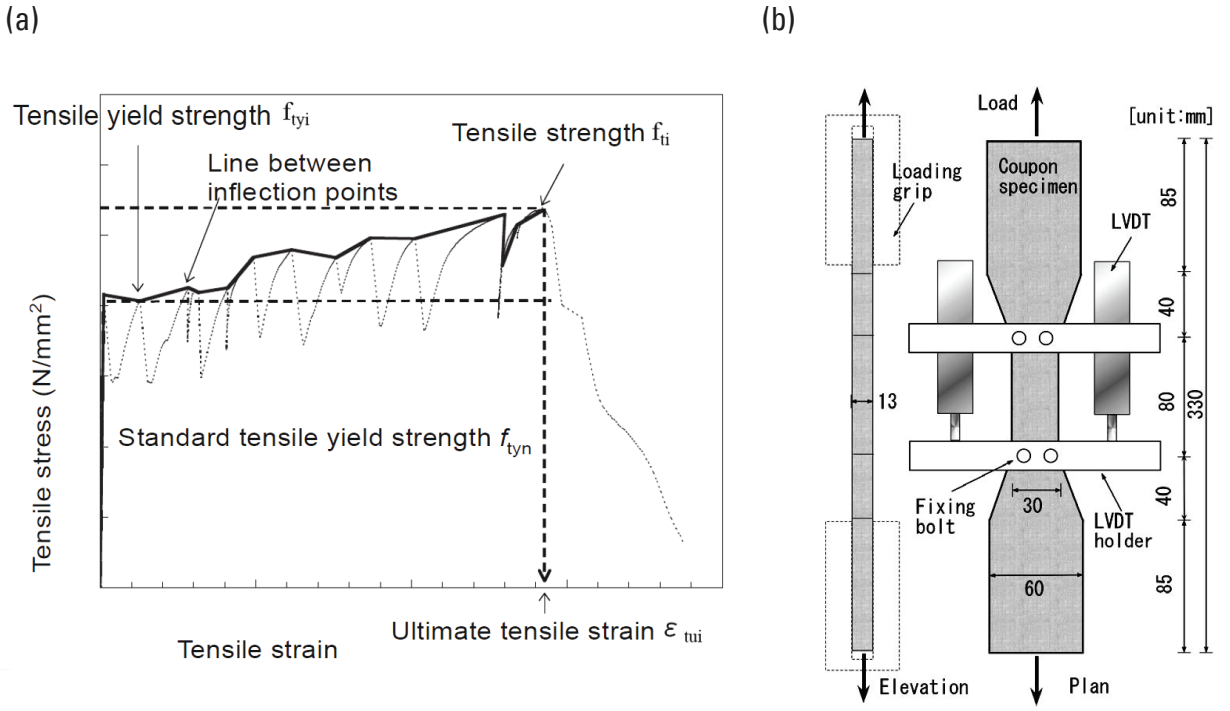

Figure 2.7: (a) Examples of SHCC behaviour under tensile loading and (b) standardized specimen layout for uniaxial tension tests on SHCC, according to the JSCE recommendation [59]

A representative tensile stress-strain relationship for SHCC derived from direct tension tests is shown in Figure 2.7a. At present, the only standardised method for testing cementitious composites in direct tension is provided by the Japan Society of Civil Engineers (JSCE) [59], which is presented in Figure 2.7b. The tensile material response can be divided into three distinct stages: (1) elastic stage; (2) multiple cracking stage and (3) crack localisation and specimen failure.

In the first stage, the specimen shows an almost linear-elastic response up to the stress at first cracking[6] σ_1. The stress at first cracking σ_1 generally corresponds to the matrix tensile strength σ_{mu} and depends on multiple parameters, i.e. the type and proportion of cement and additives, the degree of hydration of the cement paste and the pore structure. A higher cement grade and the use of silica fume can lead to a densification of the concrete structure and an increase of the matrix tensile strength. However, substitution of cement by high content of fly ash may cause the remain of unreacted fly ash particles in the matrix, which can have a similar effect as pores, thereby reducing the matrix tensile strength.

Due to varying material compositions, testing ages and curing conditions, stresses at first cracking reported range between 1.9 and 5.0 MPa. Since material and bond properties of the fibres should be selected in good agreement to the matrix tensile strength to achieve strain-hardening behaviour, PVA fibres are commonly used for lower values of σ_{mu} while HDPE fibres are used for higher values of σ_{mu}.

Even though tensile strains typically experience a disproportionate increase after approximately 70 % of the tensile strength σ_{cr} the initial slope can be simplified by linear gradient, which is defined as the tensile modulus of elasticity E_{ct}. It was found that the tensile modulus of elasticity primarily depends on the micro-structure of the cementitious composite, especially aggregate content [89] as well as air content [145]. Additionally, the tensile modulus of elasticity of the composite is influenced by the water-to-cement ratio, as well as the degree of hydration. In the case of cement substitution by fly ash, unhydrated fly ash particles - which remain as fine filler in the matrix - influence the initial slope of the stress-strain response as well. Due to the different compositions in use the values reported for the tensile modulus of elasticity E_{ct} are found to range between 15 and 20 GPa.

The second stage of the tensile load-deformation behaviour is characterised by multiple micro-cracking until the tensile strength f_t is reached at the tensile strain capacity ε_{tu}. During this stage, the element undergoes large deformations accompanied by the development of narrow cracks. In a displacement controlled regime, the tensile element exhibits stress drops each time a micro crack forms followed by an increase of tensile stress as the fibres are activated and stabilise the crack growth. This behaviour is the result of the mechanical interactions between matrix and fibres.

Figure 2.8a shows the strain field used to measure local deformations on the surface of a dumbbell specimen based upon a digital close-range photogrammetry. The progression of these deformations during loading was used to calculate the crack width development of each crack.

[6] In lieu of the stress at first cracking σ_1, the tensile yield strength, which represents the lowest stress occurring after first cracking is depicted in Figure 2.7.

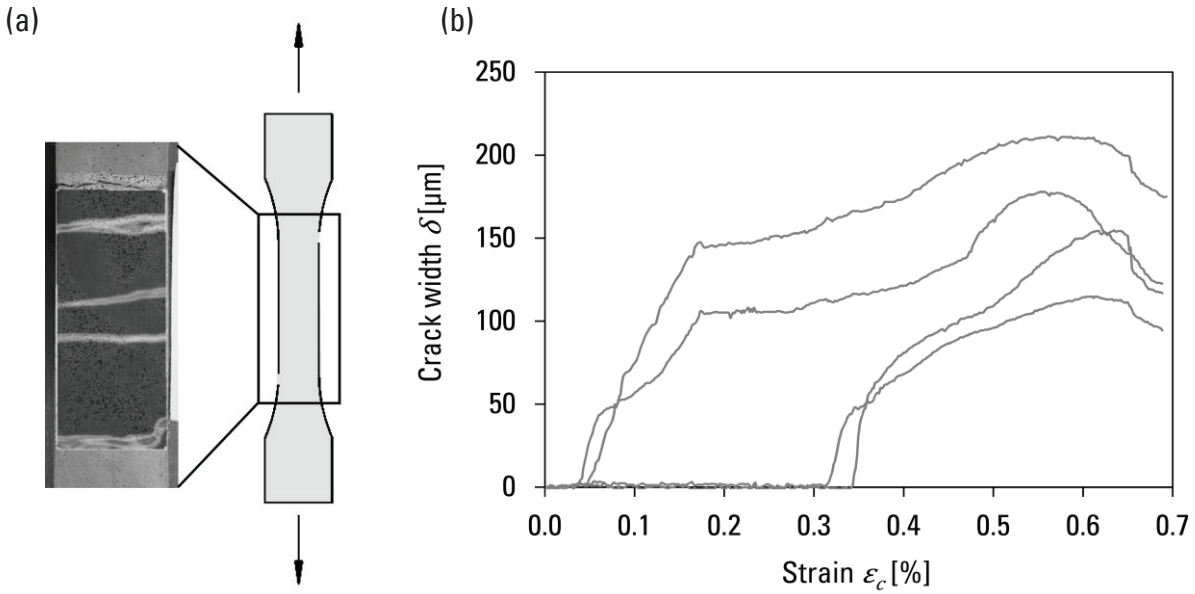

Figure 2.8: Results of photogrammetric measurements during tensile loading with (a) visualisation of the strain field indicating the location of cracks and (b) results of the individual crack width development from own tests [115]

The grey lines in Figure 2.8b depict the crack opening displacements of each individual crack during a tension test[7]. The maximum crack width during the multiple cracking stage remains limited to approximately 200 µm.

Each time a new crack forms, a steep initial increase in crack width can be observed since the fibres bridging the crack are not fully engaged. In the subsequent phase, the bridging action of fibres stabilises the crack growth and causes a moderate increase of crack widths, which can be related to progressive activation of fibres and to slip-hardening behaviour during fibre pull-out. During this stage, the crack width δ increases by approximately 60 % up to the maximum crack width δ_{max}.

The tensile strength of the composite f_t corresponds to the maximum bridging strength σ_0 of the composite in the weakest crack. It is usually reached when the crack opening exceeds the critical crack width δ_0 and mostly depends on the type and geometry of the fibres as well as their bond properties with the cementitious matrix. Since many different compositions and types of fibres have been used (cf. Table 2.1), values for the tensile strength f_t have been found to range between 2.3 and 7.6 MPa. Depending on the composition, the tensile strain capacity ε_{tu} can reach up to 5.0 %. An overview of SHCC properties reported in literature is provided in Table 2.3.

[7] Since crack widths can vary substantially along a single crack, average values for each individual crack measured at different points were used to derive the crack width development.

Table 2.3: Material properties of selected SHCC compositions (average values at an age of 28 days)

Reference	Specimen			Fibre		Compression		Tension			
	ID	Length [mm]	Size [mm]	ρ_f [%]	Type	f_{ck} [MPa]	E_m [GPa]	σ_1 [MPa]	f_t [MPa]	ε_1 [%]	ε_{tu} [%]
Kunieda et al. [69]	S-0	-	13x30	1.5	HDPE	95		4.0	6.5	0.02	1.5
	S-0-1	900	50x200	1.5	HDPE	95		4.2	5.0		0.24
	S-0-2	900	50x200	1.5	HDPE	95		3.9	4.7		0.23
Fischer and Li [44]	-	300	12.7x75	1.5	HDPE	80		4.5	6.5	0.01	4.0
Kesner and Billington [65]	SP-A	300	25x75	2.0	HDPE			1.9	2.4		0.7
	SP-B	300	25x75	2.0	HDPE	-		2.0	2.4		2.3
	SP-C	300	25x75	2.0	HDPE			1.9	2.3		1.9
Yun et al. [151, 152]	PE1.50-M	200	100[1]	1.5	HDPE	43	28.2	2.5	2.81	0.015	0.74
Curosu et al. [23, 24]	M2	250	75[1]	2.1	HDPE	140	29.5	-	5.94	-	4.3
	M-HDPE	250	24x40	2.0	HDPE	133.5	-	3.8	7.6	-	3.9
Kanakubo [63]	PE-T1	330	13x30	1.5	HDPE			3.01	4.85	0.015	1.28
	PE-T2	400	60x100	1.5	HDPE	67.3	21.0	3.86	-	0.018[2]	-
	PE-T3	200	70[1]	1.5	HDPE			5.08	5.56	0.025	0.20
	PE-T4	100	100[1]	1.5	HDPE			4.18	-	-	0.83
	PVA-T1	330	13x30	1.9	PVA			3.72	5.00	0.021	2.70
	PVA-T2	400	60x100	1.9	PVA	31.3	13.7	2.47	4.18	0.015	2.38
	PVA-T3	200	70[1]	1.9	PVA			3.17	3.38	0.021	0.07
	PVA-T4	100	100[1]	1.9	PVA			1.78	-	-	0.32

Table 2.3: Material properties of selected SHCC compositions (continued)

Reference	ID	Specimen		Fibre		Compression			Tension		
		Length [mm]	Size [mm]	ρ_f [%]	Type	f_{ck} [MPa]	E_m [GPa]	σ_1 [MPa]	f_t [MPa]	ε_1 [%]	ε_{tu} [%]
Kanda et al. [64]	P1N1	330	13x30	2.0	PVA	-			5.14		2.90
		400	60x100	2.0	PVA	-			2.76		1.18
	P1N6	330	13x30	2.0	PVA	31.6	14.3		3.95		3.17
		400	60x100	2.0	PVA				3.63		1.65
	P1N7	330	13x30	2.0	PVA	36.6	17.2		4.51		2.55
		400	60x100	2.0	PVA				3.56		1.60
	P1M3	330	13x30	2.0	PVA	30.4	14.4		3.40		2.51
		400	60x100	2.0	PVA				3.69		1.98
	P1M4	330	13x30	2.0	PVA	32.0	15.2		4.01		3.80
		400	60x100	2.0	PVA				3.60		2.10
	P2M2	330	13x30	2.0	PVA	24.0	12.3		4.00		3.96
		400	60x100	2.0	PVA				3.94		2.22
	P2M3	330	13x30	2.0	PVA	24.6	12.6		3.96		4.34
		400	60x100	2.0	PVA				3.27		2.59
Mechtcherine and Jun [100]		240	24x40	2.25	PVA			3.6	4.7	-	2.50
		500	60x100	2.25	PVA			3.2	3.8		5.00
Lepech and Li [77]	ECC-M45	304.8	13x76	2.0	PVA	64.2	-	4.79	5.94		2.20
Lárusson and Fischer [72]	ECC	500	25x50		PVA	60.0	27.3	3.50	4.00	0.02	4.00
Moreno et al. [111]	ECC	864	83x159	2.0	PVA	45.0	-	3.5[2]	2.9[2]	-	0.8[2]

[1] cylindrical specimens [2] only single values were given

2.1.4.3 Parameters affecting the tensile behaviour

Table 2.3 shows a wide variety of material properties of SHCC, which can be attributed to a broad range of material compositions and different testing procedures [100]. A step in the direction of standardisation of a test method has been taken by the recommendations in [144]. However, one should consider the affecting parameters, i.e. specimen geometry, age and curing conditions, as well as testing technique, on the resulting load-deformation behaviour when comparing the results of uniaxial tension tests for a given material composition.

Cross-section and thickness

Over time a broad variety of test setups have been developed to investigate the uniaxial tensile behaviour of cementitious materials. In some cases, cylindrical specimens were used, which offer the advantage of a simple production process. However, the tensile strength and ultimate strain obtained from rectangular specimens are often found to be higher than for cylindrical specimens [65]. These differences can be attributed to the influence of the casting process, which causes variations of initial imperfections and fibre alignment [63]. Cylindrical specimens are usually casted in vertical direction, while rectangular specimens are casted in horizontal direction, which results in a better consolidation and different flow patterns of the fresh concrete [66]. A better consolidation reduces, for example, the amount of air voids and increases the tensile strength. At the same time, the flowing pattern influences the fibre orientation and alignment (wall effect)[8]. Due to the better fibre alignment in loading direction, a better fibre effectiveness can be achieved, which increases the maximum bridging stress σ_0. These factors influence the conditions for multiple crack development and ultimately the strain capacity.

For specimens with a rectangular cross-section the tensile behaviour can also be influenced by the ratio between thickness and width. Depending on this ratio, specimens can be separated into plate and prism shapes. KANDA et al. [64] observed an increase of tensile strength f_t and tensile strain capacity ε_{tu} by 20 and 13 %, respectively, when the thickness was reduced. These findings were attributed to the effect of the specimen thickness on the fibre orientation. A small thickness of plate specimens may cause a plane fibre alignment, whereas a larger thickness can result in a three-dimensional orientation of fibres. For the latter, a lower number of fibres will be aligned in loading direction, which can reduce the fibre effectiveness [80].

[8] The wall effect describes the phenomenon that fibres align different within distinctive sections of the specimen, especially near the formwork.

The extent to which the tensile properties are affected depends on the fibre length and specimen dimensions[9]. However, for structural purposes one should bear in mind that small plate-shaped specimens tend to overestimate the tensile strength and strain capacity found in a structural member [64].

The experimental determination of the tensile properties within the frame of the doctoral work at hand were conducted on specimens with a prism cross-section.

End shape and load boundaries

Due to the rigid connection between the specimen and testing machine frame, the difference in Poisson's ratio causes a non-uniform stress distribution around the specimen end. The following stress concentration can lead to an early failure of the anchorage, which typically occurs near the specimen end. The results obtained from such experiments are thus often unsuitable for a realistic material description. A simple solution to address this problem is a strengthening of the anchorage zone, which prevents failure in this area. The requirement of a larger cross-section in the anchorage zone and a smaller cross-section in the measurement zone results in a dumbbell shape. This shape leads to a uniform stress distribution in the measurement zone and a concentration of tensile strains on this specified region. It was observed that specimens with this kind of tapering show an increased ultimate tensile strain ε_{tu} [65].

Even if an early failure of the anchorage zone can be prevented, the connection between anchorage and load frame itself can influence the measured tensile behaviour. A rotational connection might cause uneven strains to develop on the opposite sides of the specimen after the first crack appeared. With increasing strain indifference between the two sides of the specimen, the loading becomes increasingly eccentric. Such behaviour can be prevented by rigid non-rotational boundaries, which cause a uniform strain distribution throughout the cross-section. MECHTCHERINE and SCHULZE [104] compared the tensile behaviour of small dumbbell specimen in a test setup with rotational and non-rotational loading plates and found that the stress at first cracking σ_1 and tensile strength f_t as well as tensile strain capacity ε_{tu} decreased for specimens attached to rotational loading plates. A likely explanation is that the strain concentration on one side of the specimen causes local tensile stresses to exceed the maximum bridging stress σ_0 leading to early crack localisation and failure. It was suggested that a non-rotational setup leads to a more uniform tensile stress distribution, which can prevent local stress concentrations and provide a more realistic estimation of the material response.

In the frame of the doctoral work at hand a test setup developed by MECHTCHERINE [100] with a dumbbell shape and non-rotational boundaries was used to determine the characteristic tensile behaviour of the composite.

[9] Plate elements with large dimensions will also have a three-dimensional fibre orientation, if the fibre length is small compared to the thickness.

Effect of the specimen length

A comparison of reported values for tensile strength and ultimate tensile strain (cf. Table 2.3) suggests that those of larger specimens tend to be smaller when compared to small-sized specimens of the same composition.

KUNIEDA et al. [69] compared the load-deformation behaviour of large structural sized and small dumbbell-shaped specimens in uniaxial tension. The large-size specimens exhibited a higher modulus of elasticity E_{ct} and less pronounced strain-hardening behaviour in the post-cracking phase. A reduction of the tensile strength f_t and strain capacity ε_{tu} by 30 and 85 %, respectively, could be observed. In this case, the specimen shape substantially differed and hence a large portion of the observed difference was attributed to the influence of the specimen size and shape on the fibre orientation. However, a large part of these differences can also be attributed to the effect of geometrical boundary conditions, which vary inevitable for the different test setups utilised.

MECHTCHERINE and JUN [100] compared dumbbell-shaped specimens of two different sizes but identical geometrical shapes. In this case, the stress at first cracking σ_1 and tensile strength f_t were reduced by 19 and 11 %, respectively, while the tensile strain capacity ε_{tu} increased by as much as 100 %. It was suggested that changes of the first cracking σ_1 may stem from restrained shrinkage, which causes the development of tensile eigenstresses. These eigenstresses may increase with specimen size and initiate micro-cracks due to the pre-loading of the specimen. Even though the observed results in terms of strain capacity are in contradiction to the findings of [69], the geometrical shape in [100] was kept constant, which eliminates a large portion of shape and specimen end effects.

However, this inconsistency of experimental findings indicates the effect of specimen length on the tensile behaviour of SHCC. For brittle cementitious materials, such as plain concrete phenomena causing size effects are usually described by concepts based upon fracture mechanics [13]. Early approaches based upon statistical effects such as the Weibull theory [108] were found to be of less significance regarding size effects in case of plain concrete [123]. However, special attention must be given to the distinctive process of multiple cracking when concepts based upon fracture mechanics are applied to fibre-reinforced cement-based composites such as SHCC.

At the meso-level of observation, fibre bridging enables SHCC to develop multiple fine cracks. In contrast to brittle materials, strain-energy is not "consumed" by in one crack but dissipated over a large region due to the multiple cracking. The total energy dissipated, i.e. the total area under the load-displacement curve, is considered work-to-fracture, which is affected by the specimen length since the number of cracks increases with increasing specimen length. It has been observed that the tensile behaviour of SHCC is generally influenced by the specimen length during the stage of multiple cracking.

However, according to LEPECH and LI [75], fracture mechanic based concepts may not be applicable for the explanation of size effects in SHCC. Moreover, the process of multiple cracking may be more dependent on statistical size effects rather than fracture based phenomena. Reasons for this can be found in the effect of material inhomogeneity (micro-defects, air-voids), the extent of drying shrinkage and the intensity of material segregation. Flaws inherent to the matrix can influence the matrix tensile strength and subsequently the strain-hardening capacity, since the probability of a violation of the requirements for multiple micro-cracking rises.

This shows the necessity to consider the effect of specimen size, especially regarding its impact on the material structure, when analysing the load-deformation behaviour of large-scale tension members. Therefore, complementary investigations including fresh SHCC properties, air content and the scale of shrinkage were conducted within the scope of the experimental investigations of the doctoral work at hand.

Specimen age

It is well known that the mechanical properties of cement-based materials are influenced by the specimen age. In general, this time-dependent behaviour of cement-based materials can be related to the continuous binder hydration of the cement paste. Studies on SHCC showed that the matrix tensile strength σ_{mu} develops at higher rates compared to the compressive strength f_c, thus a considerable gain of tensile strength within the first 24 hours after casting was observed [76]. The tensile strength development is thereby influenced by multiple parameters, i.e. the type and content of binder, pozzolanic additives as well as the curing conditions among others. The extent to which the crack-bridging behaviour of the fibres also undergoes time-dependent processes and how this affects the development of σ_0 still needs to be investigated.

WANG and LI [147] analysed the time-dependent behaviour of SHCC and observed that the tensile strength f_t increased by approximately 80 % between 24 hours and 90 days. This increase can be attributed to the continuous binder hydration, which increases the matrix tensile strength σ_{mu}. A higher matrix cracking strength leads to a lower ratio of σ_0/σ_{mu}, which may result in a reduced tensile strain capacity ε_{tu}. Thus, strain capacity ε_{tu} was found to decrease from 4 to 3.2 % between 7 and 30 days after casting.

Preliminary investigations on specimens with ages of approximately 90 days also suggested that strain capacity ε_{tu} can decrease, while first cracking σ_1 tends to increase [115]. Possible reasons can be found in time-dependent changes of the matrix micro-structure and the properties of the fibre-matrix interface. In this case a continued hydration of the cement paste may have caused further densification of the matrix, which leads to variations of matrix strength and toughness at different specimen ages. Further time-dependent changes in the tensile cracking behaviour can be attributed to variations of the fibre-matrix bond strength, which was found to increase with specimen age [46]. High fibre stresses stemming from an increased bond strength may result in fibre rupture instead of gradual fibre pull-out, which is unfavourable for multiple cracking.

For comparability of the results obtained within the experimental framework of the doctoral work at hand, the requirement of a composite age of 28 days was adopted for tensile characteristic material values.

Curing

The development of mechanical properties is not only influenced by the matrix composition but also by curing conditions. MECHTCHERINE and JUN [100] compared the tensile properties of SHCC for sealed and unsealed curing conditions. Sealed specimens were wrapped in plastic foil and stored at $T = 25°C$ and $RH = 65\ \%$ after casting, while unsealed specimens were stored without any protection from desiccation. The stress at first cracking σ_1 and the tensile strength f_{ct} of the unsealed specimens experienced a reduction of 30 and 17 %, respectively, compared to the results for the sealed specimens. The tensile strain capacity ε_{tu} was found to increase by 32 %, possibly due to the low stress at first cracking σ_1. The change of tensile properties was attributed to the effect of sealing conditions on the drying process of the specimens. It was suggested that the unsealed specimens developed a pronounced moisture gradient due to the release of moisture. As a result, restrained shrinkage at the surface vicinity causes eigenstresses leading to an early development of micro-cracks[10].

Curing in water can prevent a moisture gradient, although it affects the tensile strength development of the matrix as well as the bond interaction between fibres and matrix. KESNER and BILLINGTON [65] conducted tension tests on specimens subjected to different curing and drying periods. An increased wet curing period from 11 to 16 days before testing resulted in twice as high tensile strain capacity ε_{tu}, while a reduction of 20 % was observed in stress at first cracking σ_1.

Specimens tested in the framework of the doctoral work at hand were stored at room temperature in sealed conditions apart from large-scale specimens.

2.2 Steel reinforcement

Section 2.1.4 focused on the micro-mechanical processes in SHCC and their effects on the mechanical behaviour under tensile and compressive loading. It was shown, how strain-hardening behaviour of a cementitious composite can be achieved and the extent to which these properties are influenced by boundary conditions relevant in structural applications. These conditions are of importance when using SHCC as a construction material for structural elements. Even though SHCC offers the possibility to be used as a single construction material, for structural applications of SHCC conventional steel reinforcement is usually utilized [70, 77, 88, 129, 140, 141].

[10] In this case differences in the progression of the stress-strain diagrams as well as deviations in the crack pattern between unsealed and sealed specimens indicated the pre-existence of micro-cracks.

The combined load-bearing behaviour of steel reinforcement and thus holds particular interest for the design of structural elements. The basis for the design and application of SHCC reinforced with steel bars is a profound knowledge of the bond behaviour as well as the mechanical behaviour of steel rebar. Especially the yielding of mild carbon steel is of interest regarding the combined load-deformation behaviour of R/SHCC.

2.2.1 Tensile behaviour of steel reinforcement

Steel reinforcement is used in conventional concrete elements to carry tensile forces after the concrete has cracked and compensate the relatively low tensile strength of concrete. For this purpose, steel is usually applied in axial direction of the main tensile forces. Important mechanical parameters, i.e. tensile strength, yielding strength, modulus of elasticity as well as strain capacity, can be derived from uniaxial tension tests on steel bars. For conventional reinforced concrete structures, one of the most important characteristic is the ability of steel to yield, which ensures the desired structural ductility, i.e. large deflections and visible cracks long before structural failure, as long as the minimum reinforcement ratio[11] is provided.

For steel reinforcement to transfer the tensile cracking load, stresses need to be transmitted between the different materials. This transfer can be achieved by structural anchorage of the rebar ends, a continuous mechanical interlocking with a roughened or corrugated rebar surface or a combination of both. The interaction between steel surface and surrounding concrete can be characterised by the bond strength. Once the bond strength is reached the rebar is usually pulled out of the concrete.

One limitation of conventional steel reinforcement in terms of durability is its susceptibility to corrosion when subjected to environmental influences. The continuous progress of steel corrosion can lead to a reduction of the steel cross-section, which lowers the tensile load-bearing capacity of the rebar. The concurrent increase in volume due to the formation of corrosion products may lead to concrete spalling, causing a further reduction in durability.

The passivating alkaline chemical environment of the surrounding cement paste protects the steel from corrosion. It is generally accepted that sufficient concrete cover and the limitation of crack widths can protect the passivating environment of the steel surface for long time. Such limitation of crack widths can be achieved by the addition of fibres, as shown in the example of SHCC, cf. Section 2.1.4. However, the application of steel reinforcement changes the global load-deformation behaviour of SHCC elements depending on the mechanical properties of steel rebar.

[11] For conventional concrete the minimum reinforcement ratio describes the amount of steel rebar which is necessary to completely carry the concrete first cracking load.

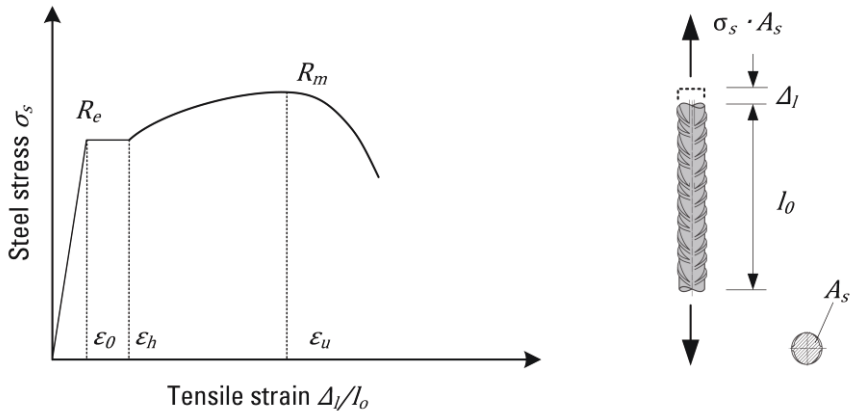

Figure 2.9: Stress-strain curve on the example of a hardened and tempered steel bar

Figure 2.9 illustrates the typical load-deformation behaviour of a conventional mild reinforcing steel under uniaxial tension. The curve is representative for the behaviour of a hardened and tempered steel. Four distinctive stages can be identified starting with elastic deformations up to the yielding strength R_e, which corresponds with the yielding strain ε_0. The second stage shows a plastic phase with a yielding plateau and a nearby constant stress level. This stage is characterised by a distortion of the crystalline structure of steel at the micro-level, which leads to irreversible deformations. Such deformations are not found to be evenly distributed over the entire length, they may occur at random regions along the rebar. The regions of non-uniform deformations, so-called Lüders bands, separate regions that have yielded from those that have not. The extension of the Lüders bands continues until they are evenly distributed over the entire rebar length, at which point a further increase in force is required to deform the steel.

The resulting increase in stress marks the beginning of the third stage, which is described as hardening of steel. During this phase, the steel specimen deforms evenly over its length, which causes a lateral contraction of the steel and a subsequent reduction of the steel cross-section. This process continues until the tensile strength R_m is reached, which corresponds to the ultimate steel strain ε_u. The last stage is characterised by strain localisation and pronounced lateral contraction at this region resulting in a softening branch of the stress-strain curve until the rupture strength is reached.

2.2.2 Mechanisms of strain localisation

The region of localisation (contraction) can stretch along a bar length of approximately two times the bar diameter; the local tensile strain may reach up to 50 % [136]. Due to large deformations in the localisation zone, the remaining part of the steel will be unloaded releasing elastic energy. The ductility of the steel is usually understood as the ability of the material to exhibit large plastic deformations before failure.

For conventional reinforcement, sufficient ductility is given when the tensile strain at the maximum load reaches a minimum of $\varepsilon_u > 2.5\,\%$ and the tensile strength exceeds the yielding strength by $(R_m/R_e) > 1.05$. High ductility is given when the ultimate tensile strain exceeds $\varepsilon_u > 5.0\,\%$ with a ratio of ultimate and yielding strength above $(R_m/R_e) > 1.08$. Therefore, the rebar performance in terms of ductility is largely influenced by the strain-hardening behaviour of the steel. The strain-hardening behaviour of steel reinforcement in uniaxial tension holds great practical and theoretical importance in the post-cracking stage of reinforced concrete. Therefore, a description of the steel deformation behaviour within a macro-crack is necessary to analyse the interaction between matrix cracking and steel yielding.

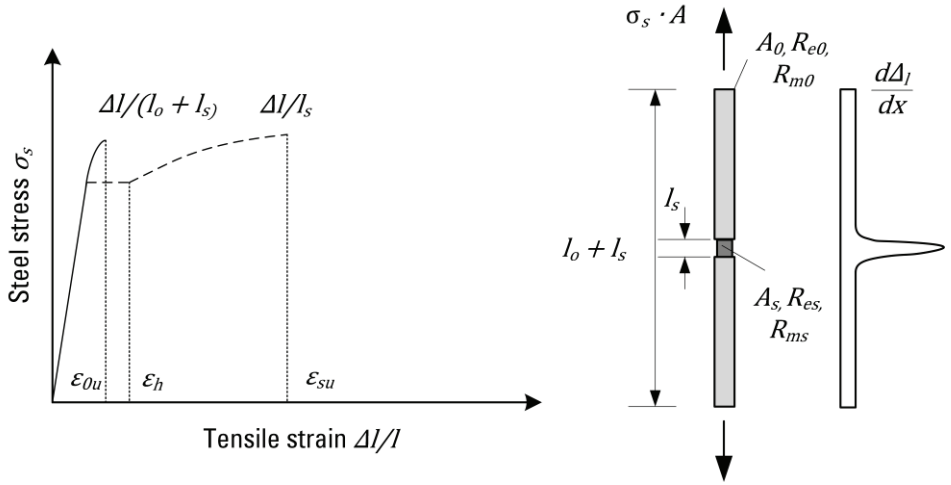

Figure 2.10: Schematic comparison of the global and local load-deformation behaviour of a steel rebar including the effect of a short process zone adopted from SIGRIST [136]

According to SIGRIST [136], steel ductility is influenced by the reduction of the cross-section during contraction and the hardening behaviour during steel yielding. Figure 2.10 depicts a simplified model for steel bars with a local reduction of the cross-section. Such localisations could occur due to variations of material properties, geometric imperfections or stress concentrations caused by a crack in the surrounding concrete. The condition to achieve strain-hardening over the entire length of a rebar can be expressed as:

$$\sigma_s = A_s \cdot R_m > A_0 \cdot R_e \tag{2.3}$$

If this condition is met for every local deformation zone along the rebar length, the material behaviour as indicated by the dotted line is achieved. If this condition is not met, due to either variations in material properties or a stiff bond with the surrounding concrete near a crack, a distributed yielding over the entire bar length cannot occur. In this case, the material model is only valid for a short process zone of the length l_s.

Even though the steel shows high ductility over this area (dashed line), the measured strain of the entire element experiences a behaviour as depicted by the continuous line, which is a relatively brittle mode of failure. The sketched model highlights the importance of the characteristic strain-hardening behaviour of steel, especially with respect to the combined interaction with macro-crack development.

2.3 Bond behaviour in steel-reinforced SHCC

The bond between concrete and steel reinforcement allows the transfer of forces between the two materials and has a significant influence on the load-deformation behaviour of a reinforced element. In general, the mechanical interaction between the materials enables a contribution of concrete to the load-bearing capacity of the reinforced element (tension-stiffening), to the anchorage at the ends of a rebar and to the restraint of creep and shrinkage deformations, among others.

The bond behaviour has been extensively investigated by numerous researchers and different tests methods have been developed, such as pull-out tests, splice tests, and cantilever beam tests. Fundamentals of the mechanical interaction between steel rebar and OC can be found in [42, 126, 127]. Even though the bond behaviour of steel rebar and fibre-reinforced concrete has been in the focus of many researchers [124], only little information on the bond behaviour of steel rebar and SHCC is available at present (see e.g. [11, 21, 51]). However, profound knowledge of this behaviour is required to understand the load-deformation behaviour of R/SHCC elements. Therefore, an overview of the governing mechanisms and the results of own experimental work [114] will be presented in this section.

2.3.1 Bond mechanisms

The interfacial action between deformed steel bars and cementitious matrix can generally be classified into three kinds, which are illustrated in Figure 2.11: adhesive forces due to chemical bond, frictional forces between the adjacent surfaces and mechanical interlocking, which is a result of the steel ribs exerting pressure on the surrounding cementitious matrix.

Adhesion forces (A) stem from the chemical bond between particles of hydrated cement paste and steel reinforcement. Since the area of influence is limited to a microscopic level, chemical bond can be assumed to act only at very low slip deformations. The relatively weak chemical bond is quickly exceeded, which leads to slipping of the surface and activation of friction forces (B).

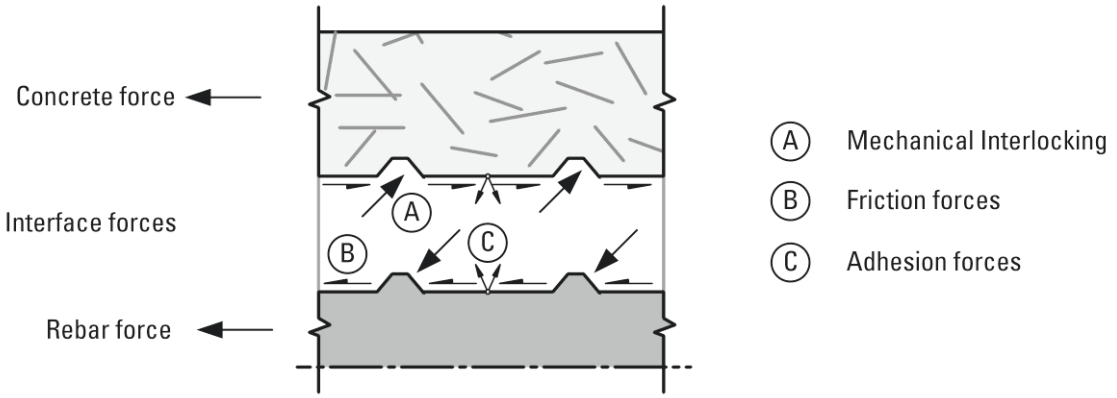

Figure 2.11: Schematic illustration of external and internal forces acting between steel surface and cement-based composite, adapted from ALVAREZ [8]

Friction forces are based upon the effect of micro-interlocking between the steel surface and rough surface of the cementitious matrix and can be assumed to be almost independent of the slip rate, which leads to a rapid activation of the steel ribs. The resistance enforced by steel ribs causes a mechanical interlocking (C) and provides the most significant contribution to the bond strength. In this case, pressure exerted from steel ribs creates compressive forces radiating out from the rebar. These forces are confined by the surrounding matrix and activate circumferential tensile stresses in the cement-based composite. The activation of these interfacial forces mostly depends on the magnitude of the relative displacement between ribs and cementitious matrix. Figure 2.12 depicts the bond stress development in relation to the relative displacement.

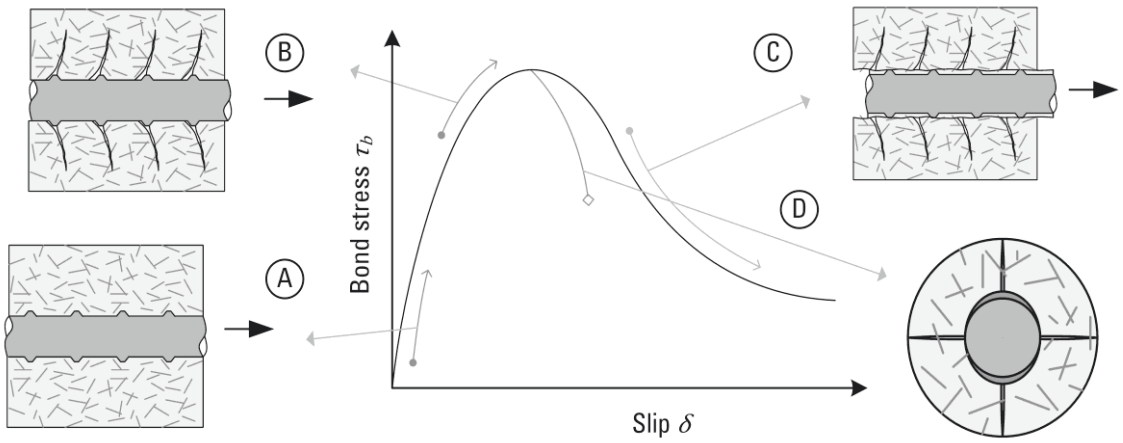

Figure 2.12: Different stages of the mechanical interaction between ribbed steel and fibre-reinforced cement-based composites, adapted from JUNGWIRTH [61]

The bond stress development can generally be divided into three stages: uncracked matrix, internal cracking and pull-out or spalling [127].

- Uncracked concrete (A): this stage applies for low bond stresses and is based primarily on chemical adhesion. Although no slip occurs in the interface, a displacement of the unloaded end can be measured due to elastic deformations.
- Internal cracking (B): according to GOTO [48], internal secondary cracks develop due to the increasing relative displacement. During this stage, the largest bond stress can be reached.
- Pull-out (C): with further loading, additional slip is provoked, which can reduce the bond stress to friction forces between the crushed matrix particles in the surrounding cementitious matrix ultimately resulting in shear failure.
- Concrete spalling (D): according to TEPFERS [139], longitudinal cracks develop when the confining circumferential stresses exceed the tensile strength of the cementitious matrix. Without sufficient concrete cover or confining reinforcement these longitudinal cracks lead to spalling failure.

2.3.2 Determination of bond properties

The bond behaviour of a rebar embedded into a cement-based composite can be determined by means of experimental investigations. Different methods have been developed to derive the stress-slip relationship, which can be used to develop a bond model as a basis for constitutive relationships[12] [126]. Common methods are flexural bending tests with lap splices or pull-out tests.

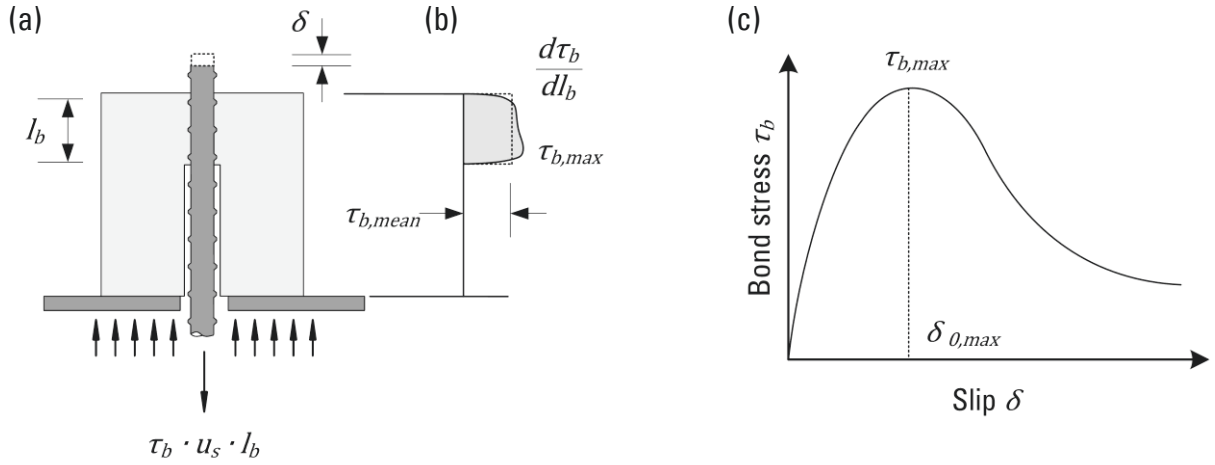

Figure 2.13: (a) Pull-out specimen with (b) distribution of bond stresses and (c) schematic representation of the resulting bond stress slip relationship adopted from SIGRIST [136]

[12] Different mechanical processes occur simultaneously over the bond length, which is why the bond-slip behaviour is considered a pseudo material property.

Pull-out tests provide a simple test setup and achieve sufficient comparability between different material compositions. The basic setup of a pull-out test is displayed in Figure 2.13a. In this case, force is applied to the steel reinforcement and transferred over a specified bond length l_b. The bond length should be limited to $l_b \leq 5d_s$, to achieve a uniform bond stress distribution over the embedment length. The bond stress τ_b can be calculated dividing the measured force F by the embedded steel surface resulting in Eq. (2.4).

$$\tau_b = F/(d_s \pi l_b) \tag{2.4}$$

The stress-strain relationship can be derived from the displacement of the unloaded end of the rebar, which is plotted over the bond stress. Since bond stresses show a non-linear distribution over the bond length, as illustrated in Figure 2.13b, the calculated bond stress can, strictly speaking, only serve as an approximation valid for short bond lengths.

Furthermore, the bond length can have significant influence on the variation of the bond properties, which become more prone to material inhomogeneity of the cementitious matrix and inconsistencies of the rib geometry with decreasing bond length. In this regard, SORETZ [137] suggested that the variation of bond properties especially for low slip values can be minimised by determining the arithmetic mean of the stress slip function with Eq. (2.5).

$$\tau_{b,mean} = \frac{\tau_{b(0,01)} + \tau_{b(0,1)} + \tau_{b(1)}}{3} \tag{2.5}$$

The slip of steel rebar under regular loading conditions depends on the actual size of the individual crack widths. According to SIGRIST [136], the bond stress in the state of serviceability for conventional reinforced concrete can be determined at an equivalent slip δ of 0.1 mm. In comparison to OC, bond stress activation is less pronounced in SHCC due to reduced crack widths of the fibre-reinforced cementitious matrix. Moreover, FISCHER and LI [44] postulated that bond stresses are only activated by microscopic discontinuities. Thus, the initial part of the bond-slip relationship holds strong relevance for the combined interaction of steel reinforcement and SHCC in tensile members.

Then again, the maximum bond strength holds importance regarding rebar anchorage and in the vicinity of large discrete cracks. The maximum bond stress $\tau_{b,max}$ and the associated maximum slip $\delta_{0,max}$ are influenced by a variety of factors for which an overview is given in Table 2.4. In the case of fibre-reinforced cement-based composites, special emphasis should be placed upon the material composition and the effect of fibres. It was found that the lack of coarse aggregates, for instance, can weaken the interlocking effect between steel ribs and cementitious matrix, which lowers the bond stiffness [44].

Table 2.4: Major factors influencing the bond behaviour, according to LINDORF [93]

Material	Structural layout	Loading
Concrete	Bond length	Longitudinal/lateral
- Composition	Concrete cover	Compression/tension
- Production	Lateral reinforcement	Static/dynamic
- Strength	Casting direction	Loading speed
- Load-deformation behaviour	Position of rebar	Other (temperature etc.)
Steel		
- Yield and ultimate strength		
- Load-deformation behaviour		
- Rebar diameter		
- Rib geometry		

BANDELT and BILLINGTON [10, 11] investigated the bond performance on reinforcement embedded in different HPFRCC materials including SHCC by means of four-point bending tests on specimens with lap splices. The setup of the beam test was developed so that splitting bond failure could be investigated. An increase of bond strength $\tau_{b,max}$ by 39 %, on average, relative to traditional concrete could be observed for beams made of SHCC.

Another parameter of interest, especially regarding dynamic loading conditions, is the bond-slip toughness, i.e. the area under bond-slip curve, which indicates the energy dissipation capacity of the interfacial bond. In general, fibre reinforcement was found to substantially contribute to the ductility of the post-splitting response, while no effects could be observed on the bond-slip response in the pull-out stage [52]. Pull-out tests with different compositions of HPFRCC containing HDPE and PVA fibres were conducted by CHAO et al. [21]. The exceptional bearing conditions of the specimens differed from the recommended test setup and led to splitting failure in all cases. Nevertheless, the results showed that under the given boundary conditions the fibres significantly contributed to the resistance against splitting failure.

In conventional reinforced concrete, the maximum bond stress $\tau_{b,max}$ should be limited to avoid longitudinal cracking. A calculation of the allowable bond stress for conventional reinforced concrete based upon the tensile strength, bar diameter and concrete cover was suggested by ELIGEHAUSEN [32] expressed by Eq. (2.6).

$$\tau_{b,lim} = 1{,}5 \cdot f_{ct} \cdot \sqrt{c/d_s} \tag{2.6}$$

This formula implies that for SHCC less concrete cover would be required given that less bond stresses are activated and that tensile strength tends to be higher than for conventional concrete. However, further research is required regarding the development of bond stresses and the parameters influencing the bond strength, i.e. rebar diameter, SHCC cover and its tensile strength.

2.3.3 Pull-out behaviour of reinforcement embedded in SHCC

Concentric pull-out tests according to RILEM RC 6 [127] were performed by the author on deformed and smooth steel bars[13] embedded into OC and SHCC [114]. The mix design of both compositions was targeted towards similar compressive strength for better comparability. The mix compositions are displayed in Table 2.5. The OC and SHCC had a compressive strength f_c of 31.3 and 34.7 MPa, respectively.

The embedment length l_b was modified from the original recommendation of $l_{bs} = 5 \cdot d_s$ to an equivalent length of five steel ribs. In this case the same number of ribs will be embedded for all different steel diameters, which allows a better comparison independent from the rebar geometry. In this case, the resulting bond stresses are expected to be slightly higher compared to the standard method. In addition, confining forces of the bearing were reduced by elastic rubber pads separating the specimen from the loading plate. This method was applied to achieve enhanced representability for actual structural bond conditions.

Table 2.5: Mix proportions of OC and SHCC in [kg/m³]

Mix	CEM 42,5	Fly ash	Sand	Fine sand	Coarse aggregates	Water	Super plasticizer	Viscosity agent	PVA fibres
OC	308	-	902	-	1000	185	-	-	-
SHCC	550	647	-	551		395	2.2	0.4	26

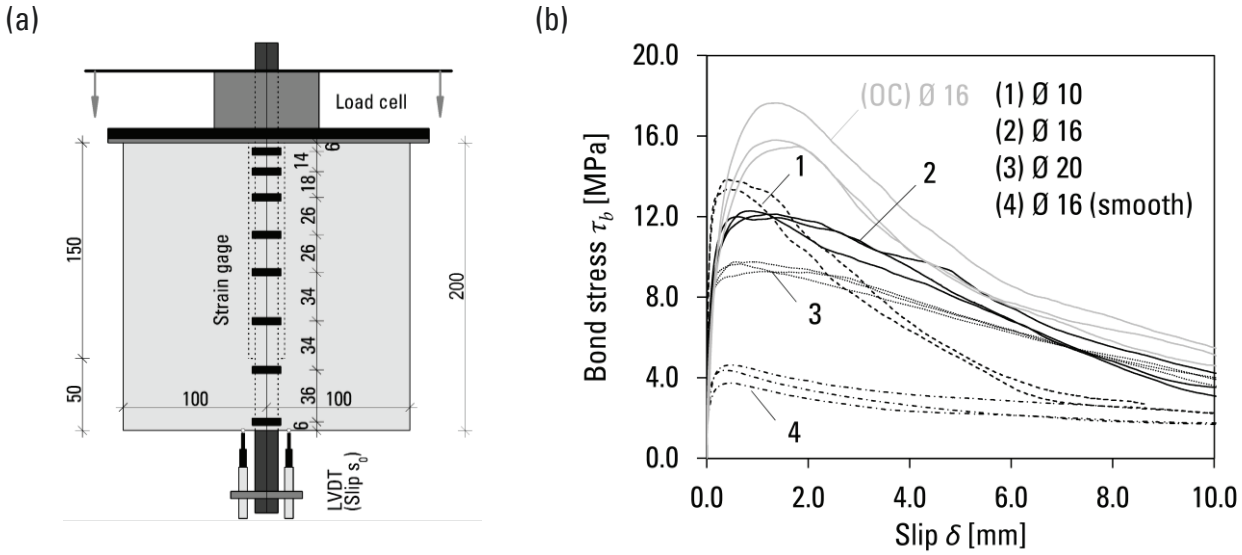

Figure 2.14: (a) Pull-out test setup used for the determination of the bond response and (b) bond stress-slip curves for different bar diameters embedded into SHCC and OC

[13] High tensile and mild steel reinforcement according to SANS 920 [131] were used for this study.

Two linear variable differential transformers (LVDTs) were attached to the free end of the rebar to determine the slip, as illustrated in Figure 2.14a. The results in the form of stress-slip diagrams are shown in Figure 2.14b. In general, a similar bond-slip behaviour compared to conventional concrete could be observed. In contrast to the findings of BANDELT and BILLINGTON [10, 11], the measured bond strength of SHCC was found to decrease by 24 % on average compared to conventional concrete. This discrepancy can be attributed to the influence of the test setup, since pull-out test and spliced beam test reproduce different bond conditions, i.e. those found for rebar anchorage and flexural concrete members, respectively.

The bond stiffness was not only similar to that of OC, but also higher bond stiffness could be observed for the lowest bar diameter. Likewise, slip corresponding to the maximum bond stress $\delta_{0,max}$ was found to decrease for SHCC specimen by 50 %, on average. A further reduction can be observed in case of the smooth rebar. The low slip values at the maximum bond stress yield the conclusion that friction forces may have a more significant influence on the bond strength than mechanical interlocking of the ribs. Part of this behaviour may stem from the low resistance of the fine aggregates to concrete crushing.

The arithmetic mean of the bond stresses $\tau_{b,mean}$ was calculated according to Eq. (2.5). A low scatter was observed for the tested specimens despite relatively short bond lengths and reduced confining forces with a coefficient of variation ranging from 0.29 to 4.25 %. This emphasises the influence of fine aggregates, which enhance the material homogeneity and the confining effect of uniformly distributed fibres. High material homogeneity can generally be assumed to provide consistent bond properties even at long bond lengths.

Moreover, it could be observed that longer bond lengths decrease the bond strength, which could be a result of the pronounced non-uniform bond stress distribution along the embedment length[14]. In either case, the bond strength decreases with increasing rebar diameter, which is in accordance to the findings of similar experimental investigations conducted by ASANO [9]. Although the experimental setup differed from the one used in this study the same dependencies could be observed. The bond toughness in general increased compared to concrete specimens with a tendency towards increasing bond toughness for large bar diameters. The shear resistance of SHCC during the steel pull-out was generally smaller compared to that of OC. Furthermore, the smallest bar diameter experienced an ultimate pull-out stress comparable to that of smooth bars. This could be attributed to the effect of the fine material constituents, which lower friction forces and reduce the pull-out strength. A summary of the mean values for three specimens of each series is given in Table 2.6.

[14] Experimental investigations were extended to a bond length of $l_b = 250\ mm$ to study the effect of long bond lengths. With a bar diameter of $d_s = 16\ mm$ a reduction of $\tau_{b,max}$ by 41 %, on average could be observed.

Table 2.6: Experimental results of pull-out tests on steel rebars embedded into SHCC and OC (standard deviations are given in parentheses)

Test series	**Steel rebar diameter**	**Bond length**	**Maximum bond stress**	Slip at $\tau_{b,max}$	**Mean bond stress**	**Compressive strength**
	d_s [mm]	l_b [mm]	$\tau_{b,max}$ [MPa]	$\delta_{0,max}$ [mm]	$\tau_{b,mean}$ [MPa]	f_c[1] [MPa]
OC	16	40	15.13 (2.69)	1.45 (0.23)	8.18 (0.40)	31.27
1	10	40	13.07 (0.40)	0.59 (0.29)	9.49 (0.03)	35.17
2	16	50	12.13 (0.15)	0.86 (0.31)	7.84 (0.19)	34.10
3	20	70	9.56 (0.25)	0.89 (0.25)	7.21 (0.31)	35.17
4	16 (smooth)	40	4.25 (0.46)	0.42 (0.03)	3.01 (0.33)	34.10

[1] for the compressive strength only one control specimen was tested

2.4 Structural behaviour of reinforced SHCC

The interaction of steel reinforcement and SHCC results in a combined load-deformation response, which is influenced by the individual material properties, as well as their interfacial bond properties. The material behaviour of SHCC and steel were described in Section 2.1.4 and 2.2.1, respectively followed by a description of their bond interaction in Section 2.3.3.

The development of reliable mechanical models to predict tensile behaviour of R/SHCC elements holds strong interest for structural applications, e.g. the calculation of deformations and tensile forces in the serviceability limit state (SLS) and ultimate limit state (ULS). Furthermore, sufficient knowledge of the strain and crack development in reinforced tensile members may provide a basis to estimate the durability of a structural member. Especially the structural behaviour in uniaxial tension should be investigated, since these principles can be transferred to the situation in reinforced beam elements subjected to bending loads, with a pronounced tension zone. Accordingly, further investigations regarding the interactions of reinforcement and SHCC in such loading conditions become necessary.

An overview of the test results reported from experimental investigations on R/SHCC under uniaxial tension is given in Table 2.7. These results are influenced by a variety of factors, i.e. material properties, specimen geometry, reinforcement ratio and geometry, bond conditions, test setup as well as age and curing conditions among others. Information on the corresponding mix composition and material properties of SHCC in use can be found in Table 2.1 and Table 2.3, respectively. It becomes evident that a general decrease in the ultimate strain can be observed in comparison with the tensile behaviour of plain SHCC. However, the ultimate tensile strain of reinforced SHCC was mostly found to reach or exceed the yielding strain of the steel reinforcement. The reason for this can be found in the effect of multiple cracking and the bond interaction between steel reinforcement SHCC, which will be presented in this section.

Table 2.7: Characteristic parameters of the tensile load-deformation behaviour of selected steel R/SHCC elements

Reference	R/SHCC specimen			Reinforcement		Steel properties			Results for R/SHCC			
	ID	Length [mm]	Cross-section [mm]	ρ_s[1] [%]	Configuration	R_e [MPa]	R_m [MPa]	E_s [GPa]	P_{cr} [kN]	P_u [kN]	ε_1 [%]	ε_{tu} [%]
Kunieda [69]	S-1-1	900	50x200	0.28	1 Ø 6	320	529	200	42	64		1.58
	S-1-2	900	50x200	0.28	1 Ø 6	320	529	200	41	65		1.60
	S-2-1	900	50x200	0.57	2 Ø 6	320	529	200	40	74		1.49
	S-2-2	900	50x200	0.57	2 Ø 6	320	529	200	40	73		1.50
	S-3-1	900	50x200	0.86	3 Ø 6	320	529	200	38	85		1.51
	S-3-2	900	50x200	0.86	3 Ø 6	320	529	200	37	85		1.51
	S-4-1	900	50x200	1.14	4 Ø 6	320	529	200	36	104		1.82
	S-4-2	900	50x200	1.14	4 Ø 6	320	529	200	36	103		1.80
Fischer and Li [44]	A	500	175x175	1.63	1 Ø 25	407	632	203	105	310[2]	.	4.02
	B	500	120x120	2.01	1 Ø 19	407	632	203	58	175	.	4.00
Yun et al. [151, 152]	PE1.50-M	500	55x55	7.12	1 Ø 16	320	-	157	-	85[3]	.	1.85[3]
Lárusson and Fischer [72]	R/ECC	1000	100x100	1.14	4 Ø 6	600	680	202	10-30	94-98	0.02	1.2-1.5[2]
	GFRP/ECC	1000	100x100	1.26	4 Ø 6.3	-	1050	46	16-21	90	0.02	1.1-1.2[2]
Moreno et al. [111]	ECC	1041	127x127	1.26	1 Ø 16	435[3]	597[3]	218[3]	63	125	0.02	3.5

[1] Reinforcement ratio as $\rho_s = A_s/(A_c - A_s)$, [2] test finished prior to rupture, [3] calculated from steel stress vs. steel strain curve

2.4.1 Effect of long bond lengths

While pull-out tests provide a tool to determine the bond properties needed, e.g. for the anchorage of steel reinforcement at the end of a structural element, their capability of a realistic prediction of the bond behaviour along the rebar in a cracked element is only limited. For conventional R/C, it can be assumed that stresses are fully transferred from concrete to the steel crossing a crack resulting in relatively large strain differences between the unloaded concrete near the crack face and highly stressed steel. The strain differences generally lead to activation of bond stresses, which are required to transfer tresses across the steel-concrete interface. Although SHCC reaches its matrix tensile strength σ_{mu} at similar elastic strain levels as conventional concrete, it seems possible that the crack-bridging capability of the fibre-reinforced cementitious composite changes the distribution of forces between steel and cracked matrix.

FISCHER and LI [44] investigated the load-deformation response of deformed steel rebars embedded into ECC in uniaxial tension and compared it to that of a rebar in conventional concrete. The experimental setup targeted the effect of multiple cracking on the distribution of strains within the steel rebar, with a special focus on the post-cracking of the cementitious composite and post-yielding of the steel reinforcement. It was shown that the ductile behaviour of the cementitious composite – with maximum strains beyond the yield load of steel reinforcement – resulted in an improved cracking behaviour compared to a conventional concrete matrix.

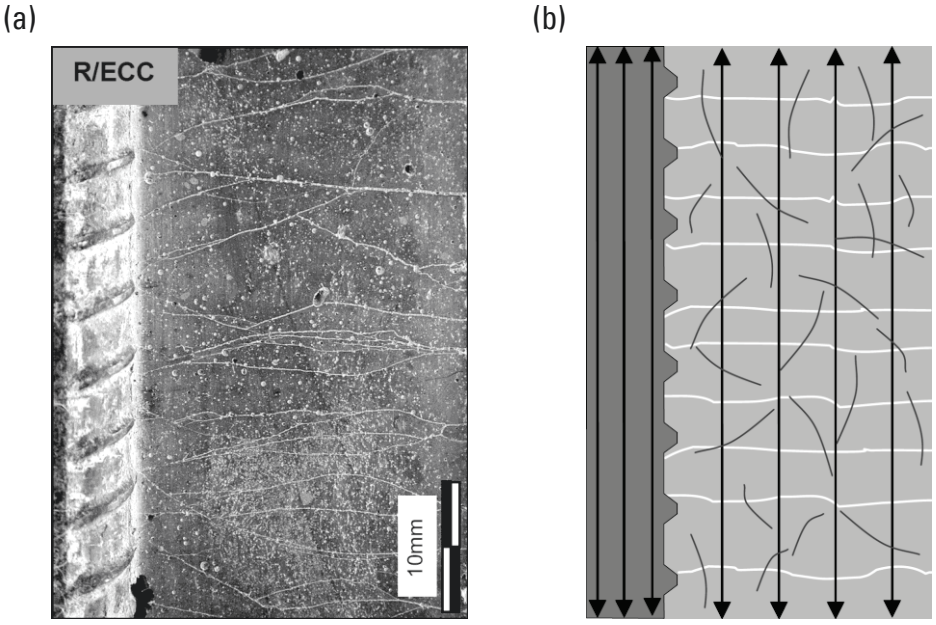

Figure 2.15: (a) Surface image of the interfacial area between steel rebar and ECC and (b) assumed transfer of stresses after initial cracking of the cementitious matrix with schematic representation of cracks and micro-fibres, according to FISCHER and LI [44]

Readings of strain gauges applied to the steel reinforcement suggest that local strain of the steel reinforcement remains largely unaffected by the formation of cracks in the cementitious matrix of SHCC. One possible implication of this is that large deformation capability and small crack openings of the cement-based composite generally prevent local damage and reduce interfacial bond stresses between reinforcement and cementitious matrix. Thus, a uniform stress distribution between SHCC and steel rebar can be assumed even after initial cracking of the cementitious matrix as depicted in Figure 2.15. However, with the utilized small specimen length and lack of sufficient load anchorage, caution must be applied, given that the stresses in the steel might not have been fully activated.

OTSUKA et al. [122] and MIHASHI et al. [109] observed the internal micro-cracking around a deformed steel bar in HPFRCC with the application of X-ray technology. The radiographs indicate the steel rebar, fibres embedded into the matrix as well as cracks. A comparison of the images in Figure 2.16 reveals that internal cracks initiate from the tip of steel ribs and propagate into the cementitious matrix forming transverse secondary cracks. Their number increases gradually with the loading up to the beginning of steel yielding, at approximately 70 % of the peak load. The evidence from this study suggests that the effect of fibre bridging can facilitate internal cracking prior to steel yielding. It was observed that a strong number of secondary cracks developed in a localised area after the yield strength of the steel bar was exceeded. The reasons for this can be found in the large plastic deformations of the steel bar during the yielding process.

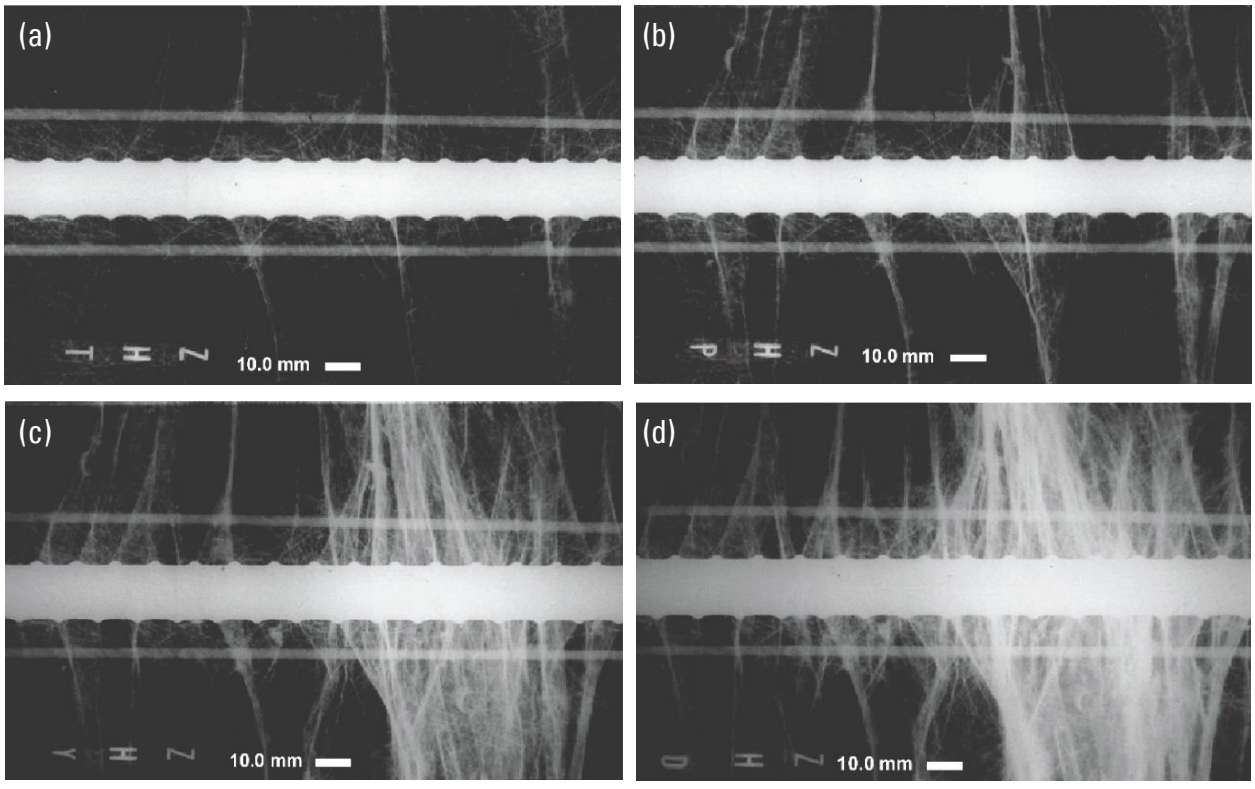

Figure 2.16: Radiographs of internal cracks along a steel rebar in HPFRCC at different strain levels according to OTSUKA et al. [122] and MIHASHI et al. [109]

LÁRUSSON and FISCHER [73] analysed the interfacial bond behaviour of steel reinforcement and ECC on specimens with the rebar positioned directly at the specimen surface. The surface was monitored with digital close-range photogrammetry, which enables the detection of crack and slip development. A visualisation of local strains on the surface of the specimen as depicted in Figure 2.17 shows an even distribution of secondary cracks during the stage of elastic steel deformations. Similar to the findings of OTSUKA et al. [122], internal secondary cracks were found to propagate to the outer surface of the specimen rather than merging into one primary crack (crack branching) as it was observed for R/C. As a result, a higher number of secondary cracks and a reduced crack brachning could be observed. The high number of secondary cracks resulted in reduced crack widths and less slip development of the matrix rebar interface, which indicates lower localised stresses and less deterioration of the interfacial bond between the rebar and the matrix. A reduction of slip development near the cracks could be observed at a strain level of 0.3 to 0.4 % suggesting the activation of mechanical interlocking after a critical crack width is exceeded.

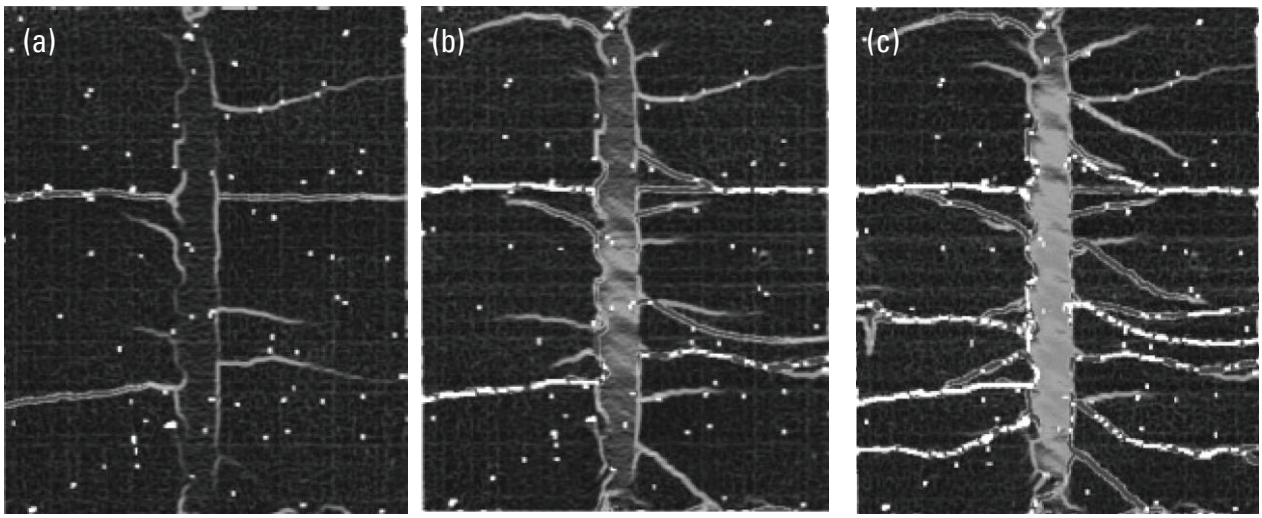

Figure 2.17: Crack formation of the rebar interface in reinforced ECC specimen at different strain levels obtained from of image correlation analysis, according to LÁRUSSON and FISCHER [73]

2.4.2 Tensile load-bearing behaviour of reinforced SHCC

The tensile load-bearing behaviour of reinforced concrete has been in the focus of research ever since steel rebar has been used as reinforcement. An overview of experimental studies on the behaviour of reinforced concrete is given by NOGHABAI [121] who also investigated the influence of strain-softening on the tensile properties of reinforced FRC tension members. Further research on the uniaxial tensile behaviour of reinforced FRC was conducted, for example, by PFYL [124]. JUNGWIRTH [61] and LEUTBECHER [79] extended the investigation to the effect of high tensile strength and micro-cracking on the tensile and cracking behaviour of steel-reinforced HPFRC. Even though only limited information on the tensile behaviour of steel R/SHCC is available, an overview will be given in this section.

In general, the load-deformation response of a steel-reinforced cementitious composite element subjected to tensile loading depends on the distinctive material characteristics of the cementitious matrix, the steel, the bond properties as well as the element geometry. Both materials, i.e. SHCC and steel, exhibit an initial elastic stage, which is characterised by their modulus of elasticity followed by a plastic yielding phase after reaching the stress at first cracking of SHCC or the yielding strength of ductile steel, respectively. However, tensile stresses and the associated deformations during the elastic and plastic phases differ for both materials. Due to the bond interaction, these deformations are mutually restrained, which generally results in a significant change in stiffness and strength of the composite element compared to that of the individual material properties as shown by the ε_s- depicted in Figure 2.18.

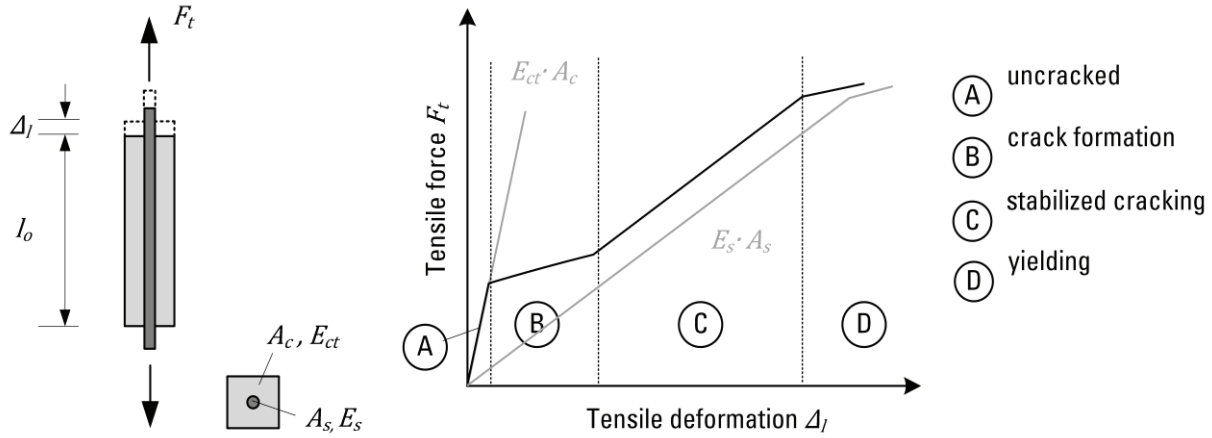

Figure 2.18: Schematic representation of the load-bearing response of a R/C tension tie subjected to uniaxial tension

The difference between the load-deformation response of the composite element (black line) and that of bare reinforcement (grey line $E_s \cdot A_s$) can serve as evidence of the contribution of concrete to the global load-bearing behaviour. The contribution of plain concrete and concurrent change of stiffness up to the tensile yielding strength of steel is often referred to as tension-stiffening of concrete. Provided that steel ductility can be activated, the following progress is characterised by plastic yielding and local strain-hardening of the steel in the vicinity of the cracks along the element. The ultimate strength of the tension member is typically reached when the loading exceeds the tensile strength of the steel reinforcement. Thus, the ultimate strain capacity of a reinforced element depends on the material properties, i.e. elastic and plastic strain capacity of the steel reinforcement and the interaction with SHCC during the loading process. Since the strain capacities of both materials substantially differ, a realistic calculation of the element load-carrying capacity and deformation requires deep understanding of the interaction between SHCC and steel reinforcement. The underlying mechanical processes during the yielding and localisation stage are best studied on tension members with one or multiple steel bars under uniaxial tensile loading.

Studies by KUNIEDA et al.

Following this approach KUNIEDA et al. [69] investigated the deformation and cracking behaviour of large size reinforced tensile elements made of Ultra High-Performance Strain-hardening Cementitious Composite (UHP-SHCC). The composition of this type of SHCC (cf. Table 2.1) is characterised by high contents of cement and silica fume, which result in a relatively high compressive strength f_c of 95 MPa, cf. Table 2.3. With an experimental setup aiming at the investigation of tension members with similar sizes found in structural applications, the specimens of a cross-section of 200 mm x 50 mm and a total length of 900 mm and a were loaded in tension.

The test programme included unreinforced and reinforced specimens with different amounts of steel rebar (bar diameter d_s of 6 mm) resulting in reinforcement ratios ρ from 0.28 to 1.14 %. A schematic representation of the tested specimens including the anchorage for the tensile load is shown in Figure 2.19a. Under considerations of an anchorage length of 200 mm, the free deformation length resulted in approximately 500 mm.

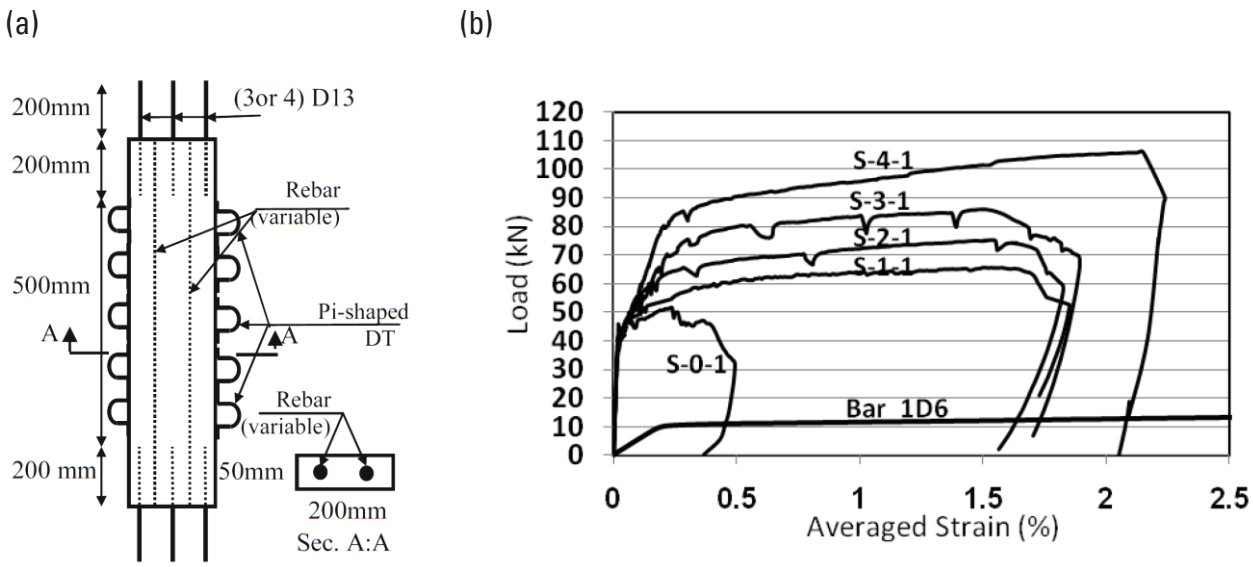

Figure 2.19: (a) Geometry of large-scale specimen and (b) load-deformation behaviour of reinforced and unreinforced (S-0-1) large-scale specimens compared to the bare steel response, according to KUNIEDA et al. [69]

Figure 2.19b illustrates the obtained load-deformation response of reinforced and unreinforced specimens in comparison to that of a bare steel rebar. It becomes apparent that the tension-stiffening is substantially increased in case of SHCC, which was found to contribute to the load-carrying capacity after the stress at first cracking σ_1 was exceeded even though the minimum reinforcement ratio was not provided.

The results show that the load-bearing behaviour of the reinforced specimens can generally be divided into three stages: (1) uncracked stage dominated by the stiffness of SHCC with nearly insignificant contribution of steel; (2) cracking stage dominated by the stiffness of steel with a continuous contribution of SHCC and (3) yielding stage dominated by the hardening modulus of steel with an increasing contribution of SHCC. Failure of the reinforced specimens was found to occur long before the actual strain capacity of the reinforcement could be reached at tensile strains ε_{ct} between 1.5 to 1.8 %. The modest strain capacity observed for the unreinforced elements (S-0-1) can possibly be attributed to the effect of specimen size (cf. Section 2.1.4.2) and was at least to some extent compensated by the reinforcement. The large contribution of SHCC during the cracking and yielding stage is the result of the crack-bridging capabilities and enhanced internal cracking of the fibre-reinforced cementitious matrix, which was previously discussed for long bond lengths. Moreover, a comparison of the crack development indicated that their number tends to increase with increasing reinforcement ratios.

Studies by LÁRUSSON and FISCHER

LÁRUSSON [72] investigated R/SHCC tensile elements produced with different types of reinforcement materials, i.e. glass fibre-reinforced polymer (GFRP) rebar and conventional steel reinforcement. With a total length of 1000 mm the tensile elements were of comparable size to the elements used in previous studies by KUNIEDA et al. [69] and had a quadratic cross-section of 100 mm x 100 mm. One steel rebar with a diameter d_s of 6.3 mm was used as reinforcement resulting in a reinforcement ratio ρ_s of 1.14 %. The specimen ends were widened resulting in a dumbbell shape of the specimen and connected to an external clamping system. The specimen setup as well as the load-deformation response of the steel-reinforced tensile member in comparison with the response of the bare steel reinforcement are shown in Figure 2.20.

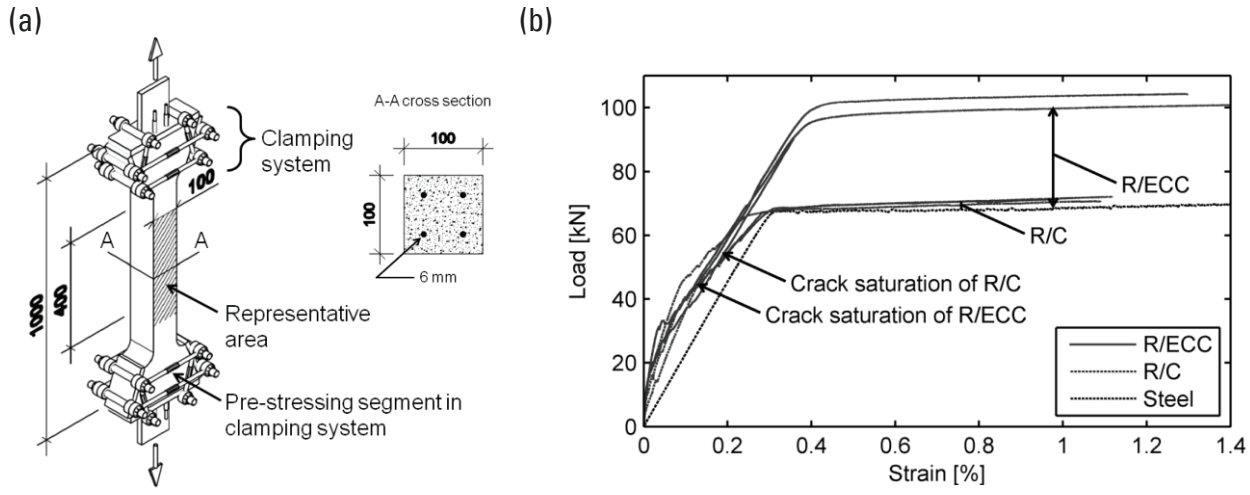

Figure 2.20: (a) Geometry of large-scale specimen and (b) load-deformation behaviour of reinforced and unreinforced large-scale specimens in comparison with that of bare steel bars, according to LÁRUSSON and FISCHER [73, 74]

The element deforms elastically during the initial stage up to the onset of initial cracks. When exceeding the stress at first cracking σ_1 a non-linear behaviour could be observed resulting in a reduction of the composite stiffness. This stage is followed by uniform yielding of the composite elements until the test was stopped. The observed results match the results obtained by KUNIEDA et al. [69], who used similar reinforcement ratios.

The observed differences regarding the stress at first cracking σ_1 and steel yield load can be attributed to the different material properties of SHCC used in two studies as well as to the different yielding strength of the steel rebars in use, cf. Table 2.7. The tensile loading was stopped at tensile strains ε_{ct} of 1.5 to 2.5 % prior to actual rupture of the specimen. Therefore, it can be expected that the actual strain capacity of the reinforced element was not yet reached. The comparison to R/C still highlights the contribution of SHCC to the load-carrying capacity even after yielding of the steel reinforcement.

The cracking on the surface of the R/SHCC specimen was observed using digital image correlation technique (DICT). It was found that new cracks form during the entire loading process after initial cracking. In comparison to plain SHCC, the analyses of the crack development indicated large differences in crack spacing and crack opening. Even though crack saturation was not reached at the ultimate testing load, maximum crack widths were found to increase from 150 µm for plain SHCC to 300 µm for R/SHCC at a tensile strain of 1.0%. In addition, crack spacings were found to increase from 7 to 8 mm (plain SHCC) to 13 to 14 mm (R/SHCC). According to the authors, these changes can partly be attributed to the effect of specimen size on the tensile behaviour of SHCC (cf. Section 2.1.4.2) and the influence of steel reinforcement on the stress distribution in the SHCC matrix. These findings highlight the influence of steel reinforcement on the tensile behaviour of SHCC, especially regarding the crack development in the fibre reinforced cementitious matrix.

Studies by MORENO and BILLINGTON

MORENO et al. [110, 111] applied an experimental setup of R/SHCC tension ties, capable of measuring the strain development along the reinforcement and observed an early strain-hardening effect of the steel rebar. A uniform distribution of tensile stresses in the composite element was ensured by the connection of steel reinforcement to welded steel couplers on both specimen ends. The coupler served as a connection element between the reinforcing bar and a stronger steel rod connected to the test frame. Additional lateral reinforcement was applied to provide sufficient anchorage to the steel coupler in SHCC.

With this setup, a relatively short anchorage length was achieved, which provides long bond lengths. Strain gauges attached to the reinforcing bar enabled the analyses of the local steel strain development and distribution. The investigation included specimens with a cross-section of 127 mm x 127 mm and total length of 1041 mm. A steel bar with a diameter d_s of 16 mm was used resulting in a reinforcement ratio ρ_s of 1.28 %. Additionally, bare steel bars of similar specimen length including the steel coupler and welded steel rod were tested in the same loading frame. This provided a realistic comparison of bare steel strains to that in the R/SHCC elements.

The R/SHCC specimens exhibited multiple cracking after the stress at first cracking was reached. The resulting load-deformation response is shown in Figure 2.21a. Up to the yielding strain of the steel reinforcement, the deformation behaviour of the composite element is similar to that reported by KUNIEDA et al. [69] and LÁRUSSON [72]. In this stage crack widths on the surface of SHCC specimens were found to be limited to approximately 100 µm. However, the stress-strain response after reaching the yielding load of the steel reinforcement at a tensile strain ε_{ct} of 0.25 % differed from the results published before.

Rather than showing continuous opening of multiple cracks, strains localised in a single macro-crack approximately when the yielding load of the steel was reached. Tensile strains were found to remain concentred in the vicinity of the crack with continuous loading until the specimen failed by fracture of the reinforcing bar at a global tensile strain ε_{ct} of 3.5%. These findings suggest that local steel strains in the crack reached the strain capacity of the reinforcing bar (approximately 12 %, see Figure 2.21b), which contradicts the previous finding implying that compatible deformations occur even during plastic yielding. This discrepancy could be attributed to the difference in bond lengths, which were substantially longer in this investigation.

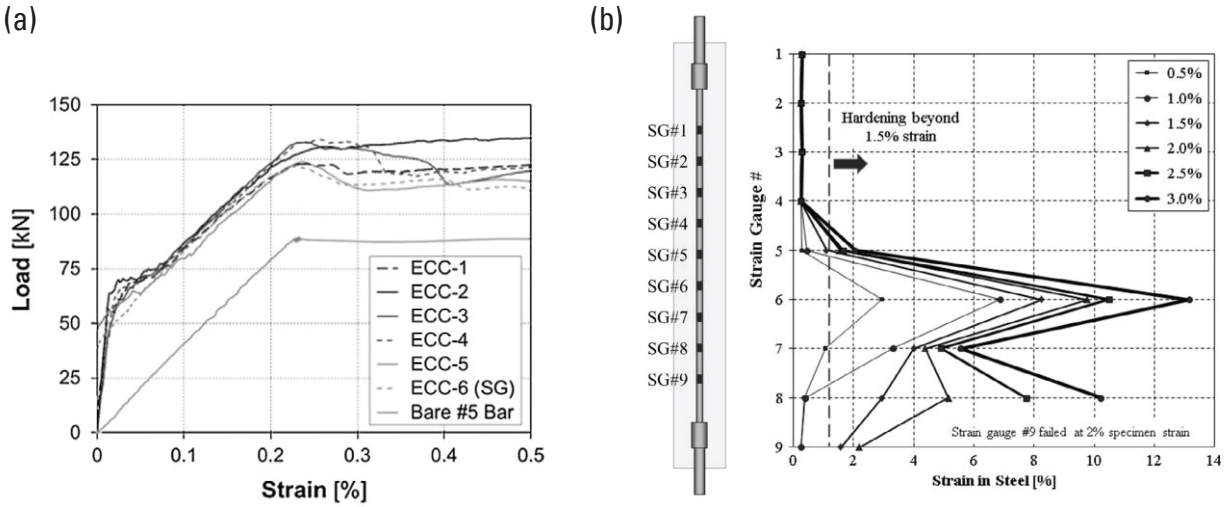

Figure 2.21: (a) Load-deformation behaviour of reinforced prismatic specimens in comparison with steel bars and (b) geometry of large-scale specimen with positions of the strain gauges and results of strain measurements, according to MORENO et al. [111]

Since relatively low global strain levels of the specimens were reached at the point of failure (i.e. when F_{max} was reached), steel yielding seemed to occur independently of the strain capacity of the SHCC. The measurement of local steel strains through instrumented strain gauges confirmed the local yielding of reinforcing bar in the vicinity of the macro-crack, as depicted in Figure 2.21b. Further research was indicated in [110, 111] to study the influence of the local crack development on the deformation behaviour, especially regarding the early strain-hardening.

2.5 Summary

In this chapter an overview of the relevant literature regarding the material behaviour of SHCC and steel reinforcement, as well as the interaction of both materials at the structural level was presented and discussed.

SHCC is a material with strain-hardening behaviour in tension characterised by the gradual formation of multiple fine cracks. Such mechanical behaviour is the result of the specific mix composition combined with the effect of fibres, which control the development of cracks. The compressive and tensile behaviour, as well as important parameters affecting them were described. It was shown that the material properties are above all influenced by the properties of the constituents and the mix composition as well as the by age and curing conditions.

Due to the complex interaction of fibres and cementitious matrix, the tensile properties of SHCC are influenced by various specimen parameters, such as the cross-section, shape, length, as well as production process and curing conditions. Under considerations of these parameters, the tensile behaviour of typical SHCC mixes was presented and it could be shown that for increasing specimen sizes the ultimate tensile strain and tensile strength of SHCC tend to decrease.

Due to limited information on the large-scale behaviour of SHCC, a deeper investigation on the tensile performance of SHCC in structural applications and related parameters is required. Therefore, part of the experimental investigations will focus on the effect of specimen size and the production process on the micro-structure of the composite and the resulting tensile behaviour. In addition, the shrinkage behaviour will be analysed as part of the experimental investigations.

Since reinforcement is required to ensure a robust behaviour of the structural element, the stress-strain behaviour of steel reinforcement was described. Specific focus was placed upon the effect of the localisation processes during the yielding and hardening stage. The mechanical interaction between steel reinforcement and cementitious matrix causes a change of the load-deformation behaviour. Moreover, the load-deformation response of R/SHCC element in tension depends on the mechanical behaviour of SHCC and steel rebars as well as their bond behaviour. In order to separate the individual contributions of the two composite materials in a R/SHCC element, an experimental investigation of the mechanical behaviour of SHCC and steel will be the subject of **Chapter 3**.

A comparison of steel rebar bond behaviour by means of stress-slip diagrams was given for SHCC and concrete. The results showed a similar slip behaviour of steel rebar in SHCC compared to that of conventional concrete. It could be concluded that the ductility of the material does not necessarily enhance the performance in terms of pull-out resistance. Especially the bond strength is found to be lower, which is a result of the lack of coarse aggregates.

Only few details can be found in literature regarding the effect of fibre reinforcement in cement-based composites at the structural level. In most cases, the research was limited to the analyses of short tensile members reinforced with one or multiple steel bars. The study of such elements offers a good basis for the analysis of the interaction with steel reinforcement in structural applications. The effect of the fibre bridging and multiple cracking on the tension-stiffening of R/SHCC has been in the focus of several research projects. It is widely accepted that SHCC and steel can undergo compatible deformations and that the tension-stiffening of the composite material can be significantly improved by using SHCC. Tension tests on R/SHCC showed multiple cracking with considerably smaller crack widths than those observed for steel-reinforced members made of OC. In this case, higher strain capacity of SHCC elements can be achieved by adding steel reinforcement. However, latest research indicates that the multiple cracking behaviour of SHCC and ductile steel behaviour can lead to an early strain-hardening of the reinforcement causing a moderate structural ductility.

Therefore, it is necessary to analyse the effect of the characteristic cracking behaviour of SHCC on the load-deformation response of SHCC elements with steel reinforcement, while a special focus should be directed upon the steel yielding. A presentation of the experimental investigations on R/SHCC tensile members will be given in **Chapter 4**.

While it has been generally assumed that the fine multiple cracking has a positive influence on the durability, recent research has shown that special attention should be paid to the carbonisation and chloride ingress. Durability models, which were proposed to account for the effect of carbonation-induced corrosion, rely on the crack width as an important factor. Therefore, the crack development of R/SHCC elements will be analysed to gain further knowledge about the crack development in R/SHCC elements.

Information about the constitutive modelling of R/SHCC remains limited at this point and was not part of this chapter. An approach for the constitutive modelling of the tensile behaviour of SHCC and steel reinforcement, as well as of the R/SHCC members will be subject of **Chapter 5**.

3 Experimental investigation at the material level

3.1 Introduction

In this chapter, the experimental investigation on SHCC and steel rebar at the material level of observation is presented and discussed. The experimental series included compressive and uniaxial tension tests on SHCC, as well as tension tests on bare steel rebar. As shown in the previous chapter, multiple parameters influence the material properties of SHCC especially regarding structural scale conditions. Since large quantities of SHCC were required for the casting of reinforced tension members, a mix was developed suitable for the production in a concrete plant.

The mechanical properties determined by the experimental testing were compared to reference specimens produced under laboratory conditions to investigate the effect of the production process on the mechanical parameters and achieve better comparability to the experimental investigation on reinforced tension members presented in Chapter 4. Special attention is given to the stress-strain relationship, the structure of the cement-based composite as well as shrinkage behaviour. An overview of the experimental framework and the parameters of interest are outlined in Table 3.1.

Table 3.1: Outline of the experimental investigations at the material level of observation

Experimental test	Type		Parameter
Compression test	SHCC cube		Compressive strength Density Porosity
Uniaxial tension test	SHCC dumbbell		Modulus of elasticity Matrix tensile strength SHCC tensile strength Crack development Ultimate strain Failure localisation
Tension test	Steel rebar		Modulus of elasticity Yield strength Tensile strength Yield strain Strain capacity
Shrinkage test	SHCC prism		Shrinkage behaviour

3.2 Uniaxial tension tests on SHCC

3.2.1 Material composition

The basis for the mixture design was a SHCC composition developed by MECHTCHERINE and BRÜDERN [18, 102] with the goal of robust strain-hardening behaviour, optimised workability and sufficient durability. The composite mixture was adapted to the requirements of the production process in the concrete plant, which included the selection of suitable constituents for concrete plant production as well as the development of a mixing procedure. The mixture design aimed at adequate workability, sufficient compressive strength for the bond interaction with steel reinforcement and strain-hardening behaviour in tension. To ensure sufficient durability – especially regarding sufficient freeze-thaw resistance of the cement-based composite – the equivalent water-to-binder ratio of the reference mixture was limited to $(w/c)_{eq} < 0.6$ as required by DIN EN 206-1[15] [38].

Table 3.2: Mass proportions of SHCC constituents in kg/m³

Mixture	Cement	Fly ash	Sand	Water	SP[1]	VA[2]	PVA fibres	w/c	$(w/c)_{eq}$[3]
M69	484	595	514	372	9.8	3.1	25	0.77	0.66

[1] Super plasticizer, [2] viscosity agent, [3] the equivalent water-to-binder ratio was calculated under consideration of a k-factor of 0.4 and an accountable amount of fly ash with 0.33 by weight of cement

Table 3.2 shows the compositions of mixture M69 developed for the experimental investigations of the work at hand. Trial mixes revealed that the production of large quantities of SHCC in the concrete plant required an increased water content and an increased amount of super plasticizer to achieve adequate workability [115]. The increased demand of water and super plasticizer may be linked to a lower energy input from the compulsory mixer of the concrete plant as well as longer processing times.

[15] To ensure the performance of the binder combinations with regard to strength and durability, EN 206 [38][38 introduced the k-factor approach. In this approach, the compressive strength and durability performance can be estimated by an equivalent water-to-binder ratio. However, the k-factor can substantially differentiate for high volume fractions of fly ash depending on the type of cement and curing conditions, which is why an experimental verification of the k-factor would be recommended for cases such as SHCC [50].

The binder comprised two components: CEM II cement with a limestone powder content of 6 to 20 % and a strength grade 42.5 N[16] as well as hard coal fly ash[17]. With these adjustments, the requirement of $(w/c)_{eq} < 0.6$ could not be satisfied. However, sufficient compressive strength and a favourable micro-structure could be verified by compressive testing and porosimetry, cf. Section 3.3. Further discussions on the durability of SHCC can be found; for example, in the work of ALTMANN [6].

Short dispersed PVA fibres were chosen as fibre reinforcement of the mix composition and added at a content ρ_f of 2 % volume fraction. The fibres were supplied by Kuraray Co. (Japan) and had a length l_f of 12 mm and a diameter d_f of 40 µm. Their mechanical properties were characterised by a modulus of elasticity E_f of 40 000 MPa and a tensile fibre strength f_{tu} of 1600 MPa.

A uniform distribution of fibres was ensured by the reduction of the maximum aggregate size, which was achieved by the selection of a uniformly graded quartz sand with a particle size of 0.06 mm < $d_a \leq$ 0.2 mm.

For a proper workability two types of admixtures were added to the mixture: super plasticizer on polycarboxylate ether base (PCE) optimised for applications in the transport industry to ensure workability and sufficient processing time as well as viscosity agent, which stabilised the fresh cementitious mix and prevented segregation and micro-scale bleeding, which might negatively affect mechanical performance. Table 3.3 lists the individual components used to produce small- and large-scale specimens.

Table 3.3: Constituents for SHCC specimen production

Component	Product
Fibres	Kuraray REC15 12 mm /RECS15[1] 12 mm
Cement	CEM II A-LL 42.5 N-HS
Quarz sand	HR 0.06 – 0.2 T / BCS 413[1]
Fly ash	steament® H4
Super plasticiser (SP)	Glenium SKY 593
Viscosity agent (VA)	Sika® UW-Compound

[1] The constituents had to be exchanged with products of equal quality since the original products were not available. The products used for large-scale experiments are given after.

[16] Cement type according to DIN EN 197-1[36]

[17] Fly ash type according to DIN EN 450-1 [40]

3.2.2 Production of specimens

This section details the mixing procedure for the developed material composition under laboratory and plant scale conditions. In particular, the mixing, casting and curing of small-scale specimens are presented. For further information on the casting process and curing conditions of the large-scale specimens the reader is referred to Section 4.3.

3.2.2.1 Reference mixes

Previous investigations suggested that for a given mixture composition the material properties are not only prone to changes of constituents, but also to changes of the mixing procedure [60]. Therefore, the mixing procedure aimed at establishing similar mixing conditions between laboratory and concrete plant production.

Laboratory batches were mixed in a Hobart HSM 30 mixer (50 Hz, 1.1 kW) with a maximum capacity of 30 l, cf. Figure 3.1a. It was found that high mixing speeds of the Hobart mixer can increase the air content up to 10 % [115]. For this reason, the mixing speed was maintained relatively low (68 rotations/minute) to achieve equivalent processing conditions as found in the concrete plant mixer. The mix sequence and the corresponding duration for the laboratory mixes were specified as follows:

- mixing of dry components, i.e. cement, fly ash, sand and VA over a period of 60 seconds until a satisfactory homogenisation of the dry mix was achieved;
- addition of mixing water including SP while continuously mixing for approximately 10 seconds;
- continuous mixing over a period of 300 seconds;
- gradual addition of short fibres while continuously mixing for approximately 60 seconds;
- continuous mixing of the complete mixture over a period of 300 seconds; and
- visual inspection of the fibre distribution and manual sampling the fresh mix.

The completion of the mixing was followed by the analysis of the fresh SHCC properties. Fresh SHCC testing included the determination of gross density, air-void content and slump flow. Due to the lack of large aggregates, the spread diameter could be determined by the Hagermann flow table[18], which was also helpful in dealing with small mixing quantities, cf. Figure 3.1b. The spread diameter, which is usually used to test the consistence of fresh mortar reached an average diameter of 225 mm[19]. The measurement showed an average gross density ρ and air-void content in the fresh state of 1.87 kg/dm³ and 2.7 %, respectively.

[18] Flow table test according to DIN EN 1015-3 [33]

[19] Previous studies showed that a spread diameter of approximately 200 mm would show adequate workability for the production of small specimen [12].

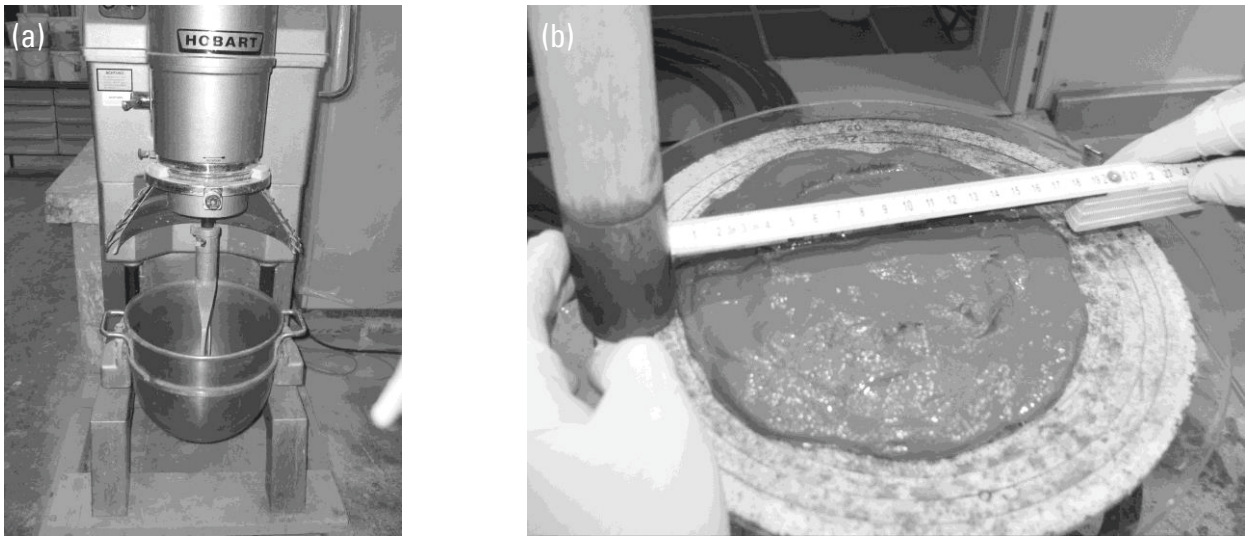

Figure 3.1: (a) Hobart mixer and (b) spread flow test on the fresh SHCC mixture using small cone

3.2.2.2 Concrete plant mixing

The manufacturing of reinforced tension members required the production of large quantities of SHCC for which a conventional concrete plant came to use. Due to technical restrictions of the concrete plant, fine-grained sand could only be added by a lifting system originally designated to the addition of steel fibres. Therefore, each batch contained a total SHCC volume of 0.85 m^3. To achieve consistent material properties throughout the duration of the investigation presented in the work at hand all major dry ingredients, i.e. cement, fly ash and sand were stored at the concrete plant facility. While sand was delivered and stored in large packs, the remaining ingredients were stored in silo containers, which were deliberately reserved for the purpose of this research project. The mixing steps and the production procedure in the concrete plant were carried out as follows:

- automated internal weighting of dry ingredients and mixing for 60 seconds;
- automated addition of water;
- continuous mixing for at least 300 seconds while manually adding SP and VA to the mix;
- manual addition of fibres after reaching sufficient homogenisation;
- further mixing for at least 300 seconds until the desired fibre distribution[20] was reached; and
- the mix was poured into a ready-mix truck and the process was repeated until all batches for one test series were completed.

[20] The subjective evaluation of the fresh state was based solely on visual inspection and experience of the staff members.

The fresh SHCC properties were tested for control purposes on samples poured directly from the ready-mix truck after the production of the first batch and again for the final mixture after the completion of all batches. The parameters of interest for the fresh mix were the slump flow, air-void content and visual control with respect to possible bleeding or segregation of the composite. Figure 3.2 shows the sampling of fresh SHCC from the final batch and the testing of slump flow.

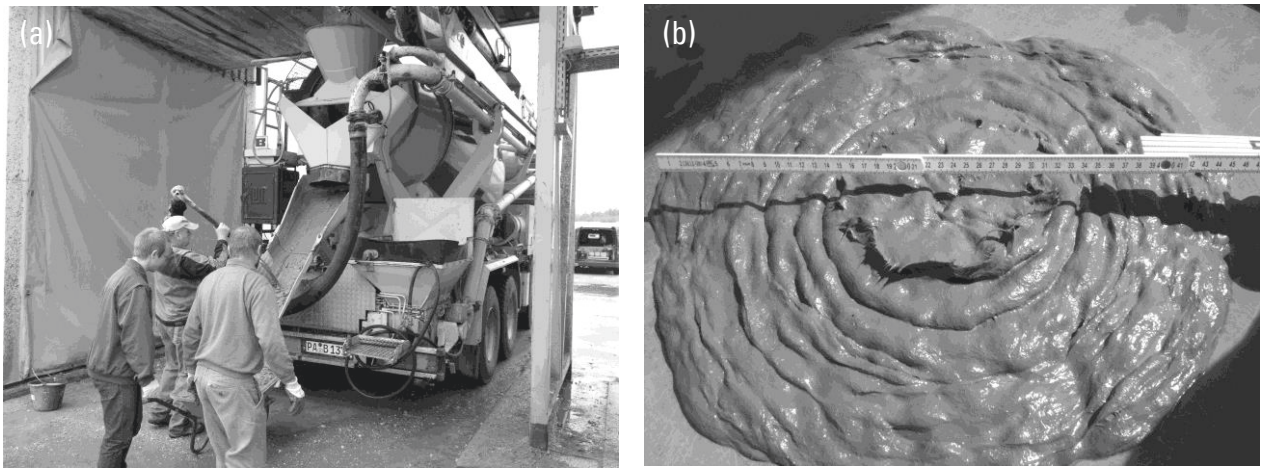

Figure 3.2: (a) Mixing of the large-scale batches and extraction of fresh SHCC sample for (b) testing of the slump flow

For large quantities of SHCC, the slump flow diameter can be determined by means of the Abrams cone[21] on a base plate with dimensions of 800 mm × 800 mm. The desired slump flow diameter was chosen to range between 450 and 600 mm. The air content was measured additionally utilising the pressure method[22]. The air content was only measured after all batches of one test series were completed.

Table 3.4 shows the results of the fresh concrete testing. The most likely cause for the observed difference between the slump flow diameter between the first batch and final casting can be found in the processing time required to produce all batches. The observed reduction of workability highlights the limitation of processing time and the requirement of extensive quality control during large-scale SHCC production. The fresh air content was found to be slightly lower compared to the reference mixtures produced in the laboratory. Especially the last series showed a further reduction, which was possibly affected by the final casting with a concrete pump.

[21] The slump flow diameter was determined according to DIN EN 12350-8 [35]. The Abrams cone had a height of 300 mm, a bottom diameter of 200 mm and a top diameter of 100 mm.

[22] The procedure was conducted in accordance to DIN EN 12350-7 [34]

Table 3.4: Fresh SHCC properties before casting of the test specimens

Series	SHCC temperature [°C]	Air temperature [°C]	Slump flow[1] [mm]	Fresh air content [%]
S03	17.0	16.0	520 / 470	2.7
S04	19.0	15.0	555 / 445	2.3
S05[2]	19.0	15.0	[-] / 430	1.9

[1] the first value was attained from the first batch, the second from the complete mixture before casting, [2] SHCC was cast with a ready-mix pump

3.2.2.3 Casting and curing of specimens

All specimens were cast immediately after production of the laboratory and concrete plant SHCC batches. For the latter, the fresh mixture was poured directly on site from the ready-mix truck and in one case by a concrete ready-mix pump[23]. The metal forms used to produce the cube, dumbbell and prism shaped specimens were treated with an oil surface agent to prevent adhesion and damage during demoulding. All specimens were produced in horizontal casting direction. It should be underlined here that no consolidation was applied since a vibration table were unavailable on site. Thus, an identical procedure was applied for fresh SHCC of the laboratory batches. Figure 3.3 depicts the moulds used for the specimen production at the concrete plant after casting.

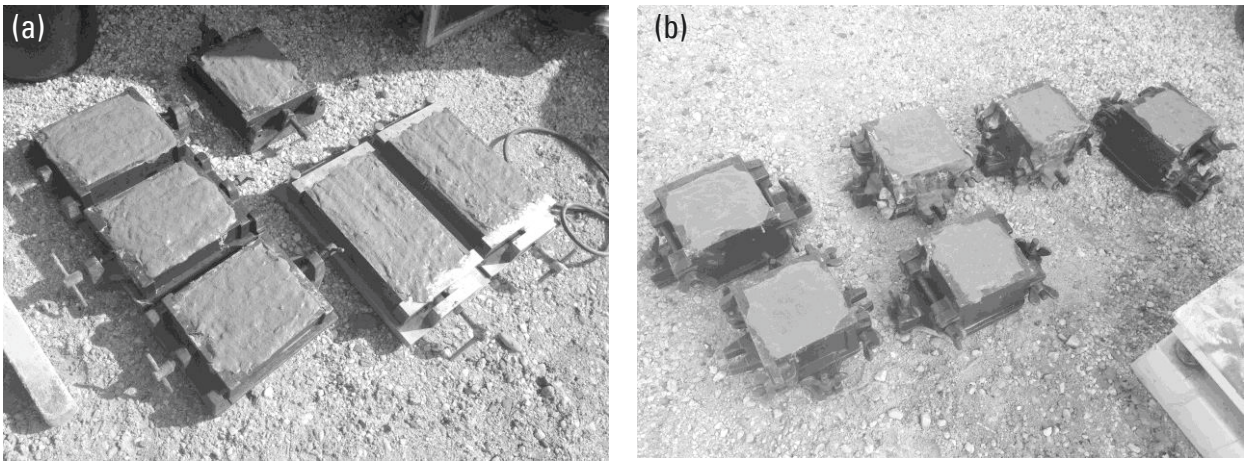

Figure 3.3: Moulds filled with SHCC after casting of the (a) dumbbell and prism specimen and (b) SHCC cubes

[23] The concrete ready-mix pump was chosen to test the pumpability of SHCC as well as the effect on the fresh and hardened material properties. In general, the SHCC mixture showed satisfactory workability for the concrete pump, while the effect of pumping on the fresh properties can be considered negligible, cf. Table 3.4.

In general, similar curing conditions were applied to specimens prepared for material testing of the laboratory and concrete plant mixes. However, slight differences were inevitable since additional time for transportation of the samples from the site of production was required. All moulds were covered with PE foil immediately after fabrication. Since the use of fly ash can delay the strength development of the hydrating cement paste (cf. Section 2.1.4), all specimens were demoulded at an age of 2 days after which they were stored unsealed in a climate-controlled room at a temperature T of 20° C and RH of 65 %. Prior to testing excess material formed during the casting on the concreting site was removed by cutting off the specimen upper surface layer.

3.2.3 Experimental setup

Direct tension tests under quasi-static, short-term loading conditions were performed to analyse the tensile behaviour with special attention to the tensile stress-strain relationship, crack pattern development and failure behaviour. In addition, the crack opening behaviour on the surface was monitored based upon digital close-range photogrammetry, which will be further explained in Section 4.5.3.1.

Table 3.5: Material classification, testing parameters and number of specimens

Series	Place of production	Age [d]		
		14	28	90
M69_H4	Laboratory	4	4	4
M69_S03		4	3	4
M69_S04	Concrete plant		3	
M69_S05			3	
Total number of specimens		8	13	8

Altogether 29 tests were conducted on small dumbbell-shaped specimens and analysed in this study. Only specimens showing failure within the measurement area were chosen for evaluation of the tensile behaviour. Table 3.5 provides an overview of the test parameters used in this investigation. Since a strong influence of the specimen age at testing is expected due to the high amount of fly ash a representative set of specimens was tested at different ages.

Based upon the discussion in Section 2.1.4, unnotched dumbbell-shaped specimens with a constant cross-section in the measurement zone were chosen. The smooth transition between the extended zone of the test frame fixation and the narrow part of the measurement zone limited stress concentrations and allowed a uniform distribution of tensile stresses. The specimens had a length of 240 mm, a width of 24 mm (in the tapered region) and a thickness of 40 mm. A dumbbell-shaped specimen is displayed in Figure 3.4a.

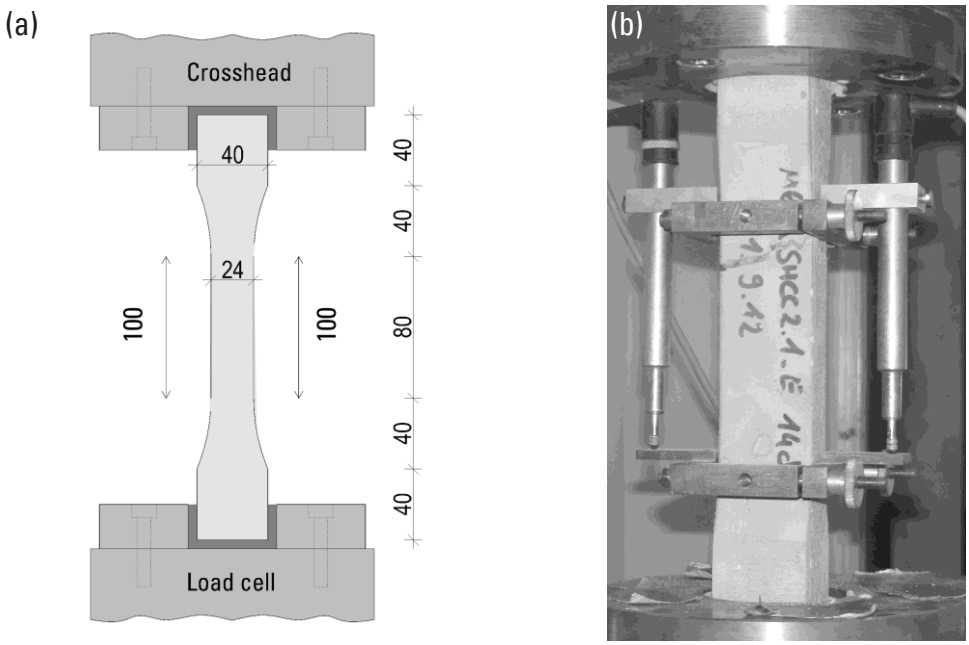

Figure 3.4: (a) Schematic view of an SHCC dumbbell specimen and its connection to the load frame and b) the complete test setup including the specimen after testing

The preparation of specimens included cutting of the concrete side to eliminate superfluous material and achieve an even surface. A testing machine type Zwick Z 1200Y was adapted to the chosen direct tension test setup. The specimen ends were glued to non-rotatable supports of the testing machine. The two-component glue on an epoxy base (X60 supplied by HBM) creates a rigid connection between the specimen ends and the steel connector attached to the crosshead and load cell of the testing machine.

The installation procedure included the gluing of one specimen end to the connector before attaching the latter to the upper crosshead of the machine. Next, the lower crosshead with incorporated load cell was moved into position and fixed to the second connector, which was subsequently glued to the remaining specimen end.

Longitudinal deformations were measured with two adjacent LVDTs covering a representative length of 100 mm as illustrated in Figure 3.4b. The frames holding the LVDTs were carefully clamped to the specimen sides to avoid the input of local stress concentrations. The tests were performed in a displacement-controlled regime with a constant displacement rate of 0.01 mm/s, while the test load was measured by the loading cell of the testing machine. Figure 3.4b shows a specimen in the machine after testing. After failure, specimens were disassembled and the final crack position as well as characteristic features of the crack surface (pores, fibre bundles etc.) were documented.

3.2.4 Experimental results and discussion

3.2.4.1 Behaviour of SHCC under uniaxial tension

The stress-strain curves derived from uniaxial tension tests are displayed in Figure 3.5. Each diagram represents the results of a specific test series; H4 for the laboratory mix and S03 to S05 for the concrete plant mixes. The results can be compared to assess the overall influence of the production process on the tensile properties of SHCC. The specimens were tested at an age of 14, 28 and 90 days. Specimens which showed immediate rupture after first crack development mainly due to anchorage failure or improper casting (e.g. cold joints, large air pores) were discarded and are not included (e.g. specimen S04_6).

The general load-deformation behaviour can be divided into three sections: elastic stage; multiple cracking and failure localisation including opening of the final crack. While the first section shows an almost linear progression of the stress-strain curve, a non-proportional increase of the tensile strain can be observed starting at approximately 75 % of the stress at first cracking σ_1. This behaviour is most likely caused by formation of micro-cracks initiating from defects inherent to the cementitious matrix.

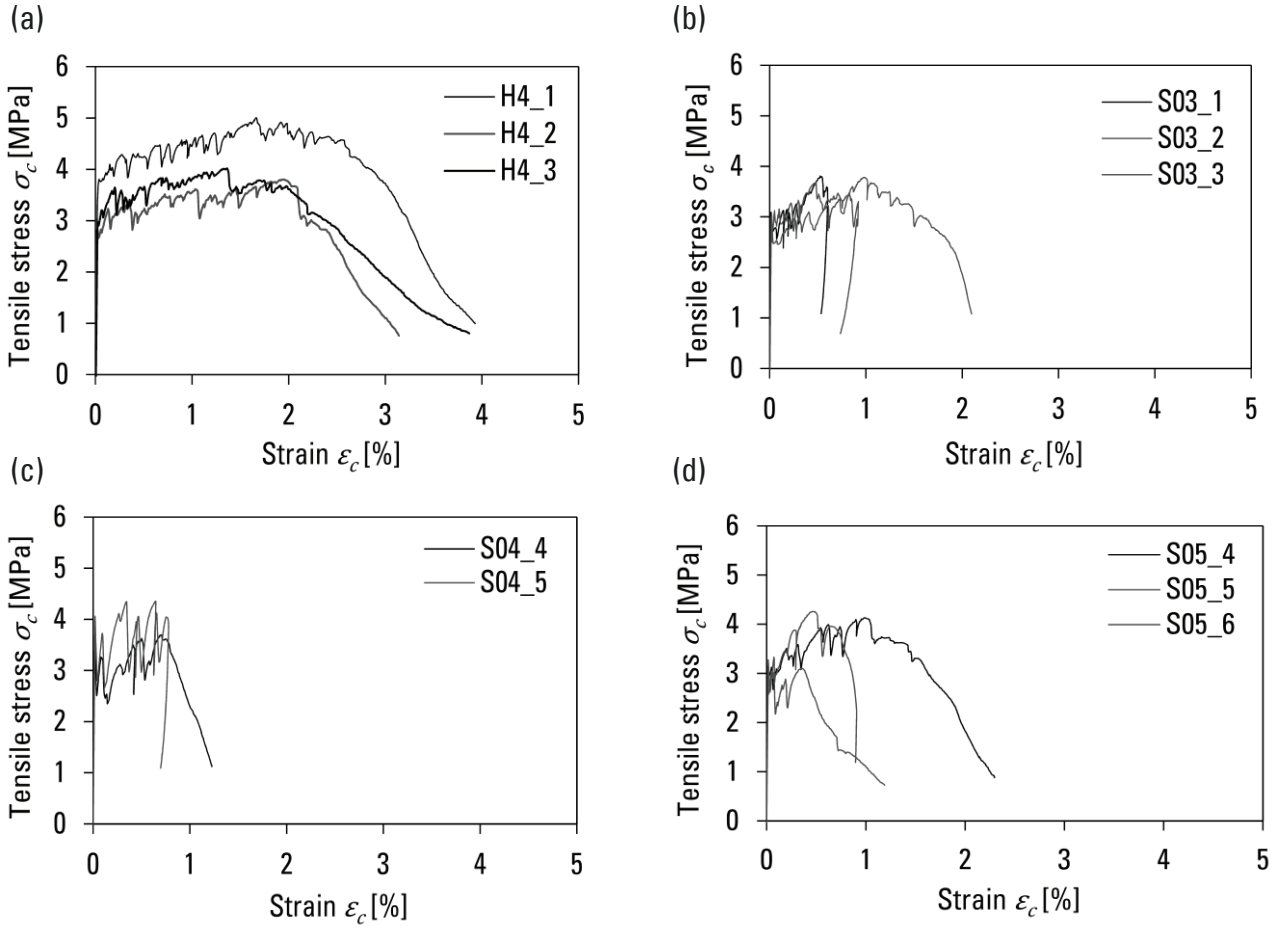

Figure 3.5: Tensile stress-stain response of SHCC specimens at a concrete age of 28 days: (a) reference laboratory mix, (b) to (d) concrete plant mixes

The micro-cracks merge into a complete crack when the stress at first cracking[24] σ_1 is reached, followed by a steep decrease of tensile stresses. Then the crack growth is found to stabilise, which can be attributed to the crack-bridging properties of fibres. Deformations increase with further loading, while new cracks are forming accompanied by sudden drops of the stress-strain curve. However, due to crack-bridging the maximum reachable stress gradually increases resulting in an overall tensile strain-hardening behaviour.

The resulting crack pattern is thereby characterized by transversal cracks with narrow crack widths. In some cases, a concentration of cracks could be observed near the specimen end, most likely resulting from stress concentrations in that region. The process of multiple cracking continuous until the tensile strength f_t is reached after which further deformations remain localised in the final crack. The tensile response during the last stage shows a descending trend, while a macro-crack opening can be observed as fibres are de-bonded completely and pulled out of the cementitious matrix.

3.2.4.2 General effects of specimen production process

Table 3.6 provides a statistical evaluation of the test results for specimens of each batch under investigation. Average values for the first cracking stress σ_1 at an age of 28 days range between 3.19 MPa for laboratory mixes and 2.88 to 3.73 MPa for the concrete plant mixes, respectively. Variations between the laboratory and concrete plant mixes can partly be related to differences of the aggregates' quality, since mechanical aggregates and geometrical properties of aggregates are known to affect the aggregate-cement paste bond properties and thus the mechanical properties of the composite [5].

Table 3.6: Results of the uniaxial tensile testing for each batch at different SHCC ages (standard deviations are given in parentheses)

Series	Laboratory			Concrete plant				
	H4			S03			S04	S05
Age	14	28	90	14	28	90	28	28
Stress at first cracking σ_1 [MPa]	3.31 (0.20)	3.19 (0.32)	4.14 (0.26)	2.67 (0.38)	2.88 (0.15)	3.14 (0.39)	3.73 (0.33)	3.00 (0.23)
Tensile strength f_t [MPa]	3.94 (0.50)	4.32 (0.46)	5.16 (0.07)	3.42 (0.23)	3.68 (0.16)	3.47 (0.16)	4.02 (0.33)	3.90 (0.41)
Strain capacity ε_{tu} [%]	1.63 (1.46)	1.89 (0.30)	1.41 (0.18)	0.63 (0.33)	0.86 (0.23)	0.85 (0.28)	0.71 (0.07)	0.55 (0.40)
Modulus of elasticity E_{ct} [MPa]	16 383 (326)	18 800 (370)	21 149 (360)	18 800 (623)	21 800 (492)	21 563 (1196)	21 628 (163)	20 800 (466)

[24] The stress at first cracking σ_1 was determined at the point where the initial progression of the stress-strain curve dropped below $E_{c,loc} \leq 0$

However, a large portion of these differences can also be related to the influence of the processing conditions on the composite micro-structure. Such influence becomes evident when comparing the first cracking stress σ_1 obtained from different concrete plant batches, i.e. S03 to S05. Even though material composition, mix constituents and the production facility were kept the same, a large variability of the first cracking stress σ_1 could be observed.

The average Young's modulus of specimens produced in the laboratory was found to be slightly lower compared to that of concrete plant mixing. In addition, tensile strength f_t increased by approximately 7 to 15 % in comparison to the specimens produced in the concrete plant. These variations between batches of laboratory and concrete plant production highlight the influence of the composite micro-structure and fibre distribution on the tensile deformation behaviour especially in regard to multiple cracking behaviour. While all specimens exhibited strain-hardening behaviour, a visual inspection showed a reduced crack development in specimen obtained from concrete plant production. As a result, the tensile strain capacity of these specimens decreased by approximately 55 to 86 %[25] in comparison to specimens produced in the laboratory.

Previous investigations showed that SHCC is relatively sensitive to variations of the micro-structure, especially regarding air-void content and fibre distribution [80]. The analyses of the pore structure of the hardened cement-based composite by linear transverse air-void detection (cf. Table 3.8) showed a generally lower pore content of the concrete plant batches. Furthermore, the lower spacing factor and higher specific surface of concrete plant mixes indicate that the average number and size of pores is smaller for laboratory mixes. Results of mercury intrusion porosimetry (cf. Figure 3.6) also indicated that fibre distribution within the cement-based composite was influenced by the production process. Such changes of the micro-structure and fibre distribution are most likely caused by changes of the rheological properties during casting and can significantly influence the tensile behaviour and the ability of multiple crack development as well as tensile strain capacity.

A similar effect can be observed in the time-dependent behaviour of SHCC produced in the laboratory. The comparison of the mechanical properties of SHCC at a specimen age of 28 and 90 d shows that the stress at first cracking σ_1 and tensile strength f_t increase by 30 and 19 %, respectively. The observed decrease in strain capacity of 25 % (related to 28 d) may stem from an increased fibre loading as a result of the increased tensile stresses. Part of these effects is a result of ongoing hydration processes, which change matrix properties as well as bond properties between fibres and SHCC. However, these changes were less pronounced for the specimens produced at the concrete plant.

[25] The tensile strain capacity was defined as the point where the decline of the stress-strain curve during the onset of the softening branch dropped below 95 % of the tensile strength.

3.3 Complementary investigations on SHCC

3.3.1 Compressive properties

Cube specimens with an edge length of 100 mm were cast to determine the compressive strength and gross density. The compressive tests were conducted in a hydraulic testing frame DB 300 with a loading speed of 5 kN/s. Table 3.7 summarises the measured values of the compressive strength and gross density (three specimens for each series). A comparison of the results reveals that the compressive strength of batches produced in the concrete plant increased by approximately 18 %, despite constant specimen geometry, mixture proportions and similar curing conditions. Therefore, possible causes can be found either in the effect of the mixing process on the micro-structure of the cementitious composite and/or the influence of the aggregate properties, which were provided by different manufacturers. However, it remains unclear why none of these parameters have affected the first cracking stress a similar way.

Table 3.7: Average values of SHCC compressive strength and density at an age of 28 days (standard deviations are given in parentheses)

Series	Laboratory	Concrete plant		
	H4	S03	S04	S05[1]
Compressive strength [MPa]	41.8 (1.8)	49.4 (1.8)	49.3 (0.8)	49.3 (0.1)
Density [kg/dm³]	1.94 (0.01)	1.95 (0.02)	1.92 (0.01)	1.94 (0.01)

[1] SHCC was cast with a ready-mix pump

3.3.2 Micro-structure of the cement-based composite

Since the results of compressive tests showed that SHCC is prone to small changes in the mixture composition and constituents as well as production processes further investigations regarding the micro-structure of the cementitious matrix were performed by means of porosimetry. The parameters under investigation included pore volume, pore size distribution, density and other porosity-related characteristics of SHCC. For large-scale specimens, the samples were extracted by drill cores. Laboratory samples were tested by cutting pieces of SHCC cubes, which were cast in the laboratory. Two methods were applied to investigate the pore structure: (1) the mercury intrusion porosimetry (MIP) and (2) the rapid air technology which are both based upon the assumption of regular pore geometries. This approach was previously confirmed to be a good approximation for cement-based materials [1].

3.3.2.1 Mercury intrusion porosimetry

The specimens were prepared according to DIN 66133 [28] and tested in a fully automated mercury porosimeter type Pascal 140 and Pascal 240 from POROTEC. With this setup, it was possible to detect pore size distribution between approximately 0.007 and 70 µm. Figure 3.6 depicts the test volume of intruded mercury, which shows two typical pore fractions of the pore structure.

The first fraction can be distinguished between approximately 0.03 and 0.1 µm and is typical for cement-based materials, which could be shown on mortar-like mixtures [47]. The second fraction in the range of approximately 0.3 to 1 µm was previously found to be characteristic for SHCC systems [130] because of fibres, which leave pore spaces in the cementitious matrix.

In this pore fraction the specimens obtained from lab production showed a much higher specific pore volume in comparison to the plant production specimens. These differences may result of a lower capability of the plant mixer to disperse fine PVA fibres, which also caused a less pronounced strain hardening of the SHCC specimen made in the plant. A better fibre dispersion often leads to an increase of porosity.

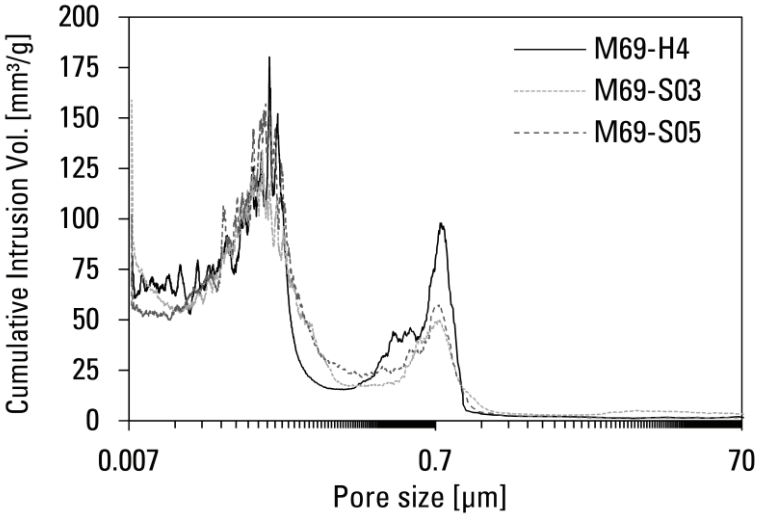

Figure 3.6: Results of the MIP measurements, comparison of the pore size distributions obtained for specimens produced in the laboratory and in the concrete plant

3.3.2.2 Linear transverse air-void detection (RapidAir)

An additional microscopic determination of the pore system according to DIN EN 480-11 [39] was conducted by a linear transverse method using the RapidAir 457 system. The system is based upon an image analysis with a laser scanning the polished surface of a specimen, which allows the determination of total pore content, spacing factor and specific surface.

Drill cores were taken of large-scale specimen and cut into different sections to expose the interior micro-structure. SHCC cubes casted during the laboratory production were cut and used as reference. The samples were sliced, grounded and lapped in preparation of the analyses. To discontinue hydration, the samples were placed into isopropanol solution and eventually dried under vacuum conditions.

Before analysis, the surface of the samples was coloured dark for higher contrast. The surface was brushed with barium sulphate powder paste filling pore spaces accessible to surface. The prepared samples are mounted on a moving stage positioned below a video camera where they traverse on a linear path, while the video system detects contrasts between the dark surface and white pores. The traverse length is reached at the edge of a sample where it is shifted in perpendicular direction to the next linear path. This process continues until the maximum number of paths is reached, which leads to a significant observable distance despite the small surface. The traverse length data is processed by an image analysis algorithm to calculate statistical pore parameters.

For each drill core and cube three cuts, near the top, bottom and middle were extracted from the specimen. The mean characteristic values of the microscopical pore system measured by the rapid air technology are displayed in Table 3.8. The parameter A reflects the content of visible pores in the cementitious matrix with a maximum diameter of 4000 µm. It is calculated by the total length of pores detected along the transverse length divided by total length traversed. The micro-pore content A_{300} represents the content of visible pores with a diameter smaller than 300 µm. The spacing factor is characteristic parameter for the greatest distance between any point in the cement paste and the next pore in the system.

Table 3.8: Average results of pore system analyses on hardened cement paste according to DIN EN 480-11 [39] (standard deviations are given in parentheses)

Series	**Laboratory**		**Concrete plant**			
	H4-1	H4-2	S03-1	S03-2	S05-1[1]	S05-2[1]
Testing age [d]	412	412	414	414	137	137
Pores of relevant size A [%]	5.95 (0.20)	6.13 (0.29)	10.50 (0.84)	10.19 (0.59)	6.23 (1.01)	6.41 (1.37)
Specific pore surface α [mm^{-1}]	45.98 (3.90)	46.89 (3.80)	64.24 (3.80)	57.60 (7.00)	58.65 (0.58)	57.71 (0.29)
Spacing factor	0.16 (0.01)	0.15 (0.01)	0.09 (0.01)	0.10 (0.02)	0.11 (0.13)	0.12 (0.01)
Micro-pore content A_{300} [%]	3.30 (0.46)	3.37 (0.41)	6.35 (0.58)	5.98 (0.42)	3.74 (0.81)	3.68 (0.88)

[1] SHCC was cast with a ready-mix pump

The low standard deviations observed for characteristic pore values suggests that a uniform distribution of the SHCC micro-structure could be achieved along the complete thickness of the specimens. In addition, specific pore surface α tend to increase while pore spacing tends to decrease indicating a higher amount of pores for large-scale SHCC production. These findings concur with observations made for the consistency of fresh SHCC, were field mixed showed a reduction of flowability with advancing processing time (cf. Table 3.4). A stiffer consistency limits the capability of SHCC to deaerate when casted without compaction, which could ultimately lead to an increased pore content. A comparison between both concrete plant mixes, i.e. S03 and S05, shows that the pore content varies substantially between the two similar batches, a fact which cannot be well explained.

3.3.3 Shrinkage behaviour

In general, concrete-like materials exhibit changes in volume at different stages, which are caused by various reasons. The load-independent deformations are usually categorised into four types: plastic shrinkage, drying shrinkage, autogenous shrinkage and carbonation shrinkage. Drying shrinkage is defined as the volume reduction caused by the desiccation of material when concrete is exposed to dryer environmental conditions compared to those in the initial pore system. By contrast, autogenous shrinkage occurs during the hardening of the cement paste without interaction to the environment. Drying shrinkage is influenced by various factors such as: (1) environmental conditions, i.e. temperature, humidity; (2) intrinsic material features to concrete, i.e. composition, aggregate size, content of fines, water-to-cement ratio and (3) geometrical properties, i.e. thickness and surface portion exposed to environment among others. Since SHCC is characterised by a high content of fine grain particles, such as cement and fly ash, shrinkage holds particular interest.

It is generally assumed that drying shrinkage of concretes containing larger sized aggregates is less than that of concrete with smaller maximum aggregate size, partly due to a higher restriction of shrinkage strains by larger aggregates [55]. It was also found that the high binder content of SHCC resulted in about 80% higher drying shrinkage strains in comparison to those of OC [147]. Thus, structural elements made of SHCC are expected to be more strongly affected by drying shrinkage deformations than those made of OC, which may influence both the resulting material properties and structural behaviour. In addition, large-scale specimens produced at the concrete plant remained in the formwork and were exposed to uncontrolled environmental conditions. Therefore, shrinkage cracks are more likely to occur in contrast to specimens cured under controlled climate conditions. In order to estimate the effect of shrinkage on the structural behaviour of R/SHCC elements in tension, additional shrinkage tests were conducted. The measurements of autogenous and total shrinkage were based upon a modified test setup according to DIN 52450 [27]. Modifications included the automatization of strain recording as well as extensions to measure strain on several specimens simultaneously.

Three specimens were cast in horizontal position and covered with foil until they were demoulded one day after casting. The deformation onset was started two days after casting for laboratory specimen and three days after casting for produced in the plant. The specimens used to measure the total shrinkage were placed into the measurement device without any further treatment. Autogenous shrinkage was measured on specimens, which were wrapped in aluminium foil immediately after demoulding to protect them from desiccation. Room temperature and relative humidity (RH) were controlled and kept constant at 20 °C and 65 %, respectively.

The results of the shrinkage measurements for the concrete plant and laboratory mixes are displayed in Figure 3.7[26]. The measured total shrinkage strain at an age of 40 days was approximately 1.7 and 1.5 ‰, respectively. This is in agreement with the findings of LÁRUSSON [72] who observed shrinkage strain of SHCC to range between 1.1 and 1.4‰ at an age of 38 days for specimens cured at 60 to 80 % RH. Autogenous shrinkage at an age of 40 days reached strains of approximately 0.4 and 0.6 ‰, respectively. In comparison to specimens produced in the laboratory, autogenous shrinkage strains increased by approximately 50% while total shrinkage strains increased by approximately 10%. The increase of autogenous shrinkage was, thereby, found to be of similar absolute value to that of total shrinkage. This suggests that autogenous shrinkage contributes substantially to changes in total shrinkage for the different production processes. The reasons behind this phenomenon are still to be clarified.

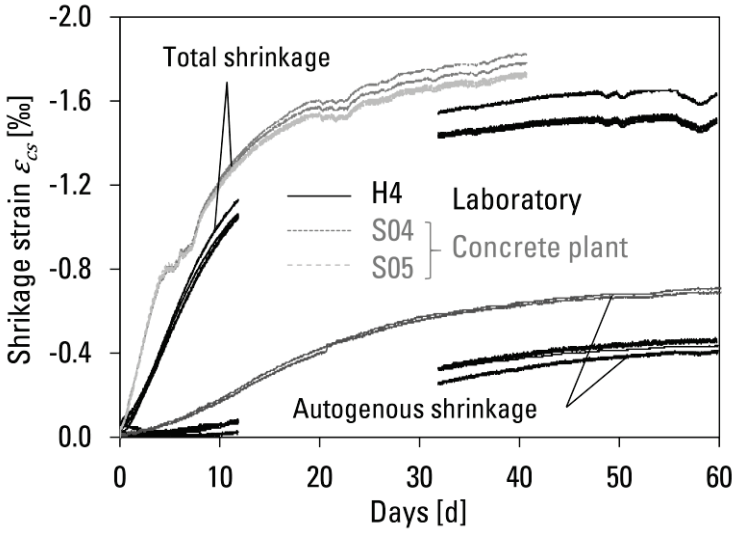

Figure 3.7: Results of total shrinkage and autogenous shrinkage measurements for laboratory and concrete plant mix productions (measurements for series H4 were discontinued between 12 and 35 days due to a fault of the recording terminal)

[26] Deformations occurring before demoulding and during the first two days were neglected in this case. Previous investigation showed that specimens exhibited expansion before and rapid shrinkage after demoulding mainly due to heat production and chemical shrinkage [60, 147].

3.4 Uniaxial tension tests on steel reinforcement

3.4.1 Experimental setup

The load-deformation behaviour of steel reinforcement was determined by means of uniaxial tension tests on deformed steel bars of Grade S500 having diameters of 10, 14 and 16 mm. The properties of interest were strength, modulus of elasticity and ductility. Hot rolled reinforcing bars, which show a high yielding capacity[27] were used for the experimental investigations of the thesis at hand. The precise geometrical parameters of the rebar are presented in Annex B. The following sections will provide an overview of the experimental setup and results as a basis for further discussions on the interaction of steel reinforcement embedded into SHCC.

Figure 3.8 shows the test configuration applied for the testing of steel bars. A hydraulic testing machine type EU 20 with a maximum load capacity of 200 kN was utilised under a load-controlled regime with an average loading rate of 0.05 kN/s. The rebar was clamped into the upper and lower crossheads of the test frame with clamping jaws, providing a firm anchorage and even distribution of pressure.

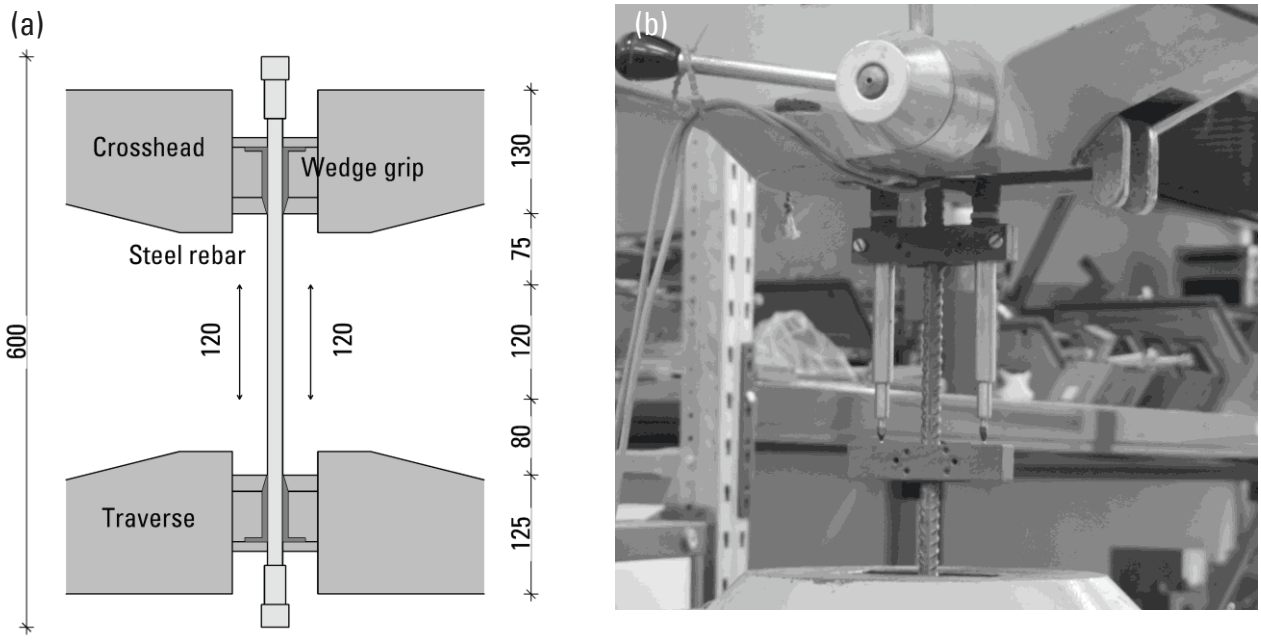

Figure 3.8: (a) Schematic representation of the test setup and (b) photograph of a rebar installed into the test frame

[27] Steel used for this investigation was classified into ductility class B according to DIN 488 [26].

The machine force was measured with an internal load cell and the strain was measured by an extensometer[28] containing the LVDTs. Two LVDTs with a gauge length L_e of 120 mm were applied to the bar with the extensometer. The deformations were calculated as the mean value from the two LVDTs. With this setup, it becomes possible to determine the steel behaviour even after local yielding of the rebar. Even though a steel with diameter d_s of 20 mm was used for the testing of reinforced elements, this type could not be tested with the described setup since the required tensile force for testing exceeded the load capacity of test frame. Figure 3.8b shows the specimen in the connectors to the test frame including the LVDTs after testing. After failure, the breaking elongation A_c was measured directly on the steel by pre-defined sections with a base length of $L_0 = 5 \cdot D_0$.

3.4.2 Experimental results

Table 3.9 gives an overview of the characteristic material parameters derived from the measured stress-strain curves. The yield strength was defined as the lowest stress measured during the yielding phase. The total extension A_{gt} represents the extension at the tensile strength based the LVDT measurement length L_e. A full overview of the steel test results can be found in Annex B.

Figure 3.9 displays the stress-strain diagram for all tested steel bars. For a better representation of differences only the strain above a tensile stress of σ_S > 500 MPa are given. The tensile deformation behaviour exhibits the typical phase of a hardened and tempered steel. The first stage shows a linear response with elastic deformations until the yielding strength R_e is reached. The second stage is characterised by a plastic yielding plateau with an almost constant stress level. During the third stage, the steel undergoes hardening accompanied by large contractions of the cross-section.

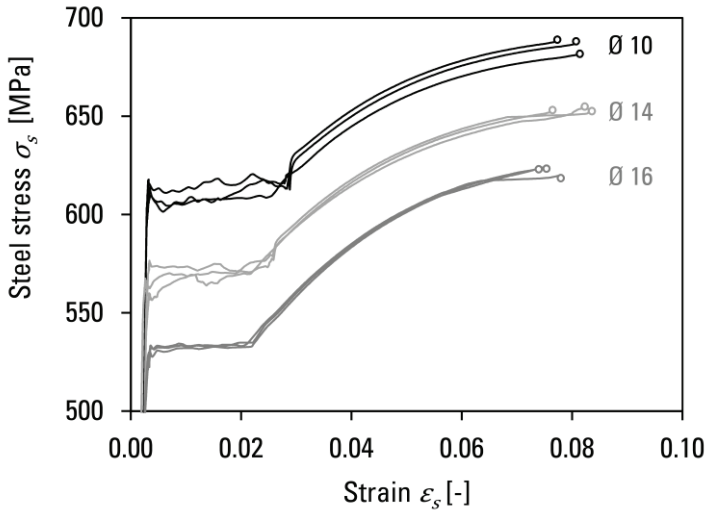

Figure 3.9: Stress-strain diagram of steel rebar with diameters d_s of 10,14 and 16 mm

[28] The extensometer measurement was conducted according to DIN EN ISO 6892-1.

Three steel bars for each diameter were tested to calculate the mean values of the tensile material parameters. The modulus of elasticity E_s remains slightly below the requirements of E_s from 200 to 210 GPa with an exception for bars with a diameter d_s of 10 mm. The yield strength exceeds R_e > 500 MPa for all specimens, while the ratio between ultimate strength and yield strength reaches (R_m/R_e) > 1.08. Thus, the tested steel offers large ductility beyond the requirement of ductility class B, cf. Section 2.2.1. With increasing diameter, the strength of steel is found to decrease while an increase in ductility can be observed. This behaviour suggests that both parameters of steel reinforcement properties underlie influences of size effects, which may be related to geometric variations of the ribbed steel bars.

Table 3.9: Tensile parameters of steel rebar (standard deviations are given in parentheses)

Steel bar diameter	**Modulus of elasticity**	**Yield strength**	**Tensile strength**	**Ductility**	**Total extension**	**Breaking strain**
Ø [mm]	E_s [GPa]	R_e [MPa]	R_m [MPa]	R_m/R_e [-]	A_{gt} [%]	A_c [%}
10	208.57 (8.73)	604.39 (4.81)	686.32 (3.57)	1.13	7.95 (0.22)	18.00 (2.00)
14	198.88 (8.94)	563.31 (7.25)	656.84 (3.85)	1.16	7.89 (0.36)	22.38 (2.18)
16	199.24 (6.72)	530.14 (2.64)	635.83 (2.30)	1.20	7.33 (0.55)	25.21 (2.95)
Mean	202.23	565.94	659.66	1.16	7.72	21.86

3.5 Summary

The material properties of SHCC and steel reinforcement were investigated to generate additional knowledge about their individual behaviour. The mechanical properties of one SHCC composition were investigated in detail, while specimens were produced both under laboratory and concrete plant conditions.

It was shown that SHCC is generally suitable for processing in a conventional concrete plant but imposes high demands on mix design, production technology and quality control. Processing times should be limited combined with continuous testing of fresh SHCC properties to ensure the desired mechanical properties, especially regarding tensile deformation behaviour.

The material behaviours under compression and tension were tested to analyse the effect of different production conditions on the mechanical properties of SHCC. An increase in compressive strength for SHCC produced in the concrete plant could be observed, while tensile strength and strain capacity were found to decrease.

Even though these changes may be related to different aggregates in use, a major part can be attributed to the influence of the production process on the composite structure, i.e. the micro-structure of the cementitious matrix, air-void content and fibre distribution. It was shown by porosity analyses, that air-void content and pore size distribution can change significantly for the same SHCC composition produced under different conditions. These differences in the composite structure may influence matrix and fibre bridging stress, which can impair conditions for multiple cracking.

The time-dependent behaviour of SHCC experienced a similar effect since tensile stresses were found to increase with specimen age. In this case a significant reduction of the crack development was observed resulting in a further reduction of strain capacity. Part of these changes may be a result of ongoing hydration processes, which change matrix properties as well as bond properties between fibres and SHCC.

Autogenous and drying shrinkage of SHCC were analysed as a basis for an estimation of shrinkage behaviour of reinforced tensile elements, which will be presented in **Chapter 4**. It was shown that a large portion of shrinkage is caused by drying with a minor contribution of autogenous shrinkage. Such phenomena need to be considered especially when investigating the tensile behaviour of reinforced elements with larger sizes. Therefore, the results will be used to further analyse the effect of shrinkage deformations on the structural response of large-scale specimens.

Uniaxial tension tests on steel reinforcement were conducted to determine strength and deformation behaviour of the steel rebar. Reinforcement with different diameters were tested. High ductility was observed independent of the bar diameter. In contrast, yielding strength and ultimate strength were found to increase with decreasing steel diameter. The experimentally determined load-deformation behaviour will serve as a basis for the discussion on the influence of steel yielding on the tensile behaviour of R/SHCC elements presented in **Chapter 4**.

4 Experimental investigations at the structural level

4.1 Introduction

The individual load-deformation behaviours of SHCC and steel reinforcement were analysed in the previous chapter, with an emphasis on the effects of large-scale production conditions on the material properties. It was found that SHCC properties are influenced by multiple variables, e.g. mixture composition, production conditions and geometry, among others. In addition to these variables, multiple cracking of SHCC with narrow crack widths can affect the bond interaction with steel reinforcement and hence change the global load-deformation behaviour of R/SHCC significantly compared to that of reinforced OC [44, 72].

To analyse the load-deformation behaviour of R/SHCC on a structural level, tests on large-scale tension members – which provided similar conditions as those found in structural applications – were performed with the aim of determining the effect of reinforcement parameters, i.e. reinforcement ratio, rebar diameter and concrete cover on the interaction of reinforcement and SHCC. In addition, crack width development on the specimen surface and strain distribution over the length of the reinforcement bars were tested to investigate the effect of steel yielding in the multiple cracking stage.

Overall, eight SHCC slabs with ribbed steel bars as reinforcement were fabricated in a concrete plant and subjected to uniaxial tensile loading. Different reinforcement configurations as well as unreinforced slabs came to use. The number and diameter of steel bars were systematically graded to analyse the effect of different reinforcement ratios on the global load-bearing behaviour of the tension member and the local stress and strain development of reinforcement and SHCC. Figure 4.1 provides a schematic view of the geometry and loading conditions of the tension member.

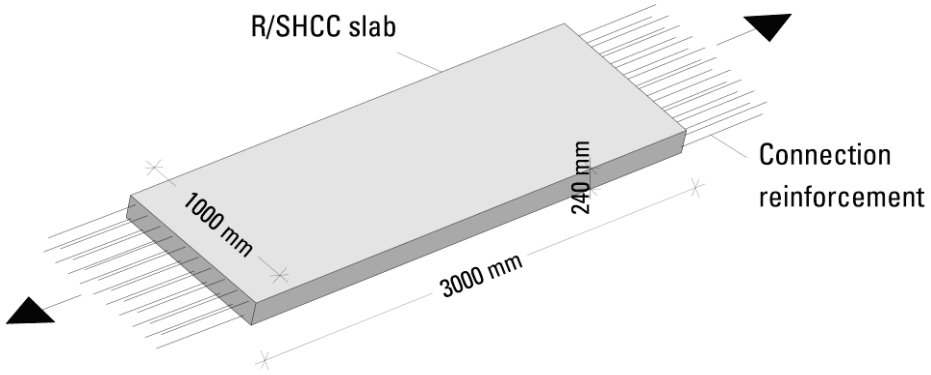

Figure 4.1: Schematic representation of the specimen geometry

The experimental framework can be divided into three main groups: (1) symmetrical double-layer reinforcement with transverse reinforcement and small concrete cover; (2) single-layer reinforcement without lateral reinforcement and large concrete cover; and (3) unreinforced slabs, which were used to isolate the bare SHCC response and acquire further information about the effect of geometrical parameters on the mechanical performance of SHCC. This approach allowed a detailed study of the combined interaction of steel and SHCC on a structural level. Table 4.1 details the specification of the slab elements and the reinforcement layout under investigation.

Table 4.1: Overview of the experimental program with design specifications of the tested specimens

Test series	Batch	Name	Longitudinal reinforcement	ρ [%]	Reinforcement configuration	c/d [-]
1	S03	10D14	10 Ø 14	0.68		1.8
	S03	08D16	8 Ø 16	0.65		1.6
	S04	08D14	8 Ø 14	0.50		1.8
	S04	08D10	8 Ø 10	0.25		2.5
2	S05	04D20	4 Ø 20	0.51		5.5
	S05	02D20	2 Ø 20	0.25		5.5
3	S05	0L-1	-	-		-
	S05	0L-2	-	-		-

4.2 Specimen geometry and reinforcement

The chosen dimensions for the R/SHCC slabs were 3000 mm x 1000 mm x 240 mm. Similar slabs made of conventional R/C were used by ALVAREZ [7] to analyse the global load-deformation behaviour of R/C tension members under uniaxial tension. A specimen length of 3000 mm provided large bond lengths, which helped to analyse the mechanical interaction between steel and SHCC on a structural level.

Goal of the specimen design was an undisturbed crack development in the state of multiple cracking, which required sufficient anchorage of tensile loads and adequate bond length for the complete activation of the surrounding cement-based composite. The maximum test load was limited by the load-bearing capacity of the test frame connection to a maximum tensile load $F_{t,max}$ of 1.5 MN. With that in mind and considering the determined material properties (cf. Section 3.3) as well as a specimen cross-section of 1000 mm x 240 mm, a maximum reinforcement ratio $\rho_{s,max}$ of 0.68 % could be achieved. Such limitation ensured an activation of reinforcement beyond the yielding strength of the steel rebar.

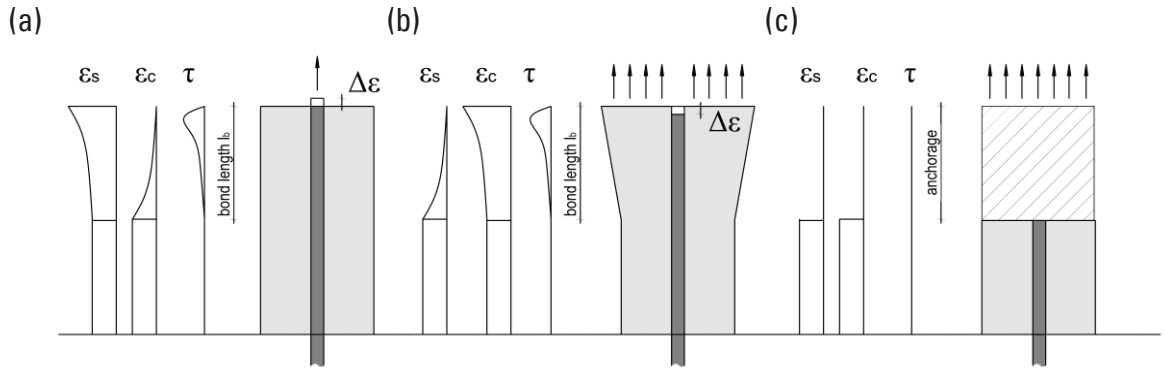

Figure 4.2: Examples of connection types for testing of reinforced tension members with loading of (a) rebar, (b) concrete and (c) uniform loading

The reaction of a R/SHCC tension member generally depends on the distribution of tensile stresses between reinforcement and SHCC, which is largely affected by the anchorage of the specimen. Such an anchorage can be achieved by direct loading of steel, SHCC or a combination of both. In most experimental investigations (cf. Section 2.4.2), the tensile force was transferred by steel[29] or SHCC, which may result in a low activation of SHCC or steel, respectively, when bond lengths are relatively short.

The bond length l_b required to achieve complete load sharing depends on the distribution of bond stresses, as depicted in Figure 4.2a and b. As shown in previous investigations, a lower development of interfacial bond slip and subsequently lower bond stresses can be observed as result of deformation compatibility between reinforcement and SHCC, which increases the required bond length. This problem can be avoided by using a mechanical connection, which provides a uniform introduction of the tensile force into the element, as illustrated in Figure 4.2c.

The layout of the anchorage for the tensile specimen within the framework of the thesis at hand was adapted to fulfil the requirements for a full bond activation for all test series.

Test series 1

The first test series included four slabs with longitudinal reinforcement ratios ρ_s of 0.68, 0.65, 0.50 and 0.25 % introduced by variation of the rebar diameter and number of bars. The longitudinal reinforcement was placed along the entire length of the specimen and connected to the load application bracket by rebar couplers. The steel rebar with varying diameters d_s from 10, 14 and 16 mm was placed in a vertical distance of approximately 170 mm resulting in a concrete cover c_{nom} of approximately 25 mm.

[29] A load introduction according to Figure 4.2a is not recommended since the load shared between steel reinforcement and the matrix (here: SHCC) is always found to exceed the strength of the rebar at the specimen ends unless the steel cross-section is increased, for example by steel couplers, cf. Figure 2.21.

Transverse reinforcement stirrups with a diameter d_s of 10 mm were placed at a spacing of 200 mm. The specimens were connected to the loading frame by welded couplers attached to the ends of the longitudinal reinforcement. Additional anchorage reinforcement was provided to strengthen the specimen ends to prevented local failure and ensure an even load distribution, according to Figure 4.2c. The reinforcement layout of the first test series is illustrated in Figure 4.3.

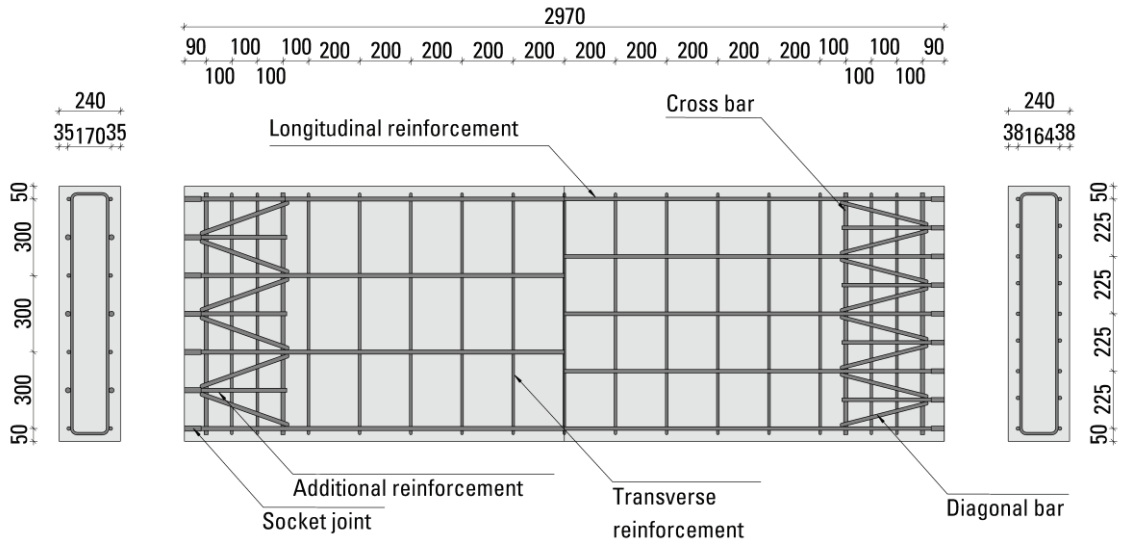

Figure 4.3: Specimen geometry and double-layer reinforcement layout for the specimens of test series 1

Test series 2

Two single-layer reinforced slabs with a constant steel rebar diameter, but varying number of bars resulting in reinforcement ratios ρ of 0.50 and 0.25 % were used for the second test series. Transverse reinforcement had to be omitted since there was no possibility to fix the corresponding steel bars during casting. However, spalling failure could be avoided by the large concrete cover and fibre bridging properties of SHCC. In addition, similar reinforcement ratios between test series 1 and 2 allowed a comparison of the load-deformation behaviour and served as an indication for the effect of concrete cover.

Steel rebar with a diameter d_s of 20 mm was used as longitudinal reinforcement and arranged at a varying distance. The rebar was placed centrally in the specimens, which resulted in a concrete cover c_{min} of approximately 110 mm. The test load was transferred by anchorage bars embedded into the specimen ends, resulting in a load distribution at the specimen ends, according to Figure 4.2b. A gradual variation of the embedment length of the connection reinforcement was used to smoothen the change of stiffness and to lower local stress concentrations. The reinforcement layouts of the second test series are illustrated in Figure 4.4 respectively.

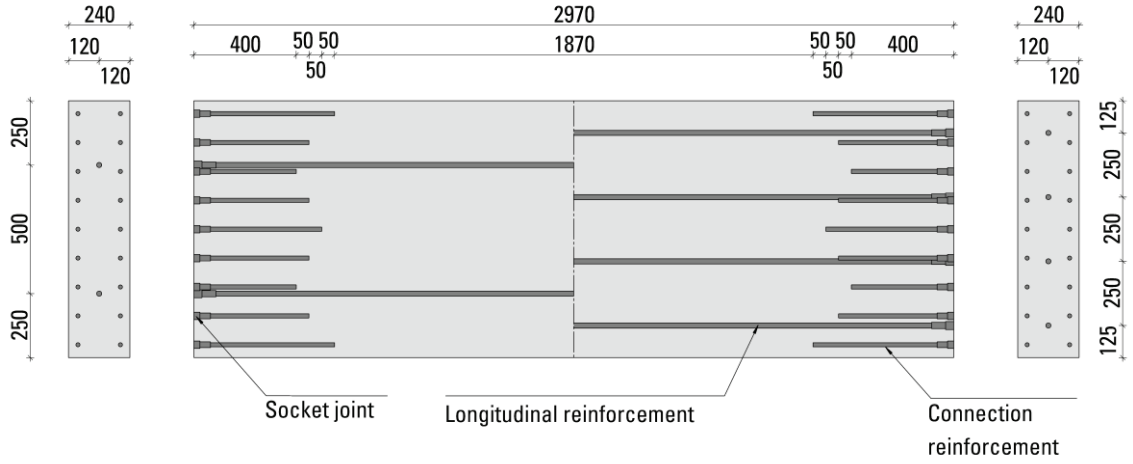

Figure 4.4: Specimen geometry and reinforcement layouts for the single-layer reinforced specimens of test series 2

Test series 3

The third test series included two unreinforced specimens, which were used to analyse the effect of specimen geometry on the tensile properties of SHCC and achieve a better understanding the contribution of the component SHCC to the load-carrying behaviour of R/SHCC elements. The tensile load was applied by anchorage bars similar to those of test series 2. The lack of longitudinal reinforcement reduces the tensile load to the load-carrying capacity of SHCC, which resulted in lower bar diameter. Figure 4.5 presents an illustration of the specimen layout of the third test series.

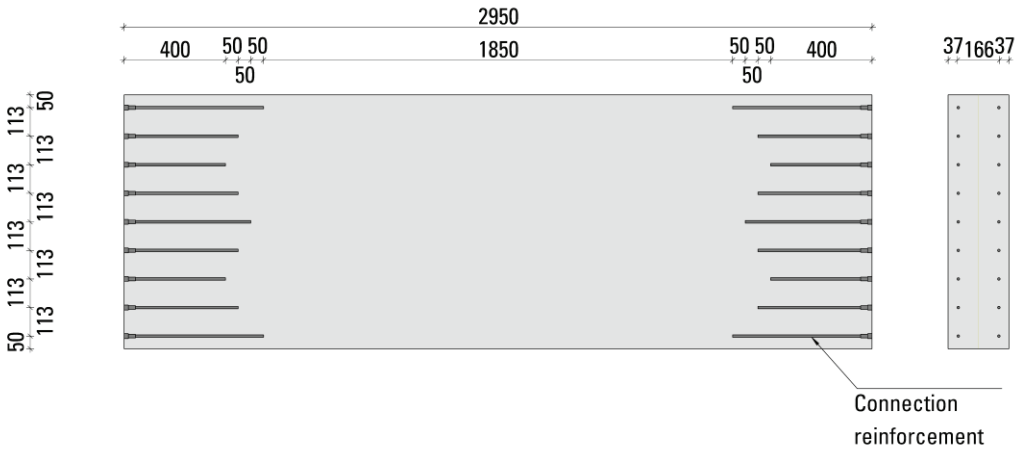

Figure 4.5: Specimen geometry and anchorage layout of the unreinforced specimens for test series 3

4.3 Production of reinforced SHCC slabs

Specimens production commenced with the assembly and welding of reinforcement cages in a workshop followed by preparation of the formwork and the support frame for transportation before the casting of specimens. Figure 4.6 shows the completed reinforcing cage after assembly. After the final assembly of all parts, the reinforcing cages were transported to the casting site and placed into the formwork. Two steel formwork systems with dimensions of 3 000 x 3 000 mm² and a height of 240 mm were available resulting in the possibility of casting three specimens with each SHCC batch. The formwork was placed on a wooden support construction with oil coated planks. The objective goal of the formwork arrangement as described was the possibility to transport the specimens in the formwork to the laboratory under avoidance of possible pre-loading of the specimens.

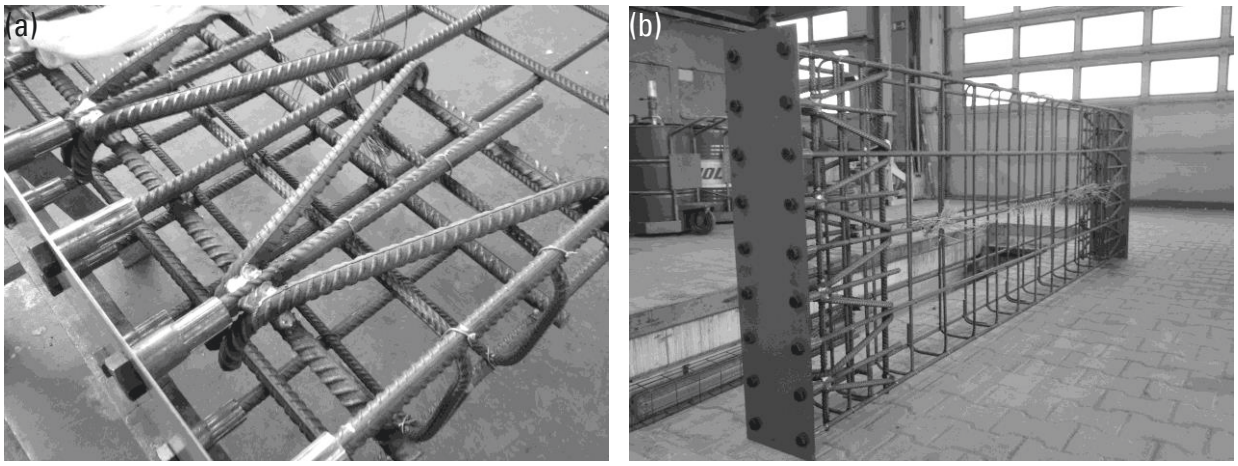

Figure 4.6: (a) View of the welded anchorage construction and (b) completed reinforcing cage after assembly

The mixing followed the same procedure as described in Section 3.2.2.2, which ensured close to identical production conditions for all test series. The structure of the SHCC investigated on drill cores (cf. Section 3.3) showed a tendency to develop compaction voids around the steel rebar. The series contained two to four batches of SHCC each batch containing a volume of approximately 0.85 m³. To ensure a constant quality, the fresh material properties were checked continuously during the casting process. The batches of test series 2 and 3 were cast with a concrete pump, which proved to enhance the fresh properties, i.e. increase the workability, especially regarding the quality of the finished surface. The concreting side of the specimens was smoothed with a trowel and covered with plastic foil to minimise evaporation of moisture and to mitigate the development of moisture gradients. The elements remained at the concrete plant until they reached an age of 28 days, after which the specimens were demoulded and transported to the laboratory. Figure 4.7 shows the casting of the specimens from the concrete mixing truck, as well as the surface treatment.

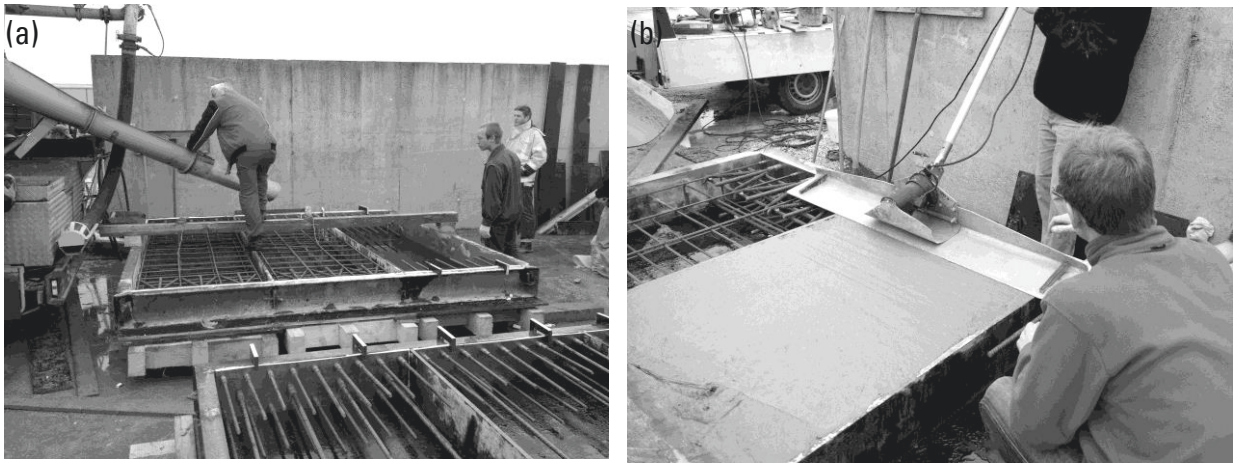

Figure 4.7: (a) View of the formwork including reinforcement cages prior to casting and (b) surface smoothening of the fresh SHCC after casting

4.4 Experimental setup

The large size of the specimens is technically demanding and imposes high requirements on the experimental setup. A setup developed by SCHRÖDER [134] who investigated the influence of bi-axial tension on the load-bearing behaviour of conventional and pre-stressed R/C slabs was adapted for this purpose. The R/SHCC slabs were placed in a custom manufactured loading frame, originally designed for testing steel cables and pre-stressing tendons. The hydraulic cylinders can apply a maximum test load of 20 MN in tension or compression. The elements were hoisted into the loading frame in an upright position and supported by a steel girder equipped with PE slip membrane to reduce frictional forces during testing.

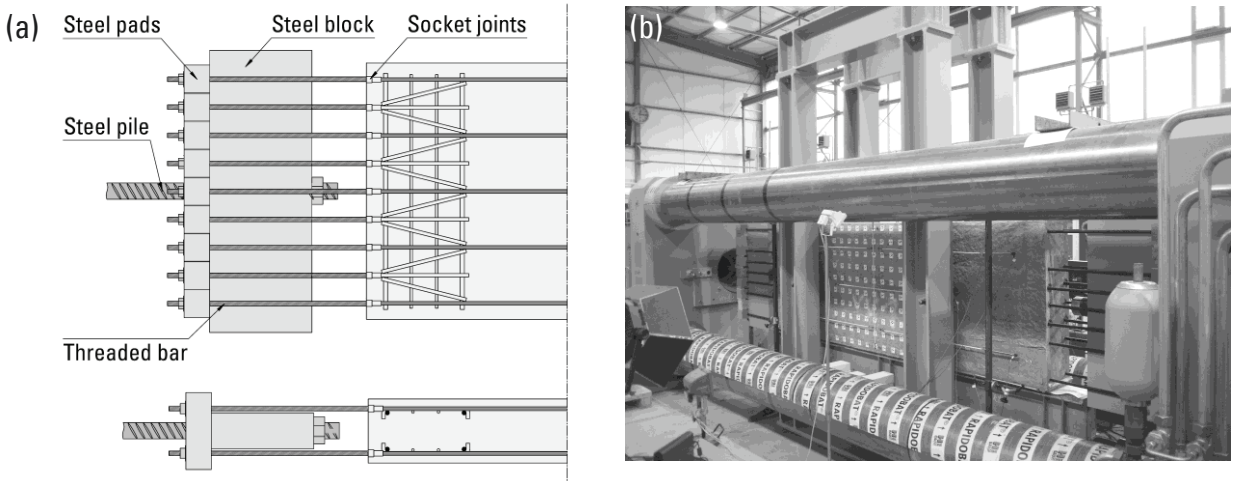

Figure 4.8: (a) Schematic view of the load introduction setup and (b) the completed test setup with a R/SHCC slab and measurement equipment

Steel rods screwed to the rebar couplers connected the specimen with a steel block, which ensured a uniform distribution of the test load over the cross-section of the specimen. Two steel piles with a diameter d_s of 65.5 mm connected the loading frame with the steel block on both sides. The connection of the test specimen is illustrated in Figure 4.8a, together with an overview of the final test setup, as shown by Figure 4.8b.

The specimen age at testing depended on the time required for the installation of measurement apparatus and varied between 61 and 86 days, cf. Table 4.3. The signals of all measurement devices were recorded with a MGCplus data monitoring system from HBM. The recorded test data was digitally stored, for which a frequency of 2 Hz was deemed sufficient. The loading of the specimen was conducted displacement controlled with a speed of 0.01 mm/s. The tensile force was measured with an internal load cell of the testing machine, while three additional load cells were used to verify the distribution of the applied forces over the cross-section of the specimen. Table 4.2 provides an overview of the instrumental setup for measuring global and local deformations on the tensile elements.

Table 4.2: Overview of the instrumental setup for deformation measurements

Instrument	Measurement	Location	Gauge length
LVDT	Longitudinal strain	Form and casting side	30 mm
	Lateral strain	Form and casting side	10 mm
	Global strain (control)	Central at specimen end	200 mm
Strain gauges	Local steel strain	Reinforcement	10 mm
Photogrammetry	Local deformation	SHCC surface (form side)	400 x 300 mm
Load cell	Tensile load of steel bars (up to 125 kN)	Steel rods (2 x bottom/top, 1 x centre)	

Global deformations were measured for control purposes by multiple LVDTs placed centrally on the top and the bottom of the specimen ends. Gauging collars glued to the SHCC surface were connected to the LVDTs by carbon tubes resulting in a gauged region with dimensions of approximately 900 x 2000 mm². Both sides of the specimen were prepared since eccentricities of the load anchorage or non-uniform shrinkage can cause bending along the vertical axis of the element.

An optical close-range photogrammetry system was used to measure the local strains on the element surface in addition to global deformations. A camera was positioned at approximately 1 m distance from the measurement field, which included a textured area of 400 x 300 mm². The system allowed a continuous monitoring of crack formation and deduction of the crack opening development. The continuous recording of the trigger signal allowed the association of the pictures to the corresponding strain level.

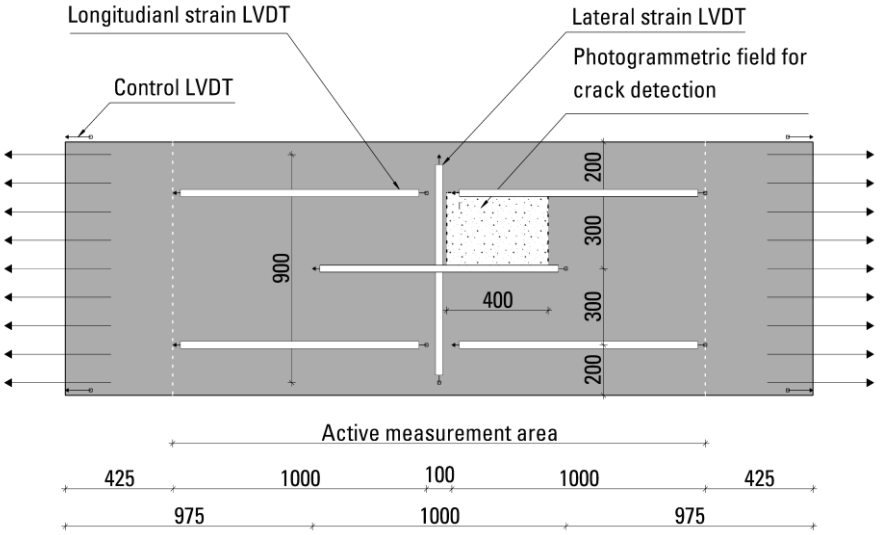

Figure 4.9: Layout of the instrumental setup on the form side of the specimen (LVDT for lateral strain measurement identical on both sides)

Figure 4.9 shows the layout of the instrumental setup for measuring global and local deformations on the tensile elements as well as the measurement length of each individual LVDT attached. Both specimen sides were equipped with an identical setup. Local strains of reinforcement bars were measured by strain gauges with a gauge length of 10 mm. The strain gauges were placed at a spacing of 300 mm starting from the centre of the steel bar to assess the stress distribution along the steel reinforcement. The strain gauges were covered with an epoxy coating to protect them from fluid and mechanical exposure during casting.

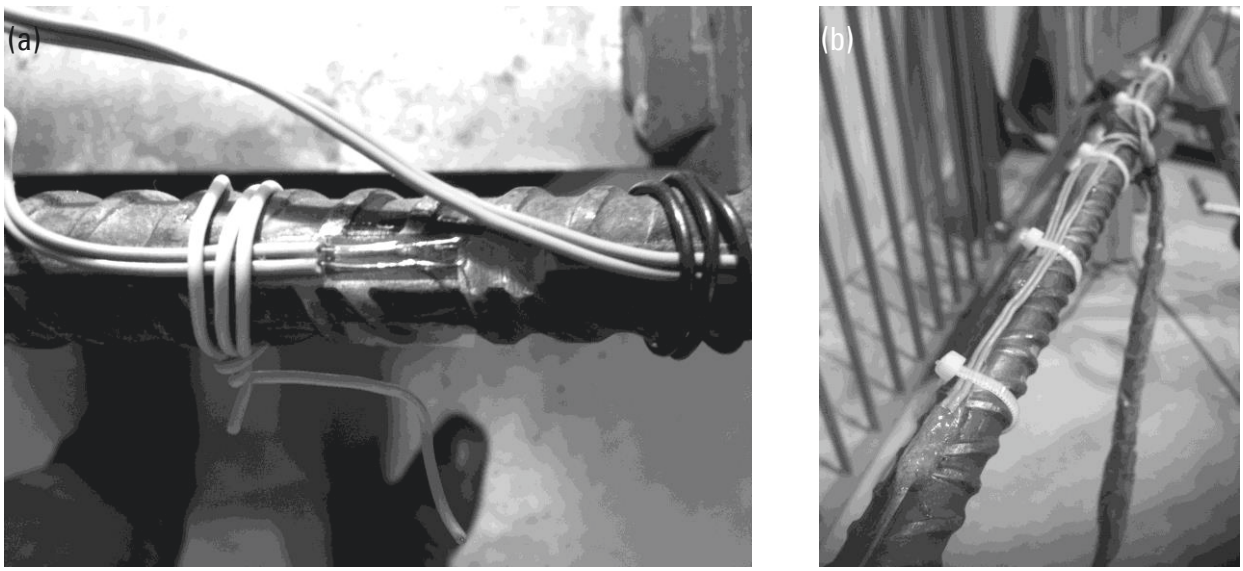

Figure 4.10: (a) Strain gauge attached to the steel reinforcement and (b) overview of the strain gauges

4.5 Experimental results

The outlined test setup was used to analyse the load-deformation behaviour of the R/SHCC tension members and the mechanisms, which influence the interaction of reinforcement and cementitious composite. For this purpose, the analysis of the experimental results will be separated into three parts. A brief overview of the test results is provided for the global load-deformation behaviour of all specimens. Furthermore, the most important effects influencing the global deformation behaviour are discussed. The influence of the individual components on the stress-strain behaviour of the R/SHCC slabs are analysed, based upon the results of the material tests presented in **Chapter 3** in which the stress-strain behaviour of SHCC and the steel reinforcement were investigated on small specimens.

The crack development of SHCC is calculated based upon local deformations recorded with digital close-range photogrammetry on the specimen surface. Additionally, the local deformation behaviour of the steel reinforcement is obtained from the strain gauges. With the measurement of the local strain development in the reinforcement, detailed conclusions on the contribution of the steel reinforcement to the global deformation behaviour of the structural element can be drawn.

4.5.1 Global deformation behaviour

4.5.1.1 Effect of shrinkage

It was shown in Section 2.1.4, how shrinkage can affect the properties of SHCC at the material level. However, shrinkage is also known to influence the behaviour at the structural level, i.e. that of reinforced elements (see e.g. [61, 72, 79]). In general, shrinkage deformations, when restrained by steel reinforcement, cause the development of internal eigenstresses which develop due to the bond interaction between reinforcement and cementitious matrix. Thus, restrained shrinkage evokes compressive stress on the reinforcement and tensile stresses in the cementitious matrix.

Stress at first cracking

For high amounts of reinforcement and pronounced shrinkage of concrete, these internal stresses may reach the strength of the cementitious matrix, which may cause the development of shrinkage cracks. For low reinforcement ratios, these effects can be neglected as long as tensile stresses do not exceed the matrix tensile strength σ_{mu} [61, 79]. However, the micro-structure of the cement-based composite may still be affected by internal micro-cracks, which can lead to a reduction of the stress at first cracking σ_1.

SEIBEL [135] investigated the influence of shrinkage on reinforced concrete tension members and showed that the stress at first cracking σ_1 of specimens subjected to desiccation decreased by 30 % in comparison to specimens cured under water. This was attributed to the effect of shrinkage-induced micro-cracking in the cementitious matrix due to internal pre-loading of the specimens.

A visual inspection of the R/SHCC slabs investigated before loading showed a reticular crack pattern on both specimen surfaces with crack widths w_{max} up to 400 µm. It was established by drill cores that these cracks were limited to a depth of approximately 2 cm. These cracks close to the surface indicate a crack development due to plastic shrinkage as a result of water evaporation near the specimen surface at an early SHCC age. Such a presence of shrinkage cracks prior to mechanical loading may cause a reduction in stress at first cracking σ_1 and could influence the crack development on the specimen surface.

Initial shrinkage deformations

Additional to the influence on the stress at first cracking and crack development, restrained shrinkage may also cause a reduction of the measured tensile force due to the compressive pre-loading of the reinforced tension member. The compressive pre-loading can be calculated by the initial shrinkage deformation of the tension members as illustrated in Figure 4.11.

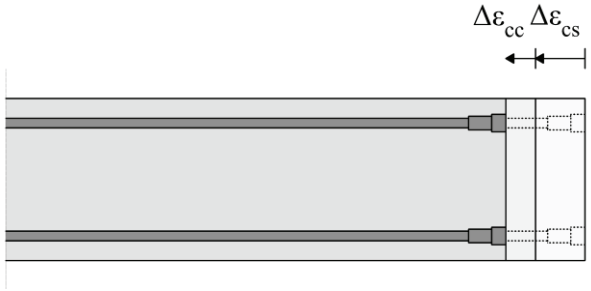

Figure 4.11: Change in internal strain of the tension member as a result of shrinkage and creep

The R/SHCC slabs tested in the study at hand were cured in the formwork and protected from desiccation by plastic foil for approximately four weeks. However, no additional curing treatment was applied before demoulding. Thus, a major part of shrinkage can be attributed to autogenous and drying shrinkage. The parameters required to estimate shrinkage deformation of the slabs can be calculated under consideration of shrinkage stains measured on SHCC prisms, cf. Section 3.3.3. A complete evaluation of these parameters is given in Annex C. As an example, the maximum shrinkage at the time of testing is assessed for Specimen 10D14 for which the contribution of drying shrinkage yields:

$$\varepsilon_{cd}(t, t_s) = \varepsilon_{cd}(\infty) \cdot \beta_{ds}(t, t_s) = 0.19‰ \tag{4.1}$$

with $\varepsilon_{cd}(\infty) = 1.0‰, \beta_{ds}(61{,}15) = 0.22$

The contribution of autogenous shrinkage results in:

$$\varepsilon_{ca}(t) = \varepsilon_{ca}(\infty) \cdot \beta_{as}(t) = 0.47‰ \tag{4.2}$$

with $\varepsilon_{ca}(\infty) = 0.6‰, \beta_{as}(61) = 0.79$

The total free shrinkage at the age of testing adds up to:

$$\varepsilon_{cs} = \varepsilon_{ca} + \varepsilon_{cd} = 0.19 + 0.47 = 0.66‰ \tag{4.3}$$

Hence, the initial deformation of the specimen can be calculated under consideration of the total shrinkage strain according to Eq. (4.4):

$$\Delta\varepsilon_{cs} = \frac{\varepsilon_{cs}}{1 + \alpha_E \cdot \rho_s} \tag{4.4}$$

with $\alpha_E = \frac{E_s}{E_c} = 11.1$ and $\rho_s = \frac{A_s}{A_c} = 0.65\ \%$

Tensile stress as the result of restrained shrinkage will partly be reduced by the effect of creep. The creep value at the time of testing can be calculated with Eq. (4.5):

$$\varphi(t, t_0) = \varphi_0 \cdot \beta_c(t, t_0) = 1.03 \tag{4.5}$$

with $\varphi_0 = 2.17, \beta_c(61{,}15) = 0.48$

In this case, the assumed onset of loading starts simultaneously with the onset of drying shrinkage after the end of the curing period. The resulting strain of the pre-deformation considering creep and shrinkage was calculated as for OC[30] according to Eq. (4.6):

$$\Delta\varepsilon_{cs} = \frac{\varepsilon_{cs}}{1 + \alpha_E \cdot \rho_s(1 + \chi \cdot \varphi)} \tag{4.6}$$

with $$\chi = \frac{{t_0}^{0.5}}{1 + {t_0}^{0.5}} = 0.79 \tag{4.7}$$

Due to the shortening of the specimen as a result of restrained shrinkage, the material curves obtained by direct tension test need to be adjusted by $\Delta\varepsilon_{cs}$. The resulting pre-deformations before application of testing loads are given for all tested specimen in Table 4.3. These results are based upon Eq. (4.6) and include drying shrinkage, autogenous shrinkage and creep.

This effect needs to be considered when comparing the curves of the individual composite components with the original material curve. The resulting differences can be expressed either by shifting of the reinforced composite strain or by a pre-loading stress of the SHCC according to Eq. (4.8).

$$\sigma_{cs} = (1 + \alpha_E \cdot \rho_s) \cdot (\Delta\varepsilon_{cs} \cdot E_s \cdot \rho_s) \tag{4.8}$$

[30] The basic creep value was estimated according to EN 1992-1-1 [37] based on the given composite composition with a class N type cement and a compressive strength of 41,0 MPa at an assumed RH of 65 %.

Table 4.3: Pre-deformation of the specimen due to creep and shrinkage

Specimen	t [d]	ε_{cs} [‰]	ρ_s [%]	α_E [-]	t_0 [d]	χ [-]	ρ_0 [-]	β_c [-]	φ [-]	$\Delta\varepsilon_{cs}$ [‰]	σ_{cs} [MPa]
10D14	61	0.66	0.68	9.1	15	0.79	2.17	0.48	1.03	0.60	0.81
08D16	69	0.70	0.65		15			0.50	1.08	0.63	0.89
08D14	84	0.78	0.50	9.2	30			0.50	0.95	0.72	0.77
08D10	80	0.73	0.25	9.6	30	0.85	1.91	0.50	0.95	0.70	0.39
04D20	66	0.68	0.51	10.0	30			0.44	0.85	0.73	0.84
02D20	86	0.80	0.25		30			0.50	0.96	0.73	0.41

4.5.1.2 Tensile load-deformation curves

The global load-deformation behaviour of the reinforced and unreinforced tension members was calculated from the average LVDT displacement on both sides of the specimen. All curves are computed based on a measurement length l_o of 1000 mm unless stated otherwise. In addition, the equivalent stress-strain response of plane steel rebar is shown to highlight the contribution of SHCC to the load-deformation behaviour of the reinforced tension member. The stress-strain curve of the bare steel response was shifted on the strain axis by $\Delta\varepsilon_{cs}$ to consider the effect of shrinkage. It should also be noted that steel strain of the plane rebar and the global strain of the reinforced element are based upon different gauge lengths, which limits the actual comparability of the curves.

Figure 4.12 provides an overview of the load-strain responses for all double layer reinforced specimens with different reinforcement ratio. As is apparent from the stress-strain curves, the load-deformation response can be subdivided into three stages.

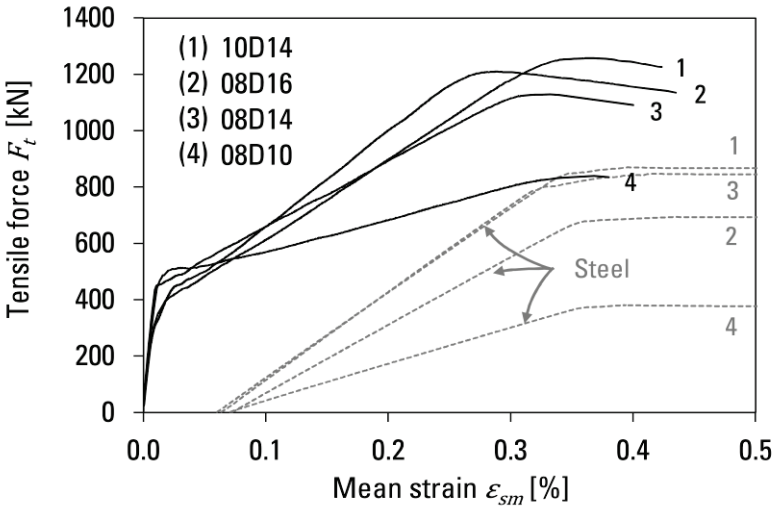

Figure 4.12: Global load-deformation behaviour of all tension members with double-layer reinforcement compared to bare steel response

During the first stage, the composite element remains un-cracked with a linear increase of stresses until the first cracks develop in SHCC. A gradual transition of the stress-strain curve between the first and second stage can be observed at strains of approximately 0.01 to 0.02 % and a loading force between 400 and 450 kN. The second stage is characterised by a lower increase of tensile stresses combined with a continuous development of multiple fine cracks. A close to linear increase of the stresses can be observed with increasing strain until the ultimate load level is reached at the yielding strain of steel reinforcement, which coincides with the beginning of steel yielding. The nominal contribution of SHCC can be derived by comparing the stress-strain curve of the reinforced tension member (solid curves) to that of the steel rebar (dashed curves). The results show that the contribution remains almost constant during the entire second stage, which can be related to the crack-bridging effect of fibres in the cement-based composite. The third stage of the stress-strain curve is characterised by a decline of stresses as a single macro-crack develops marking the beginning of failure. At this point the strains remain localised in one crack, while fibres located in the crack region are pulled out from the Cementous matrix. A local "overstretching" of rebar, which led in some cases to immediate rupture of steel rebar despite path controlled deformation regime was observed at the same time.

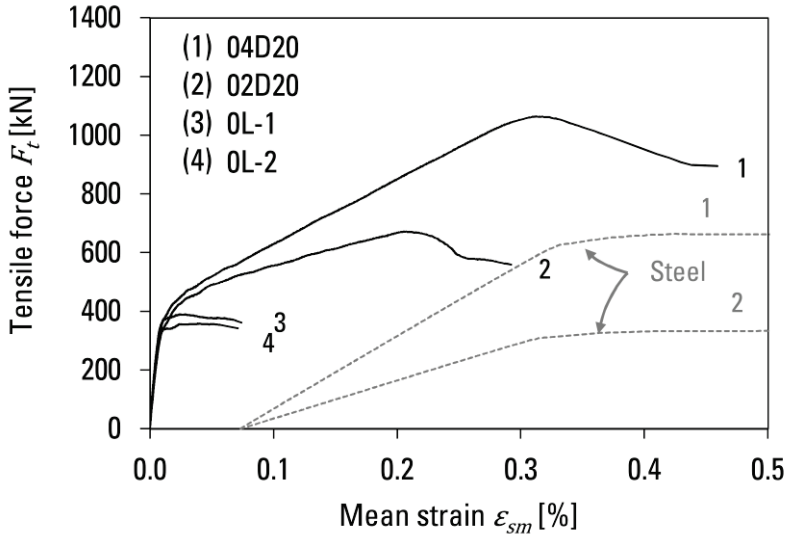

Figure 4.13: Global load-deformation behaviour of all tension members with double-layer reinforcement compared to bare steel response as well as unreinforced elements

Figure 4.13 shows the results of single layer reinforced specimens as well as unreinforced tension members. While single layer reinforced slabs experienced a tensile deformation behaviour similar to that of double layer reinforced slabs, plain large-scale SHCC specimen experienced a different load deformation response. In this case the linear-elastic phase was followed by an inelastic phase up to a strain of approximately 0.1 %. In this phase, slight tension softening was observed prior to the failure of the specimen. Such evident decrease in ductility in comparison to the results obtained on small dumbbell specimens (cf. Section 3.2.4) highlights the influence of the specimen size on the load deformation behaviour of plain SHCC.

4.5.1.3 Effect of non-uniform strain distribution

The effect of shrinkage was previously determined under the assumption of a uniform shrinkage distribution within the specimen. However, concrete elements with high thickness are known to exhibit pronounced moisture gradients within a specimen, which can lead to non-uniform strain distribution across the thickness of the specimen. Such behaviour is caused by different shrinkage strains on each side of the specimen, which can be related to the fabrication process and differences in surface roughness on the casting and formwork side. The resulting strain gradient across a specimen is schematically illustrated in Figure 4.14.

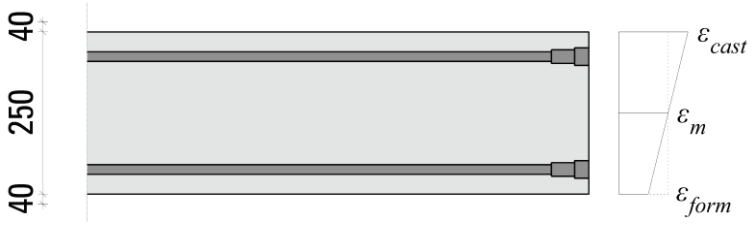

Figure 4.14: Schematic illustration of the strain distribution in a double-layer reinforced tension member as a result of non-uniform shrinkage strain

Since tension members investigated in the study at hand were found to be impacted by moisture gradients, further discussion about the effect of non-uniform strain distribution on the load-bearing behaviour of large-scale specimen is necessary. For this purpose, the displacement on both surface sides of a double-layer specimen (08D16) and unreinforced specimen (0L-1) will be considered in more detail.

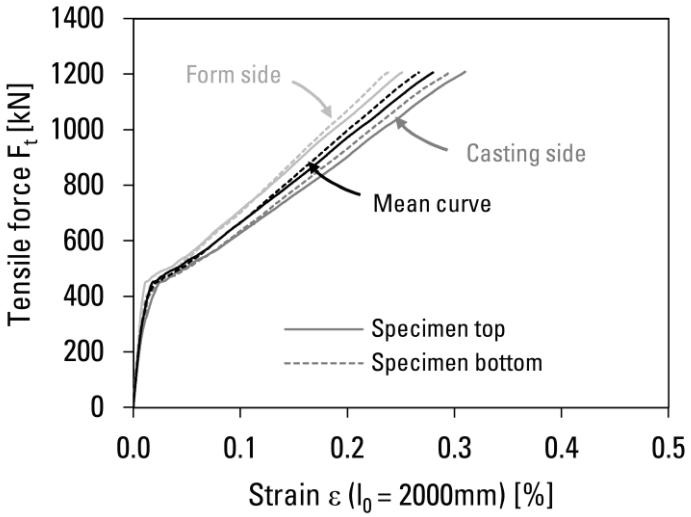

Figure 4.15: Load-deformation behaviour on different positions of reinforced specimen 08D16

Figure 4.15 offers a comparison of the calculated tensile strain development derived from LVDT measurement on both sides of the specimen. Only minor difference can be observed for the strain measured on the top and the bottom of the element. Thus, a uniform distribution of stresses was achieved by the anchorage and loading gear of the test frame.

For reinforced tension members, differences between the two opposite surfaces remain relatively small during the state of multiple cracking. Hence, it can be assumed that the interaction of SHCC with the steel reinforcement enabled a certain degree of stress redistribution. This changes dramatically after a macro-crack opens. The most likely cause of such behaviour in the post-crack regime are eccentricities caused by irregularities of the crack opening and different yielding behaviour of the reinforcement layers, which likely results from larger crack opening on one of the specimen sides.

Unreinforced elements are found to experience a more pronounced effect of eccentricities even before localisation occurs in a large macro crack, as shown in Figure 4.16. In this case, the difference between measured strain on both sides increases even before the actual first-cracking load is reached. Such behaviour indicates large stress concentrations and formation of surface cracks on one side of the specimen. Hence, the actual first-cracking stress is reached on one side of the specimen prior to the mean stress, which could serve as an explanation for the observed strain differences between both sides and non-linearity of the curve. After the first-cracking load is reached, the allocation of strain on the casting side increases, which leads to a reduction of the tensile strain on the opposing form side and even to a change into compression.

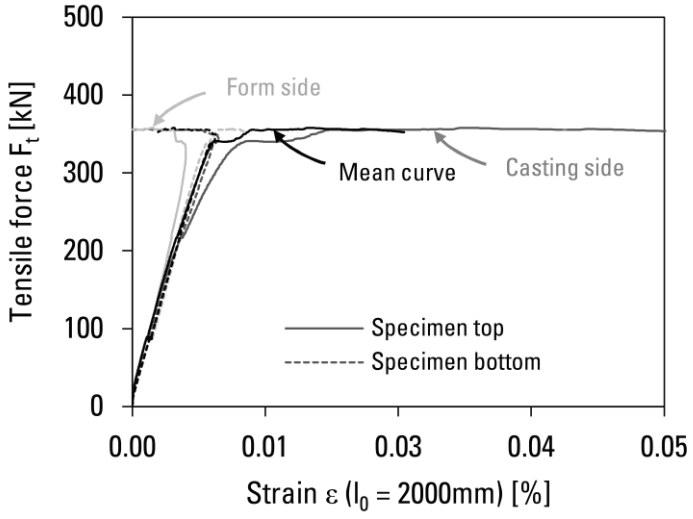

Figure 4.16: Load-deformation behaviour on different positions of unreinforced specimen 0L-1

It should be noted that a pronounced bending of the tension members could be observed during testing. At this stage a stable increase of global tensile strain remains possible as long as the peak stress at the casting side of the specimen remains lower than the tensile strength f_t of SHCC.

However, the stress redistribution capability of unreinforced tension members remains small compared to reinforced tension members, which were found to achieve a more uniform strain growth. Therefore, the critical level of stable strain development is exceeded as soon as the tensile strength of SHCC is reached, which will cause a macro-crack propagation starting from the surface into the specimen. With continuing crack growth, the effect of load eccentricity increases, which leads to unstable crack development and a decline of the global tensile load.

For the stable cracking phase, the mean value of the global strain can be calculated under the assumption of a linear strain distribution in between the casting and formwork side according to Eq. (4.9):

$$\varepsilon_m = (\varepsilon_{cast} + \varepsilon_{con})/2 \tag{4.9}$$

A summary of the measured strain distributions at the end of the first and second stage of the global deformation, i.e. first cracking and failure, is given in Table 4.4. Based upon the discussion above, the computed values at the end of the second stages can only be regarded as an indication for the stress distribution prior to failure of the specimen. Especially for specimens with centric reinforcement and unreinforced specimen, substantial strain differences between both sides can be observed even during the multiple cracking phase of SHCC.

Table 4.4: Overview of the failure position and derivation of the measured strains on the adjacent sides of the specimen

Specimen	ρ_s	First cracking			Failure[1]			Crack position
		ε_{cast} [%]	ε_{form} [%]	ε_m [%]	ε_{cast} [%]	ε_{form} [%]	ε_m [%]	
10D14	0.68	0.043	0.028	0.035	0.421	0.307	0.364	Centre
08D16	0.65	0.041	0.013	0.027	0.350	0.228	0.289	Centre
08D14	0.50	0.015	0.006	0.010	0.330	0.293	0.311	Centre
08D10	0.25	0.014	0.012	0.013	0.346[2]	0.362[2]	0.354[2]	End
04D20	0.51	0.031	-0.001	0.015	0.313[2]	0.285[2]	0.299[2]	End
02D20	0.25	0.024	0.000	0.012	0.492	0.050	0.271	Centre
0L-1	-	0.033	0.001	0.017	0.157	-0.015	0.071	Centre
0L-2	-	0.020	0.004	0.012	0.073[2]	0.058[2]	0.065[2]	End

[1] Point of failure is defined as the end of stable cracking phase [2] Measurement base 2000 mm; for another values measurement base was 1000 mm

Based upon the measured strain on each side of the specimen, the actual stress peaks on the outer layer of the cross-section at the point of first cracking can be calculated under the assumption of a linear strain distribution (cf. Figure 4.14) and under consideration of the shrinkage pre-loading (cf. Table 4.3) with Eq. (4.10)[31].

$$\sigma_{cast} = \frac{2 \cdot (\sigma_{nom} + \sigma_{cs})}{(1 + \varepsilon_{cast}/\varepsilon_{con})} \tag{4.10}$$

with

$$\sigma_{nom} = \frac{F_t}{A_s + A_c} \tag{4.11}$$

Figure 4.17 provides an overview of the nominal tensile stress and the peak stress on the casting side of the specimens measured at the first cracking load. Moreover, the tensile stress is compared to the mean tensile stress at first cracking σ_1 derived from uniaxial tension tests on dumbbell specimens. The comparison reveals that peak stresses surpass the nominal stress of the specimen. The largest difference between nominal and peak stress can be observed for the unreinforced specimen. In general, this difference stems from the non-uniform strain distribution within the slab as a result of eccentricities. The results indicate that reinforcement restrains non-uniform shrinkage subsequently lowering the effect of eccentricities. In addition, a general increase in the peak tensile stress at first cracking can be observed with increasing reinforcement ratio, while the peak stress reaches the mean stress at first cracking σ_1 of the composite material for higher reinforcement ratios. This highlights the effect of shrinkage pre-loading and eccentricities, which should be considered when evaluating the stress at first cracking and tensile strength of large-scale elements.

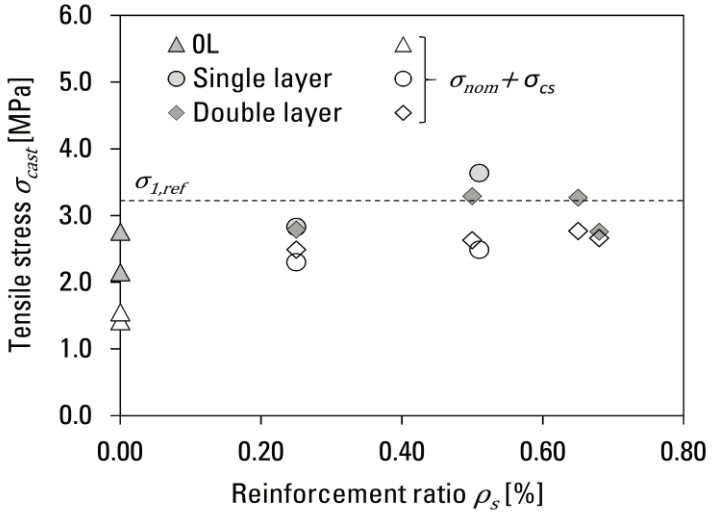

Figure 4.17: Results of the peak stress at first cracking on casting side of the specimen in comparison to the nominal stress in the specimen and first cracking stress of SHCC

[31] A linear-elastic material behaviour was assumed since only the linear-elastic stage up to first cracking was analysed.

In general, it can be concluded that the average stresses calculated for the entire cross-section can be substantially lower than the actual stress on the casting side of the specimen, depending on the reinforcement configuration. However, average stresses will be used for further discussion since they offer a better comparison between elements with different reinforcement configurations.

4.5.2 Comparison of stress-strain behaviour

The stress-strain curves of the different test series are compared to analyse the influence of different reinforcement parameters on the load-bearing behaviour of reinforced tension members. The stress-strain curves are based upon the mean displacement $\varepsilon_{c,mean}$, which was calculated according to Eq. (4.9). Pre-loading of SHCC as a result of the restrained shrinkage deformation $\Delta\varepsilon_{cs}$ was taken into account by shifting the stress-strain curve of the steel response on the strain axis according to Eq. (4.6).

The mean strain of the reinforced element is compared to the stress-strain behaviour of the isolated steel reinforcement derived from direct tension tests. The stress-strain curves of the reinforced tension members are displayed in terms of the nominal steel stress to achieve better comparability to the tensile response of the reinforcement. The nominal steel stress was derived from the tensile machine force F_t divided by the total cross-section of the steel reinforcement A_s.

$$\sigma_{s,nom} = \frac{F_t}{A_s} \tag{4.12}$$

The contribution of SHCC to the global tensile load response was isolated to highlight the effect of strain-hardening properties. The stress-strain curve was calculated by subtracting the steel load response from the global strain response of the tension member:

$$\sigma_{c,nom} = \frac{F_t - F_s}{A_c} \tag{4.13}$$

In this case, the isolated stress-strain response is compared to the load-deformation behaviour of unreinforced SHCC tension members of equal size. The goal of this comparison is to highlight the influence of steel reinforcement on the tensile material behaviour of SHCC.

4.5.2.1 Influence of reinforcement ratio for double-layer rebar

Figure 4.18 shows the stress-strain behaviour of SHCC specimens reinforced with two symmetrical layers of steel rebar. Different reinforcement ratios are compared to investigate the effect of different rebar diameters. The variation of the reinforcement ratio included rebar diameters d_s of 10, 14 and 16 mm while maintaining a constant number of rebars (n_s = 8). Hence, the results are mostly influenced by variations of bond properties and a higher contribution of steel reinforcement to the complete load-bearing capacity.

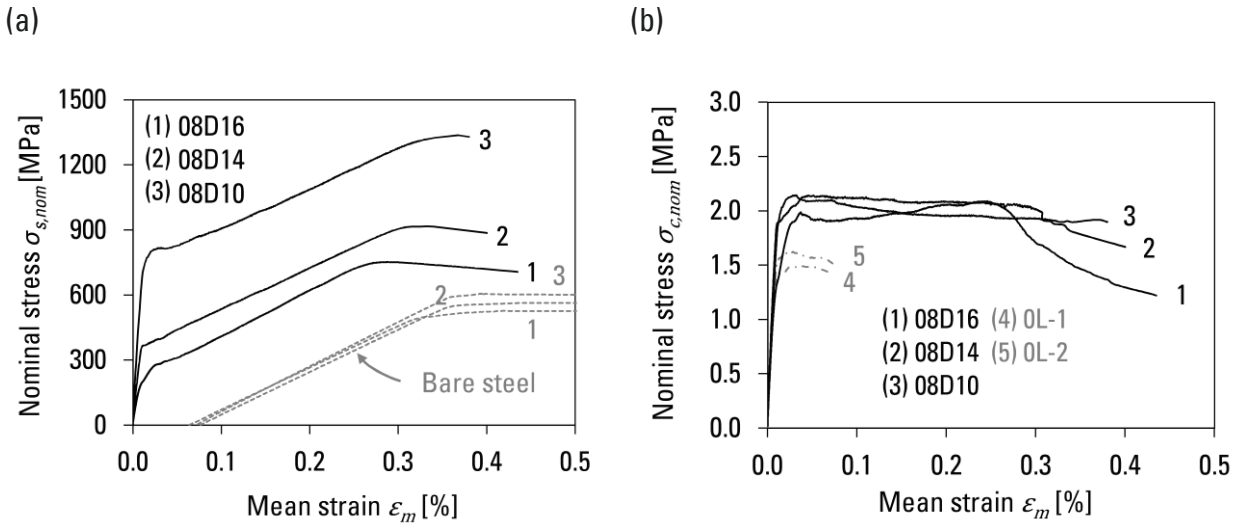

Figure 4.18: Load-deformation behaviour of double-layer R/SHCC tensile elements with different reinforcement ratios including (a) steel stress-strain response and (b) isolated SHCC load response

Figure 4.18a depicts the nominal steel stress-strain response resulting from the shared reaction of steel and SHCC in comparison to that of the bare steel rebars. It becomes obvious that the nominal steel stress decreases with increasing rebar diameter as result of the large SHCC contribution to the global load-bearing. Variations between the bare steel curves results from different total shrinkage restrains depending on the reinforcement ratio. Accordingly, varying maximum strain at the point of localisation was observed, which may be related to an overestimation of shrinkage pre-loading. In addition, measurements of steel rebar and reinforced SHCC slab were based on different gauge lengths, which also influences the measured strain at the point of localization.

Figure 4.18b shows that SHCC contributes to the shared reaction of the reinforced slabs even after the first crack occurred. In all cases a nearly constant contribution of SHCC could be observed after first-cracking up to the point of localization. However, in comparison to the unreinforced SHCC tension members, it was found that reinforcement substantially enhances the contribution of SHCC, which results in high tensile stresses carried by SHCC.

Due to the scatter observed for the tensile material properties of SHCC, which are influenced by a variety of factors (cf. Section 2.1.4.2), a distinct determination of the effect of the reinforcement ratio is not possible. It can rather be concluded that the influence of the reinforcement ratio on the contribution of SHCC holds less significance compared to the variations of SHCC material behaviour. However, the contribution of SHCC was found to be nearly independent of the amount of reinforcement for double layer reinforcement, which may be related to the effect of reduced eccentricities and lower peak stresses on the surface of the specimen (cf. Figure 4.17).

4.5.2.2 Influence of reinforcement ratio for single-layer rebar

The experimentally determined stress-strain curves for specimens reinforced with a single layer of reinforcement and the calculated contribution of SHCC are shown in Figure 4.19a. Since stresses are presented based upon the steel cross-section area, the stress-strain curves are found to depend on the reinforcement content. Similar to the double-layer reinforcement, a higher reinforcement ratio is found to decrease nominal steel stresses since most of the load is carried by SHCC.

Furthermore, specimen 02D20 experienced strain localisation prior to reaching the yielding strain of steel reinforcement. However, the point of failure occurred near the load introduction, which limits the representability of the mean strain curve. Even though the macro-crack opening occurred within the measurement area, failure was possibly induced by stress concentrations around the anchorage of the specimen.

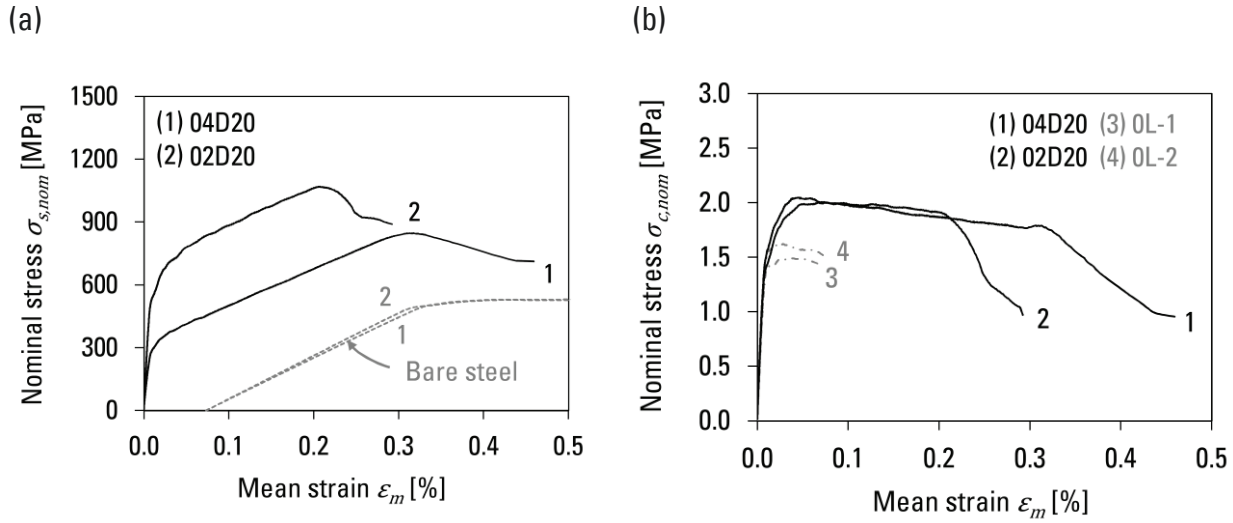

Figure 4.19: Load-deformation behaviour of single-layer R/SHCC tensile elements with different reinforcement ratios including (a) nominal steel stress-strain response and (b) isolated stress-strain response of SHCC

The contribution of SHCC shown in Figure 4.19b is higher than the tensile response of unreinforced SHCC but slightly lower than that of double-layer R/SHCC in terms of mean tensile stress and maximum tensile strain. In comparison with Figure 4.18b a decreasing contribution of the cementitious composite can be observed, which can be described as a softening response. These observations suggest that crack development and fibre bridging were influenced by the position of reinforcement within the specimen. It should be noted that larger crack widths were observed for this type of specimen, which could possibly affect the crack bridging behaviour of the cement-based composite, see Section 4.5.3.

4.5.2.3 Influence of lateral reinforcement and concrete cover

The effect of the concrete cover can be analysed by comparing two different reinforcement ratios ρ, i.e. 0.52 and 0.26 %, with double and single-layer reinforcement as represented in Figure 4.20a. In addition, number and diameter of the rebar varied, hence, the observed results are partly influenced by the effect of different bar diameters and positions within the specimen. A comparison of the stress-strain curves between double- and single-layer reinforcement reveals changes in the transition from the un-cracked to the cracked stage. Specimens with symmetrical double-layer reinforcement and small concrete cover exhibit a more distinctive "point" of first cracking. In contrast, specimens with central reinforcement showed a gradual transition from the un-cracked to the cracked stage. This behaviour may be a result of increased eccentricities as a more pronounced strain gradient across the specimen could be observed in case of central reinforcement (cf. Figure 4.17). However, in contrast to unreinforced SHCC, the reinforcement contributed to the redistribution of tensile stresses and effectively prevented the exceeding of SHCC tensile strength on the casting side, which was subjected to higher tensile strain. The stabilising action enforced on the reinforcement may have contributed to the early failure of specimen 02D20 by local "overstretching" of the reinforcement.

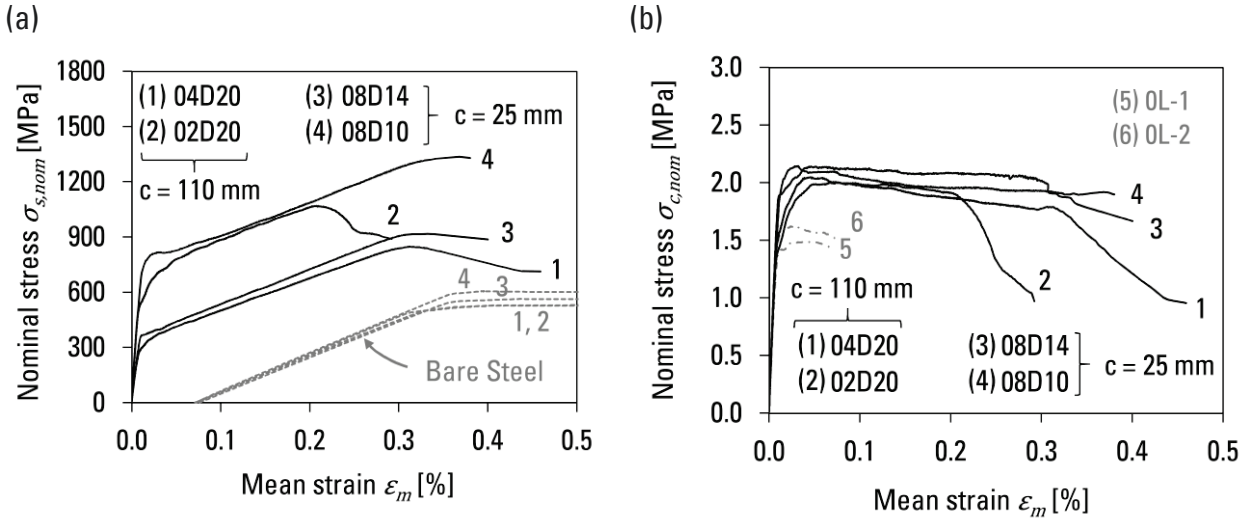

Figure 4.20: Comparison of single- and double-layer reinforced tensile elements of similar reinforcement ratios including (a) steel stress-strain response and (b) isolated stress-strain response of SHCC

Specimens with lateral reinforcement, e.g. (3) and (4), experienced slightly higher nominal steel stresses than those without. Such behaviour was expectable since the lateral reinforcement causes a reduction of the net SHCC surface area and consequently lower tensile forces carried by SHCC. However, no influence of lateral reinforcement was observed on the crack formation process, which will be further discussed in Section 4.5.3. In general, these results suggest that lateral reinforcement has a minor influence on the load-bearing behaviour of R/SHCC elements.

4.5.2.4 Influence of size

The testing of unreinforced SHCC elements allows the comparison of the tensile load-bearing behaviour of structural size elements with that of SHCC at the material level. Figure 4.21 shows the tensile stress-strain behaviour of the unreinforced SHCC slab in comparison to that of the uniaxial tension test on dumbbell specimen from laboratory (a) and concrete plant mixes (b).

Differences can be found for the stress at first cracking and tensile strength, as well as the strain capacity reached before specimen failure. The first cracking stress of the large slabs experiences a reduction of approximately 50 % in comparison to the corresponding values obtained on small dumbbell specimens. The loss in strength can partly be related to the influence of the production process, which becomes obvious when comparing Figure 4.21(a) and (b). However, a large portion of the lower stress level can be traced back to the effect of non-uniform strain distribution and the resulting eccentricities as discussed in Section 4.5.1.3.

In addition, ultimate strain capacity significantly decreases, while multiple cracking becomes much less pronounced. For large elements, a small yielding plateau can be observed before the stress-strain curve shifts to a softening behaviour followed by failure shortly after. It should be noted that the mean strain of these small and large specimens was calculated from the displacement measured by LVDTs with different gauge lengths. Even though, the strain capacity is always influenced by the gauge or specimen length, this highlights the overall effect of specimen dimensions on the load-deformation behaviour.

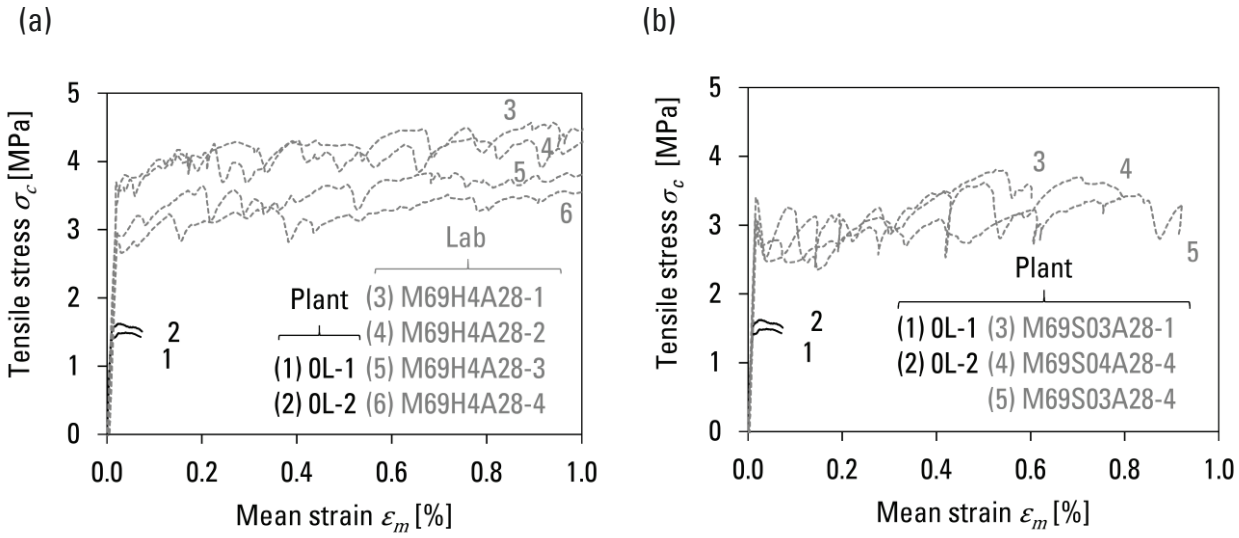

Figure 4.21: Stress-strain behaviour of unreinforced large-scale elements in comparison to that of small dumbbell specimens made in (a) laboratory and (b) concrete plant

4.5.3 Crack formation and development

The formation of cracks and their development were monitored by the digital close-range photogrammetry system ARAMIS produced by GOM Optical Measuring Techniques. Such a system enables the monitoring of the cracking behaviour despite the very high number of narrow cracks and their low visibility for which reason a conventional approach with manual assessment of crack widths and spacing is not practicable. The use of the digital close-range photogrammetry also allowed a continuous monitoring of the crack development without the need to stop the test for the manual counts. Figure 4.22 illustrates the position of the scattered measurement field and a typical example of computed deformations in this field. The results for the strain development only applies for the form side of the specimen. Crack development on the casting side may vary due to "overloading" in case of eccentric loading conditions (cf. Figure 4.15).

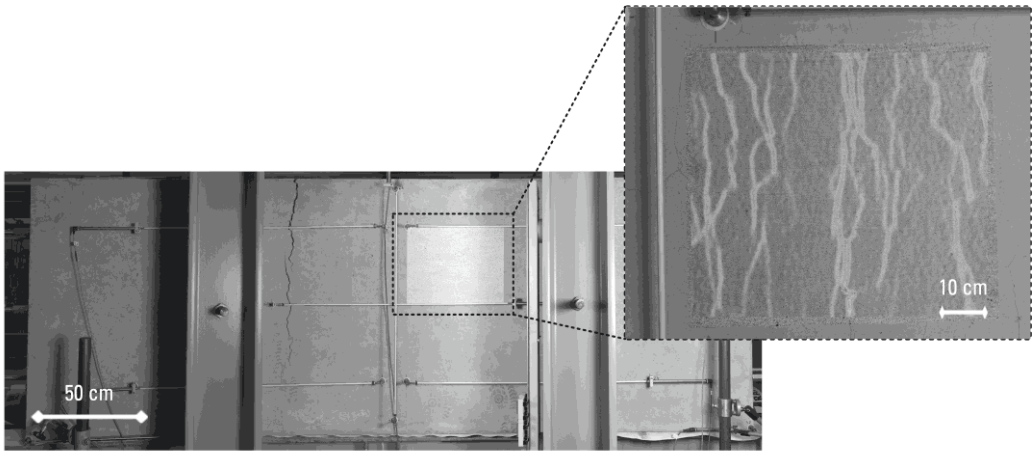

Figure 4.22: Illustration of the optical measurement field and exemplary visualisation of the analysed strain field with highlighted cracking pattern

4.5.3.1 Image analyses

In this system, cameras capture pictures of the surface of the specimen during testing. The pictures can be used to derive strain fields as a basis for calculation of displacements at any given point of the field. A similar setup as used in previous studies (see e.g. [3, 71, 149]) was applied. The setup contained a high-resolution camera, positioned at a distance of approximately 1000 mm from the specimen. At this distance and given the maximum camera resolution of 4032 px x 3024 px, it was possible to observe an area of approximately 400 x 300 mm².

The observed area was prepared with a white ground coat and black spray paint, which creates a stochastic pattern on the surface. During the testing pictures of the spray pattern were continuously captured with a time interval of 60 s while the trigger signal of the camera was recorded to synchronise the pictures with the corresponding load levels.

The recorded data including 2D coordinates and displacements was analysed using automated algorithms for the continuous interpolation of strain fields. The obtained data can be used to visualise the strain development, which is presented in Annex D or exported into standard formats for further investigation. The visualisation of different stages during the experiment can be used for a qualitative interpretation of the crack development.

The calculation algorithm of the ARAMIS system divides the observed picture area into multiple facets, which create a grid on the surface. In this study, a facet size of 15 by 15 pixels with a 2-pixel overlap was selected, which was found to be a good base for deformation analyses of SHCC in previous studies [120]. With a resolution of 200 dpi, the total area of one facet covers an area of approximately 1.9 x 1.9 mm², which results in a total count of 260 x 210 facets. Each facet is recognised by the ARAMIS system based upon their unique colour characteristics. The high contrast and the randomness of the spray paint ensured the recognition and the tracing of each facet during different loading stages.

The continuous recognition of the facet position was used to determine the displacement of the facets for each stage relative to the reference stage, i.e. the unloaded specimen. Since the integrated ARAMIS functions do not provide the possibility of an automated calculation of crack development including crack width and crack spacing a macro-based algorithm was developed for the analysis of the ARAMIS data.

The algorithm made use of pre-defined section lines, which contain coordinates calculated from the grid points for each facet crossing a section line. The calculated data included coordinates for the undeformed state $l_0(x_i)$ along with those for the deformed state $l_i(x_i)$ for each section line. The coordinates for the un-deformed and deformed states of these section lines were exported for each loading step and used to calculate the crack widths and crack distance.

The divergence between the original distance l_0 and the "deformed distance" between two adjacent grid points l_i on the section line was used to calculate the deformation between two points Δl_i as expressed in Eq. (4.14).

$$\Delta l_i = l_i - l_0 \tag{4.14}$$

with

$$l_0 = l_0(x_{i+1}) - l_0(x_i) \tag{4.15}$$

$$l_i = l_i(x_{i+1}) - l_i(x_i) \tag{4.16}$$

A crack was identified by a deformation onset of $\Delta l_i \geq 25\ \mu m$. Values below this strain were found mostly measure "noise" and elastic strain. If neighbouring facets indicated a crack, the values were added to each other until a maximum number of six facets was achieved. Hence, a multiple count of the same crack, especially in stages with high strains and large deformations, could be avoided.

$$w_{cr,j} = \sum_{i}^{i+4} \Delta l_i \tag{4.17}$$

with $\Delta l_i \geq 25\ \mu m$

The crack widths on each section line were used to compute the number of cracks $n_{cr,j}$ and their crack opening displacement $w_{cr,j}$ during each loading step. The distance between cracks was calculated by the difference between the coordinates to the position of the neighbouring crack (previously considered).

$$s_{cr,j} = l_{cr,j+1}(x_{cr,j+1}) - l_{cr,j}(x_{cr,j}) \tag{4.18}$$

This process was repeated for each section line. Altogether five section lines were used in the calculation algorithm as a basis to calculate the facet displacement. This procedure allowed to obtain the statistical distribution of the resulting crack widths, crack distances and the development of both parameters during the loading of the element. The results, especially regarding the number of cracks and their position, could be verified by comparison to the automated visualisation images of the ARAMIS system. Hence, the deformation onset Δl_i was chosen in good agreement to the distance and resolution of the recorded images.

4.5.3.2 Surface crack development

Figure 4.23 shows a detailed analysis of the crack propagation for specimen 08D16 on the form side of the specimen. In this case, the experimental data was analysed with an emphasis on the stochastic crack parameters, i.e. maximum, minimum and mean values, as shown in Figure 4.23a for crack spacing and in Figure 4.23b and c for crack widths. The results of the remaining tests can be found in Annex D.

It can be observed from Figure 4.23a that crack spacings range between approximately 10 and 350 mm at the beginning of crack development, while the maximum and average crack spacings decrease with continuous cracking. The large deviation of the measured crack spacing can be related to the non-continuous path of the cracks, i.e. cracks that partially split, which cause small crack distances, or cracks that stop, which causes a jump of the crack spacing on the concerned section line. At the final load stage crack spacings range between approximately 10 and 100 mm.

The crack width development in Figure 4.23c shows a continuous increase of the average crack width with changing deviations of the maximum and minimum values. Since only the maximum crack width on each section line was captured with this method, these curves can be directly linked to the largest crack of the analysed crack set. The minimum and maximum values are a result of the crack width distribution along one crack path, which is found to vary at each intersection with one of the five section lines. The crack width of the largest crack ranges between 120 µm < $w_{cr,max}$ ≤ 210 µm along its crack path at the final load stage, i.e. before failure of the specimen.

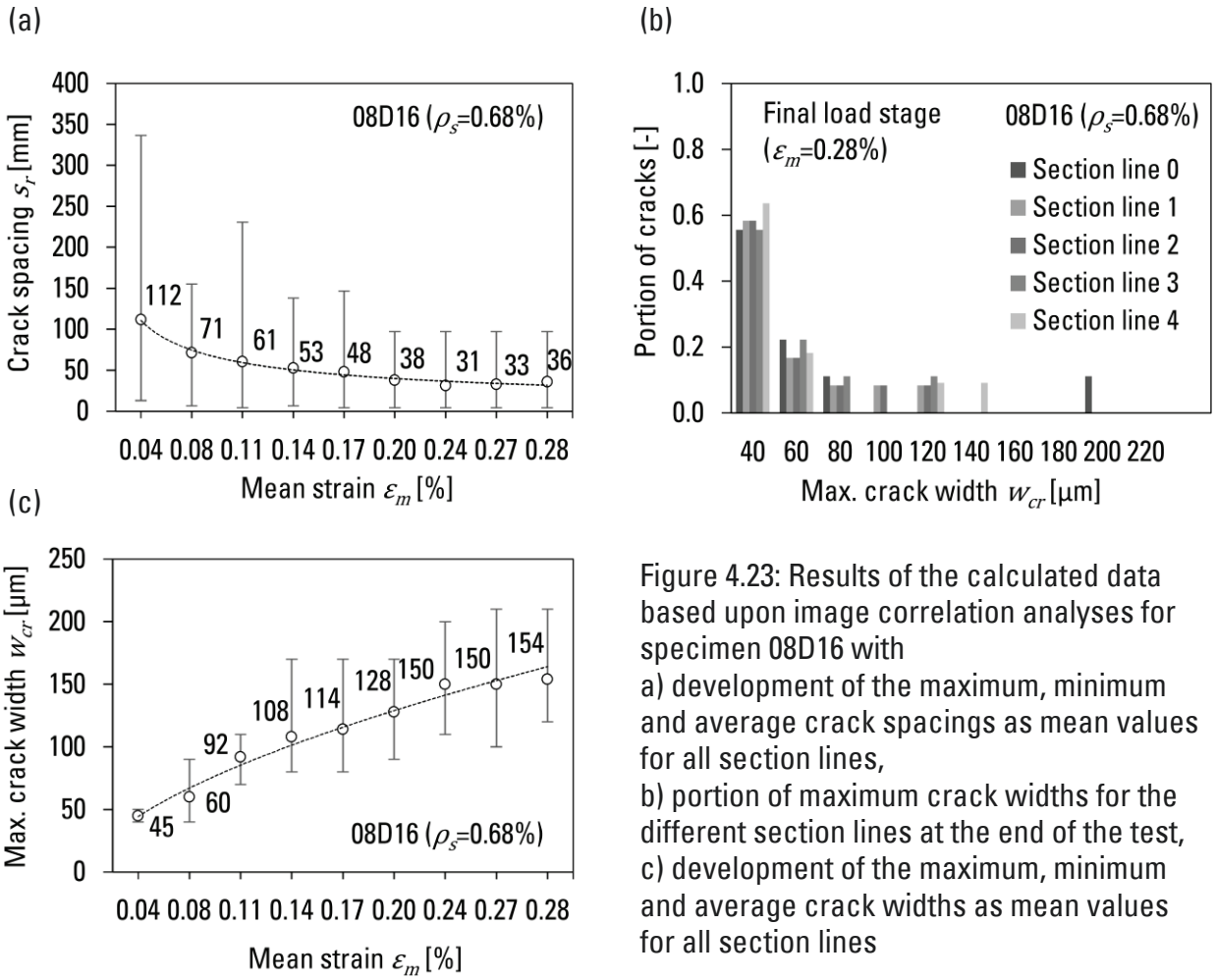

Figure 4.23: Results of the calculated data based upon image correlation analyses for specimen 08D16 with
a) development of the maximum, minimum and average crack spacings as mean values for all section lines,
b) portion of maximum crack widths for the different section lines at the end of the test,
c) development of the maximum, minimum and average crack widths as mean values for all section lines

Figure 4.23b represents the distribution of crack widths along each section line. In general, the variation between the section lines is found to be relatively low. The maximum crack opening w_{cr} of 200 µm appears only in one section line. These results indicate that the crack width substantially varies along an individual crack path and that the strain capacity of SHCC may be locally exceeded at a certain region.

In the paragraph above it was shown based upon the example of one specimen that the random crack development underlies large scatter. However, when comparing the mean values of the remaining test series the same tendencies could be observed. Hence, mean values are chosen as reference of the crack characteristic to compare the crack development of the remaining specimen. Additionally, the relatively small size of the measurement field in comparison with the entire specimen size needs to be considered. In this case, the resulting values can only be interpreted as average values for the monitored section. However, due to the small crack spacing and sufficient number of cracks, the results can be treated as representative for the entire element[32].

[32] The results were also verified by manual crack counts and measurements, which showed a good consistency of the automated analyses of the crack pattern.

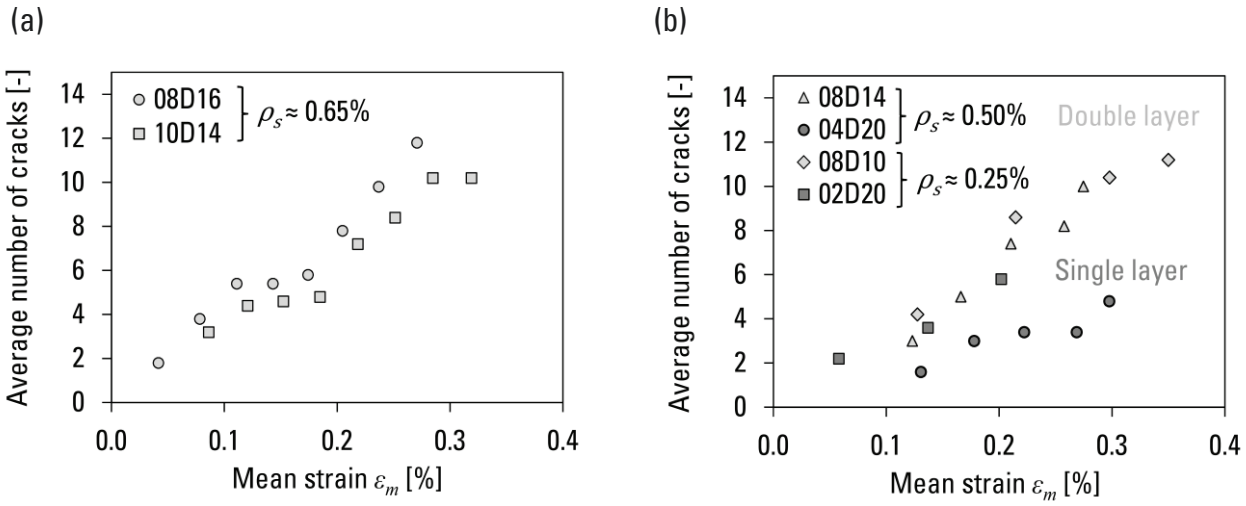

Figure 4.24: (a) Number of cracks for elements with similar reinforcement ratios but different bar diameters and (b) comparison of crack development in elements with large and small concrete cover thicknesses for different reinforcement ratios

Figure 4.24 shows the development of the cracks for each of the specimen as the maximum crack width, average crack spacing and number of cracks calculated for the corresponding mean strain of the element. For a better comparison, the results are sorted in groups of similar reinforcement ratios. The analysis of the crack development started after the stress at first cracking was reached.

The number of cracks derived as an average value from all five section lines for two different reinforcement layouts with equal rebar content is shown in Figure 4.24a. It becomes apparent that with increasing loading of the specimen, the number of cracks increases, which subsequently leads to a decrease of crack spacing. Sudden decreases in the number of cracks are a result of parallel cracks merging into one crack which leads to a lower number of cracks on specific section lines.

Figure 4.24b shows that the single-layer reinforced elements with a high concrete cover were found to experience fewer cracks than specimens having a smaller concrete cover and larger number of bars but similar reinforcement ratio, which implies larger crack widths since the total mean strain is equal for both cases. These observations are confirmed by the crack width development as shown in Figure 4.25. Hence, the average value of the maximum crack width is influenced by the content of reinforcement and the distance from the reinforcement to the SHCC surface (as well as, most likely, on the bar diameter).

By comparing the maximum crack openings of the single- and double-layer reinforced specimens, a limitation of the maximum crack opening could be observed for elements with small concrete covers, i.e. double-layer reinforcement. Single-layer reinforced elements with large concrete cover reach approximately twice the crack width as comparable specimens with small concrete cover.

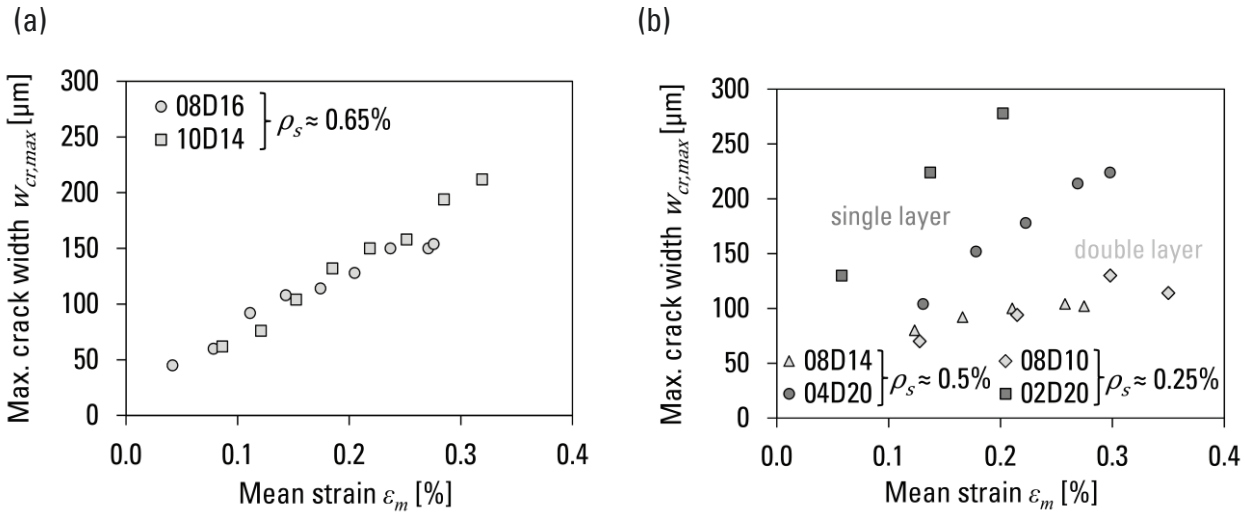

Figure 4.25: (a) Maximum crack width development in elements with similar reinforcement ratios but different bar diameters and (b) comparison of maximum crack width development in elements with large and small concrete cover thicknesses for different reinforcement ratios

Figure 4.25a shows that the rebar diameter has no distinct influence on the maximum crack width development for elements with double-layer reinforcement. However, when comparing the effect of reinforcement content, two opposing effects can be observed between the double-layer and single-layer element types, as shown by Figure 4.25b. While the double-layer reinforced specimen, i.e. 08D10 and 08D14, show no explicit differences of maximum crack width, a decrease of crack widths can be observed for the single-layer reinforced elements with increasing rebar content, cf. 02D20 and 04D20. These results suggest that crack width development is more influenced by the reinforcement ratio when concrete covers are large. No cracking within the measurement field could be observed for unreinforced elements due to the low strain development on the form side of the specimen as a result of eccentric loading (cf. Figure 4.16).

4.5.3.3 Internal cracking

Figure 4.26 shows a photograph of the representative cracking pattern inside of the tested specimen in an area unaffected by the macro-crack. The element under investigation was a double-layer reinforced element (08D16) for which the part close to the face side of the element is presented. The section was saw-cut from the specimen and carefully cut in half exposing the reinforcement. The photograph shows a uniform distribution of fine cracks similar to that monitored on the surface of the specimen.

The cracks were found to develop from the rib tips, spreading in transverse direction. Partial longitudinal splitting cracks could be observed as well indicating the activation of shear forces between the reinforcement layers. It can be assumed that due to the close spacing of fine cracks in SHCC only minimal relative displacement occurs between the steel reinforcement and surrounding cementitious matrix.

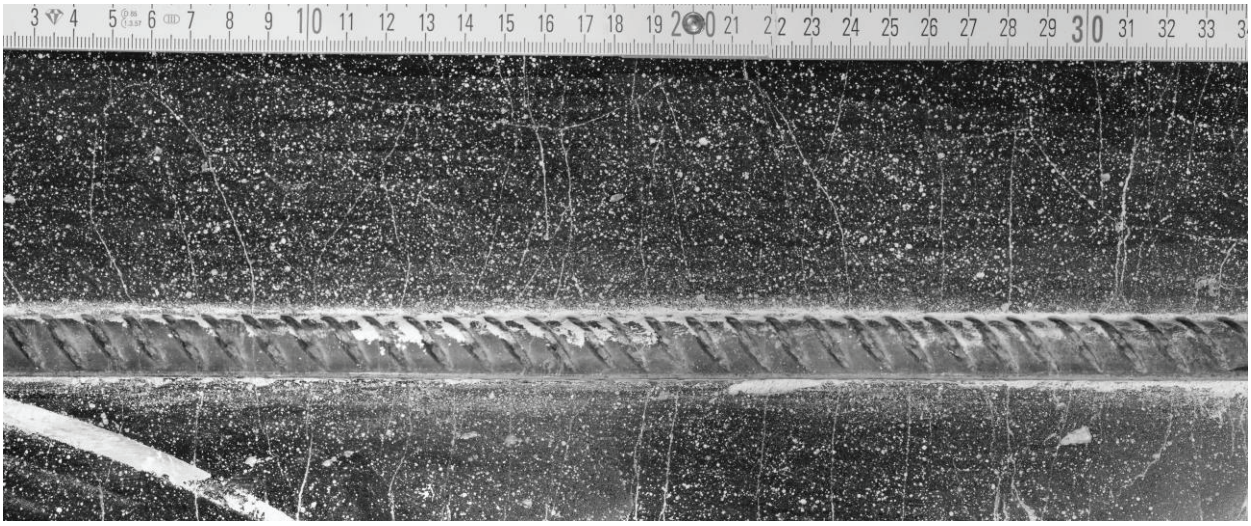

Figure 4.26: Cut of a reinforced specimen with internal cracking after the completed tensile test (colours inverted)

A photograph of the representative cracking pattern around the macro-crack is shown Figure 4.27. Large deformations of the cementitious matrix around steel ribs can be observed along the bond length close to the crack. Additionally, a large number of fine cracks became visible in the vicinity of the macro-crack. This accumulation of fine cracks is possibly a result of plastic strains of the rebar, which occurred during the crack opening. In between the ribs, SHCC was partially crushed and shear failure can be observed, which serves as an indication of pronounced rebar slippage during the macro-crack opening. Hence, interfacial bond strength must have been exceeded either prior to or shortly after the beginning of the macro-crack opening, which would cause a delamination from the steel surface.

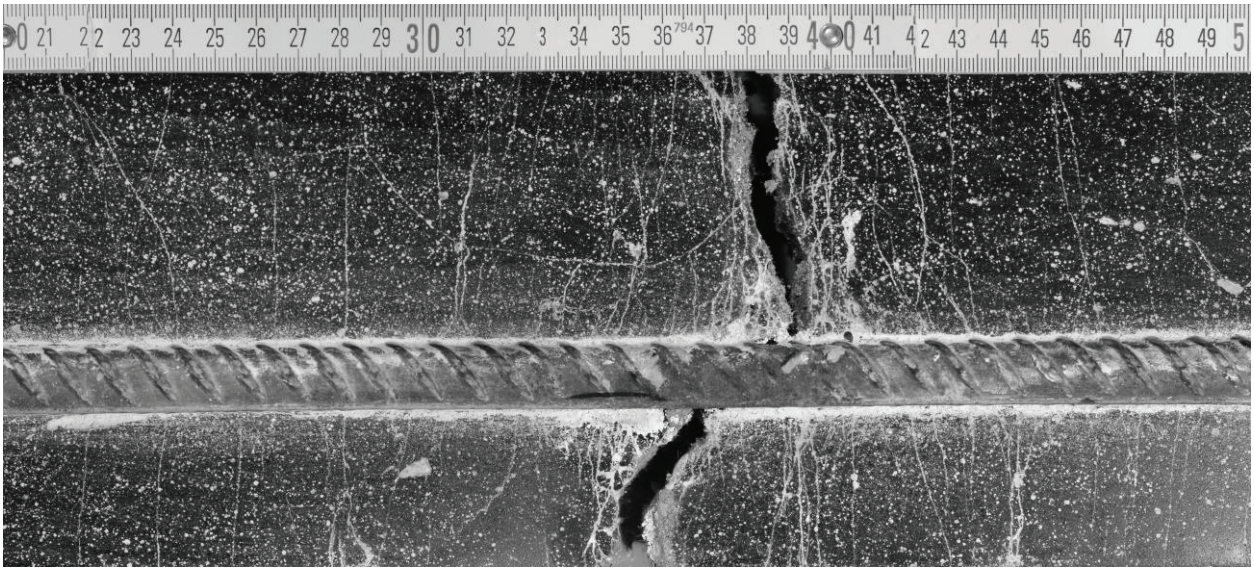

Figure 4.27: Cut of a reinforced specimen with fine cracking and a macro-crack (colours inverted)

It can be concluded that the crack bridging and resulting multiple cracking of SHCC enables similar strains in the cementitious composite and steel rebar, which prevents the development of large macro-cracks before reaching the maximum load. The multiple cracking reduces the loading of the interfacial bond area and subsequently reduces the slip. Bond slip only occurs when the element reaches its load carrying capacity, resulting in a macro-crack opening. Then, SHCC works in strain-softening regime, so that the stress transfer across the crack is considerably reduced. Thus, the tensile forces are partly redistributed to the steel reinforcement. The resulting difference in deformations of SHCC and steel subsequently activates bond interaction.

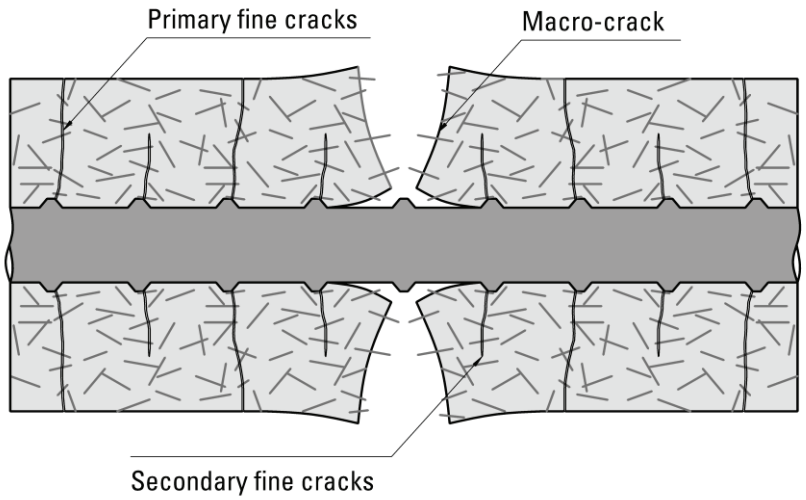

Figure 4.28: Schematic representation of a cross-section displaying the internal cracking and concrete deformation in the vicinity of a transverse macro-crack in according to Goto [48] and adapted to the effect of fibres

4.5.4 Effect of steel deformation behaviour

The observation of surface deformations allowed analysing how the interaction of steel reinforcement and SHCC affects the crack development and the tensile response of the reinforced tension member. It was found that SHCC experiences pronounced multiple cracking, which enables SHCC to substantially contribute to the load-carrying capacity. Furthermore, the results showed a dependency of the crack distribution and opening on the rebar diameter and arrangement of reinforcement. Particularly when the tensile stresses of the reinforcement reach the yield strength R_e, which causes local plastic deformations of the steel reinforcement, the cracking behaviour of SHCC seems to be affected. This leads to the conclusion that the characteristic behaviour of steel during the plastic yielding phase is an important parameter for the global load-bearing behaviour of the reinforced tension member. Hence, it is necessary to analyse local deformations of the steel reinforcement within the specimen. Figure 4.29 shows the strain measured by strain gauges along one rebar embedded into the specimen at different load stages.

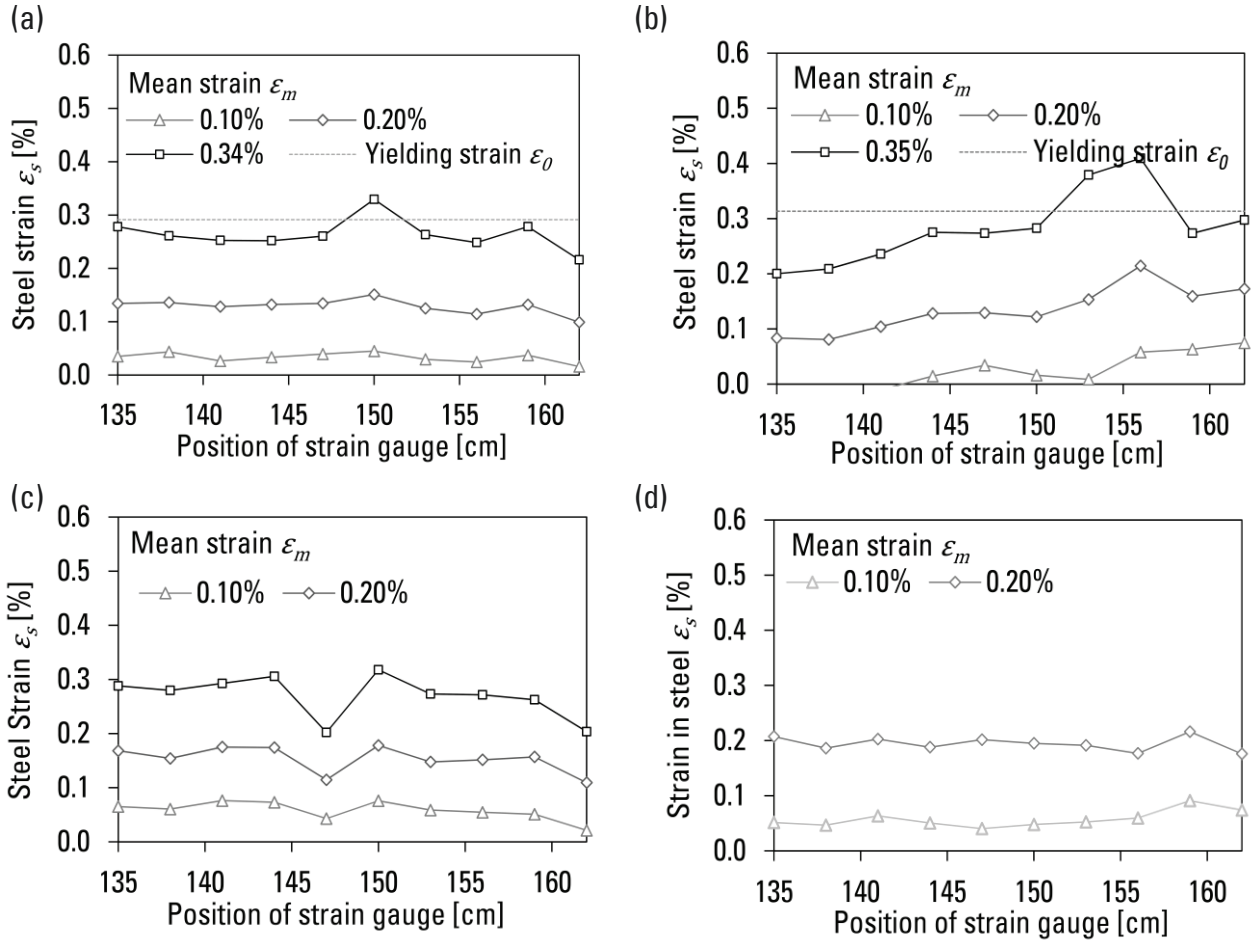

Figure 4.29: Results of strain gauge measurement on steel reinforcement for reinforcement ratios of $\rho \approx 0.50$ in specimens (a) 08D14 and (b) 04D20 as well as reinforcement ratios of $\rho \approx 0.25$ in specimens (c) 08D10 and (d) 02D20[33]

Herein, the maximum global tensile strain ε_m equals the total strain at the maximum testing load shortly before rupture. Shrinkage of the R/SHCC specimens causes a compressive pre-loading of the steel reinforcement (cf. Figure 4.11), which needs to be considered when analysing the results of strain gauge measurements. In this case compressive strains due to shrinkage pre-loading can be considered by subtraction of the total shrinkage strain $\Delta\varepsilon_{cs}$ from the measured steel strain according to Table 4.3.

In contrast to previous findings by MORENO et al. [110, 111], who observed a pronounced non-uniform strain distribution with one predominant crack, a nearly uniform strain distribution was found in the investigation at hand. However, steel strains were only presented for global tensile strains ε_m above 0.5 % (cf. Figure 2.21b), while the specimen analysed in the present study at hand exhibited fracture at lower tensile strain ε_{sm} of 0.20 to 0.35 %.

[33] The yielding strain ε_y.of the reinforcing steel was derived from direct tension tests on steel rebars for diameters d_s of 10 and 14 mm, cf. Section 2.2.1.

Figure 4.29a and b show, that in both cases the yielding strain of the steel reinforcement ε_0 was reached. Furthermore, specimen 08D10 experienced partly steel strains exceeding the yielding strain of the steel reinforcement ε_0. Even though no macro-cracks were observed in the area of strain measurements, local strains of the steel reinforcement reach high levels and likely plasticisation. Since only a small area of the reinforcement was monitored, it can be assumed that these processes may occur at multiple regions over the entire element length. This suggests that local steel strains exceed the global tensile strain of the specimen and exhibit plastic deformations even before the global yielding stress on the structural level is reached. Such local increase of plastic steel strains subsequently enforces a local elongation of SHCC combined with an enhanced crack development within a concentrated area, as shown in Figure 4.27.

The occurrence of plastic deformations in steel bars may accelerate the deterioration of the cementitious matrix around steel ribs. The additional contraction of the steel cross-section during the hardening leads to a further reduction of the mechanical interlocking. This process continues until the local maximum strain capacity of SHCC is reached, which eventually causes a macro-crack opening. At this point, the fibre bridging force decreases due to the softening behaviour of SHCC in the post-peak stage, while the excess of tensile force is transferred to the steel reinforcement. This local load redistribution enforces a higher loading and ultimately causes an early strain-hardening of the steel reinforcement, as previously observed by MORENO et al. [110, 111].

JUNGWIRTH [61] suggested that for ductile steel-reinforced HPFRC, this process always occurs when the tensile strain of the reinforced composite reaches the yielding strain ε_0 of the reinforcement. This could be confirmed for SHCC, which shows a denser crack pattern than HPFRC for all tested specimens. Hence, the global tensile force can only be carried at the structural level as long as the remaining load-bearing capacity of the reinforcement exceeds the fibre bridging stress released during the macro-crack opening. However, for conventional ductile steel reinforcement, this is only the case for low global strain levels or reinforcement exceeding the minimum reinforcement criteria (cf. Section 5.3.2).

4.6 Summary

This chapter has presented an experimental investigation on the structural behaviour of steel-reinforced and unreinforced SHCC slabs under tensile loading. Goal of this investigation was to determine the global and local load-deformation behaviour, which included analysing the crack development on the concrete surface and the local steel strains. This was achieved by variation of the bar diameter, steel content, as well as the position of the rebar and concrete cover, respectively. The results showed that SHCC substantially contributes to the load-carrying capacity of the reinforced tension members after the formation of the first cracks, which leads to a significant increase of the tension-stiffening effect. The contribution of SHCC to the global load-bearing behaviour continues until the yielding strain of the reinforcement is reached.

In case of unreinforced elements, a significant reduction of ductility and strain-hardening could be observed. Hence, conventional steel reinforcement contributes to a robust and stable crack development in the elastic steel stage. The resulting SHCC strength for large-scale specimens was found to be considerably lower than that derived in material testing on small dumbbell specimens. These differences can be partly attributed to variations of the matrix properties, while mainly they should be attributed to the effects of eccentricities. The analysis of the experimental results leads to the following conclusions:

- double-layer reinforcement contributes to a uniform distribution of tensile stresses across the element width which reduces the effects of eccentricities;
- single-layer reinforcement enhances the distribution of tensile stresses and multiple cracking of SHCC, but it can only achieve full steel activation when higher reinforcement ratios are used;
- the tensile behaviour of unreinforced elements is dominated by the effects of non-uniform strain distribution caused by non-uniform shrinkage and load eccentricities; and
- the maximum tensile stress, which is reached at the upper (casting) side of the specimens is almost equivalent to SHCC strength as measured on dumbbell specimens.

A detailed analysis of the contribution of SHCC to the global load-deformation response showed that:

- the reinforcement ratio influences the contribution of SHCC;
- reinforcement substantially contributes to reducing eccentricities caused by the presence of pre-deformations or non-uniform shrinkage; and
- lateral reinforcement has a neglectable effect on the load-bearing behaviour of R/SHCC elements.

The crack formation and development was analysed by means of digital close-range photogrammetry. The analysis of the data of the surface deformations leads to the following conclusions:

- the concrete cover influences the crack development where the number of cracks is found to be higher for small concrete covers;
- specimens with small concrete cover subsequently experience smaller maximum crack widths; and
- the reinforcement ratio has only moderate influence on the number of cracks and the crack width in comparison to the influence of the concrete cover.

The strain gauge measurement on the reinforcement showed that local steel strains exceed the global steel strain and that steel bars exhibit plastic deformations even before the global yielding stress over the total rebar length is reached. This serves as an indication of an early localisation of plastic deformation of steel reinforcement, which facilitates a macro-crack opening and eventually lead to specimen failure.

5 Derivation of constitutive relations

5.1 Introduction

The previous chapters covered the experimental investigations on the material behaviour of SHCC and steel as well as their interaction on the material and structural level. The complexity of the tensile behaviour of SHCC on the micro-mechanical level requires a certain degree of simplification when modelling the load-deformation behaviour of R/SHCC elements under tension. Therefore, the experimentally obtained results will be discussed regarding their implications on constitutive modelling. A schematic presentation of the approach is given in Figure 5.1. An approach similar to the experimental investigation was chosen by considering the isolated SHCC, steel and their bond behaviour as well as modelling the behaviour of the reinforced element. Each part of the reinforced composite, i.e. steel and SHCC, is idealized as spring element which is characterized by the individual non-linear material behaviour. Both materials are connected by an interface element showing a rigid-plastic bond behaviour.

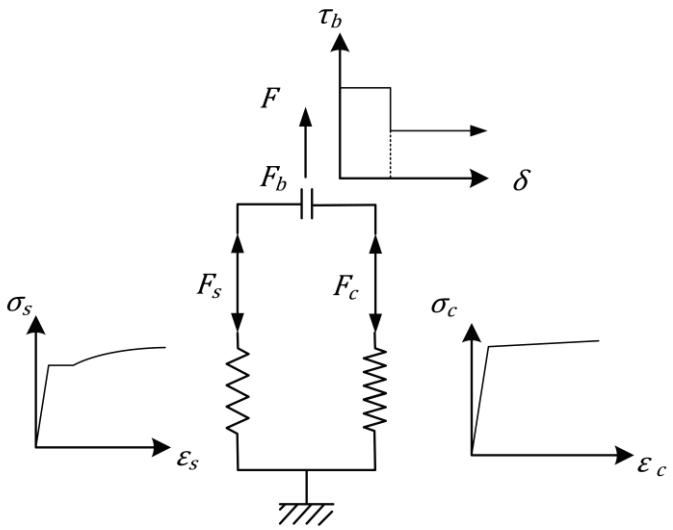

Figure 5.1: Schematic description of the composite behaviour of R/SHCC element, adapted from NOGHABAI [121]

5.2 Constitutive relations of the material behaviour

Material models allow a description of the mechanical behaviour, which can be used for example for the design of a structural member. These models are usually based upon constitutive relationships, which aim to predict the load-deformation response under defined loads. In order to investigate the behaviour of a reinforced structural member, the properties of the individual components and their interaction need to be determined. Therefore, simple material models will be presented and adapted to the results of material testing. A mechanical model for the calculation of the tensile behaviour of R/SHCC elements will be then derived on this basis.

5.2.1 Steel reinforcement

In reinforced concrete structures, steel rebar is primarily loaded in longitudinal direction, which correspond to a uniaxial loading. To evaluate the steel behaviour under such loading conditions in structural design, it was found practical to formulate an idealised stress-strain relationship. In this case, the degree of simplification may be chosen in accordance to the required accuracy of the model.

According to CEB-FIP Model Code 2010 [41], a formulation originally proposed by MENEGOTTO and PINTO [107] may be used as an idealization of the stress-strain relationship for various steel types. In this approach, the non-linear function is expressed by Eq. (5.1):

$$\frac{\sigma(\varepsilon_s)}{\sigma_0} = b\left(\frac{\varepsilon_s}{\varepsilon_0}\right) + \frac{(1-b)\left(\frac{\varepsilon_s}{\varepsilon_0}\right)}{\left(1+\left(\frac{\varepsilon_s}{\varepsilon_0}\right)^R\right)^{1/R}} \tag{5.1}$$

with
- ε_s steel strain
- σ_0 yielding stress of the reinforcement
- b ratio of the final to the initial stiffness
- ε_0 yielding strain of the reinforcement
- R parameter for the transition from elastic regime to post-yielding slope.

In this case the stress-strain relationship is approximated with the initial stiffness E_s for the elastic deformation regime and the stiffness $b \cdot E_s$ extending to the plastic deformation regime. The transition is described with a hyperbola that tangents the asymptotes. The point where the asymptotes meet corresponds approximately to the yielding stress σ_0 and strain ε_0 of the reinforcement. The shape of the transition between the two asymptotes is defined by the parameter R, which can be calculated using Eq. (5.2):

$$R = R_0 - \frac{a_1 + \varepsilon_u}{a_2 + \varepsilon_u} \tag{5.2}$$

with
- R_0 parameter to represent the first loading curve
- a_1 first parameter to represent the Bauschinger effect
- a_2 second parameter to represent the Bauschinger effect
- ε_u the ultimate strain before steel rupture

The parameters a_1, a_2 and R_0 should be selected in agreement to the yielding and hardening curve of the steel reinforcement. Figure 5.2a depicts a schematic representation of the non-linear stress-strain relationship based on the Menegotto-Pinto formulation.

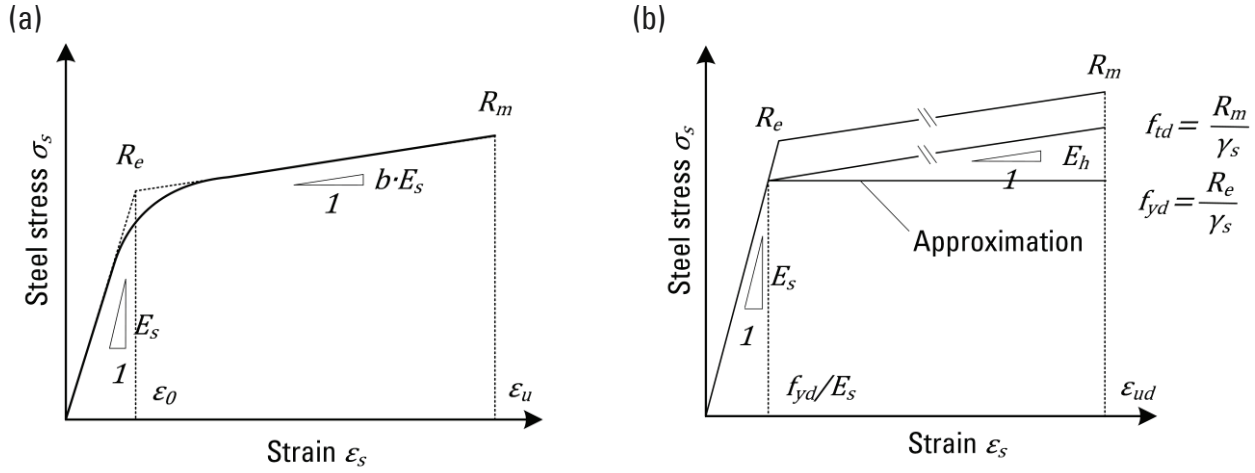

Figure 5.2: Schematic representations of an idealised material model for steel reinforcement with (a) non-linear material model according to MENEGOTTO and PINTO [107] and (b) bilinear model with and without hardening of the steel

The load-bearing behaviour of steel reinforcement can also be expressed by a simple bilinear stress-strain relationship as shown in Figure 5.2b, which depicts a bilinear stress-strain response as well as an ideal elastic-plastic approximation. An ideal elastic-plastic approximation of the stress-strain response is found to be sufficient for conventional R/C applications since it offers simple solutions for analytical approaches or reduces computational times in case of numerical calculations. In this case the hardening stage is neglected, which is tolerable in case of conventional R/C as the difference between yielding and tensile strength ($R_m - R_e$) remains as a structural reserve. However, a higher accuracy can be achieved by a bilinear simplification of the actual stress-strain relationship with an idealised hardening stage. In this case the stress-strain response can be calculated with Eq. (5.3):

$$\begin{aligned} \sigma_s(\varepsilon_s) &= E_s \cdot \varepsilon_s && \text{for} && \varepsilon_s \leq \varepsilon_0 \\ \sigma_s(\varepsilon_s) &= R_e + E_h \cdot (\varepsilon_s - \varepsilon_0) && && \varepsilon_0 < \varepsilon_s \leq \varepsilon_{ud} \end{aligned} \tag{5.3}$$

with $$E_h = \frac{(R_m - R_e)}{(\varepsilon_{ud} - \varepsilon_0)}$$

ε_{ud} design value for strain at maximum steel stress

Parameters required for the modelling of the steel behaviour are the modulus of elasticity E_s and the yield strength R_e as well as ductility parameters, i.e. characteristic strain at maximum force ε_{ud} and characteristic ratio tensile strength to yield strength (R_m/R_e). These parameters are usually defined by means of standardised material tests, which are implemented into design guidelines as a basis for structural design calculations.

Figure 5.3 shows a comparison between the experimentally determined load-deformation behaviour derived from testing of steel bars (cf. Section 3.4.2) and the non-linear model based upon the Menegotto-Pinto formulation.

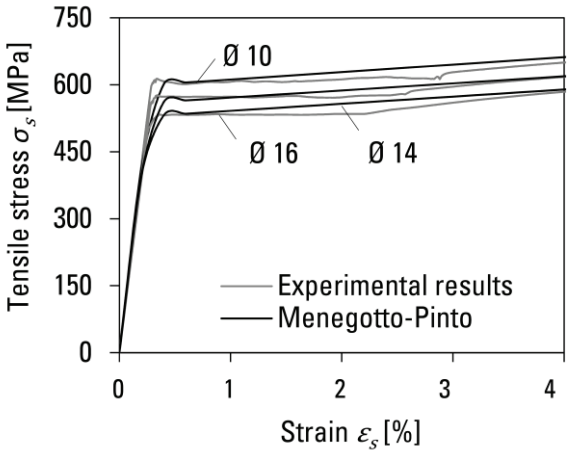

Model parameters for steel rebar			
E_{s0}	210 GPa	b	0.008
a_1	18.5	R_0	20
a_2	0.0015	ε_u	8 %
c_1	715	d_1	765
c_2	-11.4	d_2	-8.2

Figure 5.3: Experimental results for steel bars and the proposed model according to MENEGOTTO and PINTO [107] adapted by the experimentally determined parameters

In case of the hardened and tempered steel bars under investigation, the approximation is found to reproduce the experimentally observed behaviour of reinforcing steel bars reasonably well. Since the experimental results revealed dependencies of the yielding and tensile strength on the rebar diameter, values for R_e and R_m were determined by linear regression of the rebar test results, cf. Table 3.9.

$$R_e = c_1 + c_2 \cdot d_s$$
$$R_m = d_1 + d_2 \cdot d_s \tag{5.4}$$

with d_s diameter
c_1, c_2 influence factors of the bar diameter on yield strength
d_1, d_2 influence factors of the bar diameter on tensile strength.

The determination coefficients, i.e. the R^2 values, between the experimental results and the proposed values for the parameters c_1, c_2 as well as d_1, d_2 are 0.99, indicating the experimental results fit the proposed curve very well.

5.2.2 SHCC

For SHCC special attention has to be given to the strain-hardening behaviour in tension. The tensile strength and large strain capacity of SHCC needs to be considered for an effective utilisation of material properties in the design of SHCC members. A non-linear model was suggested by VOREL and BOSHOFF [146] using Hermit functions to define hardening and softening sections of the tensile stress-strain response of SHCC. The objective of this approach was to develop a material model that can be used for large-scale simulations of structural components with SHCC under different types loading conditions.

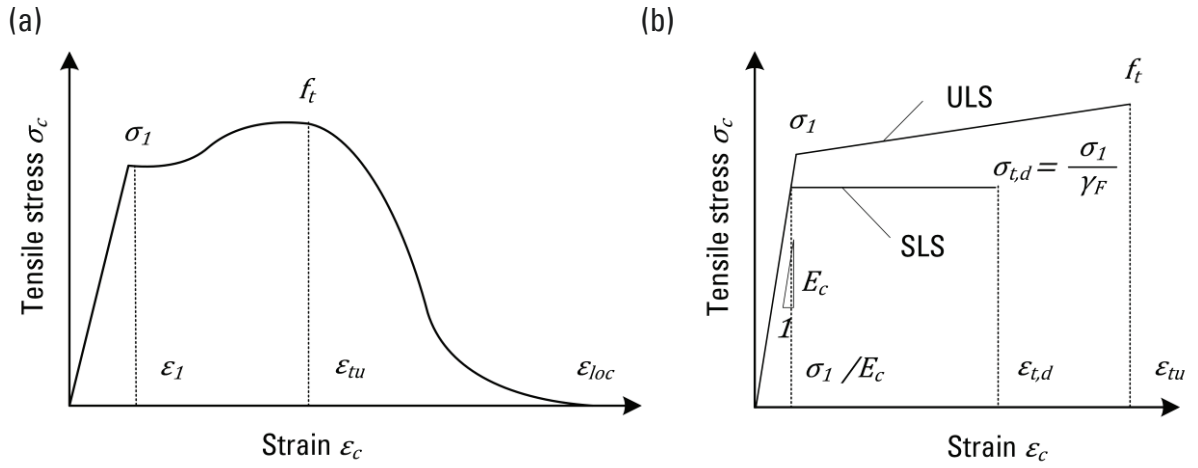

Figure 5.4: Schematic representation of the (a) material model according to VOREL and BOSHOFF [146] and (b) bilinear approach proposed by MECHTCHERINE [98]

Figure 5.4a depicts the uniaxial stress-strain curve, which corresponds to the mathematical representation of the constitutive model. The initial elastic part is assumed to be linear, whereas the non-linear part after the first cracking is defined by Hermit functions. The model parameters must be defined using experimental data. One disadvantage is the influence of the specimen length on the softening branch of the stress-strain response. In this case the formulation is only valid for a characteristic element length which equals the length of the specimen used for determination of the parameters, which limits the applicability of such a model.

$$\begin{aligned}
&\sigma_c(\varepsilon_c) = E_c \cdot \varepsilon_c && 0 \le \varepsilon \le \varepsilon_1 \\
&\sigma_c(\varepsilon_c) = \sigma_1 + (f_t - \sigma_1)\left[-2\left(\frac{\varepsilon - \varepsilon_1}{\varepsilon_{tu} - \varepsilon_1}\right)^3 + 3\left(\frac{\varepsilon - \varepsilon_1}{\varepsilon_{tu} - \varepsilon_1}\right)^2\right] && \varepsilon_1 < \varepsilon \le \varepsilon_{tu} \\
&\sigma_c(\varepsilon_c) = f_t\left[2\left(\frac{\varepsilon - \varepsilon_{tu}}{\varepsilon_{loc} - \varepsilon_{tu}}\right)^3 - 3\left(\frac{\varepsilon - \varepsilon_{tu}}{\varepsilon_{loc} - \varepsilon_{tu}}\right)^2 + 1\right] && \varepsilon_{tu} < \varepsilon \le \varepsilon_{loc}
\end{aligned} \quad \text{for} \quad (5.5)$$

For design purposes, the load-bearing behaviour of SHCC can also be expressed by a simple bilinear stress-strain relationship as shown in Figure 5.4b. According to MECHTCHERINE [98], such an elastic-plastic relationship can be applied for modelling the tensile behaviour in ULS design while a bilinear approach with strain-hardening can be used to calculate internal forces and deformations in SLS design. In this case, the analytical parameters must be obtained through fitting of numerical results or laboratory testing. The material parameters of relevance for both constitutive models are the modulus of elasticity E_c, the stress at first cracking σ_1, ultimate tensile strength f_t and the ultimate tensile strain ε_{tu}. For SLS design the material parameters need to be adapted to by adequate design factors to achieve the desired level of safety. Especially the design value of the strain capacity $\varepsilon_{t,d}$ should be selected carefully to account for the influence of the production process and pronounced shrinkage on the cracking behaviour of SHCC.

The individual stress drops which occur during the development of each fine crack can be neglected since they have a neglectable effect regarding structural analysis. CEB-FIP Model Code 2010 [41] provides a stress-strain relationship based upon a constitutive relationship in uniaxial tension up to the peak stress, i.e. the tensile strength f_t. The multiple cracking stage is analytically described by a bilinear stress-strain relationship according to Eq. (5.6):

$$\frac{\sigma - \sigma_{1,k}}{f_{t,k} - \sigma_1} = \frac{\varepsilon - \varepsilon_1}{\varepsilon_{tu} - \varepsilon_1} \tag{5.6}$$

with $\sigma_{1,k}$ 5% quantile of the stress at first cracking
$f_{t,k}$ 5% quantile of the ultimate tensile strength

Figure 5.5 shows the stress-strain relationship based upon the formulation of Eq. (5.5). The comparison between the experimental results and the chosen model parameters appears to be fairly satisfactory.

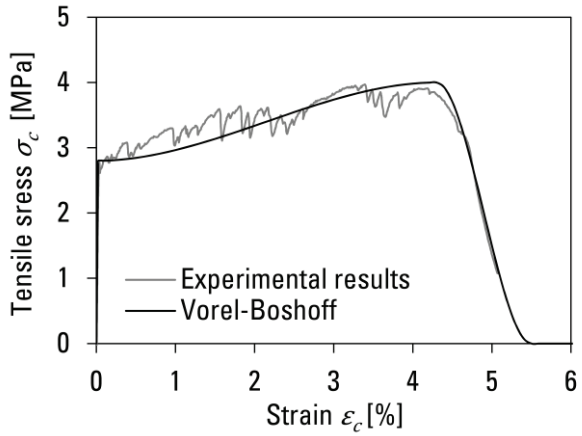

Model parameters for SHCC			
E_{cm}	13 GPa	ε_1	0.02 %
σ_1	2.8 MPa	ε_{tu}	4.3 %
f_t	4.0 MPa	ε_{loc}	5.5 %

Figure 5.5: Experimental result of a laboratory specimen tested at a specimen age of 14 days and the proposed model by VOREL and BOSHOFF [146] adapted to the experimentally determined parameters

5.2.3 Design values

The non-linear material models with its experimentally determined material parameters offer the possibility to be implemented into numerical calculations and achieve high accuracy when applied under consideration of the given boundaries. This approach serves as basis for the modelling of the tensile behaviour of the R/SHCC element given in Section 5.3. However, the application of such models will be most likely limited to research because of the experimental difficulty in performing such experiments. For this reason, some consideration will be provided considering the application of simplified bilinear stress-strain relations according to Eq.(5.3) and (5.6) and the corresponding design values.

For steel reinforcement, the yielding strength R_e and tensile strength R_m are usually specified by the rebar manufacturer according to the steel grade. In addition, CEB-FIP Model Code 2010 [41] suggests an elastic modulus E_s of 200 GPa and a minimum value for the strain at maximum stress ε_{ud} of 5% for a steel with ductility class B and a steel grade with yielding strength R_e < 600 MPa. The partial safety factor according to the semi-probabilistic design concept can be specified depending on the loading conditions with 1.15 for permanent and temporary load combinations or 1.0 for extraordinary load combinations.

For SHCC the stress at first cracking σ_1 and the tensile strength f_t and the strain capacity ε_{tu} need to be specified to develop a bilinear material model. Due to the lack of standardized test methods, design values presently require experimental material testing. Due to the variety of effects that influence the tensile behaviour an adequate design value should be chosen to achieve the desired safety level. Table 5.1 shows partial safety factors for FRC in tension based upon the limit state design concept adapted from CEB-FIP Model Code 2010 [41]. In addition, a differentiation between normal and high quality controlled production processes is proposed with a safety factor γ_F of 1.3. Under consideration of the observed variations in the material properties of SHCC, the more conservative safety factor proposed by the CEB-FIP Model Code 2010 [41] seems to be more appropriate.

Table 5.1: Partial safety factors according to CEB-FIP Model Code 2010 [41]

	ULS	**SLS**
FRC in compression	As plain concrete	
FRC in tension (limit of linearity)	As plain concrete	$\gamma_F = 1.0$
FRC in tension (residual strength)	$\gamma_F = 1.5$	

Possibly the most crucial parameter for the design of SHCC applications is the design value for the tensile strain capacity $\varepsilon_{t,d}$. To this point the determination of the characteristic tensile strain capacity ε_{tu} is only possible by means of experimental investigations. A reliable approach for the analytical determination of the cracking behaviour and the maximum tensile strain ε_{tu} remains in the focus of research and requires further examination. A summary of these approaches was given, for example, by KORB [67]. Therefore, models such models as the ones proposed are independent of the actual number of cracks and their individual crack widths. In addition, the experimental findings of the study at hand indicate that the maximum crack development as well as the related tensile strain capacity are influenced by the production process and the structural size of the tension elements. It could be observed that with increasing element size the strain-hardening behaviour is substantially reduced, which needs to be considered in the design. This study emphasises the need for further studies on the impact of the element size and the multiple cracking on the tensile deformation behaviour of fibre-reinforced cementitious composites.

5.2.4 Bond stress-slip relationship

The modelling of the interfacial bond between steel reinforcement and concrete is essential to calculate anchorage lengths, i.e. pull-out behaviour, and the description of the load-bearing behaviour of reinforced tension members. Such models differ in their degree of simplification, which has an impact on the calculation complexity. BANDELT and BILLINGTON [10] used a model originally proposed by CHAO et al. [21] to describe the pull-out behaviour of steel reinforcement embedded in SHCC, which was adapted to results of experimentally-determined bond-slip curves. Figure 5.6a depicts a schematic representation of the bond-slip relationship based on this formulation.

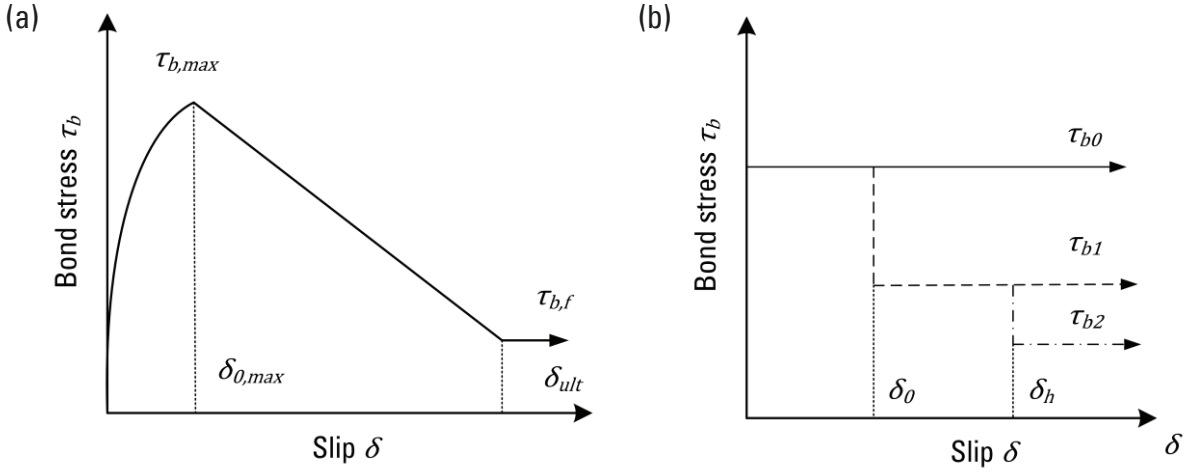

Figure 5.6: Bond stress vs. slip relation proposed for SHCC (a) according to BANDELT and BILLINGTON [10] and (b) ideal plastic model for the stress-slip relationship with linear, bilinear and trilinear material functions adopted from ALVAREZ [8] and SIGRIST [136]

According to this model the initial part of the curve, i.e. the ascending branch, can be described by a power law function according to Eq. (5.7):

$$\tau_b(\delta) = 1.17\tau_{b,max}(\delta^{0.28}) \leq \tau_{b,max} \quad \text{for} \quad \delta \leq \delta_{0,max} \tag{5.7}$$

with $\tau_{b,max}$ maximum bond stress
$\delta_{0,max}$ reinforcement slip at the maximum bond stress.

The descending part of the bond-slip curve is expressed by a linear function from the peak stress to the pull-out resistance is reached at a proposed level of:

$$\delta_{ult} = \delta(0.3\ \tau_{b,max}) \tag{5.8}$$

A simple rigid-plastic bond-slip model can also be used to calculate bond stress-slip development of the reinforcement embedded into the cementitious matrix. In this case, the initial non-linear ascending branch of the bond stress-slip curve is neglected.

In general, such models are only valid as long as the steel strains remain in the elastic range. Since local effects of the rib interaction are distributed over the entire bond length, they lose validity when a non-linear bond stress distribution occurs, for example, in between discrete cracks at high strain levels. However, a rigid-plastic model as shown in Figure 5.6b offers a good approximation of the bond interaction between SHCC and reinforcement during the multiple cracking stage. Due to the development of fine cracks, no relevant displacements occur between ribs and surrounding matrix. Hence, no slip can develop while bond stresses τ_{b0} remain fully activated as long as no plastic steel deformations occur. When a wide crack develops, the local slip combined with plastic rebar deformation may cause a reduction of the bond stress, which can be considered by a stepped bilinear or trilinear bond stress of τ_{b1} and τ_{b2}, respectively, as proposed by SIGRIST [136]. The proposed level of $0.3 \cdot \tau_{b,max}$ in Eq. (5.4) shows a good agreement with the experimental results obtained from pull-out tests and may be adapted for τ_{b1}.

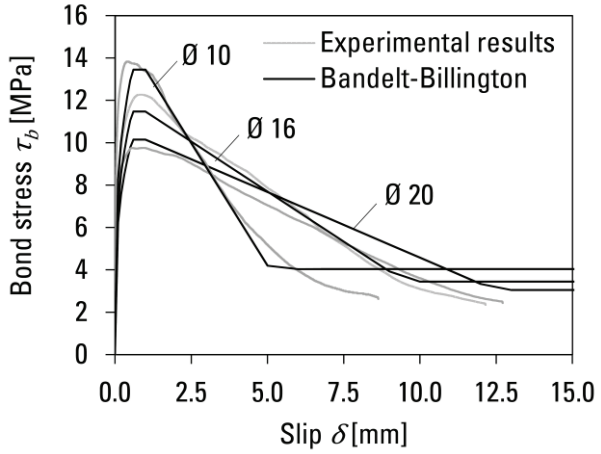

Bond parameters			
$\delta_{0,max}$	1.0 mm	b_1	0.74
a_1	16.75	b_2	2.33
a_2	0.33		

Figure 5.7: Comparison of experimental results and the proposed model adapted to the experimentally determined parameters

Figure 5.7 shows a comparison between the experimentally determined bond stress vs. slip behaviour derived from pull-out tests and the non-linear model upon the formulation of Eq. (5.2). In the case of SHCC, such a model holds interest to calculate embedment lengths, as well as for numerical analyses capturing the local interaction between crack opening and bond slip.

According to BANDELT and BILLINGTON [10] the maximum value of bond stress for SHCC was proposed with a bond strength of:

$$\tau_{b,max} = 1.2\sqrt{f_c} \quad \text{with} \quad \delta_{0,max} = 1\ mm \tag{5.9}$$

The factor 1.2 can be attributed to poor bond conditions according to CEB-FIP Model Code 2010 [41] and was found to underestimate the experimental results. Moreover, the experimental results revealed a dependency of the bond strength and maximum slip on the rebar diameter. A formulation which accounts for this effect was previously presented for conventional R/C in [19]. Following this approach, values for $\tau_{b,max}$ and δ_{ult} were determined by linear regression of the pull-out test results, cf. Table 2.6. The determination coefficients R^2, between the experimental results and the proposed values for the parameters a_1, a_2 as well as b_1, b_2 are 0.83 and 0.99, respectively, indicating that the experimental results from this study fit the proposed curve reasonably. The formulation yields:

$$\tau_{b,max} = a_1 + a_2 \cdot d_s$$
$$\delta_{ult} = b_1 + b_2 \cdot d_s \tag{5.10}$$

with d_s bar diameter
a_1, a_2 influence factor of the bar diameter on yield strength
c_1, c_2 influence factor of the bar diameter on tensile strength

5.3 Modelling of the tensile behaviour of R/SHCC

Multiple approaches have been developed to model the load-bearing behaviour of reinforced structural elements loaded in tension. These models have to be extended for the consideration of the influence of the strain-hardening properties in case of R/SHCC.

SIGRIST [136] developed an analytical model for conventional reinforced concrete based upon the calculation of bond strength and deformations around a single crack. His tension chord model required a realistic description of the elastic and plastic steel behaviour, as well as bond behaviour, which was achieved by idealised bilinear approaches of the steel deformation and bond behaviour as presented in Figure 5.2b and Figure 5.6b, respectively. PFYL [124] extended the tension chord model by SIGRIST and included the effect of fibres for steel-reinforced FRC tension members.

JUNGWIRTH [61] developed a numerical model for steel-reinforced HPFRC based upon a superposition of the stress-strain behaviour of the fibre-reinforced cementitious composite and steel reinforcement. The tensile load response of the tension member included varying modes of failure, which are influenced by the reinforcement type and ratio as well as by stress-strain response of the fibre-reinforced cement-based composite. The stress-strain response of HPFRC was derived from the number of cracks and the bridging properties, especially regarding the strain development during localisation. For steel reinforcement JUNGWIRTH used a non-linear approach combined with a bilinear ideal-plastic bond model. Hence, this model assumed that no slip is activated due to the missing relative displacement between reinforcement and surrounding matrix during multiple cracking.

LEUTBECHER [79] analysed the stress-crack opening relationship of HPFRC and proposed a discrete crack model for the combined reinforcement (i.e. rebar and fibres). In contrast to the approach by JUNGWIRTH his model is based upon a relative displacement between the reinforcing bars and the concrete matrix. The tensile behaviour was calculated considering the crack opening and a bond stress activation during the stage of progressive cracking. While this applies to HPFRC with a pronounced strain-softening material behaviour and relatively large crack widths and distances, SHCC with a strain-hardening behaviour and multiple fine cracks experiences a different behaviour since no macro-cracks and bond activation occur. Therefore, the approach from JUNGWIRTH is followed in the study at hand, since the basic requirement for a distributed cracking is given in case of SHCC.

5.3.1 Load sharing approach

The goal of the modelling is the realistic prediction of the load-bearing behaviour of reinforced structural elements under consideration of the multiple cracking of SHCC. When a tensile load is applied to the reinforced tension member, both the steel reinforcement and cementitious matrix are activated because of the bond between them, which can be idealized by the superposition of both material curves. KUNIEDA et al. [69] postulated that for R/SHCC the load-strain relationship can be divided into three distinctive regions as shown in Figure 5.8a.

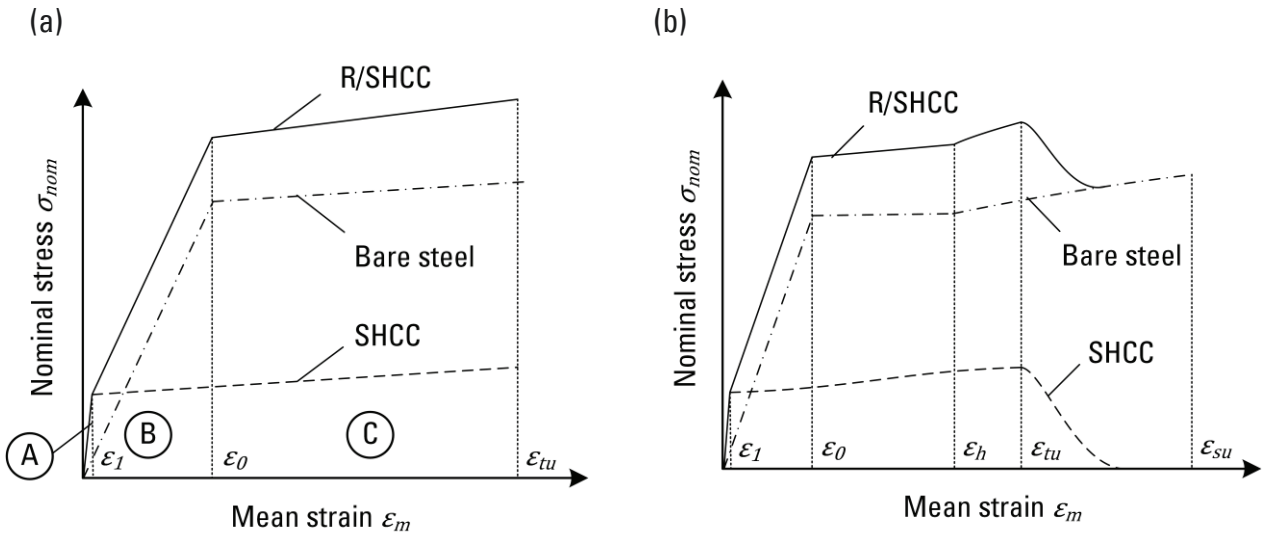

Figure 5.8: Schematic representation of the tensile load-bearing behaviour based upon the load sharing approach with (a) bilinear and (b) non-linear stress-strain relationships for steel and SHCC

The first region (A) is similar to the unreinforced tension member and characterized by the stiffness of the cementitious matrix, since SHCC is still in an uncracked state. During this stage, the strains of the concrete and steel remain equal ($\varepsilon_s = \varepsilon_c$). Thus, no significant strain difference between steel and concrete occur, which is equivalent to an ideal-plastic bond interaction, cf. Section 5.2.4. The steel and concrete stresses can be calculated for the uncracked state under application of Hooke's law with:

$$\sigma_s = E_{s\cdot} \cdot \varepsilon_s$$
$$\sigma_c = E_c \cdot \varepsilon_c \tag{5.11}$$

To consider the different stiffness in the calculation of stresses, an ideal cross-section can be determined by:

$$A_i = A_c + (\alpha_E - 1) \cdot A_s \tag{5.12}$$

with $\alpha_E = E_s/E_c$

For the uncracked state, the tensile stresses of the composite element can be calculated using Eq. (5.13):

$$\sigma_{nom} = \alpha_E \cdot \sigma_c = \alpha_E \cdot F/A_i \tag{5.13}$$

with $A_i = A_c + (\alpha_E - 1) \cdot A_s$

This behaviour is the same for R/C and R/SHCC since fibres are not activated in the elastic stage. The initial crack force F_1 depends on the stress at first cracking σ_1 of SHCC and the corresponding steel contribution due to the composite reaction:

$$F_1 = \sigma_1(A_c + \alpha_E \cdot A_s) \tag{5.14}$$

After initial cracking, the load-deformation behaviour of the second region (B) is affected by the tensile stress-strain response of the fibre-reinforced cementitious matrix, as well as the steel reinforcement. According to KUNIEDA et al. [69], "… the response in this region is the sum of the contribution from the fibres and the reinforcement …" since the micro-cracking in SHCC increases, which activates the reinforcement.

The bond behaviour during the progressive cracking stage can be regarded as ideal-plastic since steel strain ε_s and SHCC strain ε_c are remain equal due to the formation of fine cracks in SHCC. Hence, the tension-stiffening effect of SHCC can be calculated based upon the superposition of the stress-strain response of SHCC and steel reinforcement according to Eq. (5.15):

$$F = F_c + F_s = \sigma_c \cdot A_c + \sigma_s \cdot A_s \tag{5.15}$$

with A_c net cross-section of SHCC
A_s total reinforcement cross-section.

During this stage the contribution of SHCC and steel reinforcement can either be calculated based upon a bilinear stress-strain relationship according to Eq. (5.16) as shown in Figure 5.8a or by using a non-linear stress-strain relationship, for example, according to Eq. (5.5) as shown in Figure 5.8b.

$$\sigma_c(\varepsilon_c) = \frac{(f_t - \sigma_1) \cdot (\varepsilon_c - \varepsilon_1)}{(\varepsilon_{tu} - \varepsilon_1) + \sigma_1} \tag{5.16}$$

The load-bearing response transitions to the third region (C) when the yield strength of steel rebar is reached. At this point the yielding strain is exceeded and further load increase can be attributed mostly to strain-hardening of SHCC until the maximum strain capacity of SHCC is reached. However, the progression of the load-bearing response in the third region, i.e. strain-hardening or strain-softening is depending on the material properties of the used steel reinforcement especially in regard to its yielding and hardening behaviour.

5.3.2 Effect of localised strain-hardening

The experimental results of the study at hand suggest that the combination of local steel yielding and concentrated fine cracking will ultimately result in a macro-crack formation immediately after the yielding strain is reached, as previously observed by MORENO [111]. This behaviour can be related to the limited fibre bridging capabilities for large crack openings, as well as the higher local stress-strain development of the steel reinforcement in the hardening stage, cf. Section 4.5.4. However, as long as the increase in steel force F_s during the hardening is larger than the remaining concrete force F_c reduced during the softening branch of the macro-crack opening, the macro-crack growth will be stable.

In this case, the ideal plastic bond model will not be valid because of the relative displacement, which develops between reinforcement and surrounding matrix. This strain difference causes an activation of bond slip and with increasing slip a reduction of the bond strength, especially in the vicinity of the deformed steel bar. Therefore, a bilinear stepped bond model according to Figure 5.6b should be assumed to account for the bond strength reduction between yielded steel and SHCC.

MORENO [111] observed a development of multiple discrete cracks in R/SHCC elements beyond the yielding strain of steel. In this case, certain conditions must be met for a new discrete crack to develop after the yielding of the steel rebar. On the one hand, the remaining bond strength τ_{b1} must be larger than the bond stress induced by the slip around the crack. Second, the strain-hardening of the steel needs to be sufficient to compensate the stress reduction of the fibre-reinforced cementitious matrix when a macro-crack opens. On this basis, LEUTBECHER [79] developed a minimum reinforcement criterion for R/HPFRC with ductile steel reinforcement, which allows the development of multiple macro-cracks:

$$\rho_{s,min} = \frac{f_{t,k}}{R_m - R_e} \tag{5.17}$$

with $f_{t,k}$ 95% quantile of SHCC ultimate tensile strength.

This requirement can also be described as an energy dissipation criterion. The dissipation capacity depends on the ductility of the steel and is characterised as the ability of the material to dissipate energy by plastic deformations. As described in Section 2.2.1, steel rebar experiences large plastic deformations during the hardening, which causes an unloading of the remaining sections. The released elastic energy is absorbed in the region of localisation. Energy stored in SHCC adds to the elastic energy released by the unloading of the remaining steel. When the released energy exceeds the dissipation capacity in the localisation zone, which is characterised by the remaining fibre bridging and steel strength, steel rupture occurs.

The ductility of the investigated reinforcement steel with an ultimate strength to yield strength ratio of R_m/R_e of 1.16 and a tensile strength of the SHCC of $f_{t,k}$ of approximately 3.50 MPa did not satisfy the minimum reinforcement criterion for stabilised post-yielding cracking $\rho_{s,min}$ of 3.61 % in any of the tested specimens[34]. Therefore, only one macro-crack opening with subsequent softening was observed after the global yielding strain of the reinforcement was reached.

In this case, the superposition of isolated stress-strain curves for an elastic-plastic steel behaviour and a bilinear tensile SHCC response will overestimate the global strain as the minimum reinforcement criteria is not met as shown by Figure 5.9. For this purpose, an adaptation of the tensile stress-strain response of SHCC would be required, which accounts for the early strain-hardening phenomenon in low-reinforced elements.

To consider this effect in the analyses of the model, the maximum strain capacity ε_{tu} was limited to the yielding strain of the steel reinforcement. This approach allows to estimate which material parameters should be selected for modelling the SHCC behaviour during the design of reinforced SHCC members.

[34] In none of the uni-axial tension test conducted by other research groups the minimum reinforcement criterion could be satisfied, cf. Section 2.4.2. Still a stabilized post-yielding regime was reported in which one discrete crack was mostly predominant. This discrepancy can be related to the relatively short lengths of the specimens, which did not provide sufficient bond length for the full transfer of the tensile stresses into SHCC, especially under the consideration of a reduced bond strength τ_{b1}. Additionally, the ductility of steel rebar can vary substantially, cf. Table 2.7

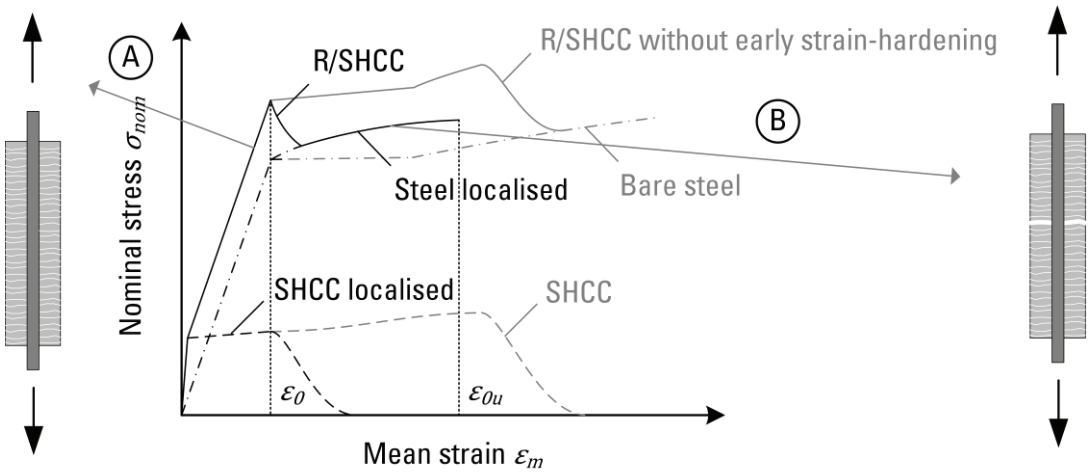

Figure 5.9: Schematic representation of the tensile load-bearing behaviour based upon the load sharing approach with focus on the post-yielding phase for a low reinforced tension member, adapted from JUNGWIRTH [61]

5.3.3 Effect of shrinkage

Shrinkage deformations restrained by steel reinforcement cause a compressive pre-loading of the reinforcement as well as an uneven loading of the specimen in case of non-uniform shrinkage. The tensile stress in SHCC as a result of shrinkage pre-loading σ_{cs} can be calculated according to Eq. (4.8). In addition, a stress reduction factor α_{cs} is introduced to account for the effects of eccentricities, which were found to result in a higher loading of the casting side (cf. Section 4.5.1.3). The total reduction of the stress at first cracking $\Delta\sigma_{cs}$ in the corresponding specimen can then be calculated according to Eq. (5.18).

$$\Delta\sigma_{cs} = \sigma_{cs} + \sigma_{1,ref}(1 - \alpha_{cs}) \tag{5.18}$$

Table 5.2 shows the stress reduction and corresponding strain, which needs to be considered when modelling the specimen response based on the SHCC behaviour.

Table 5.2: Comparison of the actual stress at first cracking under consideration of pre-loading stresses due to shrinkage and creep as well as the effect of eccentricities

Specimen	Series	$\sigma_{1,ref}$ [MPa]	σ_{cs} [MPa]	σ_{cast} [MPa]	σ_{nom} [MPa]	α_{cs} [%]	$\Delta\sigma_{cs}$ [MPa]	$\sigma_{1,mod}$ [MPa]	$\Delta\varepsilon_{cs}$
10D14	S03	3.20	0.81	1.95	1.85	95	0.97	2.23	0.60
08D16	S03		0.89	2.38	1.88	79	1.56	1.64	0.63
08D14	S04		0.77	2.52	1.86	74	1.61	1.59	0.72
08D10	S04		0.39	2.40	2.10	88	0.79	2.41	0.70
04D20	S05		0.84	2.80	1.46	52	2.37	0.83	0.73
02D20	S05		0.41	2.42	1.42	59	1.73	1.47	0.73

This approach allows the calculation of the actual stress at first cracking, which can be determined by the first cracking stress of SHCC $\sigma_{1,ref}$ and under consideration of the effect of shrinkage. Table 5.2 shows that the nominal stress of the reinforced specimen reaches about 60 to 96 % of the first cracking stress $\sigma_{1,ref}$ observed for dumbbell specimens. This suggests that large-scale specimens produced in the concrete plant can achieve similar material properties as small-scale mixes but are differently affected by eccentricities during testing of the uniaxial tension tests. Therefore, the application of this approach is limited to specimens tested under the given conditions.

Due to restrained shrinkage, the global load-bearing is shifted by the final shrinkage strain $\Delta\varepsilon_{cs}$ depending on the reinforcement ratio of the specimen as shown in Figure 5.10. Likewise, the stress at first cracking is reduced by the pre-loading stress $\Delta\sigma_{cs}$. Consequently, the point of localisation and the applicable strain capacity of SHCC can be assumed to reach $\varepsilon_0 + \Delta\varepsilon_{cs}$. The pre-loading strain is given as nominal stress and calculated based upon Eq. (4.6) including drying shrinkage, autogenous shrinkage and creep. These effects depend on the specimen age and the reinforcement ratio and has a minor effect on the load-bearing behaviour as long as the stress at first cracking of SHCC is not exceeded. However, when high degrees of reinforcement are used, for example, to fulfil the minimum reinforcement criterion according to Eq. (5.13) and achieve multiple meso-cracking, the effect on the load-bearing behaviour should be analysed.

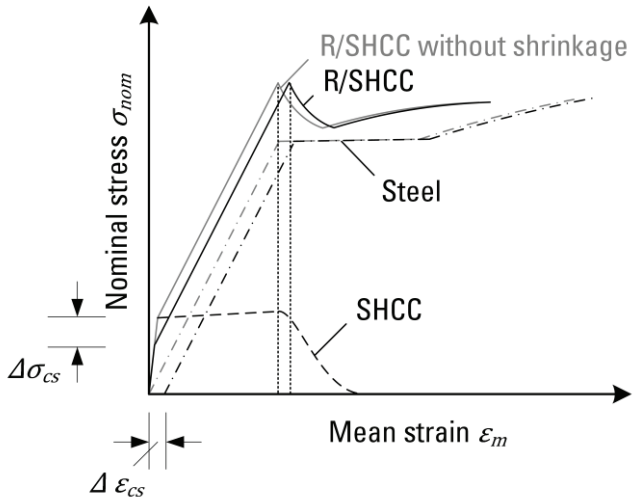

Figure 5.10: Schematic representation of the tensile load-bearing behaviour based upon the load sharing approach with focus on the effect of shrinkage, adapted from JUNGWIRTH [61]

The results of the experimental investigations for double layer reinforced specimens were compared to the stress-strain response derived from the model assumptions, cf. Figure 5.11. The model, which is based on the load-sharing approach, includes the effects of shrinkage and localized strain hardening. The agreement between the experimental results and the chosen model description appears to be satisfactory.

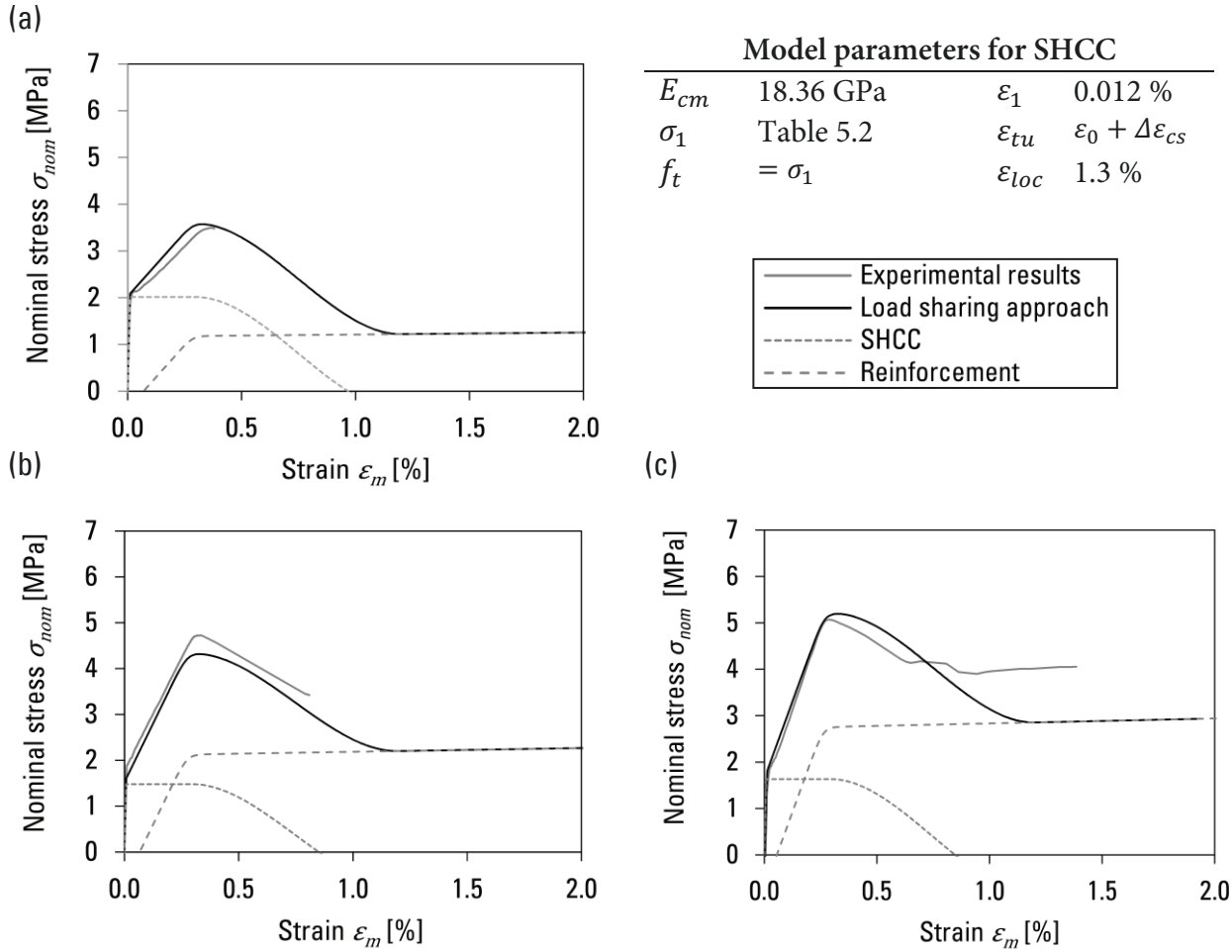

Figure 5.11: Comparison of experimental results and the proposed model for the reinforced tension-members (a) 08D10, (b) 08D14 and (c) 08D16 adapted to the experimentally determined parameters

It should be noted that the crack localization, which reduces the free deformation length of the reinforcement causes a shift in the part of the curve representing the strain-hardening regime, cf. Figure 2.10. However, the Menegotto-Pinto formulation is not capable of representing such a shift accurately, which could be an explanation for the difference in the post-localisation behaviour of the model prediction and experimental results observed in Figure 5.11c.

5.3.4 Implications for structural calculations

Another possibility to model the load-bearing behaviour of a reinforced tension member is the utilisation of the tension-stiffening approach, which focuses only on the first and second stage of the combined load-bearing behaviour. The CEB-FIP Model Code 2010 [41] describes the contribution of fibre reinforced concrete to the global tensile behaviour of a R/OC element by the tension-stiffening approach. In this model, the average steel strain over the length of the bare reinforcement is increased to estimate the effect of the tension-stiffening.

$$\varepsilon_{sm} = \varepsilon_s - \Delta\varepsilon_{ts} \tag{5.19}$$

with ε_{sm} mean strain under consideration of tension stiffening
$\Delta\varepsilon_{ts}$ contribution of SHCC to the global load-bearing behaviour

and
$$\Delta\varepsilon_{ts} = \varepsilon_s - \frac{\beta_t \cdot f_{ct}}{\rho_s \cdot E_s} - \eta_r \cdot \varepsilon_{sc} \tag{5.20}$$

This model allows predicting the load distribution up to yielding of the steel reinforcement. β_t serves as an empirical coefficient to assess the contribution of the SHCC depending on the loading condition, while η_r is a coefficient for considering the shrinkage contribution and ε_{sc} is the shrinkage strain.

A wide range of empirical models to predict the tension-stiffening factor β_t have been reported in the literature resulting in numerous variations of β_t. An overview of these models and their formulation was given, for example, by LÁRUSSON [72]. Most of these models assume a descending branch of the concrete contribution after first cracking occurs. The recommendation of the CEB-FIP Model Code 2010 [41] is given with a constant value according to Table 5.3, which was found to be the most accurate in case of SHCC. The high fibre effectiveness requires an adaptation of the coefficient β_t, which was found to reach values up to $\beta_t = 1.1$. For design purposes, a limitation to a value of $\beta_t = 0.9$ for SHCC is recommended to achieve an economical design.

Table 5.3: Values for β and η_r for deformed reinforcing bars according to CEB-FIP Model Code 2010 [41]

	Crack formation stage	**Stabilized cracking stage**
Short term, instantaneous loading	$\beta_t = 0.6$ $\eta_r = 0$	$\beta_t = 0.6$ $\eta_r = 0$
Long term, repeated loading	$\beta_t = 0.4$ $\eta_r = 0$	$\beta_t = 0.4$ $\eta_r = 1$

Restrained shrinkage of the cementitious matrix induces compression into the steel reinforcement. Hence, the effect of shrinkage needs to be considered for an accurate description of the tensile behaviour of the tension member. Figure 5.12 offers a schematic representation of the load-deformation response for a reinforced tension member made of SHCC reinforced with steel bars.

Restrained shrinkage induces tensile stresses into concrete or SHCC even before an actual load is applied, which reduces the stress at first cracking. The crack formation and stabilised cracking stage of R/SHCC shows no distinctive crack formation as the fibre bridging properties of SHCC lead to a continuous contribution to the load-bearing behaviour. Since there is no pronounced crack formation stage, shrinkage has no significant impact on the almost constant contribution of SHCC during the stabilised cracking stage.

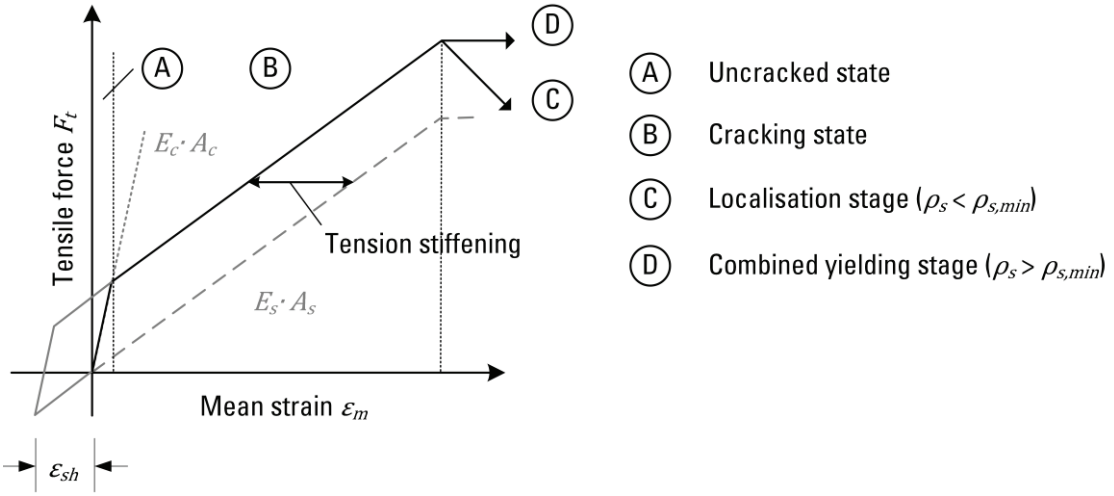

Figure 5.12: Simplified load-strain relationship for reinforced tensile members according to CEB-FIP Model Code 2010 [41] with effect of shrinkage

5.4 Summary

This chapter covered the description of the load-deformation behaviour based upon constitutive relationships for the individual materials of the reinforced tension member. Various approaches to model the tensile behaviour of steel and SHCC have been developed by researchers. A bilinear approach to describe the tensile behaviour of SHCC as well as steel reinforcement was presented and combined with a rigid-plastic bond model. Based upon these descriptions, two approaches to model the load-bearing behaviour of a reinforced tensile element are discussed, considering the obtained experimental results of **Chapter 4**.

These formulations were equipped with design values based upon experimental investigations of the material, which were presented in **Chapter 3**. Recommendations for the choice of partial safety factors were provided based upon current design standards. However, a reliable prediction of the material behaviour requires to consider the strong influence of size effects. Further research is necessary in this field to include these effects into constitutive models.

Different models to describe the bond behaviour were presented and their applicability for different stages of the reinforcement loading were discussed. Based upon the experimental findings, a rigid-plastic bond model was recommended for modelling the bond performance in the elastic steel stage, which allows a mechanical description for the interaction of steel reinforcement and SHCC in the multiple cracking stage.

The load sharing approach, which includes the superposition of the stress-strain relationship under the assumption of a rigid-plastic bond model, was found to overestimate

the ultimate tensile strain. In this case, the localisation of specimen strains and the early strain-hardening of the steel reinforcement are not adequately considered.

Therefore, this model was adapted to the effect of early strain-hardening of steel and crack localization of SHCC. In addition, shrinkage deformations, which influence the load-bearing behaviour of the reinforced tension member were considered. The proposed mechanical parameters achieve good validity with the actual behaviour measured in tension tests. It was also shown that the actual stress at first cracking under consideration of shrinkage and eccentricities achieved similar values as the material properties derived from laboratory testing.

The tension-stiffening approach allows the prediction of the load distribution up to yielding point of the steel reinforcement. In this case, the contribution of SHCC to load-bearing behaviour of the reinforced element in the multiple cracking stage is defined by the adjustment of the mean specimen strain. The β-approach also offers advantages, due to its practical implementation in structural design and analysis software. At present, most analytical or numerical programs used for structural design offer the ability of adapting the β factor or relevant parameters. This allows a realistic calculation of internal forces and deformations based upon the proposed model under consideration of shrinkage effects. However, further research to determine these effects based upon constitutive modelling is necessary for better predictability of the R/SHCC behaviour.

6 Summary and conclusions

Previous research has shown that a combination of steel reinforcement and high-performance fibre-reinforced cementitious materials such as SHCC can lead to an enhanced structural behaviour in terms of increased strength and stiffness of the R/SHCC member. These effects are the result of the characteristic properties of SHCC, which experience higher ductility and durability than conventional concrete, especially under tensile loading. The characteristic strain-hardening behaviour in tension is the result of the progressive formation of multiple micro-cracks, caused by short polymer fibres embedded into the matrix. Due to the specific composition of SHCC and the selection of constituents, a high fibre effectiveness can be achieved allowing the cementitious composite to transfer tensile stresses even after the matrix is cracked. In this case, cracks forming during the multiple cracking stage, are considerably smaller compared to cracks found in conventional reinforced concrete.

The tensile behaviour of SHCC is influenced by a variety of parameters that affect the interaction of fibres and cementitious matrix. These parameters include geometrical aspects such as shape, cross-section and thickness, as well as production related aspects such as mixing procedures, specimen age and curing conditions. Previous research indicated that especially large specimens experience a reduced tensile strength and strain capacity in comparison with smaller specimens. Additionally, the tensile properties of large-scale specimens produced in different production facilities were found to substantially deviate.

In this study, an experimental program was developed to systematically analyse the effect of the production process and the specimen size on the material behaviour of SHCC. The program aimed at investigating the effects of different parameters, such as the mixing procedure and the specimen age on the tensile deformation behaviour. Additional aspects of interest included the porosity and shrinkage behaviour of SHCC. It was shown that mechanical properties of SHCC can substantially vary for different production conditions, especially regarding structural scale applications. Therefore, it was suggested that mix design and processing times should be deliberately adjusted in scope of the desired SHCC application.

In particular, tensile strength and strain capacity show different test results from laboratory and concrete plant production. The reasons for these differences were partly found in changes of the micro-structure of the cementitious composite especially regarding air-void content and micro pore distribution. Since the fibre effectiveness depends on matrix and fibre properties, a change of the micro-structure and subsequent change of ambient stresses could influence the crack-bridging behaviour of the fibres. Additionally, a time dependency of the mechanical properties could be observed, indicating a further increase in tensile strength combined with a reduction of strain capacity at higher specimen age.

These properties need to be considered when using SHCC in combination with steel reinforcement. However, the behaviour of steel-reinforced SHCC is not only influenced by the individual material properties, as well as the bond properties between steel and SHCC. The extent to which the bond is activated depends on the degree of activated slip. Experimental investigation showed that the bond properties of SHCC substantially differ from conventional concrete due to the fine aggregates and embedded fibres.

The resulting bond interaction leads to a combined deformation behaviour of steel and SHCC. However, only limited data exists on the combined behaviour of steel and SHCC, especially on practical size elements. Previous studies have been conducted on either reinforced elements with short bond lengths or elements with very high reinforcement ratios. Recent research suggested that effects of local steel yielding cause an early hardening of the steel reinforcement when the plastic stage is reached. These effects required further investigations to identify the impact of multiple cracking of SHCC and steel yielding of reinforcement, especially regarding the effect on crack widths.

Therefore, uniaxial tension tests on large reinforced slab elements were conducted to analyse the tensile load-deformation behaviour of structural R/SHCC members. The parameters of interest included the influence of reinforcement ratio, the influence of the concrete cover and the effect of lateral reinforcement. The aim of this experimental investigation was to study the effect of multiple cracking on the contribution of SHCC to the global load-carrying capacity of R/SHCC elements, especially in the post-yielding stage of steel rebar. For this purpose, global and local deformations were measured during monotonic static tensile loading. Local surface deformations were analysed by means of digital close-range photogrammetry to study the effect of different reinforcement configurations on the cracking behaviour of SHCC. In addition, strain gauges allowed the measurement of local steel deformations on the reinforcement.

Similar to the change of tensile behaviour observed on small dumbbell-shaped specimens, large unreinforced specimens showed a further reduction of tensile strength and strain capacity. In this case, the nominal first-cracking strength of the unreinforced specimens was reduced by approximately 63 %. While part of this reduction can be attributed to changes on the micro-structure and pore distribution of the cementitious matrix, a large portion of this change was found to be caused by the effect of eccentricities. Eccentricities are a result of uneven shrinkage, imperfections and uneven load introduction and were measured by comparing the deformations on both sides of a specimen.

The investigations revealed that strain development on the casting and form side can substantially vary, while a stress at first cracking similar to that of small specimens could be observed on the higher loaded side. However, an impact of the configuration of reinforcement, i.e. symmetrical or central, was found on the effect of eccentricities and the crack width development. In the case of a symmetrical reinforcement, higher nominal strength of the element can be achieved, since the effects of uneven shrinkage were found to decrease.

It was also shown that the number of cracks increases if symmetrical reinforcement is applied, causing a better limitation of crack widths. However, the maximum strain capacity of R/SHCC elements was limited to the yielding point of steel reinforcement in all cases. Therefore, it seems likely that this limitation of strain capacity is a result of the steel deformation behaviour in combination with the specific crack behaviour of SHCC.

Similar to SHCC, ductile steel shows a pronounced yielding behaviour including strain-hardening, which is characterised by non-reversible plastic deformations. The yielding behaviour of steel reinforcement has a significant impact on the bond between the steel and the cementitious composite. Even though the bond strength and the slip development were found to be similar to conventional concrete, the load-bearing behaviour of the R/SHCC element is influenced by the tensile behaviour of SHCC, especially regarding the cracking behaviour.

Previous investigations of steel-reinforced HPFRC, which were conducted with high ductility steel reinforcement, showed a localisation of plastic strains in a single crack after the global yielding strain of the steel reinforcement was reached. Indications of this phenomenon were also observed for SHCC, which showed an early strain-hardening behaviour of the steel reinforcement at the end of the elastic stage of the related steel response. These observations could be verified for large-scale SHCC elements during the experimental investigations of this study.

In a probabilistic sense, the concentration of strains in a single crack usually occurs at the weakest part of the element. This causes a reduction of the overall strain and the energy dissipated by the reinforced elements. As long as the energy released during cracking can be dissipated by steel reinforcement, local rupture can be avoided. However, early strain-hardening of the steel reinforcement reduces the ability of the steel reinforcement to dissipate energy, which is released by the unloading of the specimen after the fibre bridging stresses decline. In this case, the condition for a multiple macro-cracking can be formulated based upon a minimum reinforcement criterion. As long as the remaining hardening capacity of the steel reinforcement exceeds the decline of loads carried by fibres, stable macro-cracking occurs.

If this condition is not met, the combination of ductile steel with strain-hardening cementitious material, such as SHCC, leads to a brittle mode of failure at a structural level. Due to the large tensile load-carrying capacity of SHCC, the use of the minimum reinforcement required for ductile element behaviour, most likely results in uneconomical amounts of reinforcement. Therefore, SHCC applications should make use reinforcing steel with a high yielding strain, a large ductility ratio (R_m/R_e) and a high hardening Modulus E_{hard}. As an alternative to conventional steel reinforcement, materials with high elastic strain such as high strength steel or GFRP bars should be investigated.

Such applications still require a reliable model to calculate deformations and internal forces that are capable of predicting the reinforced element behaviour. The results of the described tests were used to discuss the implications on constitutive models, which describe the load-bearing behaviour of the R/SHCC member. These models are based upon the behaviour of the individual material behaviour and the observed composite behaviour during tensile loading. Specific attention was given to the effect of local steel hardening and the crack opening behaviour of SHCC. Such models based on constitutive relationships can be used to describe the tensile steel and SHCC behaviour and the bond-slip behaviour with an appropriate degree of simplification. Specific attention must be given to the early hardening of the steel rebar, especially since the minimum reinforcement ratio was not reached. In this case, the superposition of the idealised constitutive material laws would overestimate the global tensile strain of the R/SHCC member. Therefore, the material response need to be adapted to include the effect of shrinkage and eccentricities. For practical purposes, the β-approach was presented, which is limited to the description of the material behaviour during the elastic steel stage.

However, these definitions are only valid for the combination of high yielding steel and SHCC. In the case of other materials as reinforcement, the validity of these mechanical models needs to be verified. To avoid extensive experimental research, this could be conducted on numerical simulations. The combination of numerical analyses and meso-scale material models based upon the crack-bridging behaviour, effectively allows the implication different material properties. It is reasonable to suppose that numerical simulations based upon crack opening relationship in combination with random fields achieve a good reproduction of the strain-hardening behaviour at the macro-level.

However, the use of these on a structural scale today remains limited by computational resources. A realistic implementation would require an implementation of the meso-scale behaviour into a structural size model. The resulting number of discrete elements and the difficulties with numerical instabilities of the computation would be substantial. Nonetheless, with further developments in the field of numerical simulation, these methods could replace analytical models, which still suffer from a lack of sophistication for a reliable application in SHCC.

References

[1] Abell, A. B.; Willis, K. L.; Lange, D. A.: Mercury Intrusion Porosimetry and Image Analysis of Cement-Based Materials. Journal of colloid and interface science. 1999, 211(1), 39-44.

[2] ACI 544.1R-96: *Report on Fiber Reinforced Concrete.* American Concrete Institute, Detroit, Michigan, Tech. Rep. 544.1R-96, 2009.

[3] Adendorff, C. J.: *The time-dependent cracking behaviour of strain hardening cement-based composite,* Master's thesis, University of Stellenbosch, 2009.

[4] AFGC:2013: *Ultra High Performance Fiber-Reinforced Concretes.* Association Française de Génie Civil.

[5] Alexander, M.; Mindness, S., Eds.: *Aggregates in Concrete.* CRC Press, 2005.

[6] Altmann, F.: *A Durability Concept for Strain-Hardening Cement-Based Composites,* Doctoral thesis, Technische Universität Dresden, 2012.

[7] Alvarez, M.: Large-Scale Tension Tests on Wall Elements. In: *Proceedings, 1st International PhD Symposium in Civil Engineering,* Budapest, Hungary, May 28-31, 1996, 22-26.

[8] Alvarez, M.: *Einfluss des Verbundverhaltens auf das Verformungsvermögen von Stahlbeton.* Birkhäuser, Basel, ETH Zürich, Switzerland, 1998.

[9] Asano, K.; Kanakubo, T.: Study on Size Effect in Bond Splitting Behavior of ECC. In: G. J. Parra-Montesinos; H. W. Reinhardt; A. E. Naaman, eds.: *HPFRCC 6: High Performance Fiber Reinforced Cement Composites 6,* Springer Netherlands, RILEM State of the Art Reports, 2012, 137-144.

[10] Bandelt, M. J.; Billington, S. L.: Bond behavior of steel reinforcement in high-performance fiber-reinforced cementitious composite flexural members. *Materials and Structures.* 2014, 1-16.

[11] Bandelt, M. J.; Billington, S. L.: Monotonic and Cyclic Bond-Slip Behavior of Ductile High-Performance Fiber-Reinforced Cement-Based Composites. In: E. Schlangen; L. Sierra Beltran; M. Lukovic; G. Ye, eds.: *SHCC3: 3rd International RILEM Conference on Strain Hardening Cementitious Composites,* Dordrecht, The Netherlands, Nov. 03-05, 2014, 393-400.

[12] Barhum, R.: *Mechanisms of the interaction between continuous and short fibre in textile-reinfoced concrete (TRC),* Doctoral thesis, Technische Universität Dresden, 2014.

[13] Bažant, Z. P.; Ozbolt, J.; Eligehausen, R.: Fracture size effect: review of evidence for concrete structures. *Journal of Structural Engineering.* 1994, 120(8), 2377-2398.

[14] Bentur, A.; Mindness, S., Eds.: *Fibre Reinforced Cementitious Composites.* 2nd ed. CRC Press, 2006.

[15] Boshoff, W. P.; Mechtcherine, V.; van Zijl, G. P. A. G.: Characterising the time-dependant behaviour on the single fibre level of SHCC: Part 2: The rate effects on fibre pull-out tests. *Cement and Concrete Research.* 2009, 39(9), 787-797.

[16] Brameshuber, W., Ed.: *Textile Reinforced Concrete - State-of-the-Art Report of RILEM TC 201-TRC.* RILEM Report rep036 ed. RILEM Publications S.A.R.L., 2006.

[17] Brameshuber, W., Ed.: *International RILEM Conference on Material Science - 2nd ICTRC - Textile Reinforced Concrete - Theme 1.* RILEM Publications, 2010.

[18] Brüdern, A.; Mechtcherine, V.: Multifunctional use of SAP in Strain-hardening Cement-based Composites. In: O. M. Jensen; M. T. Hasholt; S. Laustsen, eds.: *Proceedings pro074: International RILEM Conference on Use of Superabsorbent Polymers and Other New Additives in Concrete,* Lyngby, Denmark, Aug. 15-18, 2010, 11-22.

[19] CEB Bulletin 151: *Bond Action and Bond Behaviour of Reinforcement.* Comité Euro-International du Béton, Paris, France, 1982.

[20] CECS: *Publication No.38, Technical Specification for Fiber Reinforced Concrete Structures.* China Association for Engineering Construction Standardization, 2004.

[21] Chao, S.; Naaman, A. E.; Gustavo, J.: Bond Behavior of Reinforcing Bars in Tensile Strain-Hardening Fiber-Reinforced Cement Composites. *Structural Journal.* 2009, 106(06), 897-906.

[22] CNR-DT 204: *Guide for the Design and Construction of Fiber-Reinforced Concrete Structures.* National Research Council, Rome, Italy, 2006.

[23] Curosu, I.; Liebscher, M.; Mechtcherine, V.; Bellmann, C.; Michel, S.: Tensile behavior of high-strength strain-hardening cement-based composites (HS-SHCC) made with high-performance polyethylene, aramid and PBO fibers. *Cement and Concrete Research.* 2017, (98), 71-81.

[24] Curosu, I.; Mechtcherine, V.; Millon, O.: Effect of fiber properties and matrix composition on the tensile behavior of strain-hardening cement-based composites (SHCCs) subject to impact loading. *Cement and Concrete Research.* 2016, (82), 23-35.

[25] DAfStb-Richtlinie: *Stahlfaserbeton, Ergänzungen und Änderungen zu DIN EN 1992-1-1 in Verbindung mit DIN EN 1992-1-1/NA, DIN EN 206-1 in Verbindung mit DIN 1045-2 und DIN EN 13670 in Verbindung mit DIN 1045-3*2012.

[26] DIN 488-1: *2009-08. Reinforcing steels - Part 1: Grades, properties, marking.*

[27] DIN 52450:1985: *Testing of inorganic non-metallic building materials; determination of shrinkage and expansion on small specimens.*

[28] DIN 66133:1993: *Determination of pore volume distribution and specific surface area of solids by mercury intrusion.*

[29] DR AS 5100.5: *Draft for Public Comment Australian Standard, Bridge Design - Part 5: Concrete.* Standards Australia, Sydney, 2014.

[30] Duda, H.: *Bruchmechanisches Verhalten von Beton unter monotoner und zyklischer Zugbeanspruchung (DAfStb-Heft 419).* Berlin: Ernst & Sohn, 1991.

[31] Durán-Herrera, A.; Juárez, C. A.; Valdez, P.; Bentz, D. P.: Evaluation of sustainable high-volume fly ash concretes. *Cement and Concrete Composites.* 2011, 33(1), 39-45.

[32] Eligehausen, R.; Popov, E. P.; Bertero, V. V.: *Local Bond Stress-Slip Relationships of Deformed Bars under Generalized Excitations.* University of California, Berkeley, CA, Tech. Rep. UCB/EERC-83/23, 1983.

[33] EN 1015-3:1999+A1:2004+A2:2006: *Methods of test for mortar for masonry - Part 3, Determination of consistence of fresh mortar (by flow table).*

[34] EN 12350-7:2009: *Testing fresh concrete - Part 7: Air content - Pressure methods.*

[35] EN 12350-8:2010: *Testing fresh concrete - Part 8: Self-compacting concrete - Slump-flow test.*

[36] EN 197-1:2011: *Cement - Part 1: Composition, specifications and conformity criteria for common cement.*

[37] EN 1992-1-1: *2004+AC:2010. Eurocode 2: Design of concrete structures – Part 1-1: General rules and rules for buildings*2010.
[38] EN 206:2014: *Concrete - Part 1: Specification, performance, production and conformity*.
[39] EN 480-11:2005: *Admixtures for concrete, mortar and grout - Test methods - Part 11, Determination of air void characteristics in hardened concrete*.
[40] EN 934-2:2009+A1:2012: *Admixtures for concrete, mortar and grout - Part 2: Concrete admixtures - Definitions, requirements, conformity, marking and labelling*.
[41] fib: *fib Model Code for Concrete Structures 2010.* Wiley-VCH Verlag GmbH & Co. KGaA, 2013.
[42] fib Bulletin 10: *Bond of reinforcement in concrete.* Federation International du Béton, Lausanne, Switzerland, 2000.
[43] Filho, R. D. T.; Silva, F. d. A.; Koenders, E. A. B.; Fairbairn, E. M. R., Eds.: *2nd International RILEM Conference on Strain Hardening Cementitious Composites (SHCC2-Rio).* RILEM Publications SARL, 2011.
[44] Fischer, G.; Li, V. C.: Influence of Matrix Ductility on Tension-Stiffening Behavior of Steel Reinforced Engineered Cementitious Composites (ECC). *Structural Journal.* 2002, 99(1), 104-111.
[45] Georgiou, A. V.; Pantazopoulou, S. J.: Effect of fiber length and surface characteristics on the mechanical properties of cementitious composites. *Construction and Building Materials.* 2016, (125), 1216-1228.
[46] Georgiou, A. V.; Pantazopoulou, S. J.; Petrou, M.: Increasing ductility of FRCC with proprietary coating agents. In: J. Bastien; N. Rouleau; M. Fiset; M. Thomassin, eds.: *Proceedings of the 10th International Ph.D.Symposium in Civil Engineering,* Québec, Canada, Jul. 21-23, 2014, 25-30.
[47] Gorges, M.: *Entwicklung von Methoden zur Charakterisierung des Wirkmechanismus von Super-Absorbierenden Polymeren als Zusatzmittel für innere Nachbehandlung in Beton, Projektarbeit am Institut für Baustoffe, TU Dresden,* Projektarbeit, TU Dresden, 2011.
[48] Goto, Y.: Cracks Formed in Concrete Around Deformed Tension Bars. *Journal American Concrete Institute Proceedings.* 1971, 68(4), 244-251.
[49] Griffith, A. A.: The phenomena of rupture and flow in solids. *Philosophical Transactions.* 1994, 27163-198.
[50] Haist, M.; Müller, H. S.: Nachhaltiger Beton - Betontechnologie im Spannungsfeld zwischen Ökobilanz und Leistungsfähigkeit. In: H. S. Müller; U. Nolting; M. Haist; M. Kromer, eds.: *9. Symposium Baustoffe und Bauwerkserhaltung: Nachhaltiger Beton - Werkstoff, Konstruktion und Nutzung,* Karlsruher Institut für Technologie (KIT), May 15, 2012, 29-52.
[51] Hamza, A. M.; Naaman, A. E.: Bond Characteristics of Deformed Reinforcing Steel Bars Embedded in SIFCON. *Materials Journal.* 1996, 93(6), .
[52] Harajli, M. H.; Hout, M.; Jalkh, W.: Local Bond Stress-Slip Behavior of Reinforcing Bars Embedded in Plain and Fiber Concrete. *ACI Materials Journal.* 1995, 92(4), 343-354.
[53] Hillerborg, A.; Modéer, M.; Petersson, P. -.: Analysis of crack formation and crack growth in concrete by means of fracture mechanics and finite elements. *Cement and Concrete Research.* 1976, 6(6), 773-781.

[54] Hinzen, M.; Brameshuber, W.: Influence of Matrix Composition and Short Fibres on the Workability of Fine Grained Fibre Concrete. In: W. Brameshuber, ed.: *International RILEM Conference on Material Science,* Aachen, Sept 6 - 8, 2010, 131-140.

[55] Idiart, A. E.: *Coupled analysis of degradation process in concrete specimens at the meso-level,* PhD thesis, UPC, Barcelona, Spain, 2009.

[56] JCI-DFRCC Committee: DFRCC Terminology and Application Concepts. *Journal of Advanced Concrete Technology.* 2003, 1(3), 335-340.

[57] Joo Kim, D.: *Strain rate effect on high performance fiber reinforced cementitious composites using slip hardening high strength deformed steel fibers,* Ph.D. dissertation, University of Michigan, 2009.

[58] JSCE: *Recommendations for Design and Construction of Ultra High Strength Fiber Reinforced Concrete Structures (Draft).* Japan Society of Civl Engineers, 2006.

[59] JSCE: *Recommendations for Design and Construction of High Performance Fiber Reinforced Cement Composites with Multiple Fine Cracks (HPFRCC).* Japan Society of Civil Engineers, 2008.

[60] Jun, P.: *Behaviour of Strain-Hardening Cement-Based Composites (SHCC) under monotonic and cyclic tensile loading,* Doctoral thesis, Technische Universität Dresden, 2011.

[61] Jungwirth, J.: *Zum Tragverhalten von zugbeanspruchten Bauteilen aus Ultra-Hochleistungs-Faserbeton,* Doctoral thesis, EPFL, Lausanne, Switzerland, 2005.

[62] Kabele, P.: New developments in analytical modeling of mechanical behavior of ECC. *Journal of Advanced Concrete Technology.* 2003, 1(3), 253-264.

[63] Kanakubo, T.: Tensile Characteristics Evaluation Method for Ductile Fiber-Reinforced Cementitious Composites. *Journal of Advanced Concrete Technology.* 2006, 4(1), 3-17.

[64] Kanda, T.; Tomoe, S.; Nagai, S.; Maruta, M.; Kanakubo, T.; Shimizu, K.: Full Scale Processing Investigation for ECC Pre-cast Structural Element. *Journal of Asian Architecture and Building Engineering.* 2006, 5(2), 333-340.

[65] Kesner, K. E.; Billington, S. L.: *Tension, Compression and Cyclic Testing of Engineered Cementitious Composite Materials.* Cornell University, Ithaca, New York, Tech. Rep. MCEER-04-0002, 2004.

[66] Kesner, K. E.; Billington, S. L.; Douglas, K. S.: Cyclic Response of Highly Ductile Fiber-Reinforced Cement-Based Composites. *ACI Materials Journal.* 2003, 100(5), 381-390.

[67] Korb, S.: *Untersuchungen zum Zugtragverhalten hochduktiler Faserbetone mit zusätzlicher Textilbewehrung,* Doctoral thesis, Technische Universität Kaiserslautern, 2010.

[68] Koukolík, P.; Vítek, J. L.; Brož, R.; Coufal, R.; Kalný, M.; Komanec, J.; Kvasnička, V.: Construction of the First Footbridge Made of UHPC in the Czech Republic. *Advanced Materials Research.* 2015, 11068-13.

[69] Kunieda, M.; Hussein, M.; Ueda, N.; Nakamura, H.: Enhancement of crack distribution of UHP-SHCC under axial tension using steel reinforcement. *Journal of Advanced Concrete Technology.* 2010, 8(1), 49-57.

[70] Kunieda, M.; Rokugo, K.: Recent Progress on HPFRCC in Japan; Required Performance and Applications. *Journal of Advanced Concrete Technology.* 2006, 4(1), 19-33.

[71] Kunz, P.: *Cracking of steel reinforced Strain Hardening Cement-based Composites (SHCC) and comparison to the cracking behaviour of plain SHCC,* Project Work, Stellenbosch University/TU Dresden, Dresden, 2012.

[72] Lárusson, L. H.: *Development of Flexible Link Slabs using Ductile Fiber Reinforced Concrete,* Ph.D. dissertation, Technical University of Denmark, Lyngby, Denmark, 2013.

[73] Lárusson, L. H.; Fischer, G.: Bond slip and crack development in FRC and regular concrete specimens longitudinally reinforced with FRP or steel under tension loading. In: J. W. Cairns; G. Metelli; G. A. Plizzari, eds.: *Bond in Concrete 2012: Bond, Anchorage, Detailing - Proceedings of the 4th Bond in Concrete Conference,* Brescia, Italy, Jun 17-20, 2012, 847-854.

[74] Lárusson, L. H.; Fischer, G.; Jönsson, J.: Mechanical Interaction between Concrete and Structural Reinforcement in the Tension Stiffening Process. In: G. J. Parra-Montesinos; H. W. Reinhardt; A. E. Naaman, eds.: *High Performance Fiber Reinforced Cement Composites 6,* vol. 2, Springer Netherlands, 2012, 247-254.

[75] Lepech, M. D.; Li, V. C.: Preliminary Findings on Size Effect in ECC Structural Members in Flexural. In: A. M. Brandt; V. C. Li; I. H. Marshall, eds.: *Proceedings of the Seventh International Symposium on Brittle Matrix Composites,* Warsaw, Poland, Oct 13-15, 2003, 57-66.

[76] Lepech, M. D.; Li, V. C.: Large-Scale Processing of Engineered Cementitious Composites. *ACI Materials Journal.* 2008, 105(4), 358-366.

[77] Lepech, M. D.; Li, V. C.: Application of ECC for bridge deck link slabs. *Materials and Structures.* 2009, (9), 1185-1195.

[78] Leung, C.; Ybanez, N.: Pullout of Inclined Flexible Fiber in Cementitious Composite. *Journal of Engineering Mechanics.* 1997, 123(3), 239-246.

[79] Leutbecher, T.: *Rissbildung und Zugtragverhalten von mit Stabstahl und Fasern bewehrtem Ultrahochfesten Beton (UHPC),* Doctoral thesis, Universität Kassel, Kassel, 2008.

[80] Li, M.; Li, V. C.: Rheology, fiber dispersion, and robust properties of Engineered Cementitious Composites. *Materials and Structures* 2013, 46(3), 405-420.

[81] Li, V. C.; Stang, H.; Krenchel, H.: Micromechanics of crack bridging in fibre-reinforced concrete. *Materials and Structures* 1993, 26(8), 486-494.

[82] Li, V. C.; Wang, Y.; Backer, S.: Effect of inclining angle, bundling and surface treatment on synthetic fibre pull-out from a cement matrix. *Composites.* 1990, 21(2), 132-140.

[83] Li, V. C.: Engineered Cementitious Composites - Tailored Composites Through Micromechanical Modeling. In: N. Banthia; A. Bentur; A. Mufti, eds.: *Fiber Reinforced Concrete: Present and the Future,* Canadian Society of Civil Engineers, 1998, 64-97.

[84] Li, V. C.: Reflections on the research and development of Engineered Cementitious Composites (ECC). In: *Proceedings of the JCI International Workshop on Ductile Fiber Reinforced Cementitious Composites (DFRCC) - Application and Evaluation (DRFCC-2002),* Takayama, Japan, Oct. 2002, 2002, 1-21.

[85] Li, V. C.: On engineered cementitious composites (ECC). *Journal of Advanced Concrete Technology.* 2003, 1(3), 215-230.

[86] Li, V. C.: Strategies for high performance fiber reinforced cementitious composites development. In: S. Ahmad; M. di Prisco; C. Meyer; G. A. Plizzari; S. P. Shah, eds.: *Fiber reinforced concrete: from theory to practice, Proceedings of N. American/European Workshop on Advances in Fiber Reinforced Concrete,* Bergamo, Italy, Sept. 24-25, 2004, 93-98.

[87] Li, V. C.: Engineered Cementitious Composite (ECC): Material, Structural, and Durability Performance. In: E. G. Nawy, ed.: *Concrete Construction Engineering Handbook,* 2nd ed. Taylor & Francis, 2008, 24-1-24-46.

[88] Li, V. C.; Fischer, G.; Kim, Y. J.; Lepech, M. D.; Qian, S.; Weimann, M.; Wang, S.: *Durable Link Slabs for Jointless Bridge Decks Based on Strain-Hardening Cementitious Composites.* University of Michigan, Ann Arbor, Michigan, Tech. Rep. RC-1438, Nov. 16. 2003.

[89] Li, V. C.; Mishra, D. K.; Wu, H.: Matrix design for pseudo-strain-hardening fibre reinforced cementitious composites. *Materials and Structures.* 1995, 28(10), 586-595.

[90] Li, V. C.; Wu, C.; Wang, S.; Ogawa, A.; Saito, T.: Interface Tailoring for Strain-Hardening Polyvinyl Alcohol-Engineered Cementitious Composite (PVA-ECC). *Materials Journal.* 2002, 99(5), 463-472.

[91] Lin, Z.; Kanda, T.; Li, V. C.: On interface property characterization and performance of fiber-reinforced cementitious composites. *Concrete Science and Engineering.* 1999, 1(3), 173-184.

[92] Lin, Z.; Li, V. C.: Crack bridging in fiber reinforced cementitious composites with slip-hardening interfaces. *Journal of the Mechanics and Physics of Solids.* 1997, 45(5), 763-787.

[93] Lindorf, A.: *Bond fatigue in reinforced concrete under transverse tension,* Doctoral thesis, TU Dresden, Dresden, 2012.

[94] Löfgren, I.: *Fibre-reinforced Concrete for Industrial Construction - - a fracture mechanics approach to material testing and structural analysis,* Doctoral thesis, Chalmers University of Technology, Göteborg, Sweden, 2005.

[95] Mechtcherine, V.: *Bruchmechanische und fraktologische Untersuchungen zur Rissausbreitung in Beton,* Doctoral thesis, Universität Fridericiana zu Karlsruhe (TH), Karlsruhe, 2000.

[96] Mechtcherine, V.: Towards a durability framework for structural elements and structures made of or strengthened with high-performance fibre-reinforced composites. *Construction and Building Materials.* 2012, 3194-104.

[97] Mechtcherine, V.: Novel cement-based composites for the strengthening and repair of concrete structures. *Construction and Building Materials.* 2013, 41365-373.

[98] Mechtcherine, V.: Hochduktiler Beton mit Kurzfaserbewehrung. *Beton- und Stahlbetonbau.* 2015, 110(1), 50-58.

[99] Mechtcherine, V.; Altmann, F.: Durability of Structural Elements and Structures. In: F. H. Wittmann; G. P. A. G. van Zijl, eds.: *Durability of Strain-Hardening Fibre-Reinforced Cement-Based Composites (SHCC),* Springer Netherlands, RILEM State of the Art Reports, 2010, 89-111.

[100] Mechtcherine, V.; Jun, P.: Stress-strain behaviour of strain-hardening cement-based composites (SHCC) under repeated tensile loading. In: A. Carpinteri; P. G. Gambarova; G. Ferro; G. A. Plizzari, eds.: *FraMCoS-6: Proceedings of the 6th International Conference on Fracture Mechanics of Concrete and Concrete Structures,* Catania, Italy, Jun 17-22, 2007, 1441-1448.

[101] Mechtcherine, V.; Jun, P.: Behaviour of strain hardening cement-based composites in tension and compression. In: G. Ravindra, ed.: *Proceedings of the seventh RILEM international symposium on fibre reinforced concrete: design and applications (BEFIB 2008)*. Chennai, India: RILEM Publications, 2008, 471-481.

[102] [Mechtcherine, V.; Millon, O.; Butler, M.; Thoma, K.: Mechanical behaviour of strain hardening cement-based composites under impact loading. *Cement and Concrete Composites.* 2011, 33(1), 1-11.

[103] Mechtcherine, V.; Müller, H. S.: Effect of the test set-up on fracture mechanical parameters of concrete. In: H. Mihashi;K. Rokugo, eds.: *FRAMCOS-3: Fracture Properties and Parameters,* Gifu, Japan, 12-16 Oct, 1998, 377-386.

[104] Mechtcherine, V.; Schulze, J.: Effect of the test set-up and curing conditions on fracture behavior of Strain Hardening Cement-based Composites (SHCC). In: M. S. Konsta-Gdoutos, ed.: *Measuring, Monitoring and Modeling Concrete Properties: An International Symposium dedicated to Professor Surendra P. Shah, Northwestern University, U.S.A.* Dordrecht: Springer Netherlands, 2006, 33-39.

[105] Mechtcherine, V.; Silva, F. d. A.; Müller, S.; Jun, P.; Filho, R. D. T.: Coupled strain rate and temperature effects on the tensile behavior of strain-hardening cement-based composites (SHCC) with PVA fibers. *Cement and Concrete Research.* 2012, 42(11), 1417-1427.

[106] Mechtcherine, V.; Slowik, V.; Kabele, P., Eds.: *4th International Conference on Strain-Hardening Cement-Based Composites.* Springer Netherlands, 2017.

[107] Menegotto, M.; Pinto, P. E.: Method of Analysis for Cyclically Loaded R.C. Plane Frames Including Changes in Geometry and Non-Elastic Behavior of Elements under Combined Normal Force and Bending. In: *IABSE Symposium on the Resistance and Ultimate Deformability of Structures Acted on by Well Defined Repeated Loads,* Lisbon, Portugal ed. vol. 13, Reports of the Working Commissions, 1973, 15-22.

[108] Mihashi, H.; Zaitsev, J. W.: State-of-the-Art Report of RILEM TC 50--FMC. In: F. H. Wittmann, ed.: *Statistical nature of crack popagation,* RILEM State of the Art Reports, 1981, 1-21.

[109] Mihashi, H.; Otsuka, K.; Akita, H.; Kikuchi, T.: Bond Cracking and Tension Stiffening Properties of a Deformed Bar Embedded in HPFRCC. In: C. U. Grosse, ed.: *Advances in Construction Materials 2007,* Springer Berlin Heidelberg, 2007, 173-180.

[110] Moreno, D. M.; Trono, W.; Jen, G.; Ostertag, C.; Billington, S. L.: Tension-Stiffening in Reinforced High Performance Fiber-Reinforced Cement-Based Composites under Direct Tension. In: G. Parra-Montesinos; H. Reinhardt; A. E. Naaman, eds.: vol. 2, Springer Netherlands, High Performance Fiber Reinforced Cement Composites 6, 2012, 263-270.

[111] Moreno, D. M.; Trono, W.; Jen, G.; Ostertag, C.; Billington, S. L.: Tension stiffening in reinforced high performance fiber reinforced cement-based composites. *Cement and Concrete Composites.* 2014, 50(0), 36-46.

[112] Müller, H. S.; Anders, I.; Breiner, R.; Vogel, M.: Concrete: treatment of types and properties in fib Model Code 2010. *Structural Concrete.* 2013, 14(4), 320-334.

[113] Müller, S.; Mechtcherine, V.: Fatigue behaviour of strain-hardening cement-based composites (SHCC). *Cement and Concrete Research.* 2017, 9275-83.

[114] Mündecke, E.: *Bond between SHCC and steel reinforcement,* Project Work, Stellenbosch University/TU Dresden, 2010.

[115] Mündecke, E.; Mechtcherine, V.: *Entwicklung von konstruktiven Elementen aus hochduktilem Beton für den Einsatz im Brückenbau.* Institut für Baustoffe, TU Dresden, Tech. Rep. KF2661206KI1, 2015.

[116] Naaman, A. E.: Strain hardening and deflection hardening fiber reinforced cement composites. In: A. E. Naaman; H. W. Reinhardt, eds.: *4th International RILEM Workshop on High Performance Fiber - Reinforced Cement Composites (HPFRCC4),* RILEM Publications, Proceedings pro030, 2003, 95-104.

[117] Naaman, A. E.: Tensile strain-hardening FRC composites: Historical evolution since the 1960. In: C. U. Grosse, ed.: *Advances in Construction Materials 2007,* Springer Berlin Heidelberg, 2007, 181-202.

[118] Naaman, A. E.: High Performance Fiber Reinforced Cement Composites. In: C. Shi; Y. Mo, eds.: *High Performance Construction Materials – Science and Applications,* vol. 1, World Scientific, High-Performance Construction Materials, 2008, 91-153.

[119] Naaman, A. E.; Reinhardt, H. W.: Proposed classification of HPFRC composites based on their tensile response. *Materials and Structures.* 2006, 39(5), 547-555.

[120] Nieuwoudt, P. D.: *Quantifying the cracking behaviour of strain hardening cement-based composites,* Master's thesis, University of Stellenbosch, 2012.

[121] Noghabai, K.: *Effect of Tension Softening on the Performance of Concrete Structures,* Doctoral thesis, Luleå University of Technology, Luleå, Sweden, 1998.

[122] Otsuka, K.; Mihashi, H.; Kiyota, M.; Mori, S.; Kawamata, A.: Observation of Multiple Cracking in Hybrid FRCC at Micro and Meso Levels. *Journal of Advanced Concrete Technology.* 2003, 1(3), 291-298.

[123] Ožbolt, J.: *Maßstabseffekt und Duktilität von Beton- und Stahlbetonkonstruktionen,* Habil., Universität Stuttgart, Institut für Werkstoffe im Bauwesen, Stuttgart, 1995.

[124] Pfyl, T.: *Tragverhalten von Stahlfaserbeton,* Doctoral thesis, ETH Zürich, Switzerland, 2003.

[125] *Proceedings of the Workshop on High Performance Fibre Reinforced Cement-based Composites.* Honolulu, Hawaii (USA): 2005.

[126] Rehm, G.: *Über die Grundlagen des Verbundes zwischen Stahl und Beton (DAfStb-Heft 138).* Berlin: Ernst & Sohn, 1961.

[127] RILEM: Technical Recommendations for the Testing and Use of Construction Materials: RC 6, Bond Test for Reinforcement Steel, 2. Pull-out Test. 1970.

[128] RILEM TC 162-TDF: Test and design methods for steel fibre reinforced concrete. *Materials and Structures.* 2002, 25(7), 262-278.

[129] Rokugo, K.: Applications of Strain Hardening Cementitious Composites with multiple cracks in Japan. In: V. Mechtcherine, ed.: *Hochduktile Betone mit Kurzfaserbewehrung – Entwicklung, Prüfung, Anwendung,* . Stuttgart: ibidem Verlag, 2005, 121-133.

[130] Şahmaran, M.; Lachemi, M.; Li, V. C.: Assessing the Durability of Engineered Cementitious Composites Under Freezing and Thawing Cycles. *Journal of ASTM International.* 2009, 6(7), 1-13.

[131] SANS 920:2011: *Ed. 2.03: Steel bars for concrete reinforcement.*

[132] Scheerer, S.; Schladitz, F.; Curbach, M.: Textile reinforced Concrete - from the idea to a high performance material. In: W. Brameshuber, ed.: *Proceedings of the FERRO-11 - 11th International Symposium on Ferrocement and 3rd ICTRC - International Conference on Textile Reinforced Concrete,* RILEM Publications SARL, Proceedings Pro098, 2015, 20-34.

[133] Schlangen, E.; Sierra Beltran, L.; Lukovic, M.; Ye, G., Eds.: *3rd International RILEM Conference on Strain Hardening Cementitious Composites (SHCC3-Delft).* RILEM Publications SARL, 2014.

[134] Schröder, S.: *The influence of a biaxial tensile stress on the strength and deformation behavior of concrete and mixed reinforced concrete components,* Doctoral thesis, Technische Universität Dresden, 2013.
[135] Seibel, P.: *Experimentelle und numerische Untersuchungen zur Mitwirkung des Betons zwischen den Rissen,* Doctoral thesis, Universität Kassel, Kassel, 2001.
[136] Sigrist, V.: *Zum Verformungsvermögen von Stahlbetonträgern,* Doctoral thesis, ETH Zürich, Switzerland, 1995.
[137] Soretz, S.: Verbund zwischen Stahleinlagen und Beton als Prüf- und Verwendungseigenschaft. *Betonstahl in Entwicklung.* 1974, (56), 20-21.
[138] Suwannakarn, S.; El-Tawil, S.; Naaman, A. E.: Experimental Observations on the Tensile Response of Fiber Reinforced Cement Composites with Different Fibers. In: H. W. Reinhardt;A. E. Naaman, eds.: *Fifth International RILEM Workshop on High Performance Fiber Reinforced Cement Composites (HPFRCC5),* Jul 10-13, 2007, 33-47.
[139] Tepfers, R.: *Theory of Bond Applied to Overlapped Tensile Reinforcement Splices for Deformed Bars,* Ph.D. dissertation, Chalmers University of Technology, 1973.
[140] Toshiyuki, K.; Kabele, P.; Fukuyama, H.; Uchida, Y.; Suwada, H.; Slowik, V.: *Strain Hardening Cement Composites: Structural Design and Performance.* Springer Netherlands, 2013.
[141] Uchida, Y.; Kunieda, M.; Rokugo, K.: FRCC - Design and application in Japan. In: J. Charron; B. Massicotte; B. Mobasher; G. A. Plizzari, eds.: *Proceedings of the FRC 2014 Joint ACI-fib International Workshop Fibre Reinforced Concrete: From Design to Structural Applications,* Montreal, Canada, Jul 24-25, 2014, 58-68.
[142] van Zijl, G. P. A. G.: Durability under Mechanical Load – Micro-crack Formation (Ductility). In: F. H. Wittmann; G. P. A. G. van Zijl, eds.: *Durability of Strain-Hardening Fibre-Reinforced Cement-Based Composites (SHCC),* Springer Netherlands, 2011, 9-39.
[143] van Zijl, G. P. A. G.; Boshoff, W. P., Eds.: *Advances in cement-based materials: proceedings of the International Conference on Advanced Concrete Materials.* AK Leiden, The Netherlands: CRC Press/Balkema, 2009.
[144] van Zijl, G. P. A. G.; Slowik, V.; Toledo Filho, R. D.; Wittmann, F. H.; Mihashi, H.: Comparative testing of crack formation in strain-hardening cement-based composites (SHCC). *Materials and Structures.* 2016, 49(4), 1175-1189.
[145] Visser, C. R.; van Zijl, G. P. A. G.: Mechanical characteristics of extruded SHCC. In: H. W. Reinhardt;A. E. Naaman, eds.: *Fifth International RILEM Workshop on High Performance Fiber Reinforced Cement Composites (HPFRCC5),* Mainz, Germany, Jul 10-13, 2007, 165-173.
[146] Vorel, J.; Boshoff, W. P.: Numerical Modelling of Engineered Cement-Based Composites. In: J. Náprstek; C. Fischer, eds.: *EM 2012: 18th International Conference Engineering Mechanics,* Svratka, Czech, May 14-17, 2012, 1555-1564.
[147] Wang, S.; Li, V. C.: Polyvinyl Alcohol Fiber Reinforced Engineered Cementitious Composites: Material Design and Performances. In: G. Fischer;V. C. Li, eds.: *International RILEM Workshop on High Performance Fiber Reinforced Cementitious Composites in Structural Applications,* Honolulu, USA, May 23-26, 2006, 65-73.
[148] Wang, S.; Li, V. C.: Engineered Cementitious Composites with High-Volume Fly Ash. *Materials Journal.* 2007, 104(3), 233-241.

[149] Werner, L.: *The Cracking Behaviour of Strain Hardening Cement-Based Composites during Quasi-Static Loading,* Project Work, Stellenbosch University/TU Dresden, 2010.

[150] Yang, E.; Wang, S.; Yang, Y.; Li, V. C.: Fiber-bridging Constitutive Law of Engineered Cementitious Composites. *Journal of Advanced Concrete Technology*. 2008, 6(1), 181-193.

[151] Yun, H.; Fukuyama, H.; Yang, H.; Kim, J.; Song, Y.; Kim, S.: Tension stiffening and damage tolerance of strain-hardening cementitious composite (SHCC) tension ties. In: *Proceedings (TR48): 9th International Symposium on High Performance Concrete – Design, Verification & Utilization,* Rotorua, New Zealand, Aug. 11, 2011, 1-8.

[152] Yun, H.; Kim, S. W.; Jeon, E.; Park, W. S.; Fukuyama, H.: Tension Stiffening and Damage Tolerance of Strain-Hardening Cement Composite (SHCC) Tension Ties under Monotonic and Repeated Cyclic Loadings. In: *The 14th World Conference on Earthquake Engineering,* Beijing, China, Oct. 12-17, 2008, 1-9.

A Abbreviations and symbols

Greek letters

$\alpha_{ds1}; \alpha_{ds2}$	hardening properties of the cement paste
α_E	scale of the modulus of elasticity
β_{RH}	coefficient to consider the effect of the curing conditions
β_{as}	time-dependent development of autogenous shrinkage
β_{ds}	time-dependent development of drying shrinkage
β_t	coefficient to assess the contribution of the SHCC
σ_0	maximum fibre bridging stress
σ_1	tensile first cracking stress of SHCC
$\sigma_{1,k}$	5% quantile of the tensile first cracking stress of SHCC
σ_{pc}	fibre bridging stresses
σ_{mu}	matrix strength
σ_{nom}	nominal stress of the composite element
σ_{cast}	measured stress on the casting side of the composite element
σ_s	steel stress
ε_1	tensile strain at first cracking
$\varepsilon_{c,loc}$	strain after tensile softening
ε_{cd}	drying shrinkage strain
$\varepsilon_{cd,0}$	basic shrinkage strain
ε_{ca}	autogenous shrinkage strain
ε_{cs}	total shrinkage strain
ε_{cast}	measured strain on the casting side of the composite element
ε_{con}	measured strain on the form side of the composite element
ε_{ct}	tensile strain of SHCC
ε_s	steel strain
ε_{sh}	shrinkage strain
ε_{sm}	global specimen strain
ε_u	maximum steel strain
ε_{ult}	ultimate tensile strain of SHCC
ε_0	yielding strain of steel reinforcement
δ^*	fibre slip at the end of the activation phase
δ_0	criticl crack width
δ_{ct}	fibre slip at maximum frictional bond stress
δ_f	fibre slip

$\Delta\varepsilon_{cs}$	pre-deformation due to shrinkage
Δ_l	tensile deformation of SHCC
$\Delta_{l,cr}$	tensile deformation at first cracking
η_r	coefficient for considering the shrinkage contribution
ρ_s	reinforcement ratio
$\rho_{s,min}$	minimum reinforcement ratio
τ_b	fibre bond stress
τ_{ba}	fibre adhesive bond stress
τ_{bf}	fibre frictional bond stress.
τ_{bs}	bond stress
$\tau_{b,mean}$	mean bond strength
$\tau_{b,max}$	max bond stress
$\tau_{b,lim}$	allowable bond stress
γ_{cf}	partial safety factor

Latin letters

A_0	initial cross-section of the measurement region
A_c	breaking strain, SHCC surface of cross-section
A_{gt}	total extension
A_s	rebar surface area
b	ratio of the final to the initial stiffness
c	concrete cover
$d_s; \emptyset$	rebar diameter
E_{cm}	modulus of elasticity of SHCC in compression
E_{ct}	modulus of elasticity of SHCC in tension
E_f	fibre modulus of elasticity
E_{hard}	steel hardening modulous
E_s	modulus of elasticity of steel reinforcement
f_c	mean SHCC compressive strength
f_t	SHCC tensile strength
$f_{t,k}$	5 % quantile of SHCC tensile strength
f_{tu}	ultimate tensile strength
F_{cr}	first cracking tensile force
F_{ult}	ultimate tension force
$F_{t,max}$	load capacity of the loading frame

l_{fb}	fibre embedment length
l_{bs}	reinforcement bond length
l_s	length of the process zone
R_e	yield strength of steel
R_m	tensile strength of steel
R_m/R_e	ductility
s	bond slip
s_{max}	maximum bond slip
s_{cr}	crack distance
t	time until testing
V_f	fibre content
w_{cr}	crack width
$w_{cr,max}$	crack width of the largest crack
w_{max}	maximum crack opening
w_u	maximum crack opening at maximum fibre bridging

Abbreviations

CEB	Comité Euro-International du Beton
CEM	cement grade
DIN	German national standard
EN	Euronorm
fib	Federation internationalé du béton
FIP	Fédération Internationalé de la Précontrainte
FRC	fibre-reinforced concrete
GFRP	glass-fibre reinforced polymer
HDPE	high-density polyethylene
HPFRC	high performance fibre-reinforced concrete
LVDT	linear variable displacement transducers
MIP	mercury intrusion porosimetry
OC	ordinary concrete
PA	polyamides
PAN	acrylics
PCE	polycarboxylate ether
PE	polyethylene
PES	polyester
PP	polypropylene
PVA	polyvinyl alcohol
R	parameter for the transition from elastic regime to post-yielding slope

RC	reinforced concrete
RH	relative humidity
RILEM	Réunion Internationale des Laboratoires et Experts des Matériaux, systèmes de construction et ouvrages
SHCC	strain-hardening cement-based composite
SLS	serviceability limit state
SP	super plasticizer
T	temperature
TG	task group
UHPC	ultra high-performance concrete
ULS	ultimate limit state
VA	viscosity agent

B Results of tension tests

Table 1: Surface geometry of steel rebar

Nominal Ø [mm]	**No.**	$h_{s,h}$ [mm]	$h_{s,1/4}$ [mm]	$h_{s,3/4}$ [mm]	c_s [mm]	α [°]	β_1 [°]	b_s [mm]	e [mm]	f_R [-]
10	1	0.68	0.42	0.74	6.5	59.0	59.0	1.0	1.8	0.065
	2	0.75	0.46	0.55	6.5	46.0	62/49	1.1	1.8	
Mean		0.72	0.44	0.65	6.5	52.5	57.0	1.05	1.8	25.0%
14	1	1.07	0.54	0.73	7.5	40.0	57.0	1.3	2.7	0.072
	2	0.93	0.69	0.75	7.7	46.0	67/53	1.8	2.6	
Mean		1.00	0.62	0.74	7.6	43.0	59.0	1.6	2.7	28.6%
16	1	1.26	0.74	0.81	10.5	41.0	59.0	1.6	2.3	0.063
	2	1.22	0.75	0.80	10.5	45.0	68/52	1.6	2.3	
Mean		1.24	0.75	0.81	10.5	43.0	60.0	1.6	2.3	12.5%

Table 2: Steel rebar parameters according to DIN EN ISO 6892-1 (CoV given in parantheses)

Mechanical properties		**Mean**		
nominal Ø	[mm]	10	14	16
effective Ø	[mm]	9.92 (0.20)	13.88 (0.13)	15.96 (0.31)
cross section A_s	[mm²]	77.22 (0.39)	151.32 (0.26)	199.98 (0.62)
yield point extension A_e	[%]	0.025 (7.91)	0.021 (10.63)	0.019 (3.38)
upper yield strength R_{eH}	[MPa]	615.65 (0.91)	573.04 (0.62)	533.62 (0.16)
lower yield strength R_{eL}	[MPa]	604.39 (0.80)	563.31 (1.29)	530.14 (0.50)
extension at maximum force ΔL_m	[mm]	15.26 (2.74)	15.39 (3.88)	14.62 (3.59)
plastic extension at maximum force A_g	[%]	12.39 (2.83)	12.50 (3.97)	11.86 (3.61)
total extension at maximum force A_{gt}	[%]	7.95 (2.74)	7.89 (4.51)	7.33 (7.52)
Maximum force F_m	[kN]	53.00 (0.20)	99.39 (0.61)	127.15 (0.88)
tensile strength R_m	[MPa]	686.32 (0.52)	656.84 (0.59)	635.83 (0.36)
elongation after fracture[1] A_c	[%]	32.12 (30.71)	22.38 (9.75)	25.21 (11.72)
reduction of area[2] Z	[%]	32.12 (30.71)	36.57 (30.73)	32.76 (15.67)
modulus of elasticity[3] E	[MPa]	208,572 (0.42)	198,880 (0.45)	199,236 (3.37)

[1] The horizontal line method was applied [2] Measured on the split specimen [3] secant modulus of elasticity

08D16

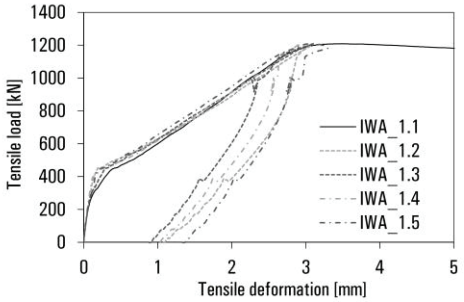

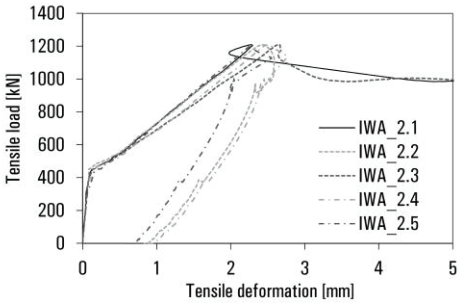

	F_1	$s_{nom,1}$	e_1	F_{tu}	$s_{nom,tu}$	s_{ult}	e_{tu}	E_{sek}
2m	452	1.88	0.020	1209	5.04	1.35	0.276	16936
1m	452	1.88	0.027	1209	5.04	1.35	0.289	17141
mean	452	1.88	0.022	1209	5.04	1.35	0.280	17004

Casting side 1.x

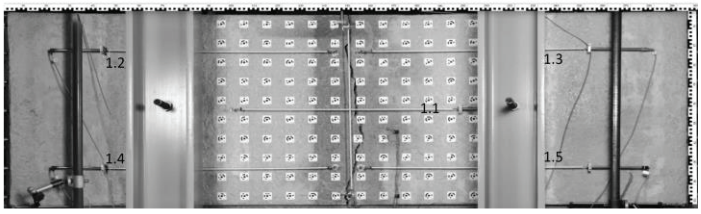

Form side 2.x

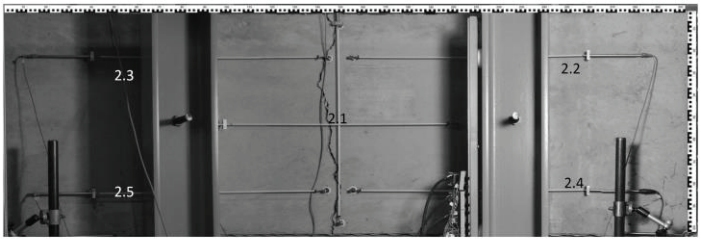

Reinforcement configuration

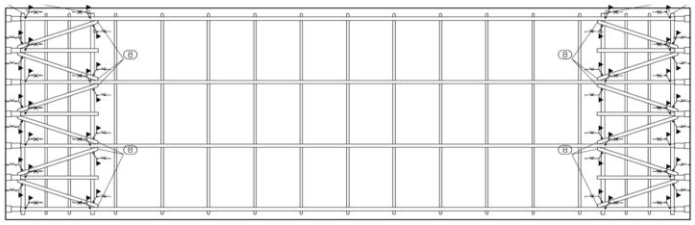

10D14

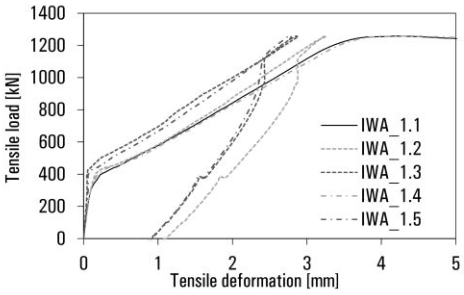

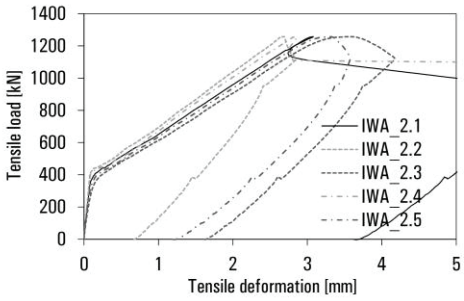

	F_1	$\sigma_{nom,1}$	ε_1	F_{tu}	$\sigma_{nom,tu}$	σ_{ult}	ε_{tu}	E_{sek}
2m	377	1.57	0.012	1053	4.39	1.51	0.299	22146
1m	377	1.57	0.015	1053	4.39	1.51	0.307	23556
mean	377	1.57	0.013	1053	4.39	1.51	0.302	22616

Casting side 1.x

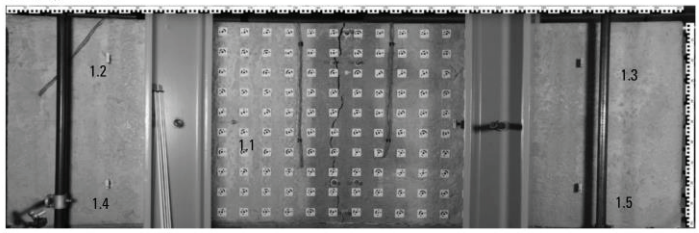

Form side 2.x

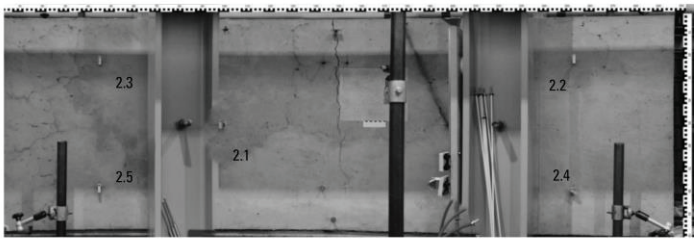

Reinforcement configuration

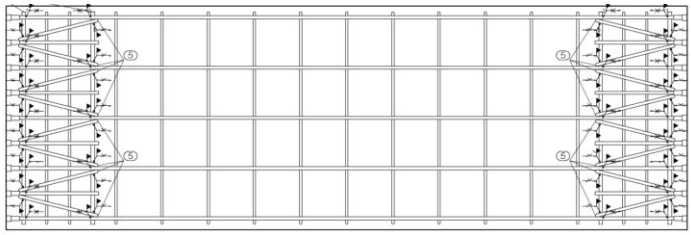

08D14

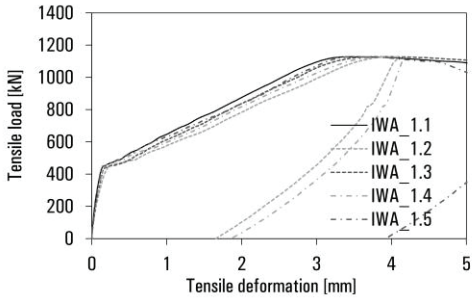

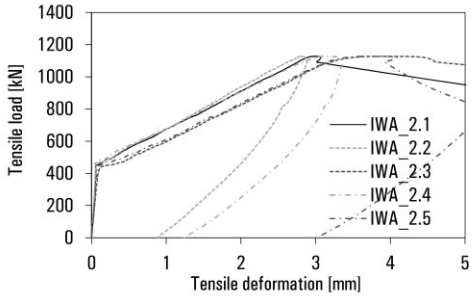

	F_1	$\sigma_{nom,1}$	ε_1	F_{tu}	$\sigma_{nom,tu}$	σ_{ult}	ε_{tu}	E_{sek}
2m	446	1.86	0.014	1125	4.69	1.87	0.345	19509
1m	446	1.86	0.010	1125	4.69	1.87	0.311	21925
mean	446	1.86	0.013	1125	4.69	1.87	0.334	19904

Casting side 1.x

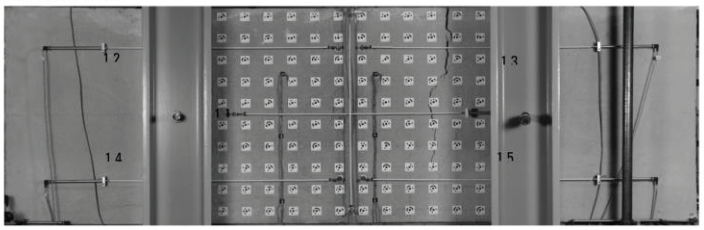

Form side 2.x

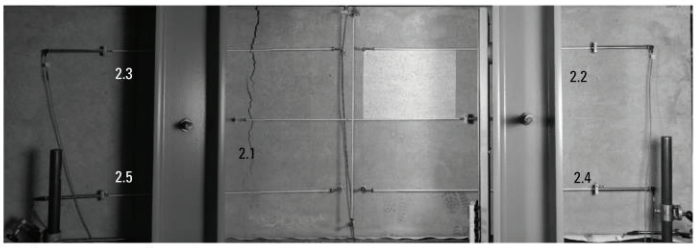

Reinforcement configuration

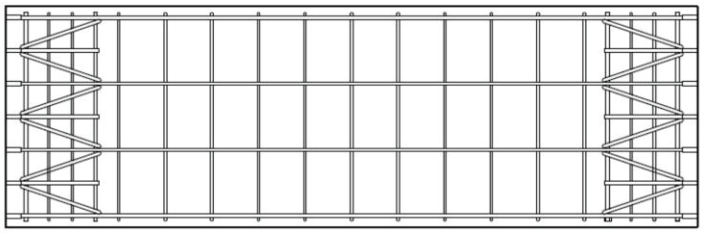

08D10

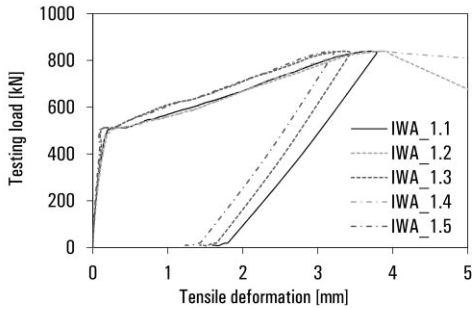

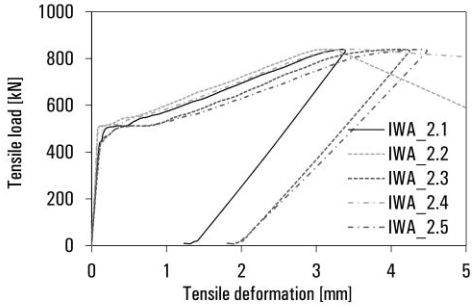

	F_1	$\sigma_{nom,1}$	ε_1	F_{tu}	$\sigma_{nom,tu}$	σ_{ult}	ε_{tu}	E_{sek}
2m	445	1.85	0.011	838	3.49	2.05	0.354	18485
1m	445	1.85	0.013	838	3.49	2.05	0.345	17532
Mean	445	1.85	0.012	838	3.49	2.05	0.351	18167

Casting side 1.x

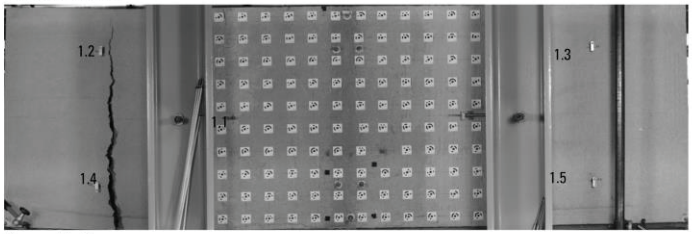

Form side 2.x

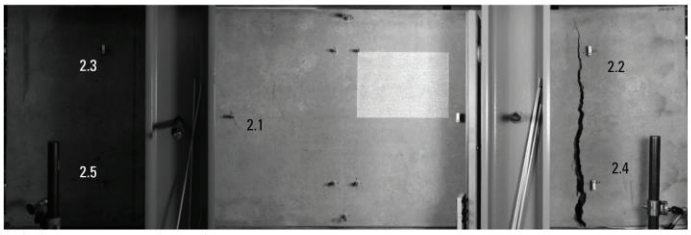

Reinforcement configuration

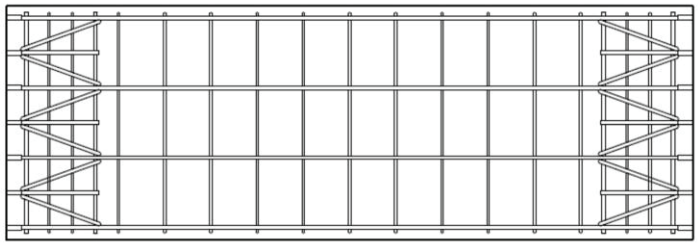

04D20

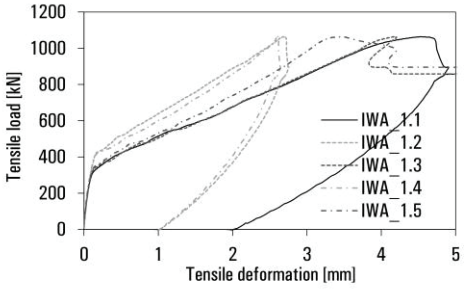

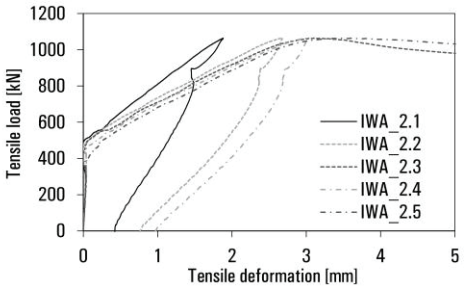

	F_1	$\sigma_{nom,1}$	ε_1	F_{tu}	$\sigma_{nom,tu}$	σ_{ult}	ε_{tu}	E_{sek}
2m	446	1.86	0.014	1125	4.69	1.87	0.345	19509
1m	446	1.86	0.010	1125	4.69	1.87	0.311	21925
mean	446	1.86	0.013	1125	4.69	1.87	0.334	19904

Casting side 1.x

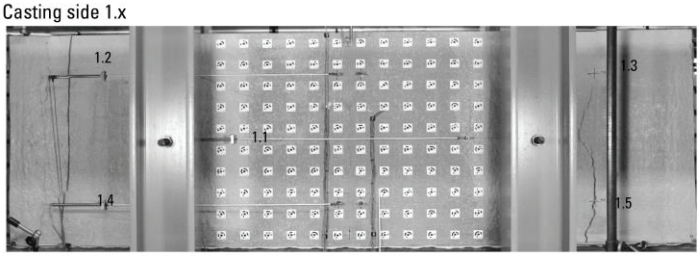

Form side 2.x

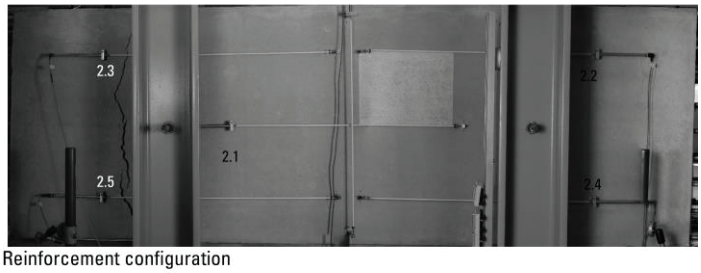

Reinforcement configuration

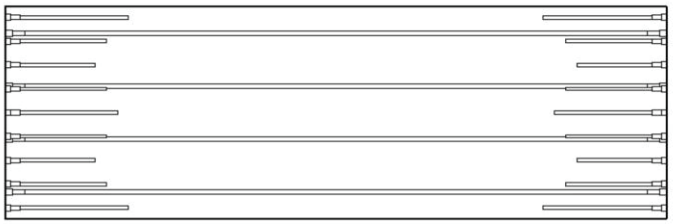

02D20

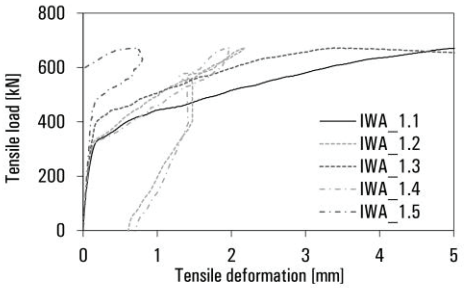

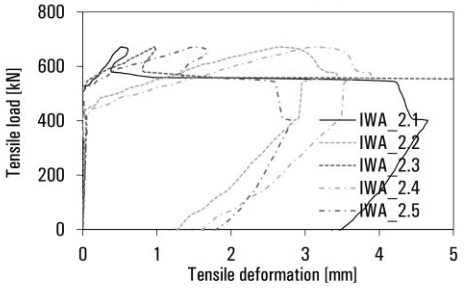

	F_1	$\sigma_{nom,1}$	ε_1	F_{tu}	$\sigma_{nom,tu}$	σ_{ult}	ε_{tu}	E_{sek}
2m	340	1.42	0.010	669	2.79	1.35	0.202	23318
1m	340	1.42	0.012	669	2.79	1.35	0.271	28902
mean	340	1.42	0.011	669	2.79	1.35	0.225	25180

Casting side 1.x

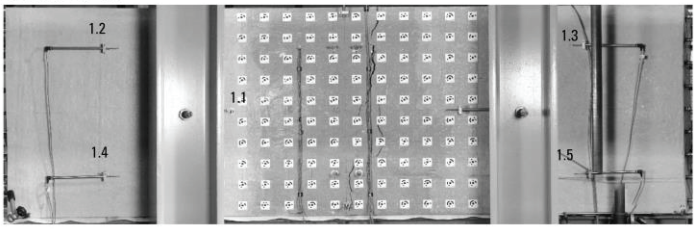

Form side 2.x

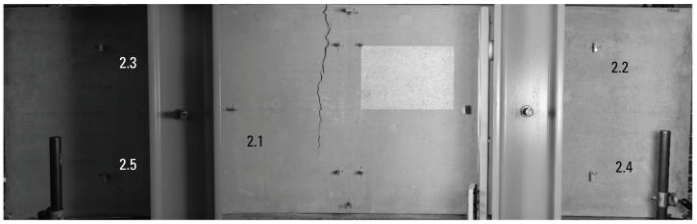

Reinforcement configuration

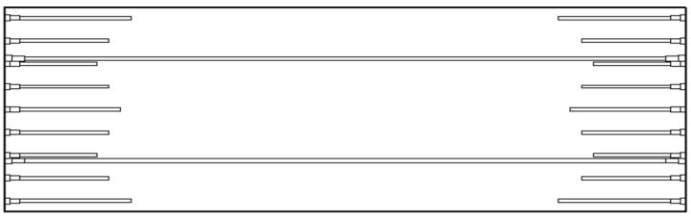

0L-1

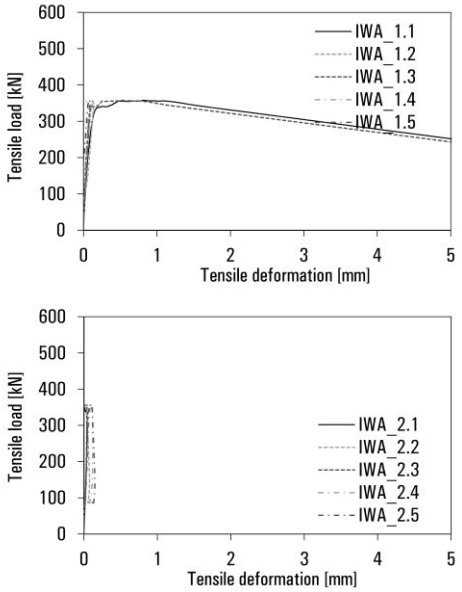

	F_1	$\sigma_{nom,1}$	ε_1	F_{tu}	$\sigma_{nom,tu}$	σ_{ult}	ε_{tu}	E_{sek}
2m	341	1.42	0.008	358	1.49	0.01	0.017	19898
1m	341	1.42	0.017	358	1.49	0.04	0.071	19182
mean	341	1.42	0.011	358	1.49	0.02	0.035	19660

Casting side 2.x

Form side 1.x

0L-2

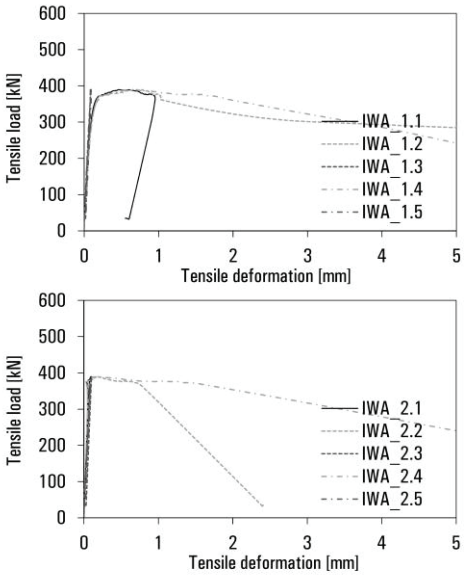

	F_1	$\sigma_{nom,1}$	ε_1	F_{tu}	$\sigma_{nom,tu}$	σ_{ult}	ε_{tu}	E_{sek}
2m	372	1.55	0.011	389	1.62	1.55	0.065	17935
1m	372	1.55	0.012	389	1.62	1.55	0.051	18457
mean	372	1.55	0.011	389	1.62	1.55	0.061	17935

Casting side 2.x

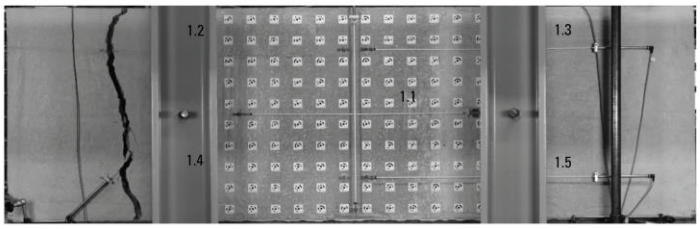

Form side 1.x

C Calculation of shrinkage deformations

The calculation of shrinkage deformations for the specimens tested in this investigation were based on final values for autogenous $\varepsilon_{ca}(\infty)$ and drying shrinkage $\varepsilon_{cd}(\infty)$ derived from shrinkage tests on SHCC specimen. Since shrinkage deformations were found to have a pronounced effect on the tensile behaviour of reinforced SHCC elements further discussions will be presented in regard to the determination of final values for autogenous and drying shrinkage adapted from the calculation of shrinkage in OC.

For constant climate conditions, the total shrinkage deformation can be calculated at a given time according to Eq. (6.2):

$$\varepsilon_{cs} = \varepsilon_{cd} + \varepsilon_{ca} \tag{6.1}$$

Where the drying shrinkage is:

$$\varepsilon_{cd}(t, t_s) = \varepsilon_{cd}(\infty) \cdot \beta_{ds}(t, t_s) \tag{6.2}$$

The final shrinkage can be calculated with:

$$\varepsilon_{cd}(\infty) = \varepsilon_{cd,0} \cdot k_h \tag{6.3}$$

Under consideration of the effect of matrix tensile strength σ_{mu} and the hardening properties of the cement paste with α_{ds1} and α_{ds2} the basic shrinkage strain $\varepsilon_{cd,0}$ can be calculated with:

$$\varepsilon_{cd,0} = 0.85 \left[(220 + 110 \cdot \alpha_{ds1}) \cdot e^{-\alpha_{ds2} \cdot \frac{f_{cm}}{10}} \right] 10^{-6} \cdot \beta_{RH} \tag{6.4}$$

The effect of the curing conditions can be calculated by accounting for the relative humidity RH:

$$\beta_{RH} = -1.55 \left[1.0 - \left(\frac{RH}{RH_0} \right)^3 \right] \tag{6.5}$$

The time-dependent development of drying shrinkage can be determined by Eq. (6.6):

$$\beta_{ds}(t, t_s) = \frac{(t - t_s)}{(t - t_s) \cdot 0.04 \sqrt{{h_0}^3}} \tag{6.6}$$

The factors h_0 and k_h hereby incorporate the effects of geometrical conditions. Autogenous shrinkage can be calculated by:

$$\varepsilon_{ca}(t) = \varepsilon_{ca}(\infty) \cdot \beta_{as}(t) \tag{6.7}$$

Where a linear approach is chosen for the calculation of the final shrinkage depending on the compressive strength of the matrix:

$$\varepsilon_{ca}(\infty) = 2.5(f_c - 10)10^{-6} \tag{6.8}$$

The time-dependent development of autogenous shrinkage can be calculated according to Eq. (6.9):

$$\beta_{as} = 1 - e^{-0.2\sqrt{t}} \tag{6.9}$$

The time-dependent shrinkage behaviour for autogenous and drying shrinkage as shown in Section 3.3.3 was compared to the shrinkage behaviour of OC[35] as shown in Figure 6.1. The comparison between the measured results and the prediction of EN 1992-1-1 reveal a relatively strong deviation between the model and actual material behaviour. This could be expected as the proposed models are based on the shrinkage behaviour of OC with cement class R.

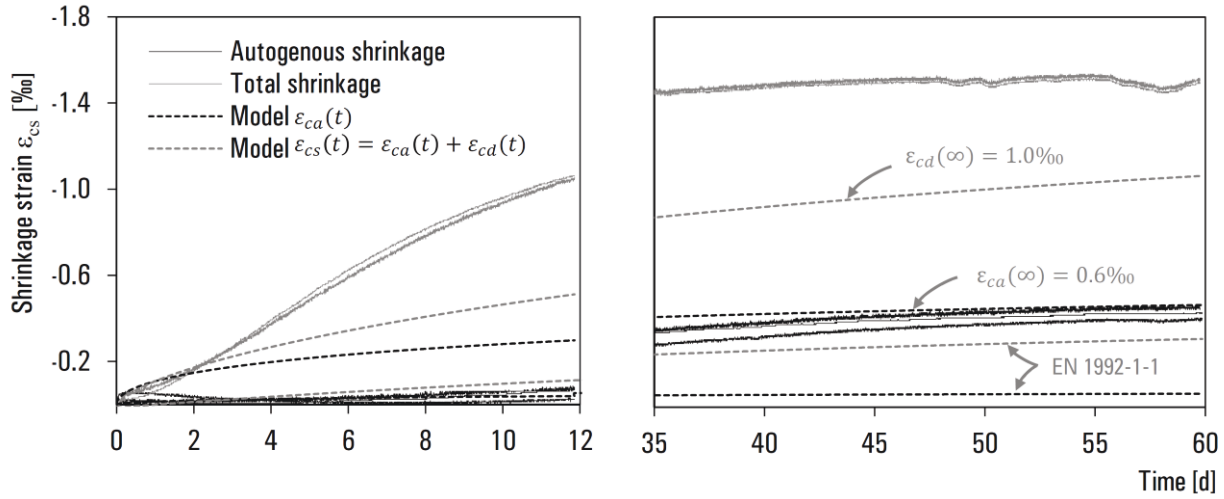

Figure 6.1: Results of total shrinkage and drying shrinkage measurements for different periods of time in comparison to the model data ($h_0 = 2 \cdot A_c/u = 190\ mm, RH = 65\ \%,\ t_s = 1\ d, k_h = 0.85,\ f_{cm} = 42N/mm^2,\ \alpha_{ds1} = 6,\ \alpha_{ds2} = 0.11$)

Due to the different composition with a high content of fines and fly ash the model cannot be transferred to SHCC directly. However, the comparison allows to determine basic model parameters adapted to the measurement results. The linear approach for ultimate autogenous shrinkage underestimates strain levels by approximately 85 %. This is similar to the strain level of drying shrinkage strain, which are underestimated by approximately 50 %.

Based on the measurement results the model parameters were adapted to SHCC with an ultimate strain for autogenous shrinkage of $\varepsilon_{ca} = 0.6$ ‰ and $\varepsilon_{cd} = 1.0$ ‰ for drying shrinkage. The resulting curves are plotted in Figure 6.1.

[35] The shrinkage deformations of OC were estimated according to EN 1992-1-1 [37].

D Crack detection

A detailed analysis of the cracking pattern was conducted to calculate the statistical distribution of the number of cracks, the crack width, crack spacing. The contribution of SHCC to the composite response (tension stiffening) was calculated without consideration of the shrinkage pre-loading which leads to an overestimation of the contribution at yielding strain of the steel reinforcement. However, in this case only the point of the relevant load stage is of interest. Thus, the shrinkage pre-loading can be neglected in this case.

Evaluation of Aramis Data for specimen 08D16 (ρ=0.68)

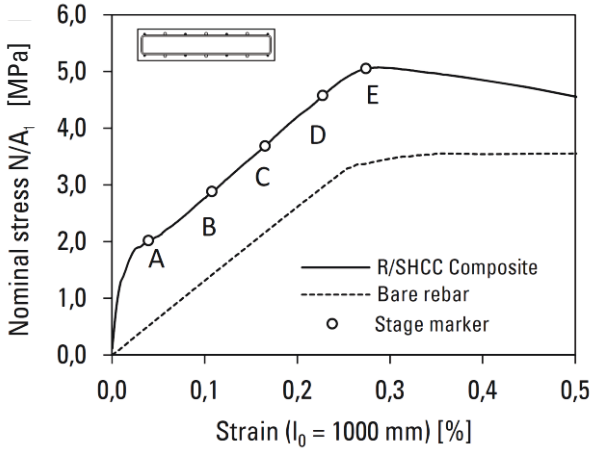

Figure D.2: Composite response

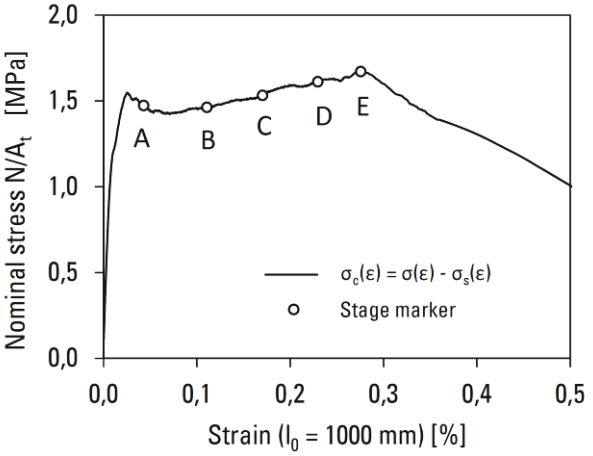

Figure D.3: Contribution of SHCC to the composite response

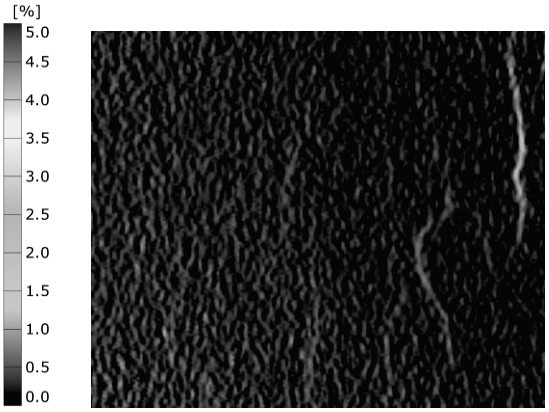

Figure D.4: Stage A (ε = 0.04 %, F$_t$ = 500 kN)

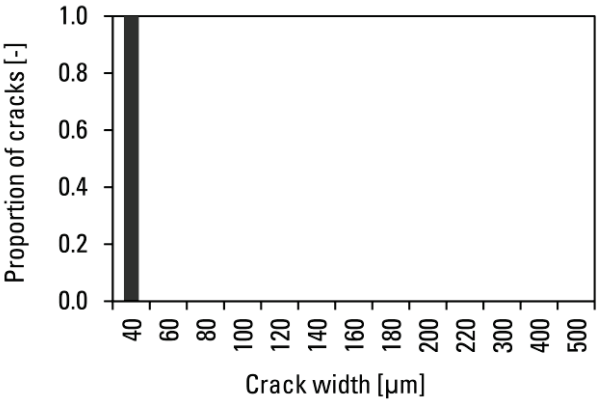

Figure D.5: Stage A (ε = 0.04 %, F$_t$ = 500 kN)

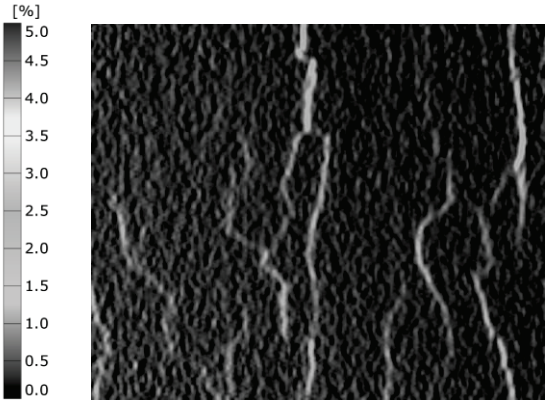

Figure D.6: Stage B (ε = 0.11 %, F$_t$ = 700 kN)

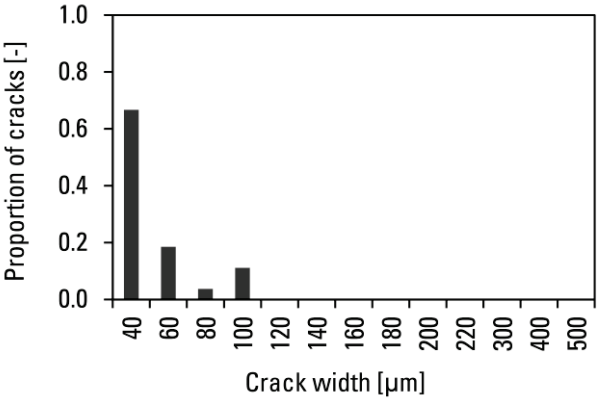

Figure D.7: Stage B (ε = 0.11 %, F$_t$ = 700 kN)

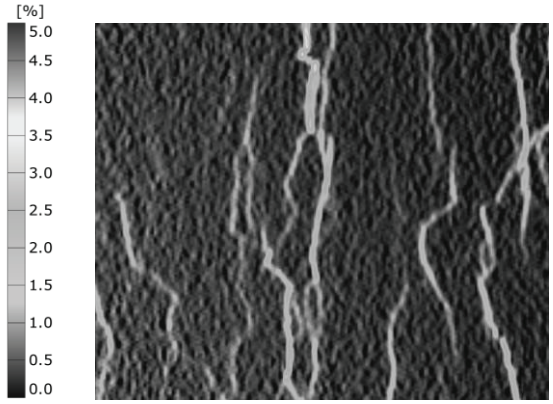

Figure D.8: Stage C (ε = 0.17 %, Ft = 900 kN)

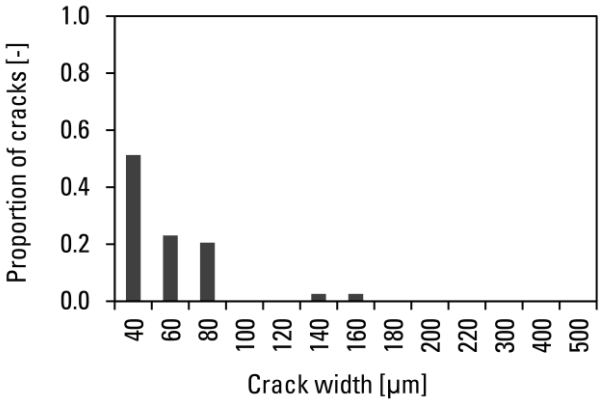

Figure D.9: Stage C (ε = 0.17 %, F_t = 900 kN)

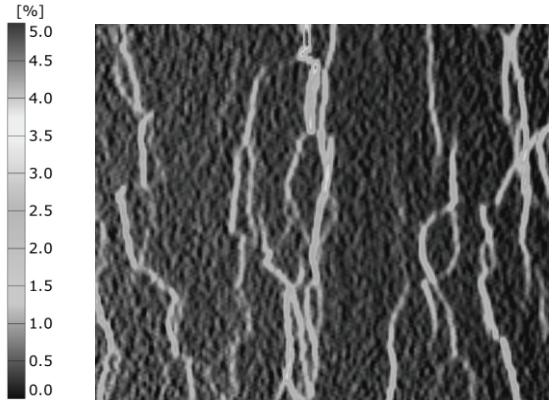

Figure D.10: Stage D (ε = 0.24 %, Ft = 1100 kN)

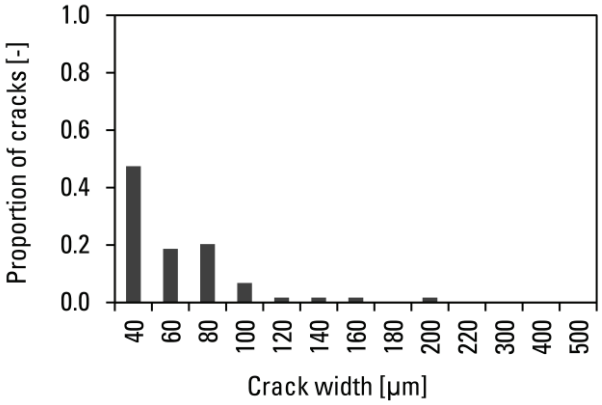

Figure D.11: Stage D (ε = 0.24 %, F_t = 1100 kN)

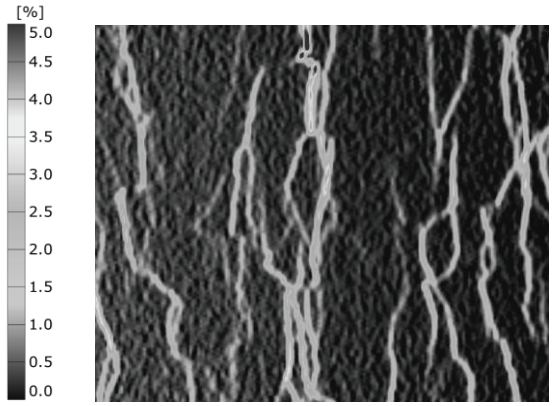

Figure D.12: Stage E (ε = 0.28 %, $F_t = F_{t,ult}$ = 1209 kN)

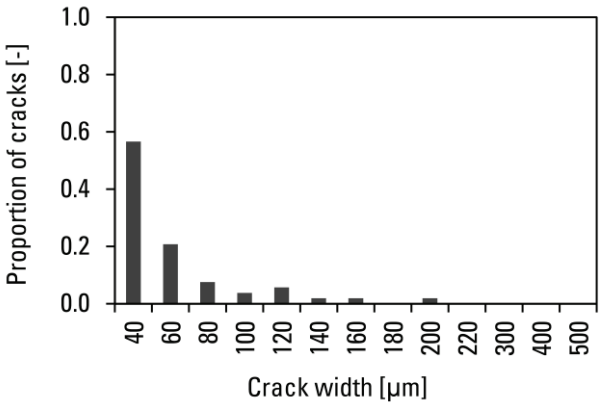

Figure D.13: Stage E (ε = 0.28 %, $F_t = F_{t,ult}$ = 1209 kN)

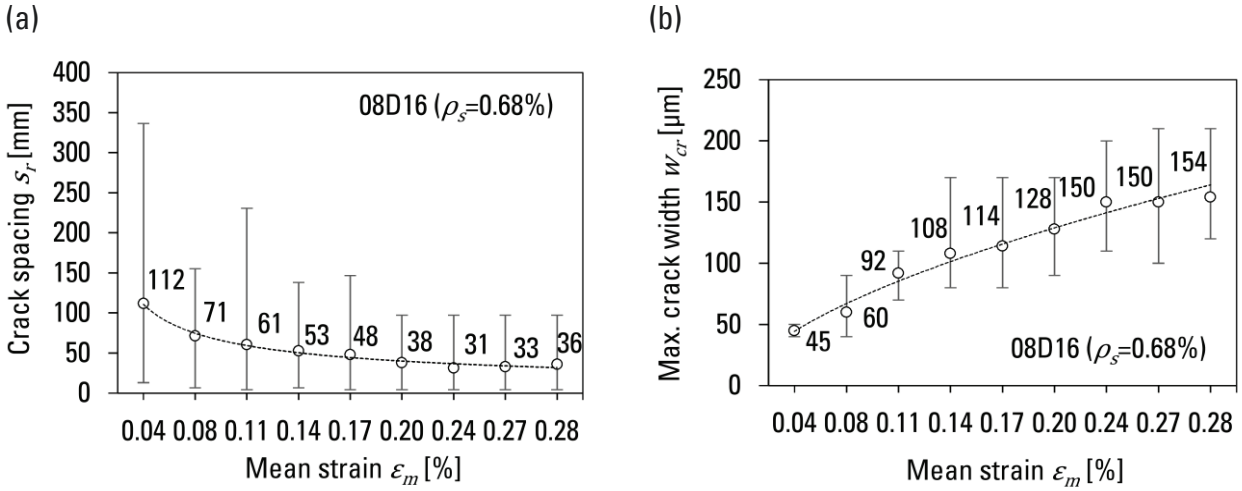

Figure D.14: Results of the calculated data based upon image correlation analyses for specimen 08D16 with
a) development of the maximum, minimum and average crack spacings as mean values for all section lines,
b) development of the maximum, minimum and average crack widths as mean values for all section lines

Evaluation of Aramis Data for specimen 10D14 (ρ=0.65)

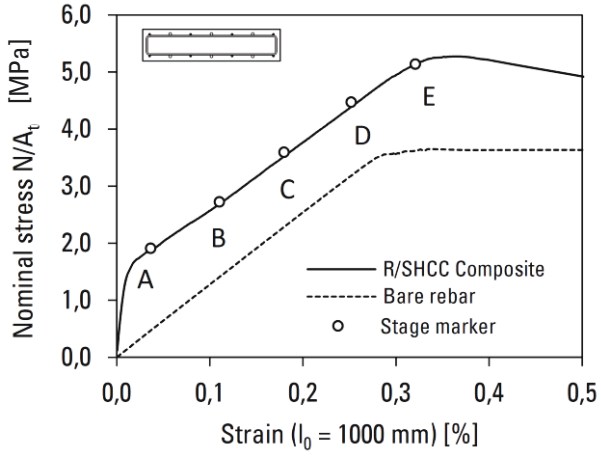

Figure D.15: Composite response

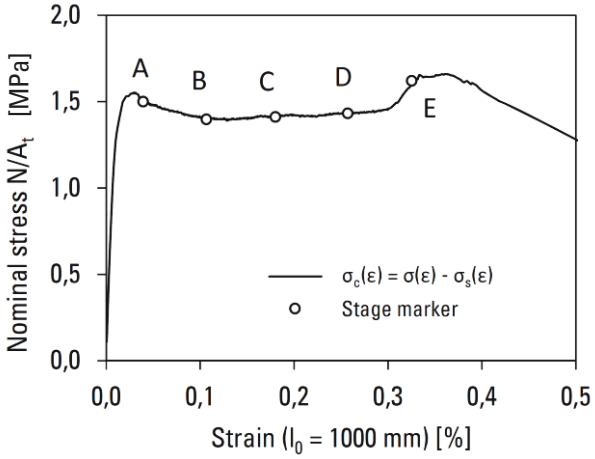

Figure D.16: Contribution of SHCC to the composite response

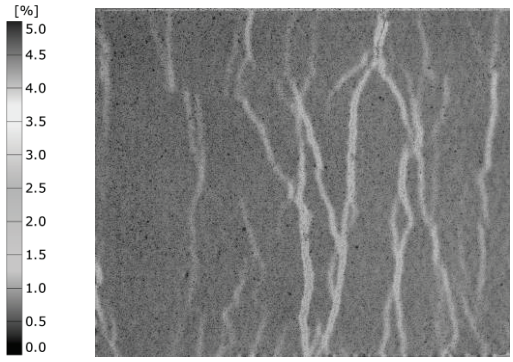

Figure D.17: Stage A (ε = 0.02%; F$_t$ = 500 kN)

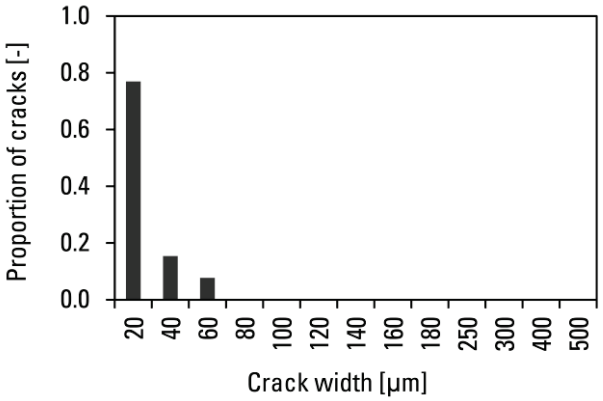

Figure D.18: Stage A (ε = 0.05%, F$_t$ = 500 kN)

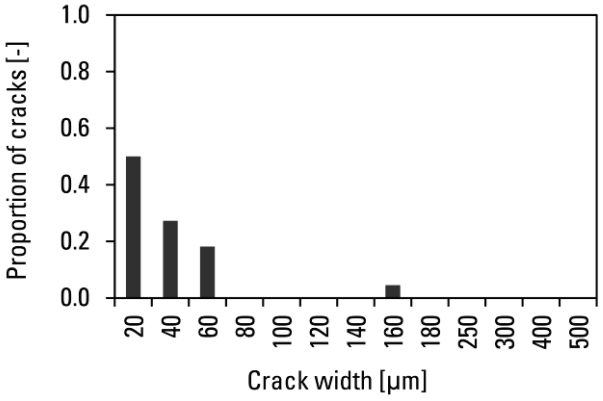

Figure D.19: Stage B (ε = 0.12 %, F$_t$ = 700 kN)

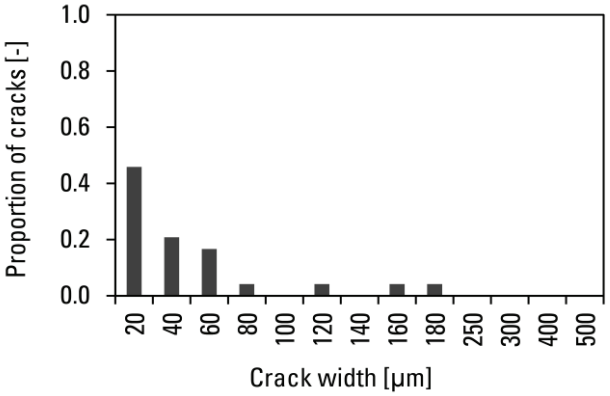

Figure D.20: Stage C (ε = 0.18 %, F_t = 900 kN)

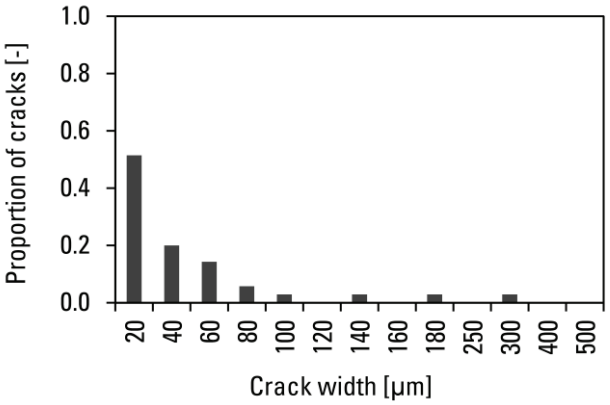

Figure D.21: Stage D (ε = 0.25 %, F_t = 1100 kN)

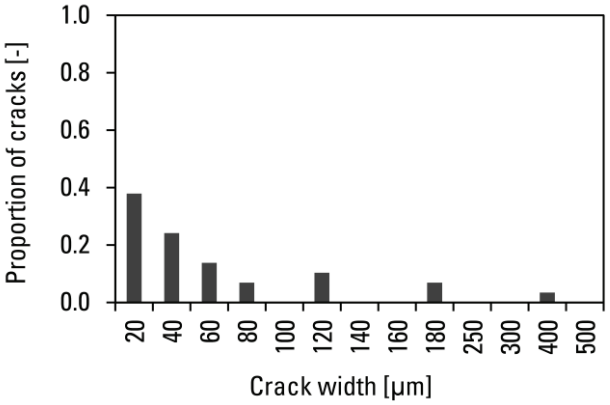

Figure D.22: Stage E (ε = 0.32 %, $F_t = F_{t,ult}$ = 1258 kN)

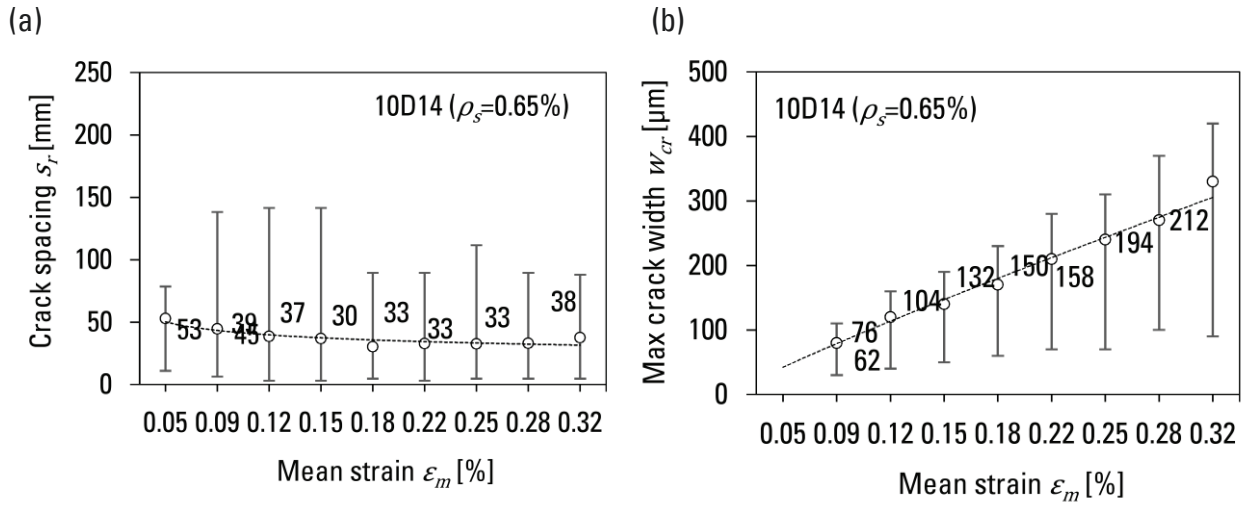

Figure D.23: Results of the calculated data based upon image correlation analyses for specimen 10D14 with
a) development of the maximum, minimum and average crack spacings as mean values for all section lines,
b) development of the maximum, minimum and average crack widths as mean values for all section lines

Evaluation of Aramis Data for specimen 08D14 (ρ=0.52)

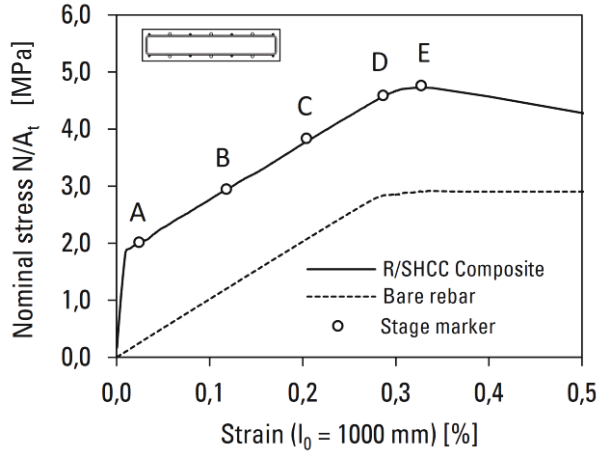

Figure D.24: Composite response

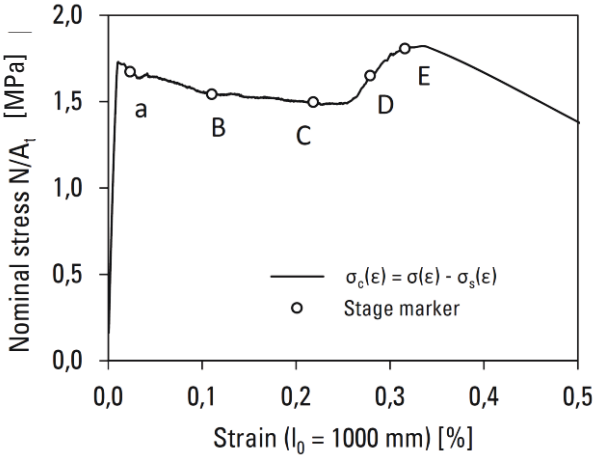

Figure D.25: Contribution of SHCC to the composite response

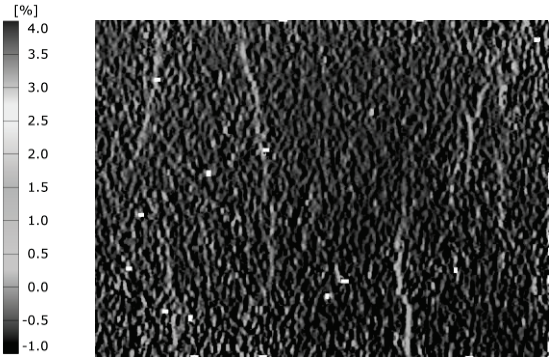

Figure D.26: Stage A (ε = 0.01%, Ft = 500 kN)

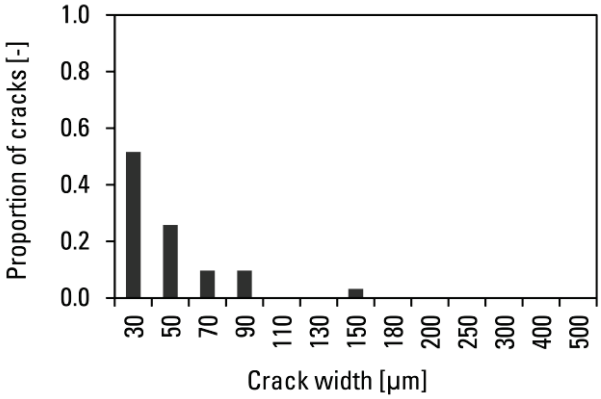

Figure D.27: Stage A (ε = 0.01%, Ft = 500 kN)

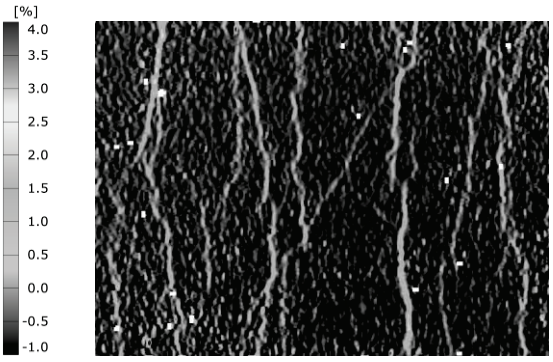

Figure D.28: Stage B (ε = 0.08 %, Ft = 700 kN)

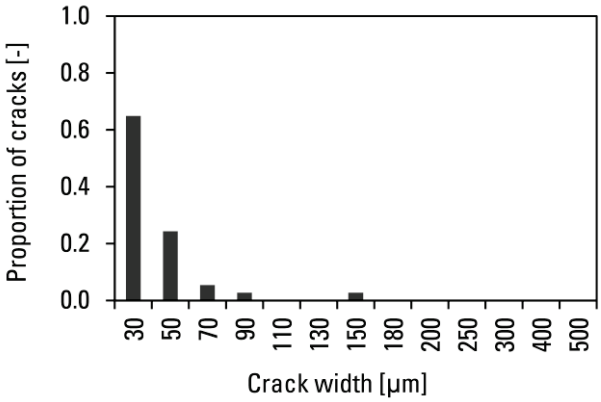

Figure D.29: Stage B (ε = 0.08 %, F$_t$ = 700 kN)

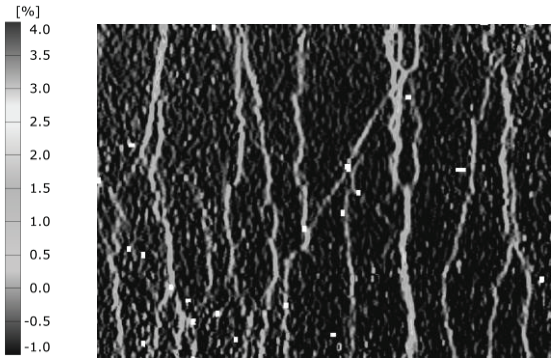

Figure D.30: Stage C (ε = 0.17 %, Ft = 900 kN))

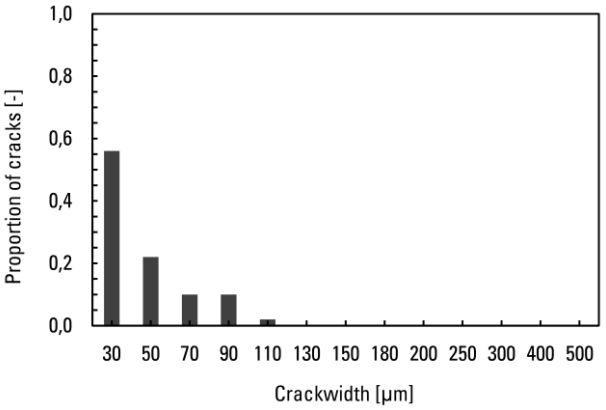

Figure D.31: Stage C (ε = 0.17 %, F_t = 900 kN)

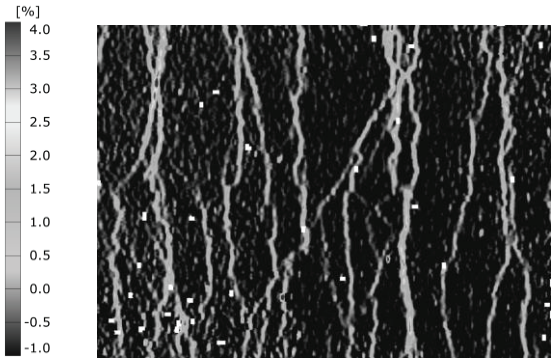

Figure D.32: Stage D (ε = 0.26 %, Ft = 1100 kN)

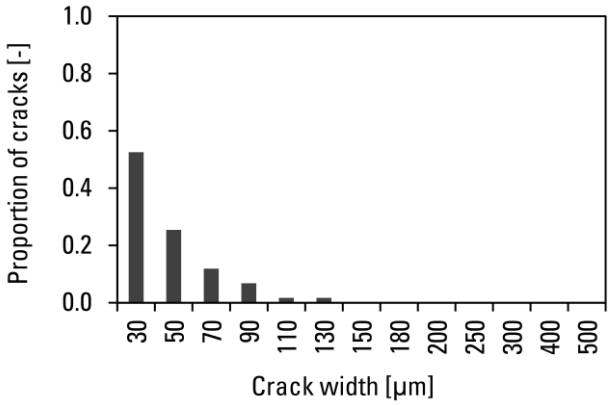

Figure D.33: Stage D (ε = 0.26 %, F_t = 1100 kN)

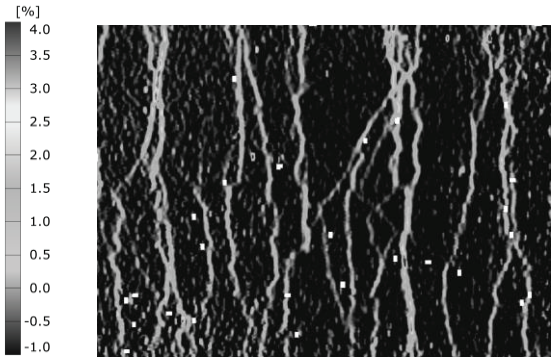

Figure D.34: Stage E (ε = 0.28 %, $F_t = F_{t.ult}$ = 1209 kN)

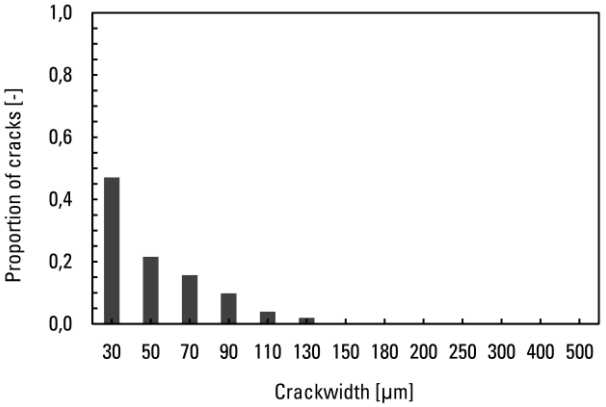

Figure D.35: Stage E (ε = 0.27 %, $F_t = F_{t,ult}$ = 1125 kN)

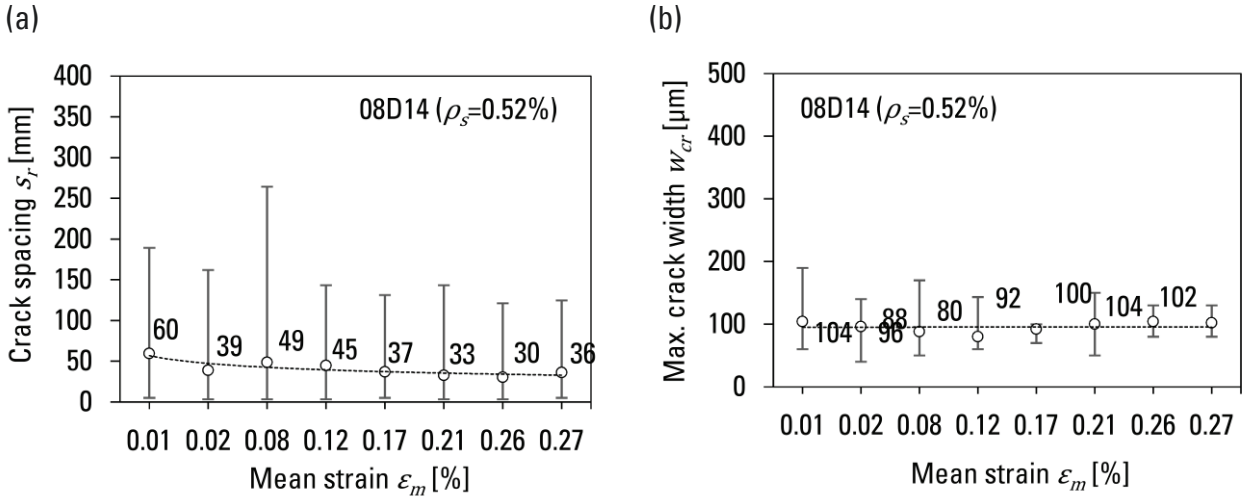

Figure D.36: Results of the calculated data based upon image correlation analyses for specimen 08D14 with
a) development of the maximum, minimum and average crack spacings as mean values for all section lines,
b) development of the maximum, minimum and average crack widths as mean values for all section lines

Evaluation of Aramis Data for specimen 04D20 (ρ=0.53)

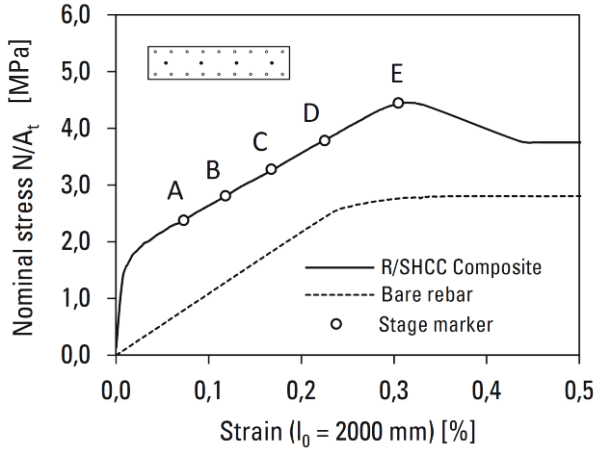

Figure D.37: Composite response

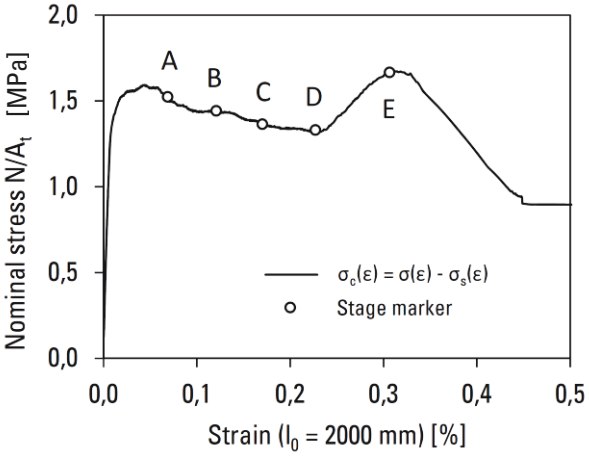

Figure D.38: Contribution of SHCC to the composite response

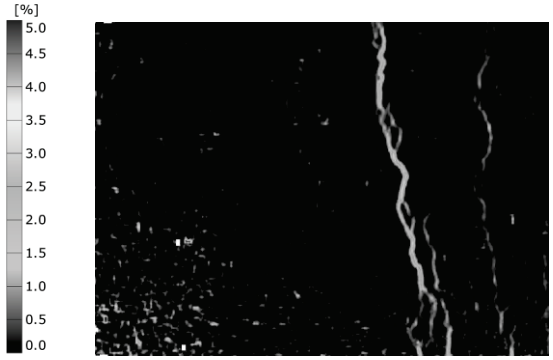

Figure D.39: Stage A (ε = 0.09%; F$_t$ = 600 kN)

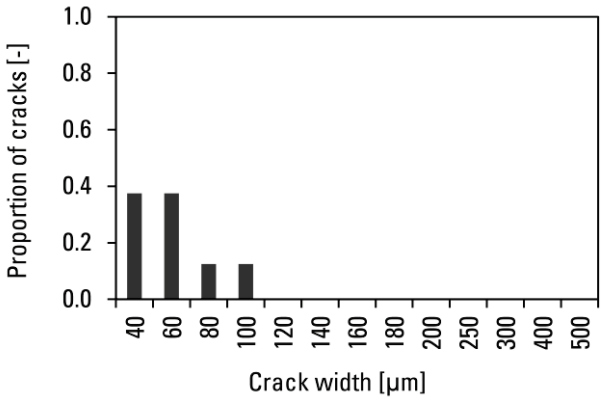

Figure D.40: Stage A (ε = 0.09%, F$_t$ = 600 kN)

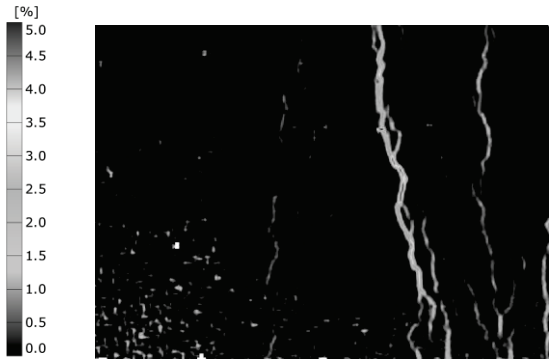

Figure D.41: Stage B (ε = 0.13 %, F$_t$ = 700 kN)

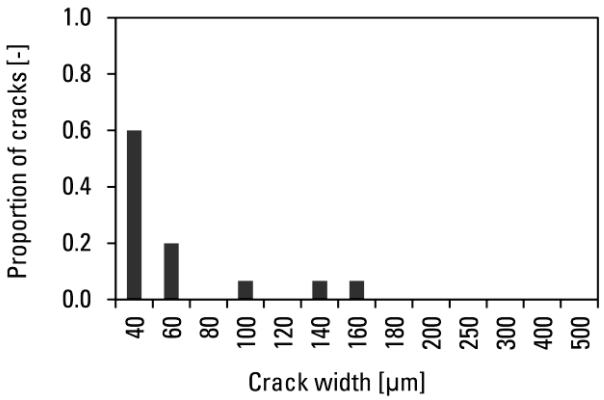

Figure D.42: Stage B (ε = 0.13 %, F$_t$ = 700 kN)

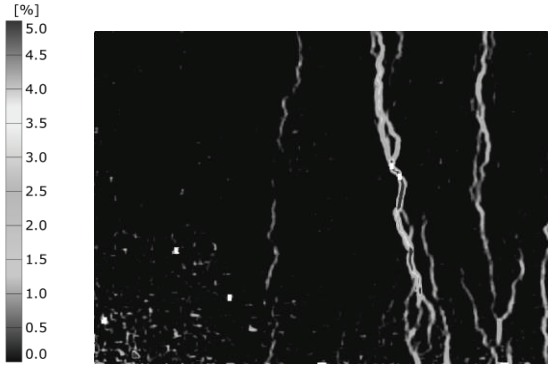

Figure D.43: Stage C (ε = 0.18 %, F_t = 800 kN)

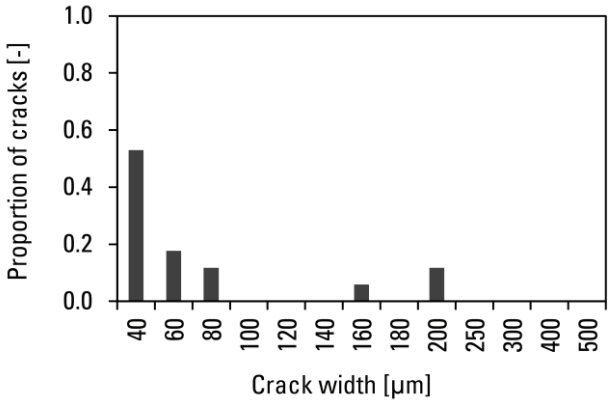

Figure D.44: Stage C (ε = 0.18 %, F_t = 800 kN)

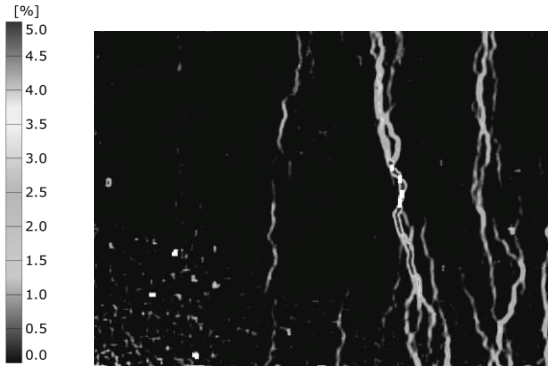

Figure D.45: Stage D (ε = 0.22 %, F_t = 900 kN)

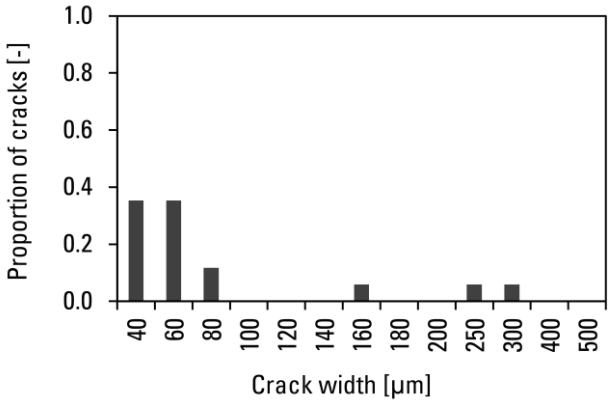

Figure D.46: Stage D (ε = 0.22 %, F_t = 900 kN)

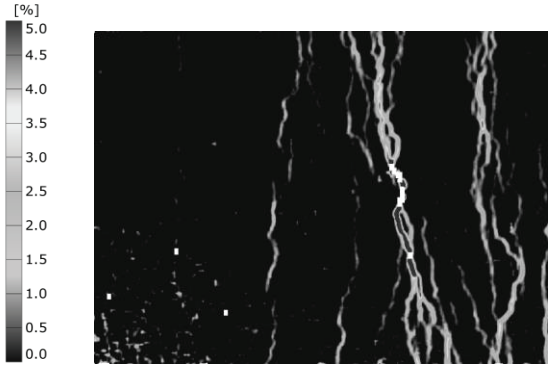

Figure D.47: Stage E (ε = 0.30 %, F_t = $F_{t,ult}$ = 1052 kN)

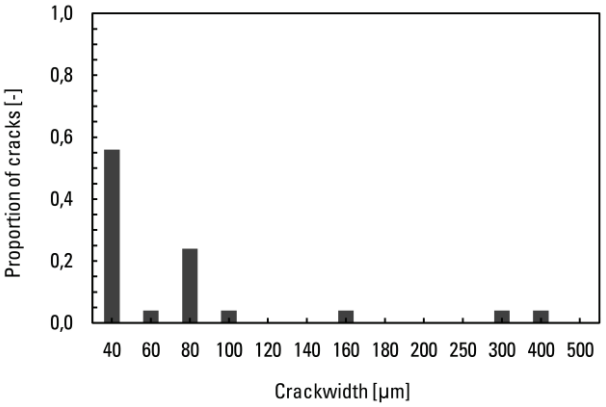

Figure D.48: Stage E (ε = 0.30 %, F_t = $F_{t,ult}$ = 1052 kN)

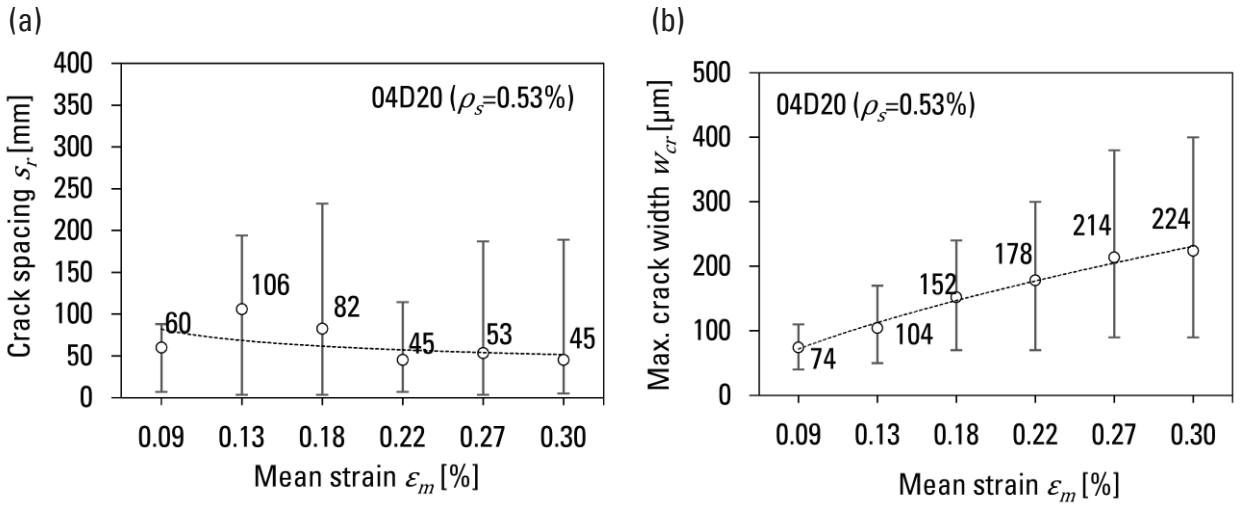

Figure D.49: Results of the calculated data based upon image correlation analyses for specimen 04D20 with
a) development of the maximum, minimum and average crack spacings as mean values for all section lines,
b) development of the maximum, minimum and average crack widths as mean values for all section lines

Evaluation of Aramis Data for specimen 08D10 (ρ=0.26)

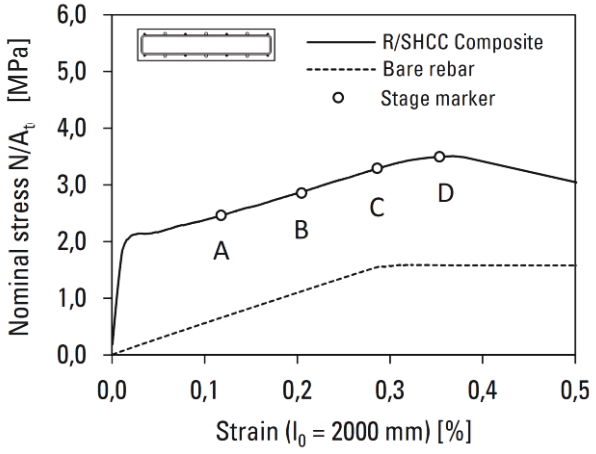

Figure D.50: Composite response

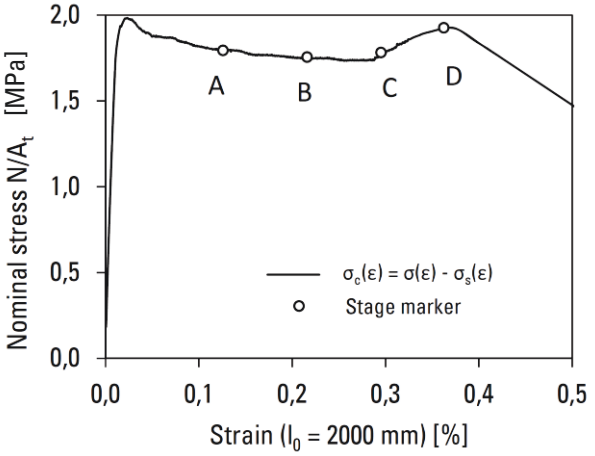

Figure D.51: Contribution of SHCC to the composite response

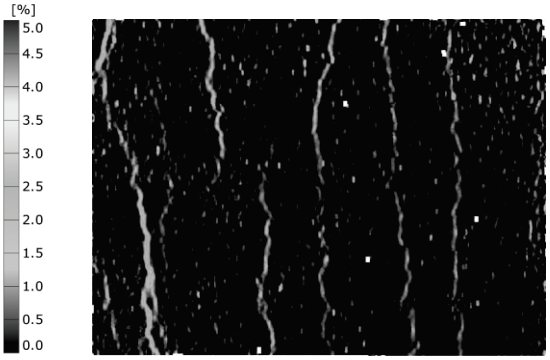

Figure D.52: Stage A (ε = 0.13%; F_t = 600 kN)

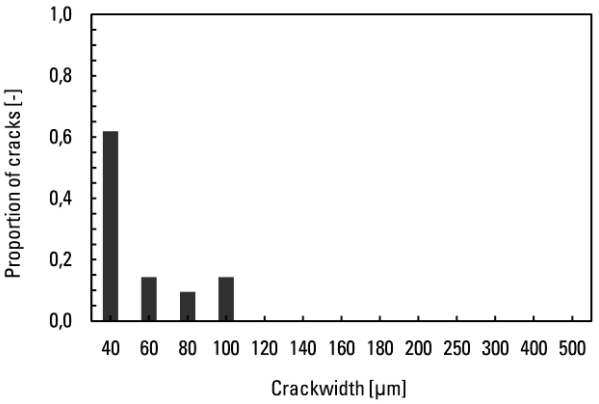

Figure D.53: Stage A (ε = 0.13%,F_t = 600 kN)

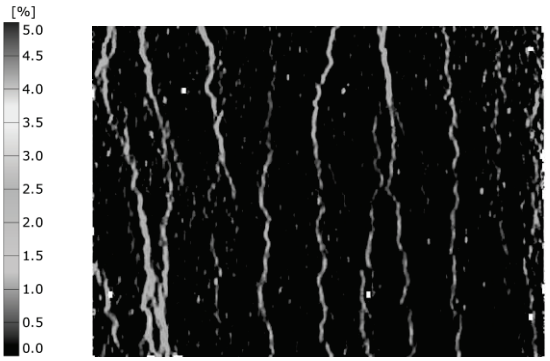

Figure D.54: Stage B (ε = 0.21 %, F_t = 700 kN)

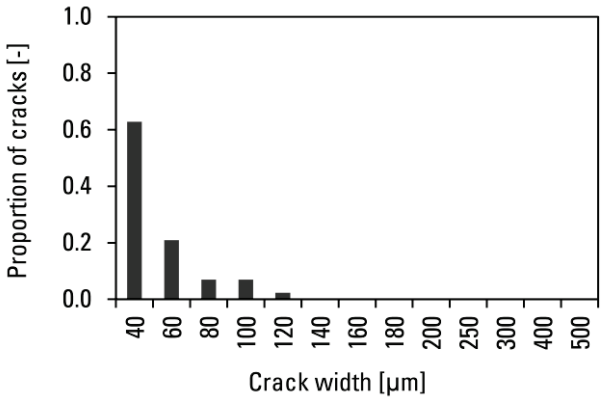

Figure D.55: Stage B (ε = 0.21 %, F_t = 700 kN)

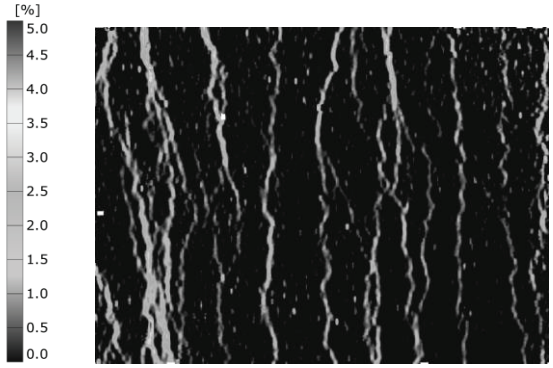

Figure D.56: Stage C (ε = 0.30 %, F_t = 800 kN)

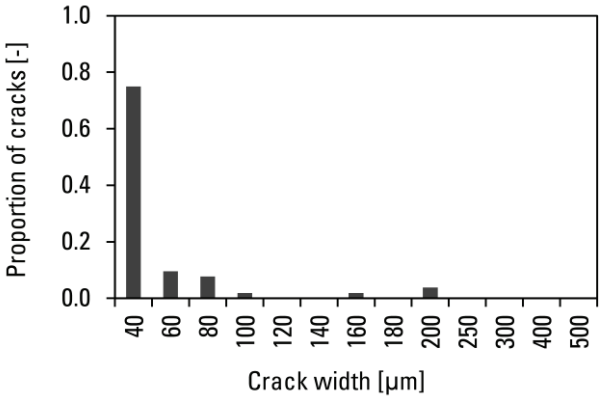

Figure D.57: Stage C (ε = 0.30 %, F_t = 800 kN)

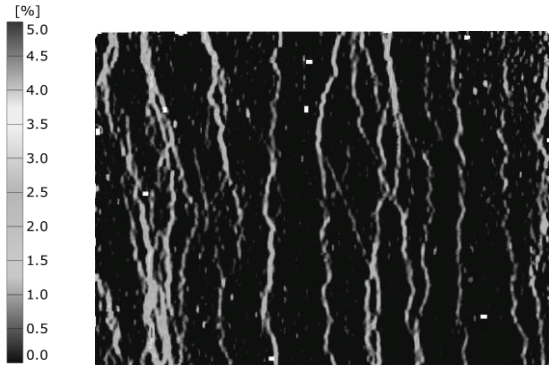

Figure D.58: Stage D (ε = 0.35 %, F_t = $F_{t,ult}$ = 837 kN)

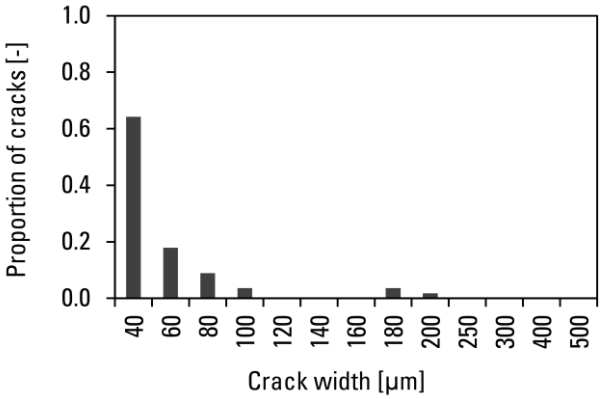

Figure D.59: Stage D (ε = 0.35 %, F_t = $F_{t,ult}$ = 837 kN)

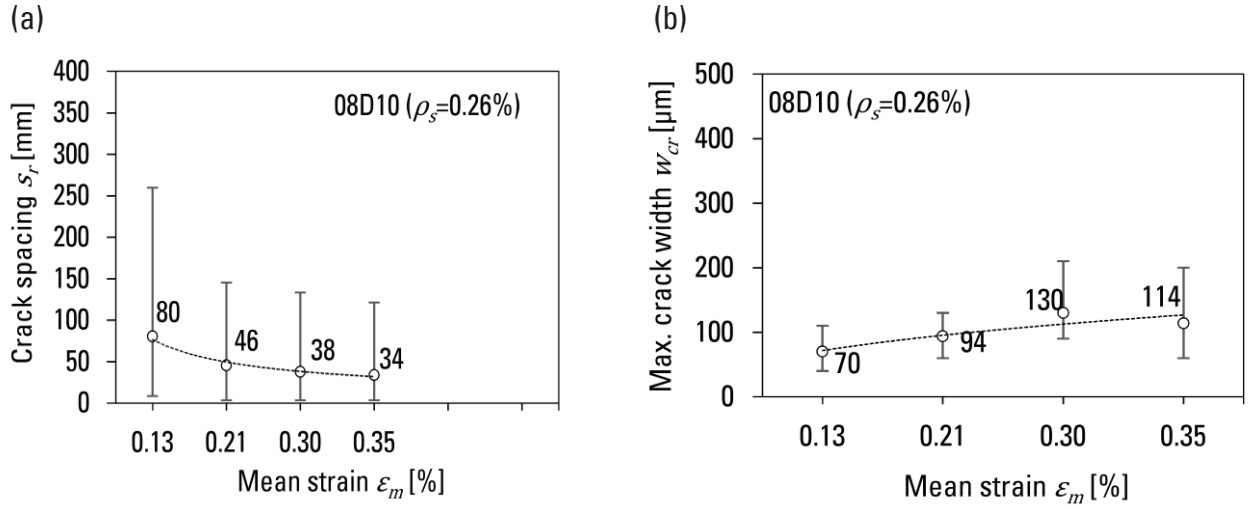

Figure D.60: Results of the calculated data based upon image correlation analyses for specimen 08D10 with
a) development of the maximum, minimum and average crack spacings as mean values for all section lines,
b) development of the maximum, minimum and average crack widths as mean values for all section lines

List of publications

1. Mündecke E., Mechtcherine V.: Untersuchung zum Tragverhalten von zugbeanspruchten Bauteilen aus hochduktilem Beton und Stahlbewehrung. Beton- und Stahlbetonbau. 2015, 110(3), 220-227.

2. Mündecke E.; Mechtcherine V.: Crack development in SHCC elements reinforced with steel bars and subjected to tensile loading. In: E. Schlangen, M.G. Sierra Beltran, M. Lukovic, G. Ye, eds.: Proceedings of the 3rd International RILEM Conference on Strain Hardening Cementitious Composites (SHCC3-Delft), Dordrecht, The Netherlands, Nov. 3.-5., 2014, 401-408

3. Mündecke E.; Mechtcherine V.: Mechanical behaviour of slabs made of strain-hardening cement-based composite and steel reinforcement subject to uniaxial tensile loading. In: J. P. Charron, B. Massicotte, B. Mobasher, G.Plizzari, eds.: Proceedings of the FRC 2014 Joint ACI-fib International Workshop Fibre Reinforced Concrete: From Design to Structural Applications, Jul. 24.-25., 2014, Montreal, Canada, 322-331

4. Mündecke E.; Mechtcherine V.: Tensile bearing behaviour of SHCC elements reinforced with steel bars. In: H. Justnes, eds.: Proceedings of the 1st Concrete Innovation Conference (CIC) 2014, SINTEF Building and Infrastructure; Jun. 11.-13., 2014, Oslo, Norway, 80 (abstract, full paper on CD)

5. Mündecke E.; Mechtcherine V.: Zugtragverhalten von stahlbewehrten Bauteilen aus hochduktilem Beton. In: B. Breitenbücher, P. Mark, eds.: Tagungsband des 54. Forschungskolloquiums des Deutschen Ausschusses für Stahlbeton (DAfStb), Bochum, Nov. 7.-8., 2013, 303-308

Schriftenreihe des Instituts für Baustoffe der TU Dresden

Heft 2009/1	**Marko Butler** Dauerhaftigkeit von Verbundwerkstoffen aus zementgebundenen Matrices und AR-Glass-Multifilamentgarnen ISBN 978-3-86780-128-7
Heft 2011/1	**Petr Jun** Behaviour of strain-hardening cement-based composites (SHCC) under monotonic and cyclic tensile loading ISBN 978-3-76780-229-1
Heft 2011/2	**Nick Bretschneider** Inverse Analyse zur Ermittlung der bruchmechanischen Eigenschaften entfestigender und verfestigender zementgebundener Werkstoffe ISBN 978-3-00-034863-1
Heft 2012/1	**Matthias Lieboldt** Transport flüssiger und gasförmiger Medien in Betonschichten mit textiler Bewehrung ISBN 978-3-86780-299-4
Heft 2012/2	**Frank Altmann** A durability concept for strain-hardening cement-based composites ISBN 978-3-86780-296-3
Heft 2013/1	**Sergiy Shyshko** Numerical simulation of the rheological behavior of fresh concrete ISBN 978-3-86780-371-7
Heft 2014/1	**Björn Höhlig** Anwendung der Radiowellentechnologie in der Beton-Technik ISBN 978-3-86780-394-6
Heft 2014/2	**Rabea Barhum** Mechanism of the interaction between continuous and short fibres in textile-reinforced concrete (TRC) ISBN 978-3-86780-381-6
Heft 2016/1	**Thomas Thiel** Entwicklung von Cellulosefaser-Leichtbeton (CFLC) und Untersuchung des bruchmechanischen Verhaltens ISBN 978-3-86780-498-1
Heft 2016/2	**Christian Wagner** Dauerhaftigkeitsrelevante Eigenschaften von dehnungsverfestigenden zementgebundenen Reparaturschichten auf gerissenen Betonuntergründen ISBN 978-3-86780-505-6

Heft 2017/1	**Ksenija Vasilic** A numerical model for self-compacting concrete flow through reinforced sections: A porous medium analogy ISBN 978-3-86780-521-6
Heft 2017/2	**Lukasz Dudziak** Mitigating autogenous shrinkage of ultra-high performance concrete by means of internal curing using superabsorbent polymers ISBN 978-3-86780-519-3
Heft 2017/3	**Knut Krenzer** Entwicklung eines Zustandsabhängigen DEM-Stoffmodells zur Nachbildung von Mischprozessen für Frischbeton ISBN 978-3-86780-522-3
Heft 2018/1	**Iurie Curosu** Influence of fiber type and matrix composition on the tensile behavior of strain-hardening cement-based composites (SHCC) under impact loading ISBN 978-3-86780-555-1
Heft 2018/2	**Egor Secrieru** Pumping behaviour of modern concretes – Characterisation and prediction ISBN 978-3-86780-562-9
Heft 2018/3	**Eric Mündecke** Tensile behaviour of steel-reinforced elements made of strain-hardening cement-based composites ISBN 978-3-86780-564-3

Weitere Dissertationen am Institut für Baustoffe, die nicht in der Schriftenreihe erschienen sind:

2011	**Sören Eppers** Assessing the autogenous shrinkage cracking properties of concrete by means of the restrained ring test
2014	**Oliver Millon** Analyse und Beschreibung des dynamischen Zugtragverhaltens von ultrahochfestem Beton